

Advanced Sensing Techniques for Active Structural Acoustic Control

by

Robert L. Clark, Jr.


Dissertation submitted to the Faculty of the
Virginia Polytechnic Institute and State University
in partial fulfillment of the requirements for the degree of

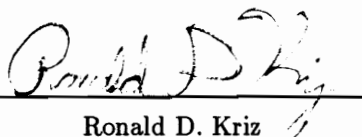
Doctor of Philosophy

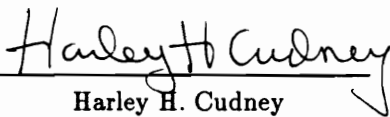
in

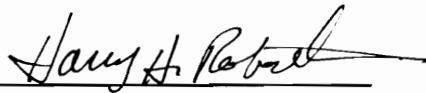
Mechanical Engineering

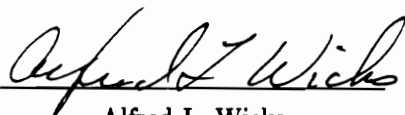
APPROVED:

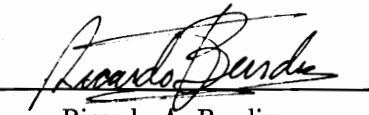

Chris R. Fuller, Chairman


Ronald D. Kriz


Harley H. Cudney


Harry H. Robertshaw


Alfred L. Wicks


Ricardo A. Burdisso

February, 1992
Blacksburg, Virginia

Advanced Sensing Techniques for Active Structural Acoustic Control

by

Robert L. Clark, Jr.

Committee Chairman: Chris R. Fuller

Mechanical Engineering

Abstract

This study presents a basis for the analytical and experimental procedures as well as design techniques required in achieving adaptive structures for active structural acoustic control (ASAC). Test structures studied in this work included a baffled simply supported beam and a baffled simply supported plate which were subjected to a harmonic input disturbance created physically with a shaker and modelled by a point force input. Structural acoustic control was achieved with piezoelectric actuators bonded to the surface of the test structure. The primary focus of this work was devoted to studying alternative sensing techniques in feed forward control applications. Specifically, shaped distributed structural sensors constructed from polyvinylidene fluoride (PVDF), distributed acoustic near-field sensors constructed from PVDF, and accelerometers were explored as alternatives to microphones which are typically implemented as error sensors in the cost function of the control approach. The chosen control algorithm in this study was the feed forward filtered-x version of the adaptive LMS algorithm. A much lower level of system modelling is required with this method of control in comparison to state feedback control methods. As a result, much of the structural acoustic coupling (i.e. system modelling) must be incorporated into the sensor design.

Results from implementation of the alternative structural and acoustic near-field

sensors chosen in this work demonstrate that the sensors can be designed to incorporate the radiation characteristics of the structure in the sensor response. Levels of acoustic attenuation achieved when implementing the chosen alternative sensors rivaled that achieved when implementing microphone error sensors in the cost function of the control algorithm. Thus this work provides a basis for the design methodology required to achieve an adaptive or “smart” structure for active structural acoustic control with integrated actuators and sensors. Each alternative sensor design is reviewed and limitations as well as advantages are discussed in view of the desired application.

Acknowledgements

I would like to thank all who have contributed to this endeavor both technically and personally. First of all, I would like to thank my advisor, Dr. Chris Fuller. He has baffled me many times with his physical insight into complex problems, and I feel that I have truly gained a holistic view of my work as a result of his experience and expertise. I must also thank him for his personal support which was provided a countless number of times at the Cellar, Arnold's and a variety of other local bars. I sincerely hope that I can be as technically stimulating to my students or co-workers and creative in my work as he has been during the course of my dissertation.

Secondly, I would like to thank the remaining committee members, each of whom were chosen based upon their personal interests and technical expertise. I feel fortunate that I could assemble such a committee with varied backgrounds. Technical advise offered by Dr. Ricardo Burdisso has provided much insight into the analytical studies performed in this work. Dr. Al Wicks deserves thanks for his help with the design and implementation of electrical circuits required for signal processing as well as methods of experimental analysis. I thank Dr. Harry Robertshaw for listening to my brain storms and helping me to tie the mathematics and physical implementation of the control process together. I would also like to thank Dr. Harley Cudney for his help with the design and implementation of piezoelectric actuators and sensors as well as discussions pertaining to future career opportunities. Finally, I would

like to thank Dr. Ron Kriz. His expertise in computational visualization techniques stimulated me to look at my work from a variety of perspectives to obtain the most physical information from it as possible, both graphically and technically. I sincerely hope that other graduate students have the same positive experience with their respective committees as I have had with mine.

In terms of sponsors, I am indebted to the Office of Naval Research and DARPA for financial support during the course of this project. In addition, I would like to thank Richard Silcox of NASA Langley for allowing me to conduct research in conjunction with associates under his direction, specifically Gary Gibbs and Don Brown in initial help with implementation of the control algorithms on the digital signal processing board. Technical expertise provided by Don Brown proved invaluable in this work, and I sincerely thank him for all of his help and advice.

I only hope that I don't forget anyone in compiling the remaining list of friends to thank. Gary Gibbs deserves thanks for his help in implementing the model reference control algorithm on the digital signal processing board. Without his assistance I might conceivably still be working on this dissertation. He and his parents have been more than hospitable in my many visits to NASA Langley. My fellow lifting partner and friend Curtis Mitchell deserves thanks for listening to my technical problems even when he wasn't interested and providing plenty of mental distractions during the course of our workout. I would like to thank my office mate, Jeff Viperman for putting up with me and my intense attitude during the course of my work, as well as the conversation on our endless journey to Houston. Bertrand and Yi Gu also helped keep me from falling asleep behind the wheel on that same journey, and I

thank them for that as I am sure they thank me for not falling asleep. I would also like to thank Chris Ruckman for help with graphics programs which provided unique methods of displaying results in this work. I owe much thanks to Dawn Williams for coordinating everything from copying papers to making sure that abstracts for conferences were submitted on time. I do not know if I would have ever published a paper or written this dissertation had not Dr. Robert Wynn provided many hours of his expertise helping me develop the appropriate formats with TEX. His expertise proved invaluable. Finally I would like to thank Dr. Will Saunders for taking time away from his busy schedule to take care of my son when my wife and I needed help as well as providing much physical insight into specifics of my work.

I thank my family for their continual support throughout the course of this work. My parents, Robert and Sharon Clark and my wife's parents, Floyd and Jane Fasnacht provided much help emotionally and financially during this endeavor. Had the mothers not come to help when our son Trey was born, I don't know what we would have done. I should also thank my son, although he doesn't understand now, for being an enjoyable distraction from my work. Naturally I saved the best for last, my wife, Dana. Thank you for providing emotional support throughout this project as well as putting up with me during my emotional highs and lows. Had you not been so forgiving and understanding, I am sure that I would have not completed this work. I sincerely hope that our best years are yet to come.

I thank God for my talents.

Contents

1	Introduction	1
1.1	Piezoelectric Actuators and Sensors	4
1.2	Overview of Sound Radiation from Vibrating Structures	10
1.3	Control Approach	19
1.4	Scope and Objectives	20
1.5	Organization	23
2	Actuator/Sensor Models for Simply Supported Beams and Plates	25
2.1	Theory	26
2.1.1	Point Force Model	27
2.1.1.1	Simply Supported Beam	27
2.1.1.2	Simply Supported Plate	29
2.1.2	Piezoelectric Actuator Model	31
2.1.2.1	Simply Supported Beam	32
2.1.2.2	Simply Supported Plate	35
2.1.3	Total Structural Response	36
2.1.4	Polyvinylidene Fluoride (PVDF) Sensor Models	37
2.1.4.1	Structural Error Sensor	37
2.1.4.1.1	Simply Supported Beam	41

2.1.4.1.2	Simply Supported Plate	42
2.1.4.2	Near-field Sensors	42
2.1.5	Structural Response (Accelerometer Sensor Model)	47
2.1.5.1	Simply Supported Beam	48
2.1.5.2	Simply Supported Plate	48
2.1.6	Acoustic Response (Microphone Sensor Models)	48
2.1.6.1	Simply Supported Beam	50
2.1.6.2	Simply Supported Plate	51
2.1.7	Wavenumber Transform	52
2.1.7.1	Simply Supported Beam	52
2.1.7.2	Simply Supported Plate	54
2.2	Time-Averaged Acoustic Intensity	55
2.3	Summary	56
3	Control Approaches	58
3.1	The Filtered-x Adaptive LMS Algorithm	59
3.1.1	Standard Implementation	59
3.1.2	Model Reference Implementation	62
3.2	Linear Quadratic Optimal Control	65
3.2.1	Standard Implementation	66
3.2.2	Model Reference Approach	68
3.3	Discussion of Practical Implementation and Summary	69
4	Design Approaches for PZT Actuators and PVDF Sensors	73
4.1	Overview of Rectangular Shaped Structural PVDF Sensors	75
4.2	Nonlinear Optimization of Actuator and Sensor Location/Dimension	83

4.2.1	Formulation of Generic Optimization Problem	83
4.2.1.1	Design Variables	86
4.2.1.2	Objective Function	89
4.2.1.3	Equality and Inequality Physical Constraints	90
4.2.1.4	Review of Optimization Procedures	92
4.2.2	Summary of Optimal Design Procedure	94
4.2.3	Optimal Design of Piezoelectric Actuator Locations	95
4.2.4	Optimal Design of PVDF Sensor Location and Dimensions	103
4.2.4.1	PVDF Structural Sensors	103
4.2.4.2	PVDF Acoustic Near-Field Sensors	107
4.2.5	Optimization of Discrete/Distributed PVDF Sensor	113
4.2.6	Summary of Computational Effort	117
4.3	Modal Shaped PVDF Strain Sensor Design Theory	118
4.3.1	Design Approach	118
4.3.2	Practical Implementation	124
4.4	Summary	132
5	Experimental Arrangement	134
5.1	Electro-Mechanical Equipment	135
5.1.1	PZT Actuators	135
5.1.2	PVDF Sensors	137
5.1.2.1	Physical Implementation of Structural Sensors	137
5.1.2.2	Physical Implementation of Acoustic Near-Field Sensors	138
5.1.2.3	Equivalent Electrical Analogies	140
5.1.2.4	Signal Conditioning	140

5.1.2.5	Practical Implementation	148
5.1.3	Controller	158
5.1.4	Instruments Used in Experiments	160
5.2	Structural Equipment	163
5.3	Summary	167
6	Experimental and Analytical Results for ASAC	170
6.1	Overview	171
6.2	Microphone Error Sensors	179
6.2.1	On-Resonance Response (349 Hz)	180
6.2.2	Off-Resonance Response (400 Hz)	187
6.3	Polyvinylidene Fluoride Error Sensors	193
6.3.1	Rectangular Strip PVDF Sensors	195
6.3.1.1	On-Resonance Response (349 Hz)	196
6.3.1.2	Off-Resonance Response (320 Hz)	203
6.3.1.3	Summary of Rectangular Strip PVDF Sensors	210
6.3.2	Optimal Design of Rectangular PVDF Structural Sensors	212
6.3.2.1	Single-Input/Single-Output (550 Hz)	212
6.3.2.2	Three-Input/Three-Output (550 Hz)	219
6.3.2.3	Summary of Optimal Design	225
6.3.3	Shaped Modal PVDF Structural Sensors	227
6.3.3.1	Off-Resonance Response (660 Hz)	230
6.3.3.2	Off-Resonance Response (700 Hz)	233
6.3.3.3	Summary of Modal Shaped PVDF Sensors	235
6.3.4	Optimally Located PVDF Acoustic Near-Field Sensors	237
6.3.4.1	Single-Input/Single-Output (550 Hz)	238

6.3.4.2	Two-Input/Two-Output (550 Hz)	241
6.3.4.3	Summary of Acoustic Near-Field PVDF Sensors . . .	246
6.3.5	Optimally Weighted Discrete/Distributed PVDF Structural Sensors	250
6.3.6	Summary of PVDF Sensors	252
6.4	Accelerometer Error Sensors (Model Reference Control)	254
6.4.1	Off-Resonance Response (320 Hz)	255
6.4.2	Off-Resonance Response (400 Hz)	259
6.4.3	Summary of Model Reference Approach	262
6.5	Discussion of Design Sensitivity	262
7	Conclusions and Recommendations	267
	List of References	271
A	PVDF Acoustic Sensor Model	281
B	Example of Model Reference Uniqueness	291
C	Modal Decomposition	295
D	Assumed Modes Method	299
	Vita	304

List of Figures

1.1	Radiation Efficiency of Plate	12
1.2	Example of k-plane results	15
1.3	Modes of Radiation	17
1.4	Simplified Controller Schematic	21
2.1	Coordinate System for Beam	28
2.2	Coordinate System for Plate	30
2.3	Electrical Configuration of PZT Actuator	33
2.4	Schematic of PVDF Coordinate System	38
2.5	Schematic of PVDF Configured on a Structure	40
2.6	Coordinate System for Near-Field Sensor	44
3.1	Schematic of Filtered-x Adaptive LMS Algorithm	60
3.2	Schematic of Model Reference Filtered-x Adaptive LMS Algorithm	63
3.3	Schematic of Model Reference Implementation	71
4.1	Schematic of Plate with PVDF Sensors and PZT Actuators	80
4.2	Modal Weighting of x-direction PVDF Sensor (PVDF2)	81
4.3	Modal Weighting of y-direction PVDF Sensor (PVDF1)	82
4.4	Flow Chart of Optimization Algorithm	84
4.5	Schematic of Optimal Design Variables	87

4.6	Coordinate System for Objective Function	97
4.7	Schematic of Plate Configured with Optimal PZT Actuators	100
4.8	Schematic of Plate Configured with Optimal PVDF Sensors	104
4.9	Modal Weighting of Single Optimal PVDF Sensor	106
4.10	Schematic of Near-field Sensor Pressure Distribution	108
4.11	Schematic of Optimal Locations of Near-field Sensors	111
4.12	Schematic of Discrete/Distributed PVDF Sensor Array	114
4.13	Modal Weighting of PVDF Sensor Array	116
4.14	Schematic of Modally Shaped 1-D PVDF Sensor	127
4.15	Schematic of Modally Shaped 2-D PVDF Sensor	131
5.1	Picture of Prototype Near-Field Sensor	139
5.2	Schematic Diagram of PVDF Electrical Circuit	141
5.3	Schematic of Voltage Amplifier	143
5.4	Schematic of 3-Mode Sensor	145
5.5	Schematic of Equivalent Circuit for 3-Mode Sensor	146
5.6	Predicted vs Measure Magnitude of FRF for 3-Mode Sensor	150
5.7	Predicted vs Measure Phase of FRF for 3-Mode Sensor	151
5.8	Schematic of Test Apparatus used to Evaluate PVDF Near-Field Sensor	153
5.9	Predicted vs Measure Magnitude of FRF for Near-Field Sensor	154
5.10	Predicted vs Measure Phase of FRF for Near-Field Sensor	157
5.11	Schematic of Instruments Used in Control Approach	162
5.12	Picture of Simply Supported Beam	164
5.13	Picture of Simply Supported Plate	165
5.14	Picture of Plate/Baffle	168

6.1	Schematic of Plate with 3 PZT Actuators	172
6.2	Comparison of Acoustic Directivity Pattern as a Function of Dynamic Range (550 Hz)	174
6.3	Comparison of Acoustic Directivity Pattern as a Function of Mass Loading	178
6.4	Measured Acoustic Directivity Pattern of Plate (349 Hz)	181
6.5	Predicted Acoustic Directivity Pattern (349 Hz)	183
6.6	Measured Modal Response of Plate (349 Hz)	185
6.7	Wavenumber Transform of Measured Modal Response (349 Hz) . . .	188
6.8	Measured Acoustic Directivity Pattern of Plate (400 Hz)	189
6.9	Predicted Acoustic Directivity Pattern (400 Hz)	191
6.10	Measured Modal Response of Plate (400 Hz)	192
6.11	Wavenumber Transform of Measured Modal Response (400 Hz) . . .	194
6.12	Predicted Acoustic Directivity Pattern of Plate (349 Hz)	197
6.13	Measured Acoustic Directivity Pattern of Plate (349 Hz)	198
6.14	Measured Modal Response of Plate (349 Hz)	200
6.15	Wavenumber Transform of Measured Modal Response (349 Hz) . . .	202
6.16	Predicted Acoustic Directivity Pattern of Plate (320 Hz)	204
6.17	Measured Acoustic Directivity Pattern of Plate (320 Hz)	205
6.18	Measured Modal Response of Plate (320 Hz)	207
6.19	Wavenumber Transform of Measured Modal Response (320 Hz) . . .	209
6.20	Predicted Acoustic Directivity Pattern with 1 Actuator (550 Hz) . . .	214
6.21	Measured Acoustic Directivity Pattern with 1 Actuator (550 Hz) . . .	215
6.22	Measured Modal Response of Plate with 1 Actuator (550 Hz)	217

6.23	Wavenumber Transform of Measured Modal Response with 1 Actuator (550 Hz)	218
6.24	Predicted Acoustic Directivity Pattern with 3 Actuators (550 Hz) . .	220
6.25	Measured Acoustic Directivity Pattern with 3 Actuators (550 Hz) . .	222
6.26	Measured Modal Response of Plate with 3 Actuators (550 Hz)	223
6.27	Wavenumber Transform of Measured Modal Response with 3 Actuators (550 Hz)	224
6.28	Acoustic Intensity of Uncontrolled Plate Response (550 Hz)	228
6.29	Acoustic Intensity of Controlled Plate Response with 3 Actuators (550 Hz)	229
6.30	Predicted Acoustic Directivity Pattern (660 Hz)	231
6.31	Measured Acoustic Directivity Pattern (660 Hz)	232
6.32	Predicted Acoustic Directivity Pattern (700 Hz)	234
6.33	Measured Acoustic Directivity Pattern (700 Hz)	236
6.34	Predicted Acoustic Directivity Pattern (Single-Input/Single-Output, 550 Hz)	239
6.35	Measured Acoustic Directivity Pattern (Single-Input/Single-Output, 550 Hz)	240
6.36	Measured Modal Response of Plate (Single-Input/Single Output, 550 Hz)	242
6.37	Wavenumber Transform of Measured Modal Response (Single-Input/Single-Output, 550 Hz)	243
6.38	Predicted Acoustic Directivity Pattern (Two-Input/Two-Output, 550 Hz)	244

6.39 Measured Acoustic Directivity Pattern (Two-Input/Two-Output, 550 Hz)	245
6.40 Measured Modal Response of Plate (Two-Input/Two-Output, 550 Hz)	247
6.41 Wavenumber Transform of Measured Modal Response (Two-Input/Two-Output, 550 Hz)	248
6.42 Predicted Acoustic Directivity Pattern for Distributed PVDF Sensor (550 Hz)	251
6.43 Predicted Acoustic Directivity Pattern (Model Reference, 320 Hz) . .	257
6.44 Measured Acoustic Directivity Pattern (Model Reference, 320 Hz) . .	258
6.45 Predicted Acoustic Directivity Pattern (Model Reference, 400 Hz) . .	260
6.46 Measured Acoustic Directivity Pattern (Model Reference, 400 Hz) . .	261
6.47 Example Frequency Response Function (Simply Supported Plate) . .	264
D.1 Schematic of Plate Configured with Mass and Spring Boundaries . . .	300

List of Tables

2.1	Material Properties of Piezoceramic Material G-1195	32
2.2	Material Properties of Polyvinylidene Fluoride	39
4.1	Material Properties of Steel Plate	95
4.2	Theoretical and measured plate resonant frequencies, f_{mn}	96
4.3	Coordinates for Evaluating Objective Function	99
4.4	Positions of Optimally Designed PVDF Sensors	105
4.5	Design Normalized Modal Sensor Weighting Distribution for Simply Supported Beam.	128
5.1	Theoretical vs. Experimental Resonant Frequencies for Simply Supported Beam.	166

Nomenclature

Symbol	Definition	Unit
A	surface area	m^2
a	radius of curvature of cylindrical plate	m
c	speed of sound in medium	m/s
E	Young's modulus	N/m^2
e_{31}	stress per charge constant in x-direction	C/m^2
e_{32}	stress per charge constant in y-direction	C/m^2
h	thickness of structure	m
\bar{I}	time averaged acoustic intensity	W/m^2
k	acoustic wavenumber	$1/m$
k_x	structural wavenumber component in x-direction	$1/m$
k_y	structural wavenumber component in y-direction	$1/m$
k_s	structural wavenumber	$1/m$
L	length of near-field sensor in x-direction	m
L_x	length of structure in x-direction	m
L_y	length of structure in y-direction	m
\bar{P}	time-averaged power	Nm/s
P_o	polarization profile	
$p(r, \theta, \phi, t)$	acoustic pressure at designated field points	N/m^2
q	response of PVDF sensor	C
S_m	modal sensor weighting for simply supported beam	
S_{mn}	modal sensor weighting for simply supported plate	
u_{mn}	velocity of mn^{th} mode	m/s
u_1	displacement response of cylindrical plate in x-direction	m
u_2	displacement response of cylindrical plate in ϕ -direction	m
u_3	displacement response of cylindrical plate in z-direction	m
V	voltage	V
v_n	normal velocity	m/s

Symbol	Definition	Unit
$W(k_x, k_y)$	wavenumber transform of structural response	m
W_{mn}	modal displacement response	m
W_m^F	modal response of beam due to point force disturbance	m
F	point force input	N
W_{mn}^F	modal response of plate due to point force disturbance	m
F	point force input	N
W_m^P	modal response of beam due to piezoelectric actuator	m
F	point force input	N
W_{mn}^P	modal response of plate due to piezoelectric actuator	m
F	point force input	N
$w(x, y, t)$	time dependent structural response	m
$\ddot{w}(x, y, t)$	time dependent acceleration response	m/s^2

Greek Letters

α	angular dimension of near-field sensor in ϕ -direction	rad
γ_m	$m\pi/L_x$	$1/m$
γ_n	$n\pi/L_y$	$1/m$
ϵ_x	strain in x-direction	
ϵ_ϕ	strain in ϕ -direction	
η	damping coefficient	
Π_{mn}	power radiated by the mn^{th} mode	Nm/s
ν	Poisson's ratio	
ρ_o	density of acoustic medium	kg/m^3
ρ'	mass density per unit length	kg/m
ρ''	mass density per unit area	kg/m
σ	radiation efficiency	
σ_{mn}	radiation efficiency of mn^{th} mode	
ω	circular frequency	rad/s
ω_m	m^{th} resonant frequency of beam	rad/s
ω_{mn}	mn^{th} resonant frequency of plate	rad/s

Chapter 1

Introduction

Only in recent years has our society accepted responsibility for the pollution of our environment and made a conscious effort to correct what seems to be an irreversible act of negligence. To this end, we have recognized that it is much easier to prevent pollution through recycling waste products and regulating industrial and automotive emissions than by trying to bury our problems in a mountain of landfills. While these introductory statements may seem unrelated to the topic of active structural acoustic control (ASAC), upon further inspection, one recognizes that noise is considered environmental pollution. For example, one must simply reside along a busy highway or near an airport to understand the meaning of noise pollution. Certainly our industrial workers operating heavy machinery in large open facilities must wear ear protection to prevent irreversible damage to their ears. While this “passive” means of eliminating noise is very effective on high frequency acoustic transmission, much of the low frequency structure-borne noise simply cannot be attenuated by passive techniques. The end result is a loss or reduction in hearing for people living or working under these conditions as well as a decrease in productivity due to the fatigue induced by this constant annoyance. Realizing that this loss of hearing is an irreversible process, just as much of the damage to our environment is irreversible,

one recognizes that the solution to this problem lies in prevention.

Prevention of this low frequency noise pollution can be achieved with active structural acoustic control (ASAC). Rather than attempting to eliminate the noise once it is airborne by passive techniques (i.e. ear protection, acoustic absorption materials, etc.), active structural acoustic control attacks the problem at the source, on the surface of the vibrating structure. This concept, which was introduced by Fuller (1989(a)), has radically altered our approach to structure-borne noise problems. Coupled with recent advances in digital signal processing and flexible control approaches afforded by adaptive control algorithms such as the filtered-x version of the adaptive LMS algorithm and neural networks, active structural acoustic control is now a reality. This technology has evolved at an interesting time since the concept of “smart structures” emerged almost simultaneously. A “smart structure” is one with both actuators and sensors either embedded within the structure or bonded to the surface with an adaptive control approach which can compensate for changes in input disturbances. In an ideal sense, a “smart structure” is one with a “nervous system” (sensors), a set of “tendons and muscles” (control actuators), and a “brain” (controller) whereby the structure continuously adapts to its changing input stimuli as well as its surrounding environment.

The concept of smart structures can primarily be attributed to recent advances in piezoelectric materials such as lead zirconium titanate (PZT) and polyvinylidene fluoride (PVDF) as well as shape memory alloys (SMA). Due to the bandwidth of operation, the piezoelectric materials are best suited for dynamic active control and will thus be the focus of this work, while the shape memory alloys are better suited

for static or very low frequency applications due to the thermal time constant of the material. Much of the research conducted in recent years has been devoted to developing smart structures for vibration control implementing the PZT material primarily as an actuator and the PVDF material primarily as an error sensor due to the fact that PVDF is approximately four times less dense than PZT and over thirty times more compliant. (This research will be reviewed in detail in the following sections devoted to actuators and sensors.) In general, the same concepts applied to vibration control can readily be achieved for structural acoustic control with the PZT actuators; however, to develop a smart structure with the appropriate distributed sensors complicates the problem.

In the case of vibration control, a sensor configured on the surface of the structure yields an electrical output directly proportional to the quantity to be minimized, the structural response. However, in structural acoustic control, the quantity to be minimized is the radiated sound, and hence the dynamics of the acoustic medium must somehow be incorporated into the sensor design or the control approach. The primary objective of this work is to evaluate different sensing techniques for active structural acoustic control and determine the basis of a design procedure for developing sensors which can be embedded within the structure, bonded to the surface of the structure, or placed in close proximity (i.e. the acoustic near-field) such that a smart structure for ASAC can be achieved.

1.1 Piezoelectric Actuators and Sensors

It is not the intent of this review to document all applications of piezoelectricity; however, to introduce this topic without giving credit to the brothers Jacques and Pierre Curie would be a disservice to the fathers of this science. By the year 1880, they observed that an application of pressure along either the transverse or longitudinal direction of a crystalline structure would lead to the production of an electrical charge in ten types of crystals, including quartz and Rochelle salt (J. Curie and P. Curie 1880). In that same year, Lippmann used the Curies' results to assert that the converse phenomenon should exist (Lippmann 1881), and the Curies experimentally confirmed this assertion by the end of the year (J. Curie and P. Curie 1881). This fundamental work formed the foundation for a diverse variety of scientific instruments such as stabilizers, oscillators, filters, accelerometers and microphone transducers to name a few. Without elaborating in greater detail on the diverse applications or history of piezoelectricity, the reader is referred to an excellent overview of the science by Collins, Miller and von Flotow (1990). For a detailed analysis of the evolution of the science up to 1945, the reader is referred to Cady's text (1964).

In recent decades, this technology has blossomed in the form of ferroelectric materials which are much more sensitive than piezoelectric crystals, yielding greater electro-mechanical coupling due to the combination of the applied electric field and spontaneous polarization. Specifically, ferroelectric ceramics were determined to have greater coupling than quartz, and the polarization is much more stable because they are polycrystals (Collins, Miller and von Flotow 1990). In the early

1940's, Von Hippel and associates at MIT (1946) and Wul of the Soviet Union (1945) independently discovered the first ferroelectric polycrystal in the form of a ceramic, barium titanate ($BaTiO_3$). While the discovery of this material generated much excitement, the Curie temperature of the material was only 120°C , limiting the operating range of the material. The ceramic implemented as a control actuator in this study, lead zirconium titanate (PZT), was discovered in 1954 by Jaffe. Not only does this material exhibit better piezoelectric coefficients than $BaTiO_3$, but it has a higher Curie temperature (340°C vs 120°C) (Jaffe 1971). This material has thus dominated the piezoelectric market for the past few decades and has been the primary material implemented in many recent applications for smart structures.

In terms of piezoelectric polymers, the Japanese were the pioneers in terms of research and development in the 1950s. Fukada (1955) observed the piezoelectric effect in wood and later made the same observation in bone (1957), finding that the piezoelectric constant was approximately twice that of wood. He later documented the same effect in Skin, blood vessels and tissues of the intestines (1968). In 1969, Kawai discovered the piezoelectric effect in polarized films, polyvinylidene fluoride (PVDF). This material displayed a piezoelectric constant (d_{31}) approximately 3 times greater than that of nine other samples tested and little change in the piezoelectric effect was noted in the material over the course of several months. Since this discovery, other polymers have been studied (Wada 1976); however, none have received the attention of PVDF, and thus it has dominated the market in research and applications in current decades. Since this material is 30 times more compliant than PZT and 4 times less dense, it has little effect on the dynamics of stiff structures constructed from materials such as aluminum and steel. Hence it has been

ideally implemented as an error sensor in applications for smart structures where PZT has typically been utilized as a control actuator. These two materials provide a method of implementing both control actuators and sensors directly in the design of the structure (i.e. smart structures).

The reality of smart structures arose from theoretical and experimental work by Swigert and Forward (1981) which involved an “electronic damper” implementing a system of electro-mechanical transducers as elements of electronic feedback loops to control the mechanical vibration of an end supported mast. The structure studied consisted of a hollow fiberglass cylinder called an omni-antenna mast. The concept of applying electronic damping consisted of using piezoceramic sensing transducers mounted to the surface of the structure to detect surface strain and simultaneously amplifying and phase shifting the output of these sensing transducers such that the signals could be used as the input for the driver transducers located elsewhere on the structure. This initial study opened the doors for much of the interest and work in the area of smart structures today.

By 1985, Bailey and Hubbard presented research which implemented PVDF as an active damper for structural vibration control of a cantilever beam. By implementing both constant gain and constant amplitude controllers, Bailey and Hubbard experimentally demonstrated that the PVDF actuator could significantly increase the baseline loss factor (i.e. the natural damping of the structure) when the structure was subjected to an initial displacement at its end (1985). In 1986, Fanson and Chen addressed the problems of vibration control associated with large flexible space structures implementing PZT control actuators, proposing that the “actuators be

built into the structure as dual-purpose structural elements in interest of efficiency and design". In this study, the piezoceramic elements were collocated on the structure (i.e. symmetric about the top and bottom of the beam) and were wired 180° out of phase such that uniform bending was achieved about the neutral axis of the beam when actuated. Crawley and de Luis later modelled the surface-bonded and embedded actuators consisting of lead zirconate titanate (PZT) in cantilever beams (1987), titling their work *Use of Piezoelectric Actuators as Elements of Intelligent Structures*, thus possibly emphasizing naming the science of adaptive, intelligent or smart structures. Following these preliminary works, many studies were devoted to vibration control of one-dimensional structures with PZT and PVDF (Burke and Hubbard 1987), (Plump *et al.*, 1987), (Miller *et al.*, 1990), (Fuller *et al.*, 1990, 1991(a)) and (Clark *et al.*, 1991(a,b)) to name a few.

As the technology evolved, interest in controlling more complicated two-dimensional structures emerged. A theoretical study by Dimitriadis, Fuller and Rogers (1991) resulted in a dynamic model for rectangular shaped PZT actuators which were implemented by collocating to piezoceramic elements symmetrically about the top and bottom of the plate and wired 180° out of phase to produce uniform bending about the neutral axis of the structure. The model was observed to reduce to that of distributed line moments about the boundaries of the actuator due to the applied voltage. The model was later extended for applications in circular coordinates by Dimitriadis and Fuller (1991). During that same period, Lee had been working on models for distributed actuators and sensors constructed from PVDF to achieve critical damping on a cantilevered plate (1989). This work was later followed by a study by Lee and Moon (1990(a,b)) whereby modal sensors and actuators for both

one-dimensional and two-dimensional structures were considered. All experimental work was however restricted to the one-dimensional case. In all of these studies, the distributed sensors and actuators were restricted to vibration control applications in developing smart structures.

The application for smart structures in active structural acoustic control approaches was initiated in 1989(a) by Fuller in a theoretical study which outlined the control of sound transmission and radiation from elastic plates with vibration inputs. This work was rapidly followed by another theoretical study implementing piezoelectric actuators as control inputs for minimizing structure-borne sound (Dimitriadis and Fuller 1991, Fuller 1989(b)). Fuller (1989(c)) followed this theoretical study with a series of experiments implementing a single piezoelectric actuator bonded to the surface of a simply supported plate to control structure-borne sound resulting from a disturbance created with a shaker attached to the structure. These studies were later followed by a variety of theoretical and experimental investigations implementing piezoelectric actuators for controlling sound radiation from vibrating structures (Wang *et al.*, 1991(c)) and (Clark and Fuller 1990(a,b), 1991(c)). The preliminary studies for developing a smart structure for structural acoustic control were in place; however, the microphone error sensors used in the cost function must be replaced with structural sensors to complete the design. A recent study by Baumann *et al.*, (1991) included the structural acoustic coupling by means of *radiation filters* in a broad band state feedback control approach. These *radiation filters* were constructed in the control algorithm from the response of an array of accelerometers distributed on the surface of the structure, converting vibration states to radiation states. The goal of this study is to incorporate the *radiation filters* directly in the

sensor design for feed forward control implementation.

To this end, the objective of this work is to evaluate both structural and acoustic error sensors implemented in the cost function of the multi-channel filtered-x version of the adaptive LMS algorithm. Error sensors considered in this studied are as follows:

1. Microphones,
2. Shaped PVDF sensors,
3. Optimally located and dimensioned rectangular PVDF structural sensors,
4. Optimally located rectangular PVDF acoustic near-field sensors.
5. Accelerometers.

As outlined earlier, design and implementation of structural error sensors for active structural acoustic control approaches must incorporate the coupling between the structure and the acoustic medium in the cost function. To accomplish this task, prior knowledge of the mechanisms of sound radiation from vibrating structures is required. An overview of these mechanisms is presented in the following section to provide the reader with the necessary background for understanding the basic concepts included in the design process.

1.2 Overview of Sound Radiation from Vibrating Structures

Active structural acoustic control can be distinguished from vibration control by one very fundamental parameter, *radiation efficiency*. In vibration control, one must minimize the response of all structural modes if the objective is to reduce the overall response of the structure. However, in structural acoustic control, some structural modes are termed “efficient” acoustic radiators and some are termed “inefficient” acoustic radiators, thus the design objective is modified such that only those structural modes which efficiently couple with the acoustic medium are controlled. This observation, noted in a prior study by Fuller (1989(a)), greatly reduces the dimensionality of the controller. The radiation efficiency of a structure is defined as follows:

$$\sigma = \frac{\bar{P}}{\rho_o c A \langle \bar{v}_n^2 \rangle}, \quad (1.1)$$

where σ is the radiation efficiency, \bar{P} is the radiated acoustic power, ρ_o is the density in the acoustic medium, c is the speed of sound in the acoustic medium, A is the surface area of the vibrating structure, and $\langle \bar{v}_n^2 \rangle$ is the average mean square velocity of the vibrating structure (Fahy 1985). In this particular study, test structures were restricted to simply supported beams and simply supported plates since both the structural response and acoustic response can be obtained analytically. In this case, one can study the radiation efficiency of each structural mode, and this radiation efficiency was previously defined by Wallace (1972(b)) as follows:

$$\sigma_{mn} = \frac{\Pi_{mn}}{\rho_0 c L_x L_y \langle |\bar{u}_{mn}|^2 \rangle} \quad (1.2)$$

where σ_{mn} is the radiation efficiency of the mn^{th} mode, Π_{mn} is the power radiated by the mn^{th} mode, L_x and L_y are the dimensions of the panel in the x and y-direction respectively, and $\langle |\bar{u}_{mn}|^2 \rangle$ is the temporal and spatial average of the square of the velocity of the mn^{th} mode. As an example, the radiation efficiency of a number of the primary modes of the simply supported plate used in this study is presented in the graph of Figure 1.1.

As indicated in the graph, when the structural wavenumber, defined by

$$k_s = \sqrt{\left(\frac{m\pi}{L_x}\right)^2 + \left(\frac{n\pi}{L_y}\right)^2}, \quad (1.3)$$

is less than the acoustic wavenumber, defined by

$$k = \frac{\omega}{c}, \quad (1.4)$$

the radiation efficiency of all modes approaches one. However, when the structural wavenumber is greater than the acoustic wavenumber, the radiation efficiency of each mode is readily distinguished from the other. Specifically, when k/k_s is less than 0.3, the modes with even-even modal indices such as the (2,2) mode are much less efficient than modes with odd-odd modal indices such as the (1,1) mode. Fortunately, in structural acoustic control applications, this is typically the regime of

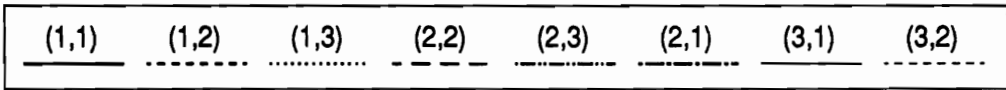
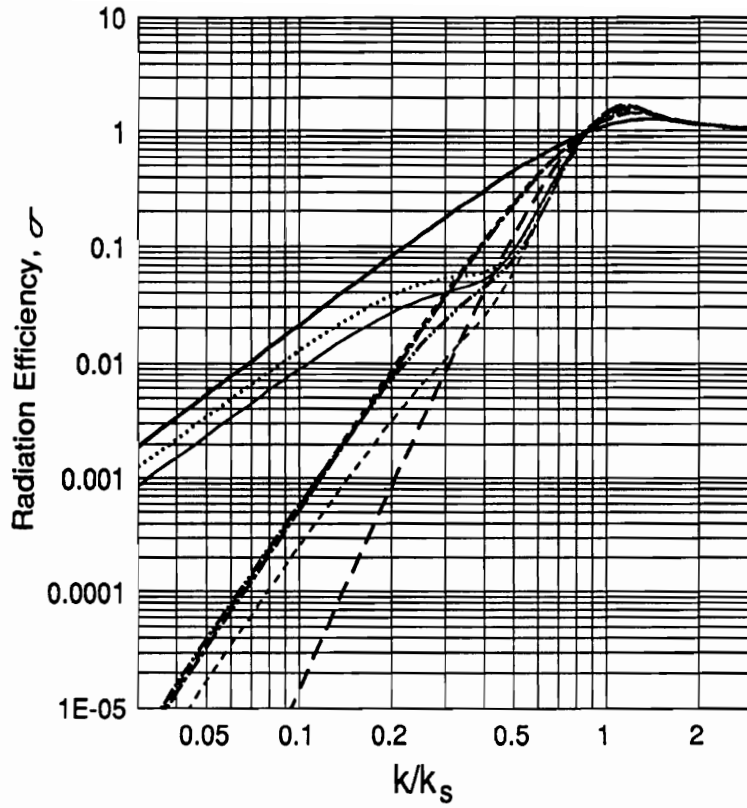


Figure 1.1: Radiation Efficiency of Plate

operation. As a result of this observation, it makes little sense to spend significant effort trying to control the (2,2) mode, when it is several orders of magnitude less efficient than the (1,1), (1,3) or (3,1) structural modes. Hence the dimensionality of the controller is readily reduced, and structural acoustic control is achieved by either *modal suppression* or *modal restructuring*. Both of these terms were previously defined by Fuller *et al.*, (1989(b)). In the case of *modal suppression*, the amplitudes of each structural mode contributing to the response are reduced significantly, thereby reducing the vibration response as well as the acoustic response. However, in the case of *modal restructuring*, the phase relationship between structural modes is restructured such that destructive interference occurs in the acoustic field. In contrast to modal suppression, modal restructuring often results in an increase in the vibration response of the structure. This type of analysis is not restricted to rectangular panels as both circular plates and cylinders can all be characterized by a similar analysis of radiation efficiency.

Another concept worthy of introduction is the wavenumber transform of the structural response. The typical approach used in describing the acoustic field based on the structural response is to study the modal amplitudes of the controlled or uncontrolled structural response. However, as the number of modes included in the structural response increases, physical interpretation of the significance of both the phase and magnitude of each mode becomes more difficult. In addition, the stationary parts of the radiating surface are not included in this form of analysis since the significance of the baffle is not apparent. To alleviate this problem of interpretation, an alternative method of studying the response will be introduced. This method is based on a wavenumber transform, which is analogous to obtaining the frequency

spectrum from a time-dependent signal (Fahy 1985). To obtain the wavenumber transform, a Fourier integral transform of the spatial response is evaluated.

$$F(k_x, k_y) = \int_{-\infty}^{+\infty} \int_{-\infty}^{+\infty} f(x, y) \exp(-jk_x x) \exp(-jk_y y) dy dx \quad (1.5)$$

Replacing $f(x, y)$ with the spatial response of the simply supported plate, given as:

$$w(x, y, t) = W_{mn} \sin\left(\frac{m\pi x}{L_x}\right) \sin\left(\frac{n\pi y}{L_y}\right) \exp(j\omega t), \quad (1.6)$$

and evaluating the integral over the boundaries of the plate, the wavenumber transform is obtained for each mode as follows:

$$W_{mn}(k_x, k_y) = W_{mn} \int_0^{L_x} \int_0^{L_y} \sin\left(\frac{m\pi x}{L_x}\right) \sin\left(\frac{n\pi y}{L_y}\right) \exp(-jk_x x) \exp(-jk_y y) dy dx. \quad (1.7)$$

Plotting the magnitude of this function yields physical insight into the structural acoustic response. An idealized example of a wavenumber spectrum is presented in Figure 1.2 to convey the concepts. In reality, the wavenumber spectrum is defined in two dimension with both positive and negative components; however, the concepts are more readily conveyed in the one-dimensional example presented. The acoustic wavenumber, presented in equation (4), is the critical number defining the region between structural wavenumber components which radiate acoustic energy and components that simply create near-field acoustic disturbances. The radiating

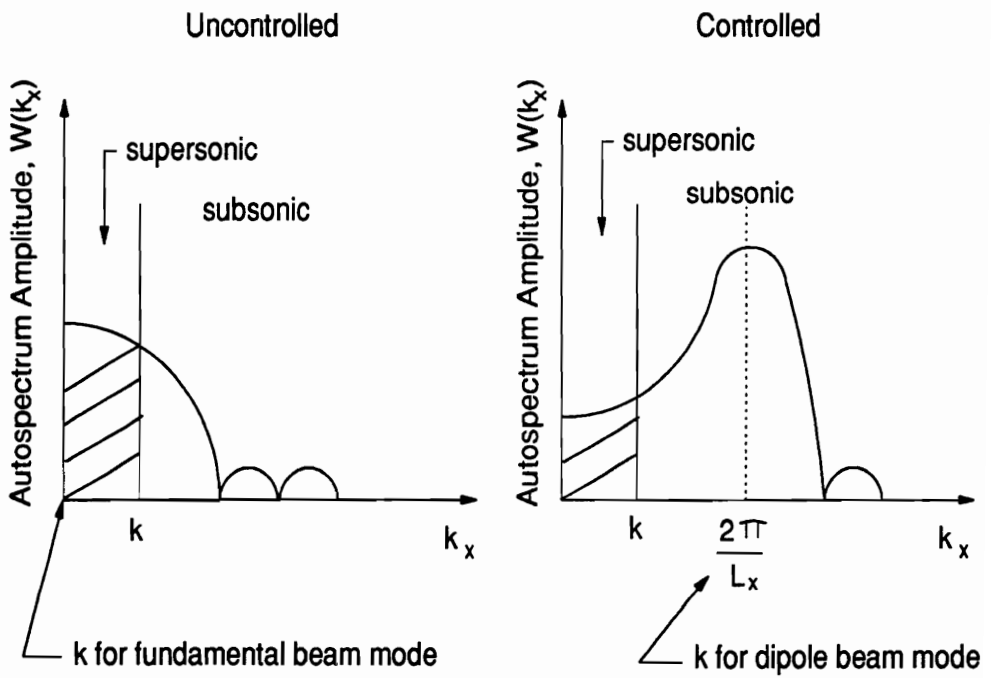


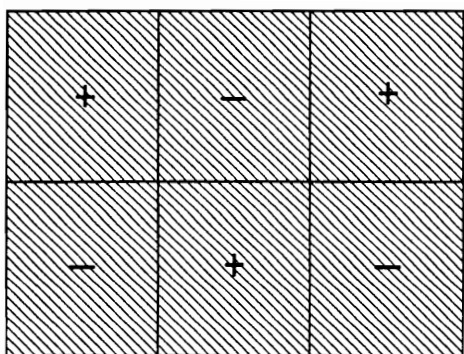
Figure 1.2: Example of k-plane results

region is termed the supersonic region and is the shaded region in Figure 1.2 where the structural wavenumber is less than the acoustic wavenumber (Fahy 1985). The non-radiating region is termed the subsonic region and is defined when the structural wavenumber is greater than the acoustic wavenumber.

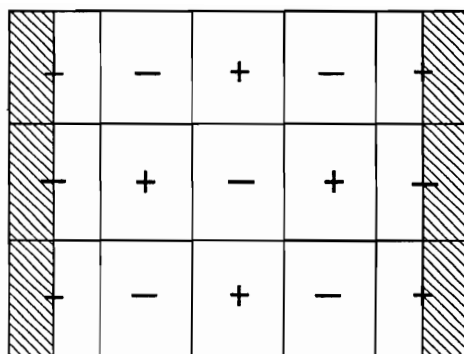
Using this technique to describe the relationship between the structural and acoustic response of the structure yields physical insight into the mechanisms of sound radiation. In essence, one simply needs to design an error sensor which yields an electrical response proportional to the area under the supersonic region of the wavenumber transform to control the sound radiated to the acoustic far-field. This statement is more readily made than accomplished; however, methods of designing sensors to accomplish this task will be outlined in this work.

Synthesizing the discussion of mode radiation efficiency and the wavenumber analysis leads to the topic of different “types” of radiation. Reviewing a classical work by Maidanik (1962), reveals physical insight into these different “types” of mode radiation. Consider the four types of mode radiation for a plate with simply supported boundary conditions presented in Figure 1.3. These four types of radiation are termed corner mode radiation, x-edge mode radiation, y-edge mode radiation and surface mode radiation. The corresponding requirement for each of these four conditions is defined as follows:

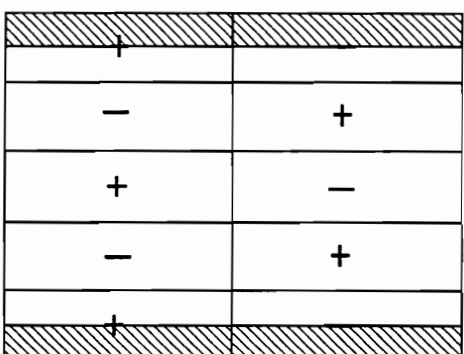
- a. $k^2 > k_m^2 + k_n^2$: surface mode radiation,
- b. $k < k_m, k > k_n$: x-edge mode radiation,
- c. $k > k_m, k < k_n$: y-edge mode radiation,



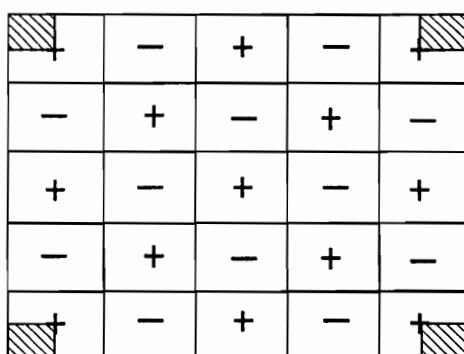
(a) surface mode radiation



(b) x-edge mode radiation



(c) y-edge mode radiation



(d) corner mode radiation

Figure 1.3: Modes of Radiation

d. $k < k_m, k < k_n$: corner mode radiation,

where $k_m = m\pi/L_x$ and $k_n = n\pi/L_y$. Surface mode radiation corresponds to the regime in presented in Figure 1.1 where $k/k_s > 1$ and hence the radiation efficiency of the mode approaches 1. A schematic of this form of radiation is conveyed in the cross hatched region of Figure 1.3(a). The two types of edge radiation, x-edge mode radiation and y-edge mode radiation are presented in Figure 1.3(b) and Figure 1.3(c) respectively. In each of these two cases, the term edge mode radiation stems from the observation that the strips of half-cell width along the edges normal to the axis for which the primary wavenumber (i.e. k_m or k_n , depending on direction) is less than the acoustic wavenumber remain largely uncanceled (Smith 1964). The least efficient of the four types of mode radiation is corner mode radiation which derives its name from the fact that only the corner quarter-cells contribute significantly to the far-field sound radiation. Hence, for structural acoustic control, conditions 2-4 listed above corresponding to edge-mode and corner mode radiation are the primary radiation modes of interest since we restrict the operating regime to $k/k_s < 1$.

To tie the three concepts together, we will discuss the relationship between the radiation efficiency and the modes of radiation to that of the wavenumber transform. Consider the “controlled” wavenumber transform of Figure 1.2. If the driving frequency is increased while maintaining the same wavenumber spectrum, one observes that the supersonic region is thus expanded. One can view the spectral line corresponding to the wavenumber, k , as a cursor. When this “cursor” is moved past the structural wavenumber corresponding to the second mode illustrated in Figure 1.2, the radiation efficiency of that mode approaches 1 as indicated in Figure (1.1), and this type of radiation is termed surface mode radiation as indicated in Figure

1.3(a).

Knowledge of the radiation efficiency, wavenumber transform, and different types of mode radiation greatly enhances our understanding of the structural acoustic problem and hence provides insight into the transducer design process. One might postulate in advance that sensors need not observe the less efficient even-even structural modes to effectively control the sound radiation from the structure. In addition, based on the concept of edge radiation, one might also hypothesize that the edge of the plate would be an ideal location for a sensor constructed from a rectangular strip of PVDF. Each of these assumptions based upon the physical mechanisms of sound radiation will be supported later in the results from this study.

1.3 Control Approach

To this point, all components necessary to create an adaptive structure for active structural acoustic control have been discussed, including an overview of the physical mechanisms of sound radiation which must be incorporated into the design. However, in addition to the appropriate sensors and actuators, an appropriate controller is required to achieve the overall design objective, which is to minimize the total far-field radiated sound power in the presence of a potentially changing input disturbance. A feed forward active controller is chosen to accomplish this task in the form of the time domain filtered-x version of the adaptive LMS algorithm. In contrast to feedback control approaches, a much *lower* level of system modelling is required to implement the controller (a frequency domain LMS controller requires no system modelling). Since a model of the system dynamics is not required to pre-

dict selected states as is the case for feedback control, the time domain feed forward implementation simply requires a model of the transfer function between each error sensor and control actuator. These transfer functions are measured experimentally and implemented thru finite impulse response (FIR) filters.

A conceptual schematic of a feed forward active controller is presented in Figure 1.4 in its most general form. The adaptive plant includes the structure with coupled radiation field, control actuators, error sensors and control dynamics. The reference plant consists of the models or plants required to create the desired response at the chosen error sensor locations. The adaptive plant essentially modifies its behavior ($\bar{A}P(k)$) to achieve the same response as that of the reference plant ($\bar{R}(k)$), by driving the error $\bar{E}(k)$ to a minimum. This is accomplished with the active control algorithm by optimizing the control inputs in order to minimize the least mean square of the error signal, which is the difference between the control input $\bar{A}P(k)$ and the desired response $\bar{R}(k)$.

Note that when it is required to totally attenuate the response of the adaptive plant at the error sensors, the reference plant is set open loop. Since $\bar{R}(k)$ will equal zero in this case, $\bar{E}(k)$ is simply equal to the output of the adaptive plant $\bar{A}P(k)$.

1.4 Scope and Objectives

The primary objective of this work is to study different types of error sensors implemented in active structural acoustic control and determine their respective advantages and limitations. These four basic error sensors were previously itemized in the actuator/sensor subsection of this introduction. Upon determining the ad-

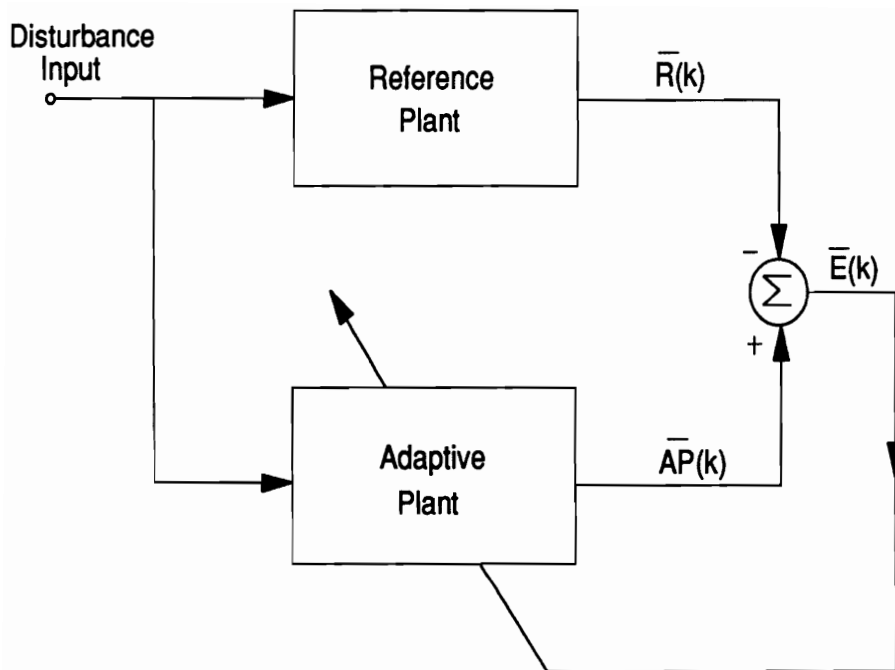


Figure 1.4: Simplified Controller Schematic

vantages and limitations of each error sensor, a design approach for achieving an adaptive structure for active structural acoustic control will be outlined based upon the simple structures used in this study. In addition to developing analytical models of each type of sensor, experiments were conducted to evaluate both the models and the global levels of sound attenuation which can be achieved. Models for the piezoelectric actuators were taken from a previous study by Dimitriadus *et al.*, (1991) and hence were not specifically evaluated in this study. However, experiments have been previously conducted by Fleming (1990) and Clark *et al.*, (1991(a,b)) suggesting that the dynamic models can be used with reasonable accuracy to predict the response of either a simply supported plate or a simply supported beam.

In order to reduce the number of variables considered in the study, this work is limited to control of a steady state harmonic structural disturbance. Hence this work is intended as a foundation for future studies implementing multi-frequency or broad-band input disturbances. Many structures of practical interest in structural acoustics can be represented by isotropic rectangular plates. Hence a simply supported, rectangular baffled plate was implemented as the plant for evaluating different types of structural acoustic error sensors. This plant was chosen since the behavior of both the structural response and acoustic response are well known from closed form analytical methods. In addition, the physical mechanisms of the control approach can be readily demonstrated as discussed earlier.

In the analytical study, linear quadratic optimal control theory (LQOCT) is utilized to minimize the response at the chosen error sensors and resolve the required optimal control voltage corresponding to each piezoelectric actuator. The optimal control

voltage was computed based on LQOCT as opposed to the LMS algorithm due to greater computational efficiency. The two methods were analytically determined to yield the same optimal solution; however, when implementing the LMS approach, the algorithm must converge to the least mean square solution over a number of iterations, just as is accomplished in the lab. Hence the number of computations required to determine the optimal solution are much greater in this case. All analytical studies were conducted with the IBM VM1 computing system as well as an AT compatible personal computer at VPI&SU. In the experimental studies, the filtered-x version of the adaptive LMS algorithm was implemented on a TMS320C25 digital signal processing board resident in an AT compatible personal computer.

1.5 Organization

To provide the necessary background for developing the analytical models required to predict the structural acoustic response of the simply supported beam and simply supported plate, all theoretical models are presented in chapter 2. The linear quadratic optimal control approach used to predicted the controlled structural acoustic response is outlined in chapter 3 along with an overview of the filtered-x version of the adaptive LMS algorithm which was used in the experimental studies to achieve control of the test structure. Based upon the sensor models developed in chapter 2 and the control approach presented in chapter 3, design approaches for achieving unique sensors constructed from polyvinylidene fluoride are developed in chapter 4. At this point, the method of constructing the test structures as well as the instrumentation required to conduct experiments is reviewed in chapter 5 for practical implementation of the sensor designs. Experimental and analytical results

for all types of sensors are discussed in the results which are presented in chapter 6. Upon presenting the results, a discussion of the important concepts resulting from this work is presented in the conclusions of chapter 7.

Chapter 2

Actuator/Sensor Models for Simply Supported Beams and Plates

For the extent of this work, the simply supported beam and simply supported plate served as test structures for studying the behavior of different types of structural and acoustic error sensors. Since a shaker was utilized as the input disturbance and piezoceramic patches were implemented as control actuators on each test structure, appropriate analytical models of each input were derived. In addition, analytical models for each of the different types of error sensors were formulated to develop an overall design approach for the smart structure system. Since the analysis was conducted for a harmonic steady state input disturbance, modal analysis was used to express the response of the structure in terms of the input disturbance and control actuators. The overall system response is thus obtained from a superposition of the modal response resulting from the disturbance and each control actuator. The analytical model for each error sensor was also expressed in terms of the modal coordinates to simplify computations.

In the following analytical expressions, many of the derivations of material which has been documented in past studies will be omitted from the text in an effort to maintain some control over the length of this dissertation. However, in each case, the reader is referred to the appropriate reference for all supporting details. All expressions for the structural and acoustic response of both the simply supported beam and simply supported plate presented in this work are valid only for the case of light fluid loading and are hence not applicable in the fully coupled case. Derivations which are unique to this work will be presented in an appropriate appendix to maintain consistency in the flow of this work.

2.1 Theory

The total structural response of a lightly damped simply supported beam can be expressed as a summation of the modal amplitudes as follows (Meirovitch 1967):

$$w(x, t) = \sum_{m=1}^{\infty} W_m \sin(\gamma_m x) \exp(j\omega t). \quad (2.1)$$

Since one cannot readily evaluate an expression over an infinite sum, the number of modes utilized in the summation will be limited to 10. Due to the frequency response characteristics of the structure, the response of the higher order modes to low frequency excitation is negligible. Similarly, the response of a simply supported plate can be expressed in terms of its modal coordinates as follows (Meirovitch 1967):

$$w(x, y, t) = \sum_{m=1}^{\infty} \sum_{n=1}^{\infty} W_{mn} \sin(\gamma_m x) \sin(\gamma_n y) \exp(j\omega t), \quad (2.2)$$

As in the case of the simply supported beam, the range of summation will be restricted to a finite number of modes. However, due to the increased modal density (i.e separation between resonant frequencies) the first 25 modes are included in the response, letting $m = 1, 2, \dots, 5$ and $n = 1, 2, \dots, 5$.

Given the response of the beam and plate in terms of the modal coordinates, the response of each structure is readily obtained for a variety of input disturbances. For the purpose of this study, a model for the response of each structure to a point force disturbance as well as a distributed input due to a piezoelectric actuator is required.

2.1.1 Point Force Model

The shaker implemented in the experiments was attached to each structure via a stinger configured with a force transducer. The analytical model most closely approximating this configuration is the point force input disturbance.

2.1.1.1 Simply Supported Beam

The modal response of a simply supported damped beam to a harmonic point force of magnitude F and located at a spatial coordinate of x_d from the origin of the structure depicted in Figure 2.1 can be expressed as follows (Meirovitch 1967):

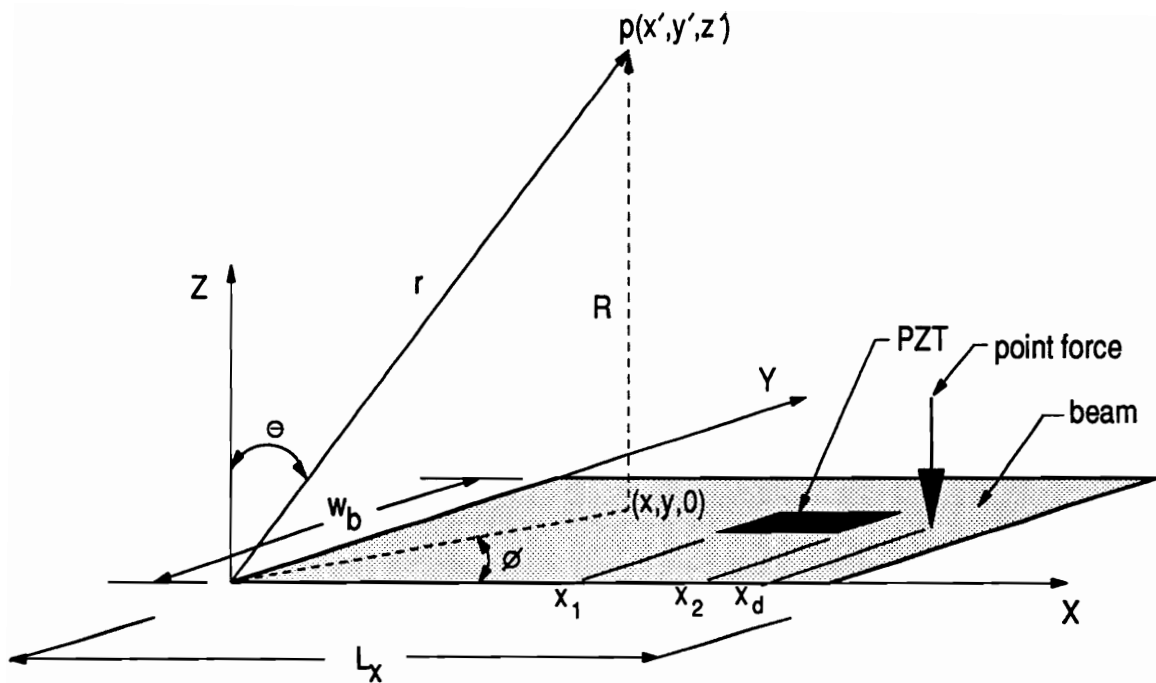


Figure 2.1: Coordinate System for Beam

$$W_m^F = \frac{2F \sin\left(\frac{m\pi x_d}{L_x}\right)}{\rho' L_x (\omega_m^2 - \omega^2 + j2\eta\omega\omega_m)}. \quad (2.3)$$

The resonant frequencies of the simply supported beam expressed in the previous equation are given by:

$$\omega_m^2 = \frac{D_e}{\rho'} \left(\frac{m\pi}{L_x}\right)^4, \quad (2.4)$$

where the beam flexural stiffness is defined by

$$D_e = \frac{Eh^3w_b}{12}, \quad (2.5)$$

and

- E = Young's modulus of beam
- h = thickness of beam
- w_b = width of beam
- η = damping ratio
- ρ' = mass density of beam per unit length.

2.1.1.2 Simply Supported Plate

Solving the equation of motion for the plate subjected to harmonic excitation of a point force located at spatial coordinates (x_d, y_d) depicted in Figure 2.2 yields the following expression for the modal amplitudes (Meirovitch 1967).

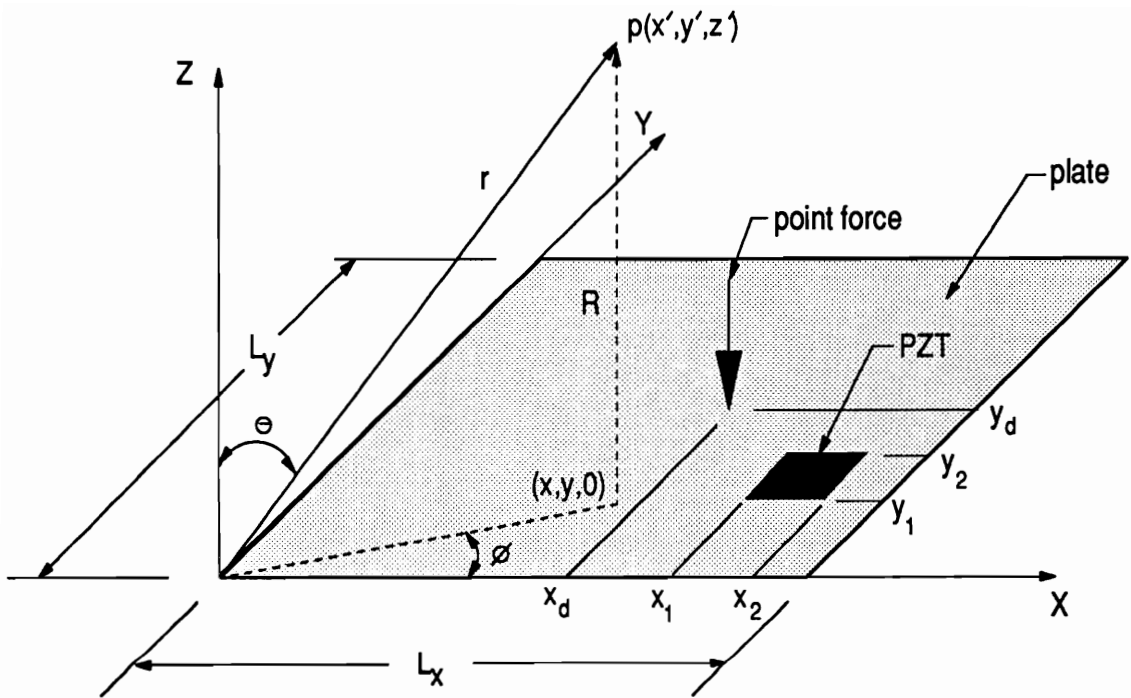


Figure 2.2: Coordinate System for Plate

$$W_{mn}^F = \frac{4F}{\rho'' L_x L_y} \frac{\sin(\gamma_m x_d) \sin(\gamma_n y_d)}{(\omega_{mn}^2 - \omega^2 + j2\eta\omega\omega_{mn})}. \quad (2.6)$$

The resonant frequencies of the simply supported plate expressed in the previous equation are given by:

$$\omega_{mn}^2 = \frac{D_e}{\rho} [(\gamma_m)^2 + (\gamma_n)^2]^2, \quad (2.7)$$

where the plate flexural stiffness is defined by

$$D_e = \frac{Eh^3}{12(1 - \nu^2)}, \quad (2.8)$$

and

$$\gamma_m = \frac{m\pi}{L_x}$$

$$\gamma_n = \frac{n\pi}{L_y}$$

E = Young's modulus of plate

h = thickness of plate

ν = Poisson's ratio of plate

η = damping ratio

ρ'' = mass density of plate per unit area.

2.1.2 Piezoelectric Actuator Model

The piezoceramic elements implemented in the control experiments were constructed from G-1195 lead zirconium titanate with material properties itemized in Table 2.1. Each piezoelectric actuator was constructed from two piezoceramic elements bonded symmetrically to the top and bottom surface of the structure and wired 180° out

Table 2.1: Material Properties of Piezoceramic Material G-1195

Name	Symbol	Value	Units
Piezoelectric Strain Coefficient	d_{31}	166×10^{-12}	m/V
Density	ρ	7600	kg/m^3
Elastic Modulus	E_{33}	4.9×10^{10}	N/m^2
Elastic Modulus	E_{11}	6.3×10^{10}	N/m^2

of phase such that, when contraction was induced in one element, expansion was induced in the other, resulting in uniform bending about the neutral axis of the structure. A schematic diagram of the electrical configuration of this basic actuator is presented in Figure 2.3. Previous work by Crawley and de Luis (1987), Dimitriadis *et al.*, (1991) and Clark *et al.*, (1991(a)) demonstrated that these distributed strain actuators can be approximated by applying line moments at the boundaries of the actuators. Experimental studies dedicated to characterizing the nature of the inputs Fleming (1990), Clark *et al.*, (1991(a,b)) revealed that the analytical model for the response of the piezoelectric actuator resulted in a reasonable prediction of the dynamic response of the structure. The reader is referred to these studies for greater details of the following actuator related derivations.

2.1.2.1 Simply Supported Beam

If we solve the equation of motion for the simply supported beam configured with a piezoelectric actuator attached as detailed previously at spatial coordinates of (x_1, x_2) depicted in Figure 2.1, the resulting modal response can be derived (Clark 1991a).

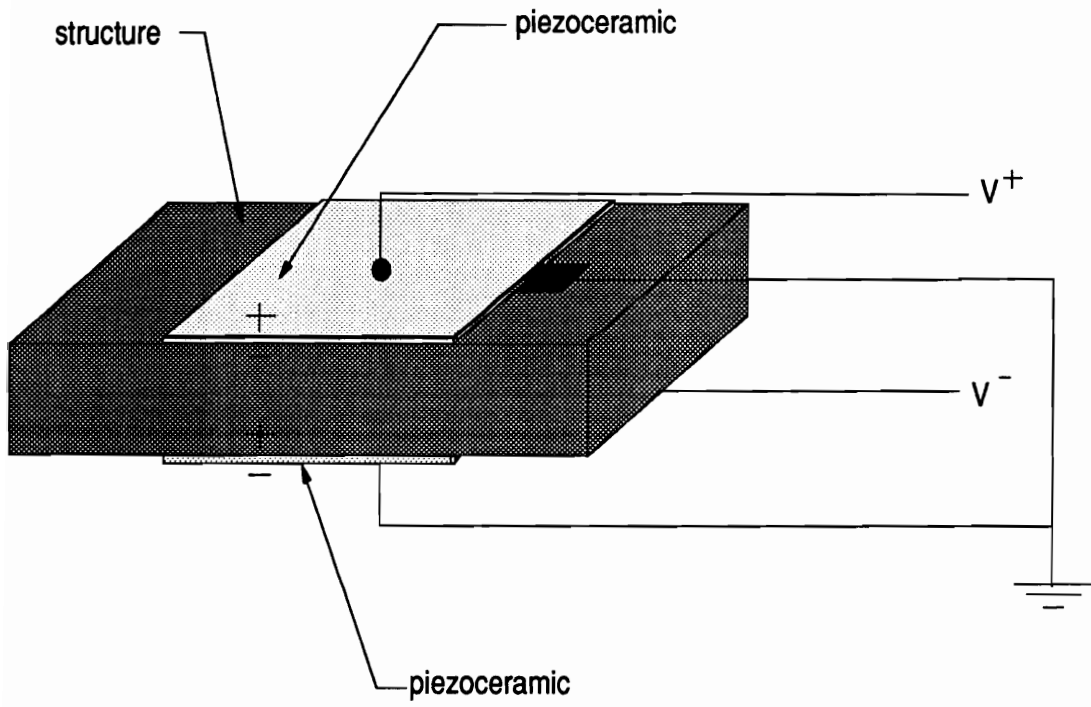


Figure 2.3: Electrical Configuration of PZT Actuator

$$W_m^p = \frac{2C_o \epsilon_{pe} w_{pe} m \pi}{w_b \rho' L_x^2 (\omega_m^2 - \omega^2 + j2\eta\omega_m\omega)} (\cos(\gamma_m x_1^p) - \cos(\gamma_m x_2^p)) \quad (2.9)$$

Constants used in the above equation are defined as follows.

$$\epsilon_{pe} = \frac{d_{31} V^p}{t}. \quad (2.10)$$

$$C_o = -\frac{2P}{3(1-P)} h^2 E. \quad (2.11)$$

$$P = -\frac{E_{pe}}{E} K. \quad (2.12)$$

$$K = \frac{6th(h+t)}{(h^3 + 8t^3) + 6ht^2}, \quad (2.13)$$

where:

- w_b = width of beam
- w_{pe} = width of piezoelectric actuator
- x_1^p = x-coordinates of left corner of p^{th} actuator
- x_2^p = x-coordinates of right corner of p^{th} actuator
- V^p = complex voltage of p^{th} actuator
- t = thickness of piezo patch
- E_{pe} = Young's modulus of piezo patch

2.1.2.2 Simply Supported Plate

Similarly, an expression for the modal response of the simply supported plate configured with a piezoelectric actuator located at spatial coordinates of (x_1, y_1) and (x_2, y_2) illustrated in Figure 2.2 can be derived as follows (Dimitriadus *et al.*, 1991):

$$W_{mn}^p = \frac{4C_o\epsilon_{pe}}{\rho''L_xL_y(\omega_{mn}^2 - \omega^2 + j2\eta\omega_{mn}\omega)} \left(-\frac{\gamma_m^2 + \gamma_n^2}{\gamma_m\gamma_n} \right) \times [(\cos(\gamma_mx_1^p) - \cos(\gamma_mx_2^p))(\cos(\gamma_ny_1^p) - \cos(\gamma_ny_2^p))]. \quad (2.14)$$

Constants used in the above equation are defined as follows.

$$\epsilon_{pe} = \frac{d_{31}V^p}{t}. \quad (2.15)$$

$$C_o = -\frac{Eh(1+\nu)}{6(1-\nu)} \frac{P}{[1+\nu - (1+\nu_{pe})P]}. \quad (2.16)$$

$$P = -\frac{E_{pe}(1-\nu^2)}{E(1-\nu_{pe}^2)} K. \quad (2.17)$$

$$K = \frac{6th(h+t)}{(h^3 + 8t^3) + 6ht^2}, \quad (2.18)$$

where:

- (x_1^p, y_1^p) = coordinates of lower left corner of p^{th} actuator
- (x_2^p, y_2^p) = coordinates of upper right corner of p^{th} actuator
- V^p = complex voltage of p^{th} actuator
- t = thickness of piezo patch
- E_{pe} = Young's modulus of piezo patch
- ν_{pe} = Poisson's ratio of piezo patch.

2.1.3 Total Structural Response

The total structural response of the simply supported beam or the simply supported plate can hence be obtained from a superposition of the modal response computed for the point force input disturbance and each piezoelectric control actuator as follows. The modal amplitudes for the simply supported beam are obtained as follows:

$$W_m = W_m^F + \sum_{p=1}^P W_m^p. \quad (2.19)$$

The modal amplitudes are obtained similarly for the simply supported plate:

$$W_{mn} = W_{mn}^F + \sum_{p=1}^P W_{mn}^p, \quad (2.20)$$

where P defines the number of piezoelectric actuators used in the response. Given the total structural response as a function of the modal coordinates, appropriate models for sensors can be developed.

2.1.4 Polyvinylidene Fluoride (PVDF) Sensor Models

The material chosen for designing shaped structural error sensors as well as acoustic near-field sensors in this study was polyvinylidene fluoride. This material was chosen due to its high sensitivity as well as its low compliance and mass density in comparison to typical material properties of structures for proposed applications. The electrical response of this material is proportional to the integral of strain induced within the volume of the sensor. The three directions in which strain can be applied are indicated in the schematic diagram of Figure 2.4. Associated with the x, y and z-direction of the material are the piezo stress constants d_{31} , d_{32} and d_{33} ($(C/m^2)/(N/m^2)$) respectively. Values for each of these constants as well as material properties of PVDF are included in Table 2.2.

PVDF sensors implemented in this study were either bonded to the surface of the structure or shaped as a segment of a shell of large radius and placed in the acoustic near-field of the structure. The analytical models required to predict the response of each type of sensor are outlined below.

2.1.4.1 Structural Error Sensor

An expression for the electrical response of an element of PVDF distributed over the surface of a structure was previously formulated by Lee and Moon (1990(b)) from laminated plate theory. This expression was derived in terms of charge and is a function of the strain induced in the structure. The expression is written as follows:

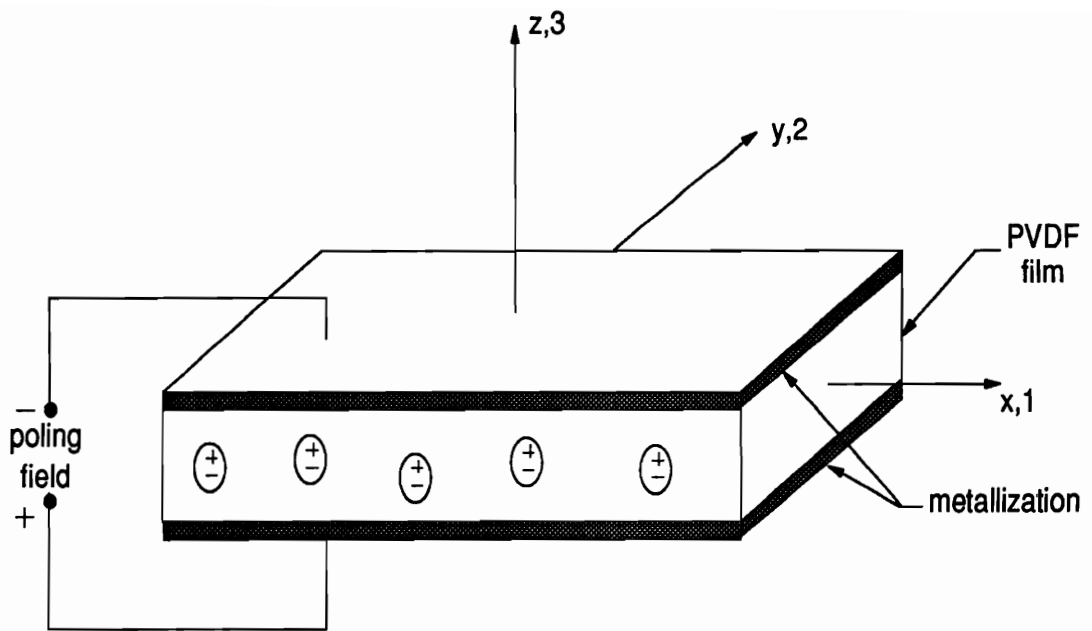


Figure 2.4: Schematic of PVDF Coordinate System

Table 2.2: Material Properties of Polyvinylidene Fluoride

Name	Symbol	Value	Units
Strain per charge	d_{31}	23×10^{-12}	$(C/m^2)/(N/m^2)$
Strain per charge	d_{32}	3×10^{-12}	$(C/m^2)/(N/m^2)$
Strain per charge	d_{33}	-33×10^{-12}	$(C/m^2)/(N/m^2)$
Stress per charge	e_{31}	23×10^{-12}	C/m^2
Stress per charge	e_{32}	3×10^{-12}	C/m^2
Stress per charge	e_{33}	-33×10^{-12}	C/m^2
Density	ρ	1780	kg/m^3
Elastic Modulus	E	2×10^9	N/m^2
Permittivity	ϵ	106×10^{-12}	F/m

$$\begin{aligned}
 q(t) = & \frac{(h_p + h_s)}{2} \int_A P_o(x, y) F(x, y) \left(e_{31} \frac{\partial^2 w}{\partial x^2} + e_{32} \frac{\partial^2 w}{\partial y^2} \right. \\
 & \left. + 2e_{36} \frac{\partial^2 w}{\partial x \partial y} \right) dx dy \exp(j\omega t), \quad (2.21)
 \end{aligned}$$

where q is the response of the PVDF in units of charge, h_p is the thickness of the PVDF laminae, h_s is the thickness of the structure, $F(x, y)$ is the function describing the effective surface electrode, $P_o(x, y)$ represents the polarization profile, e_{31} , e_{32} and e_{36} are the piezoelectric field intensity constants and w is the response of the structure as a function of the x and y-direction.

When the lamina is placed on the structure with no skew angle as depicted in the schematic of Figure 2.5, $e_{36} = 0$, which is the case for the present study. Upon substituting the response of the given test structure (i.e simply supported plate or simply supported beam) into equation (2.21), the electrical response of the sensor can be computed as a function of the dynamic response of the structure. Since this

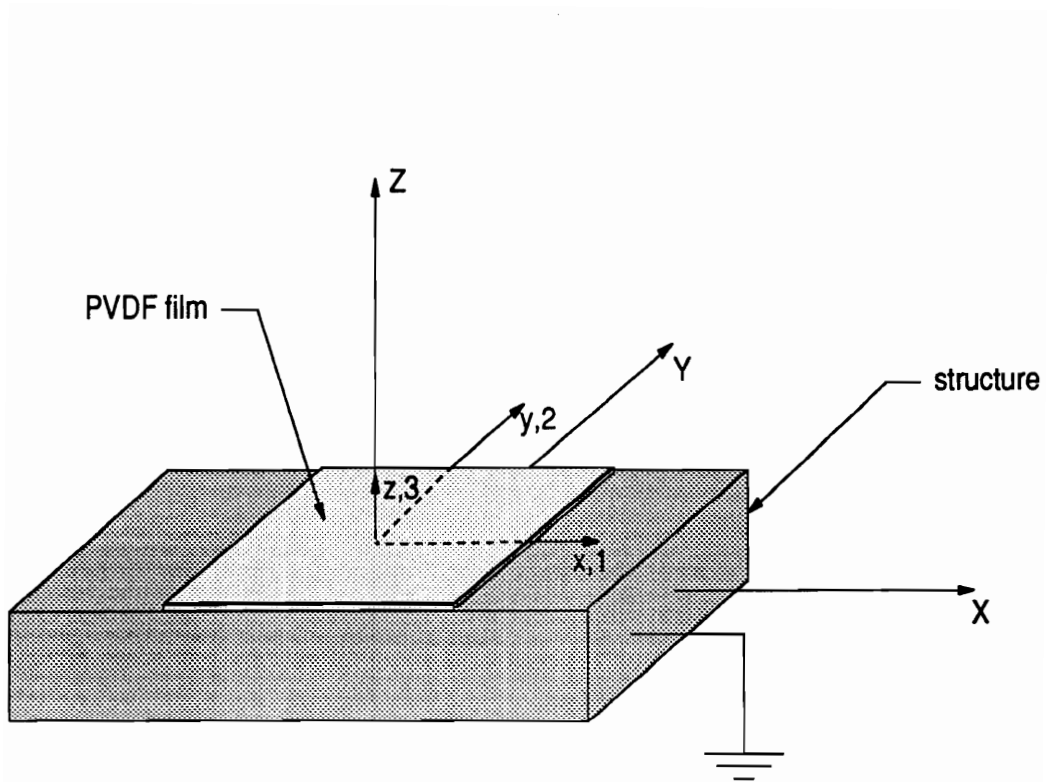


Figure 2.5: Schematic of PVDF Configured on a Structure

expression was formulated in terms of charge, the resulting voltage can be obtained by dividing the expression by the sensor capacitance. The sensor capacitance is typically much greater than that of the instrument used to measure the output voltage; therefore, the capacitance of the instrument can be ignored when computing the voltage. Appropriate circuits to assure this condition will be discussed later in chapter 5 which is devoted to the experimental arrangement.

2.1.4.1.1 Simply Supported Beam

Since the response of the simply supported beam is expressed as a function of the x-direction only, equation (2.21) can be written as follows assuming a constant polarization profile:

$$q(t) = \frac{(h_p + h_s)}{2} \int_0^{L_x} F(x) (e_{31} \frac{\partial^2 w}{\partial x^2}) dx \exp(j\omega t). \quad (2.22)$$

Upon substituting the expression for the response of the simply supported beam into the above equation, the electrical response of the sensor can be expressed as a function of the modal coordinates:

$$q(t) = \frac{(h_p + h_s)e_{31}}{2} \exp(j\omega t) \sum_{m=1}^M W_m \int_0^{L_x} F(x) \left(\frac{m\pi}{L_x}\right)^2 \sin\left(\frac{m\pi x}{L_x}\right) dx. \quad (2.23)$$

One must simply choose the desired sensor shape (i.e. $F(x)$) to compute an exact electrical response. This will be done in the following chapter for both rectangular sensors and modal sensors.

2.1.4.1.2 Simply Supported Plate

As in the case of the simply supported beam, substituting the expression for the response of the simply supported plate into equation (2.21) yields the electrical response of the PVDF sensor in terms of the sensor shape and modal response of the structure:

$$q(t) = \frac{(h_p + h_s)}{2} \sum_{m=1}^M \sum_{n=1}^N W_{mn} \int_0^{L_x} \int_0^{L_y} F(x, y) \left(e_{31} \left(\frac{m\pi}{L_x} \right)^2 + e_{32} \left(\frac{n\pi}{L_y} \right)^2 \right) \times \sin\left(\frac{m\pi x}{L_x}\right) \sin\left(\frac{n\pi y}{L_y}\right) dx dy \exp(j\omega t). \quad (2.24)$$

Both rectangular shaped sensors and modal sensors will be discussed in the following chapter.

2.1.4.2 Near-field Sensors

In addition to locating distributed PVDF sensors on the surface of the structure, acoustic near-field sensors were constructed from PVDF and placed in close proximity to the structure as an alternative design approach. The initial design concept was based upon a membrane type sensor. In this case, the PVDF was stretched uniformly in both directions and bonded to a rectangular frame to create the membrane. The dominant strain component is nonlinear due to the fact that the strain induced in a membrane due to a harmonic forcing function results in a strain due to tension whether the membrane is displaced in a negative sense or positive sense.

In other words, a harmonic pressure of frequency f applied to the surface of the sensor will result in an electrical response at a frequency of $2f$. Another component of strain was observed at the desired input frequency; however, this term was due to nonlinearities in the structural response of the membrane, resulting in a poor signal to noise ratio. The response of this component was greatest near the first mode of the membrane due to the curvature induced in the sensor as a function of the harmonic pressure applied over the surface.

As a result of this observation, the logical method of increasing the response of the sensor at the desired frequency was to design a sensor with curvature such that the out of plane displacement with respect to the x - y axis and hence strain in the x - y plane induced in the sensor would increase. To this end a sensor was shaped in the form of a segment of shell (i.e. a cylindrical plate) as depicted in Figure 2.6. Design techniques for achieving this sensor shaped will be presented in the chapter outlining the experimental arrangement. The boundaries in the x -direction and ϕ -direction are assumed to be simply supported. The equations of motion for this cylindrical plate as well as the solution for the response are presented in Appendix A. It should be noted that an exact analytical solution to the differential equations does not exist; however, the solution is expanded in terms of a set of admissible functions which satisfy both the natural and geometric boundary conditions to obtain an approximate response of the shell segment. These admissible functions were previously given by Timoshenko (1940) and Junger and Feit (1986) as follows:

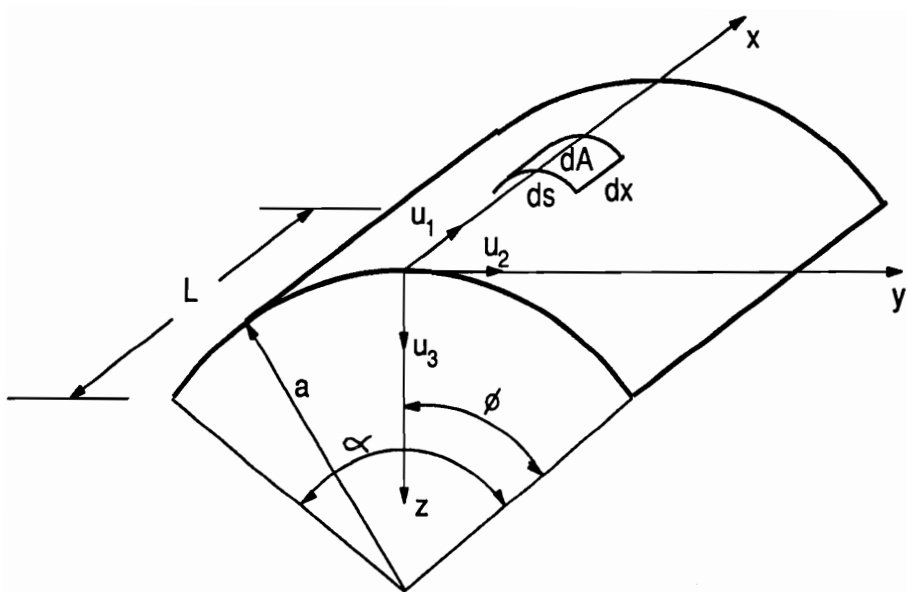


Figure 2.6: Coordinate System for Near-Field Sensor

$$u_1(t) = \sum_{m=1}^M \sum_{n=1}^N A_{mn} \sin\left(\frac{n\pi\phi}{\alpha}\right) \cos\left(\frac{m\pi x}{L}\right) \exp(j\omega t), \quad (2.25)$$

$$u_2(t) = \sum_{m=1}^M \sum_{n=1}^N B_{mn} \cos\left(\frac{n\pi\phi}{\alpha}\right) \sin\left(\frac{m\pi x}{L}\right) \exp(j\omega t), \quad (2.26)$$

$$u_3(t) = \sum_{m=1}^M \sum_{n=1}^N C_{mn} \sin\left(\frac{n\pi\phi}{\alpha}\right) \sin\left(\frac{m\pi x}{L}\right) \exp(j\omega t), \quad (2.27)$$

where α and L are the respective ϕ -direction and x -direction dimensions, and u_1 , u_2 and u_3 express the response of the shell segment as indicated in Figure 2.6. The solution for the response of each mode is obviously coupled in three dimensions. Hence for each mn mode, an eigenvalue problem must be solved. The details of this solution are presented in Appendix A. The strain resulting from this approximate solution can be computed as follows:

$$\epsilon_x = \frac{\partial u_1}{\partial x} = - \sum_{m=1}^M \sum_{n=1}^N \frac{m\pi}{L} A_{mn} \sin\left(\frac{n\pi\phi}{\alpha}\right) \sin\left(\frac{m\pi x}{L}\right), \quad (2.28)$$

and

$$\epsilon_\phi = \frac{\partial u_2}{a \partial \phi} - \frac{u_3}{a}. \quad (2.29)$$

Hence,

$$\epsilon_\phi = -\frac{1}{a} \sum_{m=1}^M \sum_{n=1}^N \left(\frac{n\pi}{\alpha} B_{mn} + C_{mn} \right) \sin\left(\frac{n\pi\phi}{\alpha}\right) \sin\left(\frac{m\pi x}{L}\right), \quad (2.30)$$

where ϵ_ϕ is the strain induced in the ϕ -direction, ϵ_x is the strain induced in the x-direction, and α and L are the respective dimensions of the sensor in the corresponding directions. An expression for the electrical response of the PVDF sensor as a function of the strain induced in the x and y-direction was presented previously in equation (2.24). The formulation for the response of the acoustic near-field sensor follows this format since the electrical response of the material is proportional to the integral of strain over the surface of the sensor. In this case, the material is oriented such that the strain in the x-direction is aligned with e_{32} and the strain in the ϕ -direction is aligned with e_{31} . Consider a differential element of the cylindrical plate presented in Figure 2.6. The elemental area dA is represented by the product of dx and dS , where $dS = a d\phi$. Hence, given an expression for the strain in each respective dimension, the response of the PVDF acoustic near-field sensor can be obtained by integrating the surface strain of the element depicted in Figure 2.6 with respect to the stress/charge constants, e_{31} and e_{32} as follows:

$$q(t) = \int_0^L \int_0^\alpha (e_{31}\epsilon_\phi + e_{32}\epsilon_x) a d\phi dx \exp(j\omega t), \quad (2.31)$$

Substituting equations (2.28) and (2.30) into equation (2.31), and integrating over the surface of the sensor, the electrical response in units of charge can be expressed as a function of the modal coordinates of the sensor:

$$q(t) = - \sum_{m=1}^M \sum_{n=1}^N \left[\left(\frac{ae_{32}\alpha}{n\pi} \right) A_{mn} + e_{31} \left\{ \left(\frac{L}{m\pi} \right) B_{mn} + \left(\frac{\alpha L}{mn\pi^2} \right) C_{mn} \right\} \right] \times (1 - \cos(n\pi))(1 - \cos(m\pi)) \exp(j\omega t). \quad (2.32)$$

As is obvious from the above expression, only those modes of the sensor for which both m and n are odd will contribute to the electrical response. The coefficients A_{mn} , B_{mn} and C_{mn} are functions of the frequency response characteristics of the shell segment as well as the nature of the input. Expressions for computing these modal coefficients as a function of a uniform pressure or a summation of distributed pressures applied over the surface of the sensor are included in Appendix A. A discussion of the specifics of the implementation of these acoustic near-field sensors is presented in chapter 4 of this work. In general, the design of the acoustic near-field sensor is not unique to any specific type of structure. The response is simply dependent upon the acoustic pressure radiated from the surface of the structure. If this response can be computed analytically or estimated from experimental data, an expression for the electrical response of the near-field sensor can be obtained.

2.1.5 Structural Response (Accelerometer Sensor Model)

For harmonic excitation of a structure, the acceleration is proportional to the displacement as a function of $-\omega^2$. Based upon this result and the knowledge of the displacement response of the structure, a model for an accelerometer error sensor is readily obtained for both the simply supported beam and simply supported plate, assuming that the sensor is small with respect to the structural wavelength. These models are used for comparing analytical results with experimental results when

implementing accelerometers as error sensors on the surface of the structure.

2.1.5.1 Simply Supported Beam

Multiplying the displacement response of the simply supported beam by $-\omega^2$ yields an expression for the acceleration response (as long as the sensor is small with respect to the wavelength) as follows:

$$\ddot{w}(x, t) = -\omega^2 \sum_{m=1}^M W_m \sin(\gamma_m x) \exp(j\omega t), \quad (2.33)$$

where $\ddot{w}(x, t)$ is the time dependent acceleration at position x .

2.1.5.2 Simply Supported Plate

Similarly, the acceleration response of the simply supported plate can be obtained:

$$\ddot{w}(x, y, t) = -\omega^2 \sum_{m=1}^{\infty} \sum_{n=1}^{\infty} W_{mn} \sin(\gamma_m x) \sin(\gamma_n y) \exp(j\omega t), \quad (2.34)$$

where $\ddot{w}(x, y, t)$ is the time dependent acceleration at spatial coordinates (x, y) .

2.1.6 Acoustic Response (Microphone Sensor Models)

As outlined earlier, the simply supported beam and simply supported plate were chosen in this study since an analytical expression for both the structural and acoustic

response exists. Due to the low frequency excitation of the structures and the finite dimensions of the anechoic chamber, microphone error sensors could not be located in the acoustic far-field as required to satisfy the basic assumptions for far-field conditions (Bies 1976):

$$R \gg \frac{\lambda}{2\pi}, \quad (2.35)$$

$$R \gg l \quad (2.36)$$

and

$$R \gg \frac{\pi l^2}{2\lambda}, \quad (2.37)$$

where R is the distance from the source to the acoustic field point, λ is the wavelength of the radiated sound, and l is the maximum source dimension. As a result, for the purpose of comparing analytical and experimental results Rayleigh's integral was evaluated at the appropriate acoustic field point with respect to the test structure. For low frequency excitation, the microphone can be approximated as a point acoustic sensor. Rayleigh's integral formulation is given as follows:

$$p(\vec{r}, t) = \frac{j\omega\rho_o}{2\pi} \int_S \frac{\tilde{v}_n(\vec{r}_s) \exp(-jkR)}{R} dS, \quad (2.38)$$

where \vec{r} is the position vector of the acoustic field point, \vec{r}_s is the position vector along the elemental surface, S , with normal velocity, $\tilde{v}_n(\vec{r}_s)$, and R is the magnitude of the vector $\vec{r} - \vec{r}_s$. The coordinate system used to compute the acoustic pressure for both the beam and the plate was the same as that adopted by Wallace (1972a,1972b) and is depicted in Figure 2.1 and Figure 2.2 respectively. The expressions for the point pressure radiated from each respective structure follows, and it should be noted that these expressions were numerically integrated at the desired acoustic field point to obtain the acoustic pressure due to the vibrating response of the structure. Each of these expressions can be used to model the response of a microphone positioned at the chosen field point since a microphone acts as a point sensor at low frequencies of excitation.

2.1.6.1 Simply Supported Beam

Differentiating equation (2.1) once with respect to time yields an expression for the velocity of the simply supported beam which can be substituted into Rayleigh's integral. The resulting expression for the acoustic response can be written as follows:

$$p(x', y', z', t) = -\frac{\omega^2 \rho_o}{2\pi} \exp(j\omega t) \sum_{m=1}^M W_m \int_0^{w_b} \int_0^{L_x} \sin\left(\frac{m\pi x}{L_x}\right) \times \frac{\exp(-jk\sqrt{(x' - x)^2 + (y' - y)^2 + (z')^2})}{\sqrt{(x' - x)^2 + (y' - y)^2 + (z')^2}} dx dy, \quad (2.39)$$

and:

(x', y', z') = spatial coordinates of acoustic field point
 $(x, y, 0)$ = spatial coordinates on beam
 k = wavenumber in acoustic medium
 c = speed of sound in acoustic medium
 ρ_o = density of acoustic medium.

Coordinates relating to this expression are found in Figure 2.1 and are also discussed in the reference by Wallace (1972(a)).

2.1.6.2 Simply Supported Plate

Differentiating equation (2.2) once with respect to time to obtain an expression for the velocity of the simply supported plate and substituting this expression into Rayleigh's integral yields an equation for the radiated sound at a chosen field point:

$$\begin{aligned}
 p(x', y', z', t) = & -\frac{\omega^2 \rho_o}{2\pi} \exp(j\omega t) \sum_{n=1}^N \sum_{m=1}^M W_{mn} \int_0^{L_x} \int_0^{L_y} \sin\left(\frac{m\pi x}{L_x}\right) \sin\left(\frac{n\pi y}{L_y}\right) \\
 & \times \frac{\exp(-jk\sqrt{(x' - x)^2 + (y' - y)^2 + (z')^2})}{\sqrt{(x' - x)^2 + (y' - y)^2 + (z')^2}} dy dx, \quad (2.40)
 \end{aligned}$$

and:

(x', y', z') = spatial coordinates of acoustic field point
 $(x, y, 0)$ = spatial coordinates on plate
 k = wavenumber in medium
 c = speed of sound in medium
 ρ_o = density of medium.

All coordinates used in the previous expression are depicted in Figure 2.2 and greater details of the analysis can be found in the reference by Wallace (1972(b)).

2.1.7 Wavenumber Transform

To implement the wavenumber transform of the structural response as a cost function in the control approach, an expression relating the modal amplitudes of the structural response to the amplitudes of the wavenumber spectrum must be obtained. Using this technique to describe the relationship between the structural and acoustic response of the structure provides a unique method of developing a cost function to minimize the radiated sound. The wavenumber transform was presented in equation (1.5) and is recalled below:

$$F(k_x, k_y) = \int_{-\infty}^{+\infty} \int_{-\infty}^{+\infty} f(x, y) \exp(-jk_x x) \exp(-jk_y y) dy dx$$

Although the number of components in the spectrum is obviously infinite, even within the supersonic region, a finite number of spectral amplitudes at particular wavenumber values may be chosen for computational purposes. Physically this corresponds to minimizing the sound at corresponding radiation angles as previously outlined by Fuller and Burdisso (1992(a)). While this is an esoteric approach for developing a cost function for structural acoustic control, it is physically realizable through model reference control, as will be detailed later in chapter 4.

2.1.7.1 Simply Supported Beam

An expression for the wavenumber transform of the spatial response of the simply supported beam is obtained by substituting equation (2.1) into equation (1.5) presented in chapter 1. The response of the beam is expressed as a function of one

dimension; however, the wavenumber transform is computed over two dimensions to represent the decay in acoustic response as a function of the y-dimension. Replacing $f(x)$ with the spatial response of the beam of equation (2.1), and evaluating the integral over the boundaries of the beam (since the out-of-plane response of the baffle is zero), the wavenumber transform can be expressed as follows Fahy (1985):

$$W(k_x) = \sum_{m=1}^{\infty} W_m \frac{(m\pi/L_x)[(-1)^m \exp(-jk_x L_x) - 1]}{[k_x^2 - (m\pi/L_x)^2]} \left(\frac{\sin(\frac{k_y w_b}{2})}{\frac{k_y}{2}} \right). \quad (2.41)$$

Note that the shape of the wavenumber transform along the k_x -axis remains unchanged over the k_y -axis except for the magnitude of the wavenumber spectrum. As indicated in the equation above, the amplitude of the wavenumber spectrum decays as a function of k_y uniformly for all k_x . Thus the wavenumber spectrum in the k_y -direction serves to predict the attenuation in the acoustic response as the angle of radiation from the normal to the structure increases. Any spectral line of the wavenumber transform can be implemented in the cost function of the control algorithm. However, only those components for which $-k < k_x < k$ correspond to radiation in the acoustic far-field. Hence, the obvious choice is to restrict ones region of analysis to this regime. For example, choosing to minimize the spectral line corresponding to $k_x = 0$ results in a reduction of sound at an angle of $\theta = 0$ as outlined previously by Fuller and Burdisso (1992(a)) since

$$k_x = k \sin(\theta). \quad (2.42)$$

2.1.7.2 Simply Supported Plate

A similar expression for the wavenumber transform of the spatial response of the simply supported plate can be obtained by substituting the expression for the structural response of the plate presented in equation (2.2) into equation (1.5).

$$W(k_x, k_y) = \sum_{m=1}^M \sum_{n=1}^N W_{mn} \int_0^{L_x} \int_0^{L_y} \sin\left(\frac{m\pi x}{L_x}\right) \sin\left(\frac{n\pi y}{L_y}\right) \times \exp(-jk_x x) \exp(-jk_y y) dy dx \quad (2.43)$$

Evaluating the two-dimensional integral over x and y results in the following expression (Fahy 1985):

$$W(k_x, k_y) = \sum_{m=1}^{\infty} \sum_{n=1}^{\infty} W_{mn} \frac{(m\pi/L_x)[(-1)^m \exp(-jk_x L_x) - 1]}{[k_x^2 - (m\pi/L_x)^2]} \times \frac{(n\pi/L_y)[(-1)^n \exp(-jk_y L_y) - 1]}{[k_y^2 - (n\pi/L_y)^2]} \quad (2.44)$$

As in the case of the simply supported beam, the supersonic region of this transform corresponds to sound radiation to the acoustic far-field. Since the transform is defined in two dimensions, this corresponds to the following expression:

$$-k < \sqrt{k_x^2 + k_y^2} < k, \quad (2.45)$$

where k_x is the structural wavenumber in the x -direction and k_y is the structural wavenumber in the y -direction.

2.2 Time-Averaged Acoustic Intensity

For the purpose of evaluating the flow of acoustic power away from the radiating structure, the time-averaged acoustic intensity has proven to be a powerful tool in both analytical and experimental studies. Since this technique will be used to interpret results in chapter 6, the method of computing this quantity is outlined based upon the two microphone technique discussed by Petterson (1979). The technique is based upon a finite difference approximation of the gradient of the pressure computed at two acoustic field points in the direction chosen to compute the power flow. Due to Euler's inviscid equation of motion in a fluid, the velocity of the fluid can be obtained from the density of the medium and the gradient of the pressure for harmonic motion as follows:

$$j\omega\rho_o\vec{v} \doteq -\nabla p, \quad (2.46)$$

where:

- ρ_o = density of fluid
- \vec{v} = velocity of fluid
- p = acoustic pressure.

Hence the pressure is averaged to determine the approximate pressure between the two acoustic field points as follows:

$$p_{12} \simeq \frac{p_1 + p_2}{2}, \quad (2.47)$$

and the velocity is estimated between the two field points by the finite difference technique as follows:

$$v_{12} \simeq \frac{-(p_2 - p_1)}{\rho_o \Delta_{12}}, \quad (2.48)$$

where:

Δ_{12} = distance between acoustic field points
 p_{12} = pressure between the two field points
 v_{12} = velocity between the two field points.

One should note that both p_1 and p_2 are in general complex quantities. Based upon these approximations to the velocity and pressure, the time-averaged acoustic intensity can be approximated as follows:

$$\bar{I}_{12} \approx \frac{|p_1||p_2|}{2\rho_o\omega\Delta_{12}} \sin(\phi_1 - \phi_2), \quad (2.49)$$

where \bar{I}_{12} is the time averaged acoustic intensity between the two field points and ϕ_1 and ϕ_2 are the phase angles associated with the respective pressures p_1 and p_2 .

2.3 Summary

At this point, all analytical expressions required to model the disturbance, control input and error sensors for either the simply supported beam or simply supported plate have been presented. In addition, all expressions necessary to compute physical quantities such as the acoustic directivity pattern, structural response and time averaged acoustic intensity have been outlined. All that remains is to couple these analytical models approximating the chosen sensors and control actuators with an appropriate control approach for predicting both the controlled acoustic response and structural response of the two structures utilized in this study. The control

approaches used in both the simulations and experiments are outlined in chapter 3. Specifics of the design approach and implementation of the PVDF error sensors and PZT control actuators are included in chapter 4.

Chapter 3

Control Approaches

Feed forward control was implemented in this study by two distinctly different control approaches. In each approach, the cost function (i.e. functional to be minimized) was the same: the sum of the square of the modulus of the time varying signal output of each error sensor. The first approach is based upon the multi-channel version of the filtered-x adaptive LMS algorithm and was implemented on a TMS320C25 digital signal processing board for the purpose of conducting experiments. In the second approach, linear quadratic optimal control theory (LQOCT) is used to compute the optimal control solution for the chosen design problem analytically. While both approaches result in the identical optimal control solution, LQOCT requires much less computational time in the analytical studies. For example, in minimizing the acoustic response of a simply supported plate with three inputs (PZT actuators) and three outputs (microphones), the LMS algorithm typically converged to the optimal control solution in approximately 3.2 *million* iterations. While this can be accomplished in a matter of milli-seconds on a digital signal processing board experimentally, over one hour of CPU time was required on the IBM VM1 computer to simulate the experiment. Since LQOCT can be used to compute the *identical* optimal control response in approximately 2 minutes of CPU

time, this control approach was chosen for conducting the analytical studies and in the sensor design algorithms. Both control approaches are outlined below including a model reference implementation which can be used in conjunction with structural sensors such as accelerometers to achieve acoustic control.

3.1 The Filtered-x Adaptive LMS Algorithm

The method of control chosen for practical implementation is the multi-channel filtered-x version of the adaptive LMS algorithm. The standard implementation of the MIMO LMS algorithm is initially reviewed whereby the response due to the disturbance at the chosen error sensors is minimized with the control inputs. Upon outlining this method of control, the equations will be modified for implementation of model reference control whereby the response of the system is driven to some predetermined value at the chosen error sensors.

3.1.1 Standard Implementation

A schematic diagram of the filtered-x version of the adaptive LMS algorithm is presented in Figure 3.1 for reference with the following discussion. The multi-channel version of this algorithm was previously described by Elliot *et al.*, (1987), and will be briefly reviewed in this section. The output of an error sensor can be modelled at the n 'th time step as:

$$e_l(n) = e_l^D(n) + \sum_{m=1}^M \sum_{j=0}^{N-1} P_{lmj} \sum_{i=0}^{N-1} w_{mi}(n-j)x(n-i-j), \quad (3.1)$$

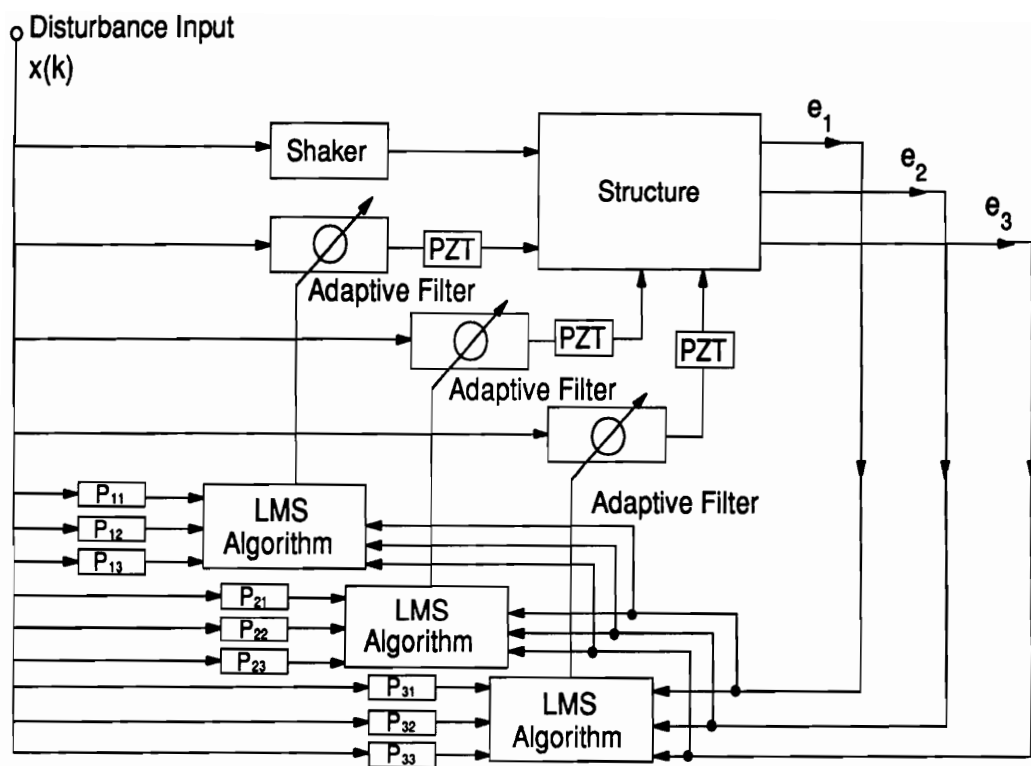


Figure 3.1: Schematic of Filtered-x Adaptive LMS Algorithm

where:

n = time step number

m = actuator number

l = error sensor number

i = filter coefficient number

$e_l^D(n)$ = error due to the disturbance at the l^{th} error sensor

$x(n)$ = input reference source

w_{mi} = coefficients of the adaptive fixed impulse response (FIR) for the m^{th} actuator and the i^{th} coefficient

P_{lmj} = j^{th} coefficient of the transfer function between the output of the m^{th} adaptive filter and the l^{th} error sensor

M = number of control actuators

N = number of filter coefficients.

In the LMS algorithm, the mean square error signal is defined by:

$$J = E \left[\sum_{l=1}^L e_l^2(n) \right], \quad (3.2)$$

where E is the expectation operator. Since this error function is quadratic, only one minimum solution exists. The outputs of the fixed filters, P_{lmj} , at each time step n , were used by the LMS algorithm to minimize the mean square error signal by modifying the coefficients of the adaptive filter as follows:

$$w_{mi}(n+1) = w_{mi}(n) - \mu \sum_{l=1}^L e_l(n) r_{lm}(n-i), \quad (3.3)$$

and

$$r_{lm}(n-i) = \sum_{j=0}^{N-1} P_{lmj} x(n-i-j). \quad (3.4)$$

Upon achieving control, the adaptive fixed filter coefficients converge to a steady state value. In the standard feed forward implementation, the desired response at the l^{th} error sensor is zero. Hence the adaptive filter coefficients, when multiplied by the reference signal, yield a response equal in magnitude and opposite in sign to the disturbance present at each error sensor, (i.e. e_l^D) when the number of actuators equals the number of error sensors. The response at each error sensor is thus driven to some minimum value depending on the computational accuracy of the machine or digital signal processing board being used.

3.1.2 Model Reference Implementation

For the case of model reference control, the desired response at the l^{th} error sensor is no longer zero, but rather some predetermined system response, e_l^{des} . The schematic diagram of 3.1 can be modified to include this reference plant model as illustrated in 3.2. Thus the standard implementation of the LMS algorithm presented in equation (3.1) can be modified to include the desired response at the l^{th} error sensor as follows:

$$e_l(n) = e_l^D(n) + e_l^{des}(n) + \sum_{m=1}^M \sum_{j=0}^{N-1} P_{lmj} \sum_{i=0}^{N-1} w_{mi}(n-j)x(n-i-j), \quad (3.5)$$

The desired response at each error sensor is created from a finite impulse response (FIR) filter just as the system time delays and frequency response characteristics are included in the filtered-x FIR coefficients, P_{lmj} . These coefficients are required to incorporate the transfer functions between the error sensors and the control actuators as well as the inherent time delays in the system into the control algorithm. The filtered-x coefficients are measured by driving each control actuator sequentially

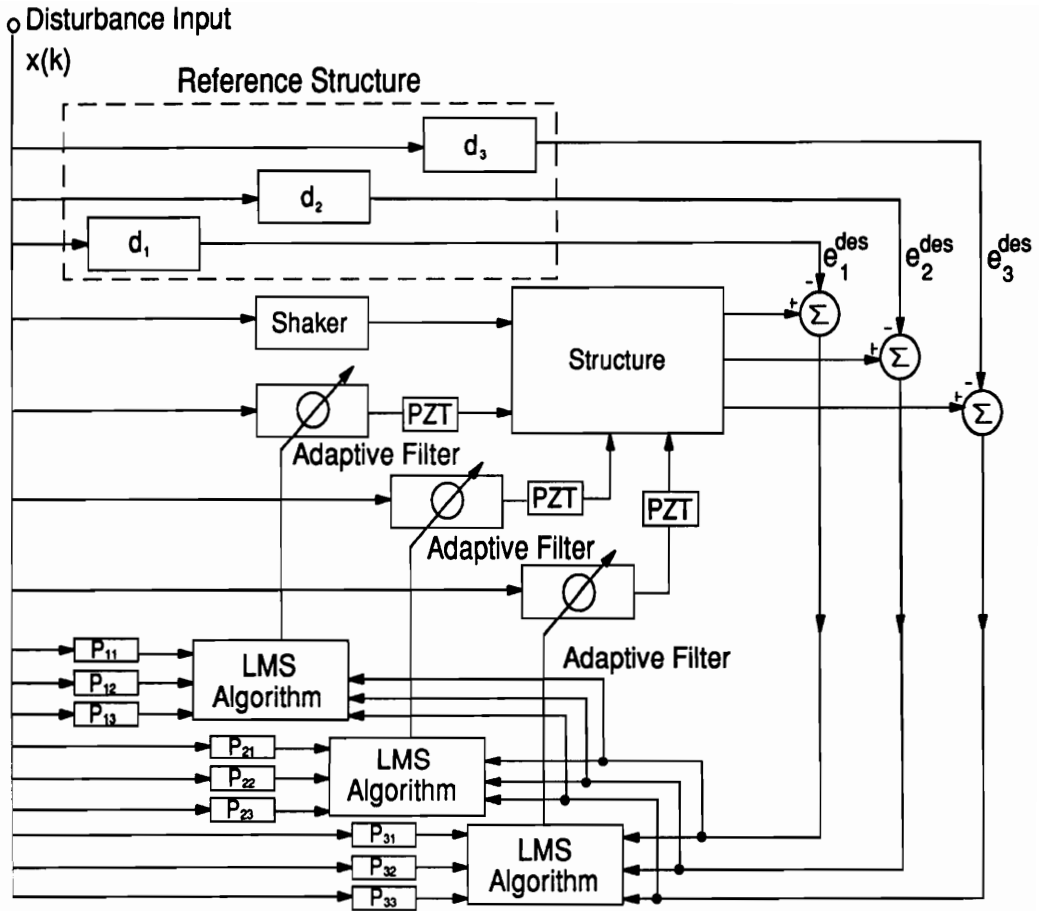


Figure 3.2: Schematic of Model Reference Filtered-x Adaptive LMS Algorithm

with a constant phase and amplitude harmonic signal and measuring the transfer function between the output of the l^{th} error sensor and the m^{th} control actuator. A similar technique is used to experimentally determine the desired response e_l^{des} at each chosen error sensor. This response is computed from a set of FIR filter coefficients as follows:

$$e_l^{des}(k) = d_{l_0}x(k) + d_{l_1}x(k - 1), \quad (3.6)$$

where d_{l_0} and d_{l_1} are the two filter coefficients required to model the desired harmonic response at the l^{th} error sensor. These coefficients can be obtained either analytically or experimentally. If obtained analytically, an accurate model of the plant must be used as in state feedback methods; however, an alternative option exists with the feed forward approach.

For example, if the objective is to eliminate microphone error sensors in favor of structural error sensors such as accelerometers, the microphone error sensors can initially be implemented in the control approach. The desired response at these error sensors is typically zero, unless minimizing the response at the chosen microphone locations results in significant spillover in the residual acoustic field (i.e. regions other than where the microphones are positioned). However, in typical applications, microphone positions are chosen such that this undesired characteristic is not prevalent and thus the desired response e_l^{des} is zero at each of the l_{th} microphone positions. Upon obtaining the desired control response, the structure is configured with a number of accelerometers at least equivalent to the number of control actuators and located at unique structural coordinates. (The number of error sensors

must be at least equivalent to the number of control actuators and located at unique coordinates on the structure for the controlled response to be unique.) The transfer function between the response at each accelerometer and the reference signal $x(k)$ is measured and stored as a set of FIR coefficients, d_{l_0} and d_{l_1} at each of the l^{th} structural error sensor positions.

Upon measuring the transfer function at the spatial coordinates of each structural error sensor, the necessary information for creating the model reference response is experimentally obtained. The control based upon the microphone error sensors can now be eliminated. The difference in this control approach is that the structural response at each error sensor is driven to that corresponding to the controlled acoustic response as opposed to driving the response of each structural error sensor to zero. The resulting acoustic directivity pattern is identical to that achieved when implementing the microphone error sensors as demonstrated in Appendix B, yielding a unique method of achieving structural acoustic control.

3.2 Linear Quadratic Optimal Control

While the previously outlined control approach was modeled for analytical studies, it was primarily used for practical experimental implementation. Linear quadratic optimal control theory was utilized to compute the optimal control voltages for the present analytical studies. These two control approaches were observed to yield the same optimal solution in a previous study by the authors (Clark and Fuller (1991(f))). The standard approach for implementing LQOCT is outlined whereby the response at each error sensor modeled is minimized. Upon describing this method of control,

the equations will be modified to yield the controlled model reference response of the chosen structure.

3.2.1 Standard Implementation

As in the LMS algorithm, the cost function is formulated as a sum of the squares of the response at each point error sensor as follows:

$$C = \sum_{b=1}^{ne} e_b e_b^* \quad (3.7)$$

where:

- e_b = output of error sensor
- e_b^* = complex conjugate of e_b
- ne = number of error sensors.

The error sensor output can be formulated in terms of the transfer functions between the sensors and both the disturbance and the control actuators as follows:

$$e_b = \left(\sum_{s=1}^{na} T_{bs} \hat{V}_s \right) + T_{bD} F \quad (3.8)$$

where:

- T_{bs} = transfer function between s^{th} actuator and b^{th} error sensor
- T_{bD} = transfer function between the disturbance and b^{th} error sensor
- \hat{V}_s = complex voltage of s^{th} actuator
- F = input force
- na = number of control actuators.

The transfer functions listed above are not to be viewed as specific to any particular type of error sensor. For example, if the structural response is taken as an error

signal, the transfer function between the chosen error sensor and the disturbance can be constructed by substituting equation (2.3) into equation (2.33):

$$T_{bD}^a = -\omega^2 \sum_{m=1}^M \frac{W_m^F}{F} \sin(\gamma_m x_b). \quad (3.9)$$

Similarly, the same transfer function can be created for the resulting radiated pressure by substituting equation (2.3) into equation (2.39):

$$T_{bD}^p = -\frac{\omega^2 \rho_o}{2\pi} \sum_{m=1}^M \frac{W_m^F}{F} \int_0^{w_b} \int_0^{L_x} \frac{\sin(m\pi x_b/L_x) \exp(-jk\sqrt{(x' - x_b)^2 + (y' - y_b)^2 + (z')^2})}{\sqrt{(x' - x_b)^2 + (y' - y_b)^2 + (z')^2}} dx dy, \quad (3.10)$$

or a spectral line of the k-transform respectively by substituting equation (2.3) into equation (2.41):

$$T_{bD}^k = \sum_{m=1}^M \frac{W_m^F}{F} \frac{(m\pi/L_x)[(-1)^m \exp(-jk_x L_x) - 1] \sin(k_y w_b/2)}{[k_{x_b}^2 - (m\pi/L_x)^2](k_y/2)}. \quad (3.11)$$

The transfer functions for the control actuators, T_{b_s} , can be constructed from equations (3.9), (3.10), and (3.11) by simply replacing the force, F , with the applied voltage \hat{V} , and the modal amplitudes corresponding to point force excitation, W_m^F , with the modal amplitudes corresponding to excitation by the p^{th} piezoceramic actuator, W_m^P .

Proceeding with the solution, we take the partial derivative of the cost function of

equation (3.7) with respect to each control input, which is represented in equation (3.8). By taking the partial derivative of the cost function with respect to the real and imaginary part of each control voltage input and equating each respective expression with zero, one obtains a system of equations whose solution yields the optimal control inputs since the minimum of the cost function has zero slope. This system of linear equations can be expressed in general form as follows:

$$\left\{ \sum_{b=1}^{ne} \left(\sum_{l=1}^{na} T_{bl} \hat{V}_l + T_{bD} F \right) T_{bs}^* = 0 \right\}; \quad s = 1, na. \quad (3.12)$$

The previous set of equations can be represented with linear algebra.

$$[A][\hat{V}] = [b], \quad (3.13)$$

where $[A]$ is the matrix defining the transfer functions between the error sensors and control actuators, $[\hat{V}]$ is the vector containing the complex optimal control inputs and $[b]$ is the vector containing the input disturbance. Since the number of unknowns is equivalent to the number of equations, the solution is obtained as follows:

$$[\hat{V}] = [A]^{-1}[b]. \quad (3.14)$$

3.2.2 Model Reference Approach

To include a reference response in the model, the cost function defined in equation (3.7) must be modified. As opposed to minimizing the response at the coordinates of a chosen error sensor, the difference between the response at that error sensor and

the desired response is minimized. In other words, the response at the error sensor is driven to the model reference response. The cost function presented in equation (3.7) is thus modified as follow:

$$C_{ref} = \sum_{b=1}^{ne} (e_b - r\hat{e}f(x_b))(e_b - r\hat{e}f(x_b))^*, \quad (3.15)$$

where $r\hat{e}f(x_b)$ is the desired response at the b^{th} error sensor. The system of linear equations presented in equation (3.12) can be modified to include the reference response as follows:

$$\left\{ \sum_{b=1}^{ne} \left(\sum_{l=1}^{na} T_{bl} \hat{V}_l + T_{bD} F - r\hat{e}f(x_b) \right) T_{bs}^* = 0 \right\}; \quad s = 1, na. \quad (3.16)$$

Obviously if the reference response, $r\hat{e}f(x_b)$, is set equal to zero, the above expression reduces to equation (3.12).

3.3 Discussion of Practical Implementation and Summary

Two basic control approaches have been outlined, the filtered-x version of the adaptive LMS algorithm and linear quadratic optimal control theory. The linear quadratic optimal control approach was presented as a method of predicting the controlled response of the system primarily for the purpose of sensor design which is outlined in the following chapter. The MIMO filtered-x adaptive LMS algorithm was discussed in view of practical implementation of feed forward control for conducting

experiments on test structures. In typical applications of the LMS algorithm, the control inputs are utilized to simply minimize the response of the disturbance at the chosen error sensors. However, as demonstrated in this chapter, the LMS algorithm is readily implemented in model reference control applications. Hence structural acoustic coupling can be included in the cost function of the controller to achieve the desired structural acoustic response when implementing point structural error sensors such as accelerometers.

Model reference control was implemented with accelerometers configured as structural error sensors on the simply supported plate as illustrated in the schematic diagram of Figure 3.3. As demonstrated in Appendix B, when the number of actuators is at least equal to the number of reference sensors (i.e. accelerometers), then the reference response of a structure with a set of unique eigenfunctions is uniquely defined using the model reference approach. This result is very useful since the original cost function can be formulated with as many error sensors as desired; however, the number of error sensors resulting in the desired control condition can be reduced to a number of structural sensors equivalent to the number of control actuators implemented as previously discussed by Clark and Fuller (1991(d)). The method of implementation is represented in the schematic diagram of Figure 3.3 to graphically convey the concept. While a significant number of microphone error sensors are depicted in the acoustic field, the number of structural sensors (accelerometers) implemented in the model reference control approach must simply equal the number of control actuators used to achieve the desired response (i.e. two in this case). The cost function is then constructed from the residual structural response at a number of coordinates at least equivalent to the number of control actuators, and the re-

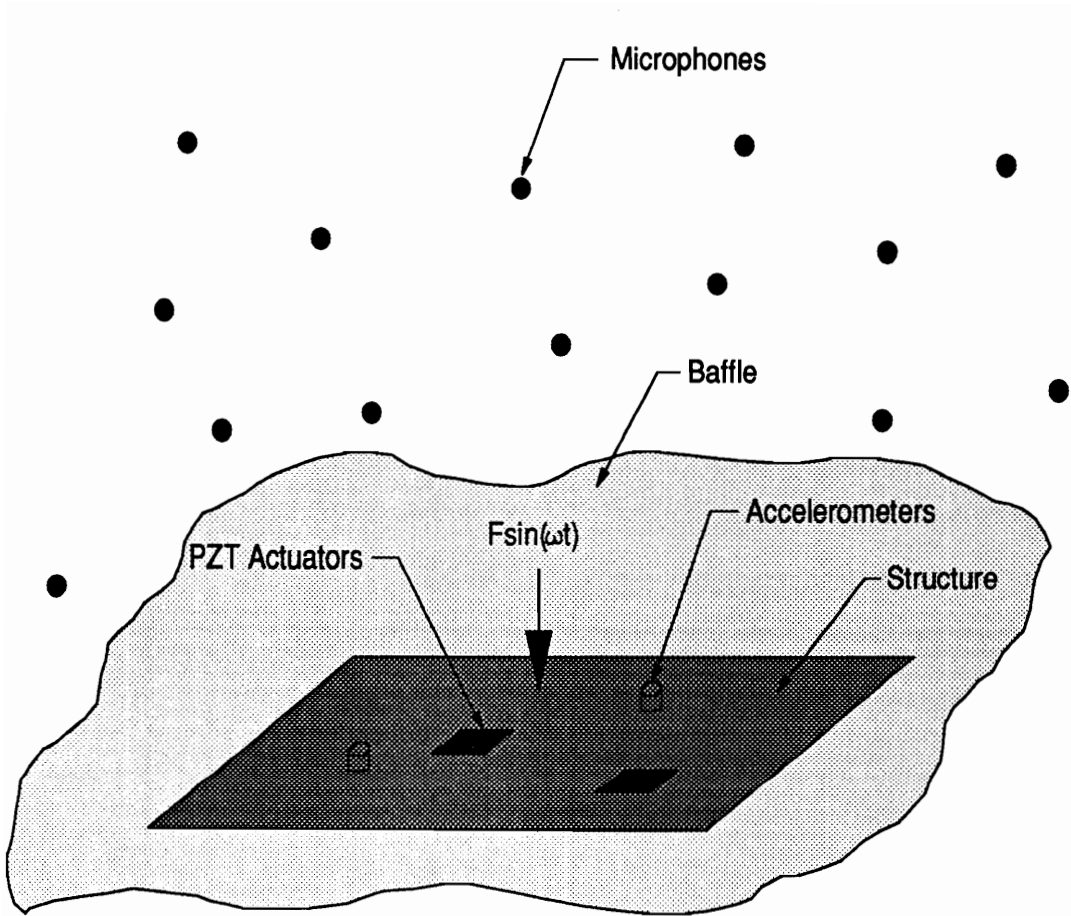


Figure 3.3: Schematic of Model Reference Implementation

sponse is driven to the predetermined value at each coordinate. Thus for example, if global sound attenuation is achieved with two control actuators and the microphone error sensors illustrated, then only two uniquely positioned structural error sensors are required to achieve the same acoustic directivity pattern and hence the same performance as proved in Appendix B.

Chapter 4

Design Approaches for PZT Actuators and PVDF Sensors

Previous studies by Clark and Fuller (1990(a,b)) have demonstrated both analytically and experimentally that increasing the number of control channels yields a further increase in the levels of far-field sound attenuation. With this brute force approach, the only limitation placed on the level of attenuation is the number of control channels and corresponding transducers which can be feasibly implemented. While this approach has merit, an alternative design approach exists. In many cases, by positioning the control actuators on the structure with some prior knowledge of the structural modes contributing to the sound radiation, the number of control channels can be significantly reduced. As the modal density of the structural response increases, this task of choosing “optimal” locations for control actuators becomes more difficult. One could write an algorithm which tests every possible location; however, this approach would require an unacceptable amount of computer time. As an alternative, optimal design approaches can be implemented to choose appropriate locations for control actuators through nonlinear optimization techniques. This approach was previously investigated analytically for structural acoustic control applications by Wang *et al.*, (1991(a)) and has since been demon-

strated experimentally by Clark and Fuller (1991(e)).

In addition to optimizing the positions of the control actuators, the position and dimensions of rectangular structural PVDF error sensors can be optimized such that when implemented in the cost function of an appropriate control algorithm, minimizing the electrical response of these sensors results in a reduction of the far-field sound radiated. This nonlinear optimization of sensor position and dimensions has been investigated both analytically and experimentally by Clark and Fuller (1991(e)) on the test structures of this study and is proposed as a design approach for eliminating microphones located in the acoustic field as error sensors. In addition, the positions of acoustic near-field sensors constructed from PVDF have been optimized to meet the same objective. These sensors are proposed for applications which restrict attaching the sensor material to the structural surface or when the surface is covered by a matrix support material such as foam. While optimization of sensor position is readily achieved for harmonic applications, this technique is complicated by multi-frequency input disturbances.

To address this problem and provide a foundation for future work, a technique for optimizing the weighting of the electrical outputs of an array of distributed PVDF sensors bonded to the structural surface is discussed. In this application, the same sensors can be implemented regardless of the frequency of the input disturbance. The smart sensor is created by weighting the response of each sensor element with a number between 1 and -1 and summing this weighted response to create the “optimal” sensor response. While more signal processing will be required with this approach (possibly a neural network), greater flexibility is afforded in the design pro-

cess. Each of the previously mentioned sensor design approaches are documented in this chapter with an overview of the nonlinear optimization algorithm used to achieve the desired design objectives.

In addition to the rectangular structural error sensors and acoustic near-field sensors constructed from PVDF, shaped or “weighted” PVDF error sensors are studied as an alternative method of eliminating microphones located in the acoustic field in the control approach. These “weighted” sensors are shaped, in the one-dimensional case, as a function of the mode shapes to obtain the desired polarization profile which results in an electrical response proportional to the acoustic response to be minimized. A previous study by Clark *et al.* (1992(b)) demonstrated both analytically and experimentally that PVDF sensors can be shaped for structural acoustic control applications. In the two-dimensional case, the design approach for achieving the “weighted” sensor is outlined; however, the two-dimensional sensor is not readily constructed due to the complexity of the required polarization profile.

4.1 Overview of Rectangular Shaped Structural PVDF Sensors

Before proceeding with optimization techniques for obtaining the appropriate dimensions and position of rectangular PVDF structural error sensors, the basic characteristics of this sensor are outlined. The discussion will be restricted to applications on the simply supported plate, realizing that the same concepts apply to the one-dimensional simply supported beam. The plate is the more complicated of the two design problems since its structural response is a function of two dimensions as

outlined in equation (2.2). Recalling equation (2.24), which represents the response of an element of PVDF bonded to the surface of the plate, one must simply define the area of application, $F(x, y)$, to obtain the corresponding electrical response of the sensor as a function of the structural response. In the case of rectangular error sensors, this function is defined simply as follows:

$$F(x, y) = (u(x - x_3) - u(x - x_4))(u(y - y_3) - u(y - y_4)), \quad (4.1)$$

where $u(*)$ is defined to be the spatial step function in the appropriate dimension. Substituting this expression into equation (2.24) and integrating over the boundaries yields the following result:

$$q_u(t) = \frac{(h_p + h_s)}{2} \sum_{m=1}^M \sum_{n=1}^N W_{mn} \left[e_{31}^o \frac{mL_y}{nL_x} + e_{32}^o \frac{nL_x}{mL_y} \right] (\cos(\gamma_m x_4^u) - \cos(\gamma_m x_3^u)) \times (\cos(\gamma_n y_4^u) - \cos(\gamma_n y_3^u)) \exp(j\omega t), \quad (4.2)$$

where (x_3^u, y_3^u) are the coordinates of the lower left corner of the u^{th} PVDF strip, and (x_4^u, y_4^u) are the coordinates of the upper right corner of the u^{th} PVDF strip. Observe that while the previous equation represents the response of a single rectangular strip of PVDF, sensors of arbitrary shape can be modeled with this equation by simply dividing the irregular shape into subdivisions of rectangular elements and summing the response from each element, with the correct phasing, similar to numerical integration.

In equation (4.2) one should recognize that the frequency response characteristics

of the structure are included in the modal amplitudes defined by W_{mn} . As a result, if one considers the response of the sensor as a function of the modal coordinates, omitting the specific response of the structure (i.e. the modal amplitudes W_{mn}), the modal weighting of each sensor as a function of the chosen spatial coordinates of the structure can be derived:

$$M_{mn} = \left[e_{31}^o \frac{mL_y}{nL_x} + e_{32}^o \frac{nL_x}{mL_y} \right] (\cos(\gamma_m x_4^u) - \cos(\gamma_m x_3^u)) \times (\cos(\gamma_n y_4^u) - \cos(\gamma_n y_3^u)), \quad (4.3)$$

where M_{mn} are the modal weighting coefficients of the rectangular sensor. The first observation which can be made about this expression is that the modal weighting is always a real number. Hence the phase relationship between each structural mode remains unaltered by the spatial window created by the rectangular PVDF sensor. As a result of this observation, the phase relationships between structural modes cannot be specified in the sensor design when implementing a *single* element of PVDF. The second observation pertains to the position of the sensor on the structure. The cosine functions serve to partly define the relative contribution of each structural mode in the electrical response of the sensor as a function of the chosen spatial coordinates. If the sensor is centered over a nodal line of the structure, the resulting electrical response as a function of all modes with the corresponding nodal line will be zero. This observation can be used to the designer's advantage since some structural modes are inefficient acoustic radiators and hence do not require control in the presence of more dominant radiating structural modes. The relative weighting of each structural mode is also controlled by the modal indices

since the PVDF sensor is a strain sensing device. Consider the following component of equation (4.2):

$$\left[e_{31}^o \frac{mL_y}{nL_x} + e_{32}^o \frac{nL_x}{mL_y} \right].$$

As indicated in the expression, the weighting of each mode is dependent upon the dimension of the structure as well as the modal indices. As a simplified example, consider a square plate with $L_x = L_y$. Considering only the weighted response of the sensor as a function of the above expression, one recognizes that all modes for which the modal indices m and n are equal have the same weighting. In addition, the greater the separation between modal indices, the greater the contribution of that structural mode to the electrical response of the sensor as a function of the above expression. For example, if structural modes with indices ranging from $m = 1, \dots, 5$ and $n = 1, \dots, 5$ are the only modes included in the response of the structure, the (1,5) and (5,1) modes will have the greatest contribution to the electrical response of the sensor based upon the above expression. If desired, the level of response to these higher order modes can be attenuated to some degree by positioning the sensor on or near nodal lines as discussed earlier. However, this quality of being more sensitive to modes with greater separation between the modal indices is not totally undesirable due to the mechanisms of sound radiation. As outlined in chapter 1, modes with a large separation in the modal indices are considered edge radiators when $k/k_s \ll 1$ and are of greater concern than the corner radiators.

Based upon the observations outlined above, a preliminary study was conducted implementing rectangular PVDF structural error sensors configured on the surface

of a simply supported plate as illustrated in Figure 4.1. Since the radiation efficiency of the plate modes for which both modal indices m and n are even are the least efficient acoustic radiators for $k/k_s < 0.25$, the initial design concept was to place two rectangular elements of PVDF across the surface of the plate in the x and y -direction respectively as depicted in Figure 4.1. The modal weighting for the x -direction and y -direction sensor was computed from equation 4.3 and is illustrated in Figure 4.2 and 4.3 respectively for each sensor. In each case, the modal weighting was normalized with respect to the dominant mode displayed in the sensor response. As illustrated in Figure 4.2, the x -direction sensor (PVDF2) does not observe any mode with an even modal indice. The even modes in the y -direction of the plate were eliminated from the sensor response by placing the sensor on the center-line of the plate with respect to the y -direction. Similarly, the even modes in the x -direction were eliminated by centering the sensor on the center-line of the plate with respect to the x -direction. As illustrated in Figure 4.3, the y -direction sensor (PVDF1) does not observe modes for which the modal indice n is even. Minimizing the response of each of these error sensors will place more emphasis on modes for which both m and n are odd and to a lesser degree modes for which one modal indice is odd and the other is even. Tests were conducted for both on and off-resonance operating conditions and results from this design approach will be discussed in Chapter 6. While this simple design approach based upon the physical mechanisms of structure-borne sound was conducted for the purpose of evaluating the rectangular PVDF structural error sensors, more complicated design approaches were achieved through the nonlinear optimization techniques outlined below.

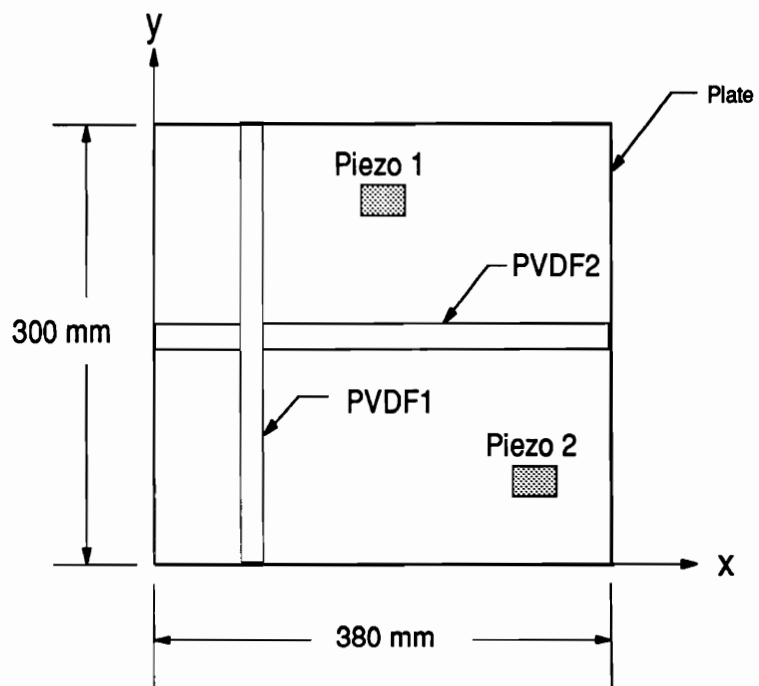


Figure 4.1: Schematic of Plate with PVDF Sensors and PZT Actuators

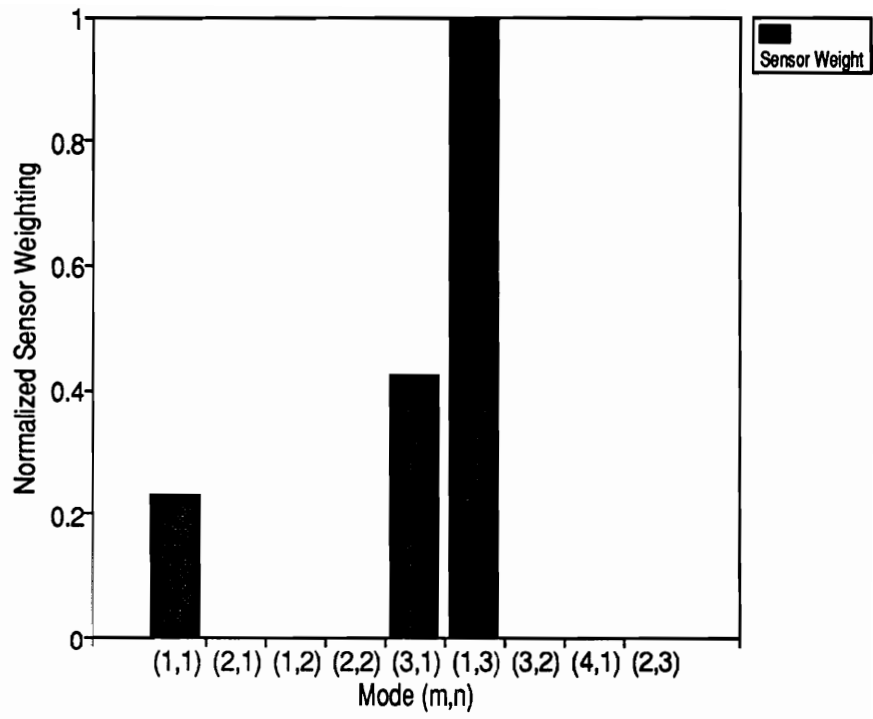


Figure 4.2: Modal Weighting of x-direction PVDF Sensor (PVDF2)

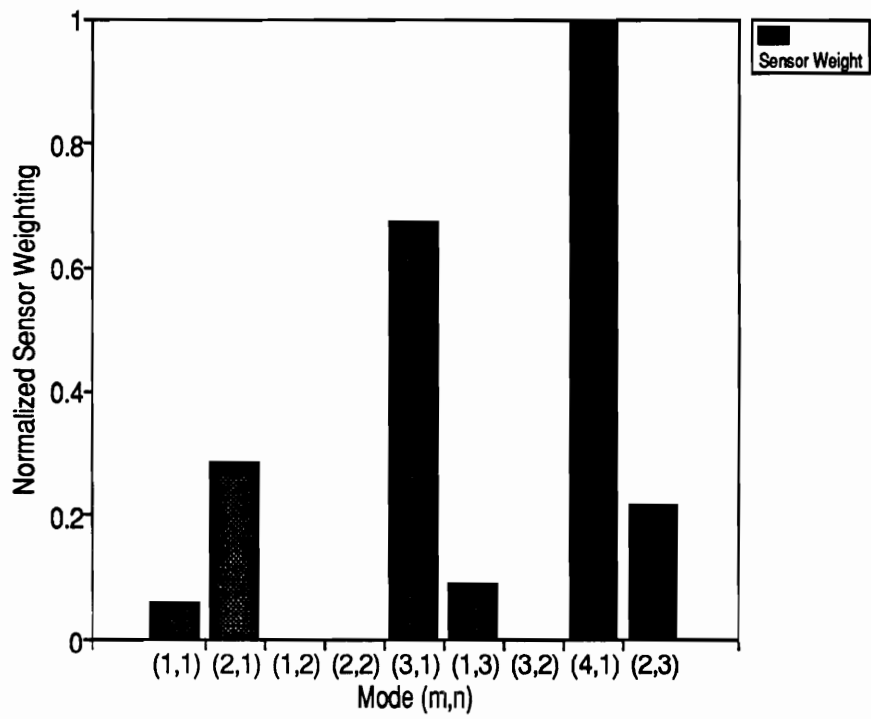


Figure 4.3: Modal Weighting of y-direction PVDF Sensor (PVDF1)

4.2 Nonlinear Optimization of Actuator and Sensor Location/Dimension

The optimal location of single and multiple piezoelectric actuators for controlling structure-borne sound was theoretically obtained as previously outlined by Wang *et al.*, (1991(b)) utilizing an acoustic objective function consisting of the sum of the mean square radiated sound pressures by a finite number of microphones approximating the total radiated acoustic power. This objective function was implemented in the optimization routine as opposed to the expression for the radiated acoustic power to reduce computational time. A flow chart of the solution strategy, which is similar to that presented earlier by Wang *et al.*, (1991(b)), is presented in Figure 4.4. As illustrated, two alternative paths exist in the flow chart. In the first path, the optimal location of the control actuator(s) is determined, and upon converging to a solution meeting the required accuracy test, the second path of the algorithm is executed. The size of the actuator is not optimized since excessive voltage levels are required to drive the actuator as the size is decreased, thus constraining the lower dimension, and limitations on practical manufacturing of the PZT material constrain the upper dimension. In the second path, the optimal size *and* location of a rectangular PVDF error sensor(s) is determined with the same acoustic objective function and the previously computed coordinates for the optimal location of the rectangular control actuator(s).

4.2.1 Formulation of Generic Optimization Problem

The core algorithm for determining the optimal piezoelectric actuator location or the optimal PVDF error sensor size and location are identical. Linear quadratic

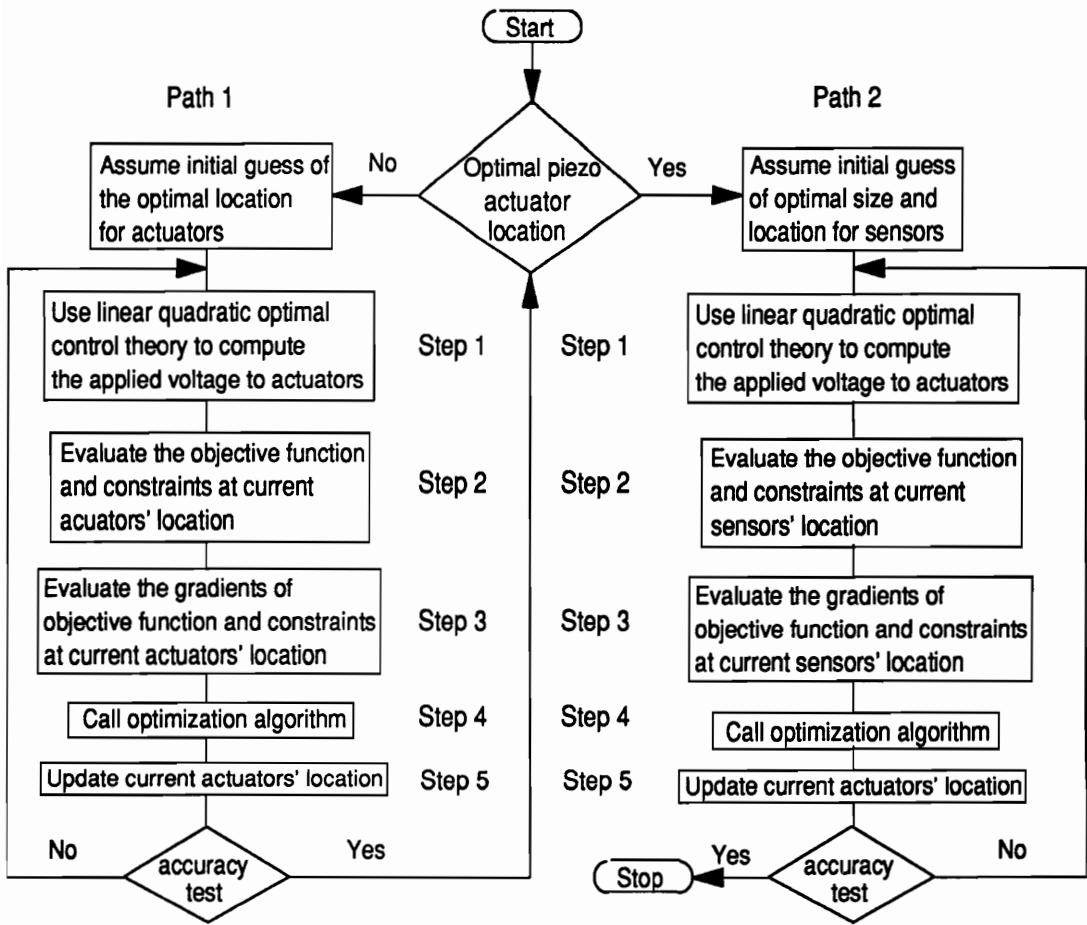


Figure 4.4: Flow Chart of Optimization Algorithm

optimal control theory is used to compute the optimal control voltage for the given control actuator/sensor configuration in step 1, regardless of whether path 1 or path 2 is taken. Linear quadratic optimal control theory was discussed in detail in chapter 3, and the main concept is to realize that, given a set of error sensors and control actuators configured with a plant (i.e. the simply supported plate), the optimal control voltages to the actuators can be computed with this technique. Upon determining the optimal control voltage for the given actuator/sensor configuration, the objective function and constraints are evaluated in step 2. The objective function is the functional expression containing the overall design objective, which in the case of structural acoustic control is an expression of the total sound power radiated. In step 3, the gradients of the objective function and constraints are computed for the current actuator location or current error sensor size and location, depending on whether path 1 or path 2 is taken respectively. Upon determining the gradients, the optimization algorithm is invoked in step 4, and the actuator or sensor design parameters are updated depending on the chosen path. The accuracy test is completed based upon the updated parameters and the program either terminates or proceeds.

If path 1 of the algorithm depicted in Figure 4.4 is executed, the error sensors chosen in the cost function of the control approach are microphones with coordinates corresponding to those implemented in the objective function. Microphones were chosen in this path since they provide the best estimate of the *desired* cost function, which in this case is the same as the objective function (i.e. far-field sound power). Note that the cost function is used to describe the functional to be minimized in the actual control implementation while the objective function is used to describe

the functional to be minimized in the nonlinear optimization approach. Upon converging to a solution, the optimal location of the control actuator for minimizing far-field sound radiation is obtained.

If path 2 of the algorithm is executed, the piezoelectric actuator location obtained from path 1 is used as the control input, and as opposed to microphone error sensors, the PVDF error sensors are implemented in the cost function since the electrical response of these sensors is the quantity to be minimized in the control algorithm. As opposed to optimizing the actuator position, the location and dimensions of the rectangular PVDF sensors are the variables to be optimized in this path of the design optimization. Optimization of the sensor design parameters continues until the objective function is reduced to the same level as that obtained in path 1. At this point, the maximum control authority of the actuator over the acoustic field has been obtained. Further optimization of the PVDF sensor design parameters cannot increase the level of acoustic control achieved with the given optimally located control actuators.

4.2.1.1 Design Variables

Whether the piezoelectric actuator location is being optimized or the PVDF error sensor size and shape are being optimized the format of the design variables is identical. A schematic of the simply supported plate configured with a rectangular piezoelectric patch whose location and size is to be optimized is presented in Figure 4.5. The dimensions of the rectangular element in the x and y-direction of the coordinate system will be denoted w_{x_i} and w_{y_i} respectively. The spatial coordinates

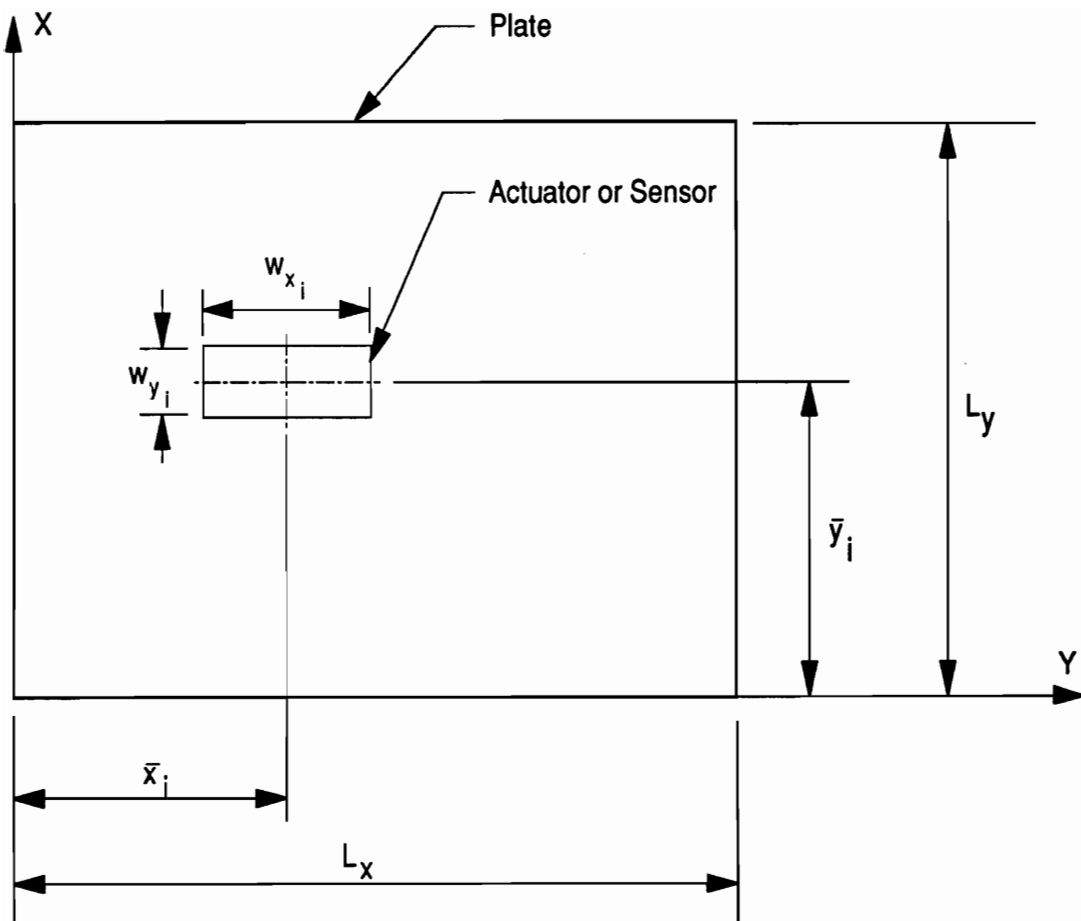


Figure 4.5: Schematic of Optimal Design Variables

of the center of the rectangular element will be denoted \bar{x}_i and \bar{y}_i with respect to the x-y axis. These variable parameters are independent of whether the rectangular element is termed an actuator or a sensor. If path 1 of the algorithm is chosen, the total radiated sound pressure can be written as a function of the coordinates of the control actuator(s) as well as the control voltage as follows:

$$p_t = p_t(\bar{x}_{a_i}, \bar{y}_{a_i}, w_{x_{a_i}}, w_{y_{a_i}}, V_{a_i}), \quad (4.4)$$

where the subscript a indicates coordinates of an actuator, and the subscript i refers to the i^{th} actuator. In this section of the algorithm, the actuator dimension was fixed, and only the location of the actuator was optimized. Actuator size was omitted from the design parameters due to physical limitations imposed by the size of commercially available material as well as maximum voltage limitations imposed as actuator size decreases. The optimal control voltage, V_{a_i} is a function of the location of the actuator as well as the dimensions, and hence, rewriting equation (20) as a function of the variables included in the optimization, we obtain:

$$p_t = p_t(\bar{x}_{a_i}, \bar{y}_{a_i}, V_{a_i}(\bar{x}_{a_i}, \bar{y}_{a_i})). \quad (4.5)$$

Now, if path 2 of the optimization algorithm is chosen, and hence the PVDF error sensor size and location is optimized, the total pressure can be expressed as follows:

$$p_t = p_t(\bar{x}_{s_i}, \bar{y}_{s_i}, w_{x_{s_i}}, w_{y_{s_i}}, V_a(\bar{x}_{s_i}, \bar{y}_{s_i}, w_{x_{s_i}}, w_{y_{s_i}})). \quad (4.6)$$

where the subscript s indicates coordinates of the PVDF error sensor, and the subscript i refers to the i^{th} sensor. At this point in the design approach, the optimal actuator location has been computed. However, at each step in the algorithm the optimal control voltage to the actuator is updated, resulting in the minimization of the error sensor response for the current sensor design parameters. As a result, the control voltage to the actuators is now a function of the sensor design parameters.

4.2.1.2 Objective Function

The desired goal is to locate the actuator and sensor in such a way that the total far-field sound radiation from the structure is minimal. Based on this goal, the logical choice for an objective function is one based on the sound power. Wang, Dimitriadis and Fuller (1991(c)) chose the integral of the square of radiated sound pressure over a hemisphere of the structure as the objective function. This objective function can be formulated as follows:

$$\Phi_p = \frac{1}{R^2} \int_0^{2\pi} \int_0^{\pi/2} |p_t|^2 \sin(\theta) d\theta d\phi. \quad (4.7)$$

In view of practical implementation, Wang *et al.*, (1991(c)) proposed a finite sum of the mean square radiated sound pressures measured by a limited number of microphones as an approximation to the above objective function. This method of implementation is a discretized version of the total sound power presented in equation (4.7), and the objective function can be represented by the following summation:

$$\Psi_p = \sum_{i=1}^{N_{mic}} |p_{t_i}(R_i, \theta_i, \phi_i)|^2. \quad (4.8)$$

In implementing equation (4.8), a reasonable number of pressure sensors should be chosen such that the global estimate of the objective function is not lost; however, the number of pressure sensors should not be so great as to significantly increase the computational time of the program.

4.2.1.3 Equality and Inequality Physical Constraints

The optimal design parameters for both the actuator and sensor were constrained to meet physical limitations such as plate boundaries as well as limitations on control voltage to the actuator. If path 1 of the algorithm was chosen, the position of the piezoelectric actuator must be constrained within the boundaries of the plate. For the case of multiple actuators, the design parameters were further constrained to prevent overlap between actuators. Finally, the allowed control voltage was limited to 400 volts peak to peak in accordance with previous tests conducted demonstrating the approximate point of failure of actuators with the same dimensions and material properties (Clark *et al.*, 1991(a)). Design variable constraints are listed below.

1. Constrain piezoelectric actuator to plate boundaries:

$$\bar{x}_{a_i} - w_{x_{a_i}}/2 \geq 0$$

$$\bar{x}_{a_i} + w_{x_{a_i}}/2 \leq L_x$$

$$\bar{y}_{a_i} - w_{y_{a_i}}/2 \geq 0$$

$$\bar{y}_{a_i} + w_{y_{a_i}}/2 \leq L_y \quad (4.9)$$

2. Constrain overlap between control actuators:

$$\begin{aligned} & [(\bar{x}_{a_{(i+1)}} - \bar{x}_{a_i})^2 + (\bar{y}_{a_{(i+1)}} - \bar{y}_{a_i})^2]^{1/2} - \frac{1}{2}[(w_{x_{a_i}}^2 + w_{y_{a_i}}^2)^{1/2} \\ & - (w_{x_{a_{(i+1)}}}^2 + w_{y_{a_{(i+1)}}}^2)^{1/2}] > 0 \end{aligned} \quad (4.10)$$

3. Constrain voltage to piezoelectric actuator:

$$|V_{a_i}| \leq 400 \quad (\text{volt p-p}) \quad (4.11)$$

It should be noted that the above constraint on the control voltage further constrains the dimensions of the control actuator, which is the reason that the actuator size was not chosen as a design parameter.

In path 2 of the algorithm, the sensor size and location must be constrained such that the sensor resides within the plate boundaries. In addition, for the case of multiple sensors, the solution was constrained to prevent overlap between sensors. All sensor constraints are listed below.

1. Constrain PVDF error sensor dimensions to that of the plate:

$$\begin{aligned} 0 & \leq w_{x_{s_i}} \leq L_x/2 \\ 0 & \leq w_{y_{s_i}} \leq L_y/2 \end{aligned} \quad (4.12)$$

2. Constrain PVDF error sensor to plate boundaries:

$$\begin{aligned}
 \bar{x}_{s_i} - w_{x_{s_i}}/2 &\geq 0 \\
 \bar{x}_{s_i} + w_{x_{s_i}}/2 &\leq L_x \\
 \bar{y}_{s_i} - w_{y_{s_i}}/2 &\geq 0 \\
 \bar{y}_{s_i} + w_{y_{s_i}}/2 &\leq L_y
 \end{aligned} \tag{4.13}$$

3. Constrain overlap between PVDF error sensors [17]:

$$\begin{aligned}
 &[(\bar{x}_{s_{(i+1)}} - \bar{x}_{s_i})^2 + (\bar{y}_{s_{(i+1)}} - \bar{y}_{s_i})^2]^{1/2} - \frac{1}{2}[(w_{x_{s_i}}^2 + w_{y_{s_i}}^2)^{1/2} \\
 &- (w_{x_{s_{(i+1)}}}^2 + w_{y_{s_{(i+1)}}}^2)^{1/2}] > 0
 \end{aligned} \tag{4.14}$$

4.2.1.4 Review of Optimization Procedures

Upon determining the constraints on the design parameters, the optimization routine is invoked. An IMSL subroutine named N0ONF (IMSL User's Manual, 1989), which solves a general nonlinear programming problem, was implemented to compute the optimal solution for both path 1 and path 2 of Figure 4.4. The gradient of the design parameters was estimated within the successive quadratic programming algorithm by means of an IMSL (IMSL User's Manual, 1989) subroutine called CDGRD, which applies the central finite difference method to approximate the gradient. The general constrained optimization problem can be stated mathematically with the objective function (Arora 1989):

$$f(\vec{x}) = f(x_1, x_2, \dots, x_n), \tag{4.15}$$

subject to the equality constraints

$$h_j(\vec{x}) = 0; \quad \text{for } j=1, m_e \quad (4.16)$$

and the inequality constraints

$$g_j(\vec{x}) > 0; \quad \text{for } j=1, m_{e+1}, m \quad (4.17)$$

where m_e is the number of equality constraints, and m is the total number of constraints. Both the objective function, f , and the constraint functions, h_i and g_i , are assumed to be continuously differentiable. The solution technique is based on the iterative formulation and solution of quadratic programming subproblems. The subproblems are obtained by using a quadratic approximation of the Lagrangian and linearizing the constraints as follows:

$$\min_{\vec{d} \in \mathbb{R}^n} \frac{1}{2} \vec{d}^T [H_k] \vec{d} + \nabla f(\vec{x}_k)^T \vec{d} \quad (4.18)$$

subject to

$$\nabla h_j(\vec{x}_k)^T \vec{d} + h_j(\vec{x}_k) = 0; \quad \text{for } j=1, m_e \quad (4.19)$$

and,

$$\nabla g_j(\vec{x}_k)^T \vec{d} + g_j(\vec{x}_k) = 0; \quad \text{for } j=1, m_{e+1}, m \quad (4.20)$$

where $[H_k]$ is a positive definite approximation of the Hessian, and \vec{x}_k is the current iterate. If \vec{d}_k is chosen as the solution of the subproblem, then a line search can be used to find the new point \vec{x}_k (IMSL User's Manual 1989).

$$\vec{x}_{k+1} = \vec{x}_k + \lambda \vec{d}_k, \quad \lambda \in (0, 1], \quad (4.21)$$

such that a “merit function” will have a lower function value at the new point. The augmented Lagrange function is used as the merit function for this problem (Schittkowski 1989). This iteration process is continued until the accuracy test is passed, otherwise the design parameters are updated and the algorithm is executed for another consecutive iteration.

4.2.2 Summary of Optimal Design Procedure

The previous sections outlining the nonlinear optimization algorithm were written with optimization of multiple actuator/sensor configurations in mind. For the purpose of this work, the nonlinear optimization approach is used first to choose the optimal location of a single PZT control actuator and secondly to simultaneously choose three PZT control actuators configured on the surface of the simply supported plate. In addition, for each of the corresponding actuator designs, the nonlinear optimization algorithm is used initially to design a single structural PVDF error sensor

Table 4.1: Material Properties of Steel Plate

Name	Symbol	Value	Units
Elastic Modulus	E	20.4×10^{10}	N/m^2
Density	ρ	7700	kg/m^3
Poisson's Ratio	μ	0.28	-
Damping Ratio	η	0.001	-

and secondly to simultaneously design three structural PVDF error sensors for the respective control actuator designs.

In addition to the structural PVDF error sensors, nonlinear optimization is used to choose the appropriate locations of the acoustic near-field sensors constructed from PVDF. In the case of the acoustic near-field sensors, optimization was restricted to position only since the input to each sensor must be obtained numerically from the near-field acoustic response of the structure and is hence computationally intensive as will be discussed later in this chapter.

4.2.3 Optimal Design of Piezoelectric Actuator Locations

The optimal design approach is specific in nature to the constituent material properties of the structure and geometry chosen in the study. Hence, dimensions and material properties of the structure to be tested must be determined before executing the optimal design approach. For the purpose of this study, the simply supported plate was constructed of steel and measured 380 mm x 300 mm x 1.96 mm as indicated in Figure 4.1. Constituent material properties of the steel plate are itemized in Table 4.1 for reference. Based upon these material properties, the

Table 4.2: Theoretical and measured plate resonant frequencies, f_{mn} .

Mode (m,n)	Theoretical Frequency (Hz)	Measured Frequency (Hz)
(1,1)	87.6	87
(2,1)	188.5	187
(1,2)	249.7	247
(2,2)	350.6	347
(3,1)	356.5	352
(3,2)	518.6	517
(1,3)	519.9	520
(4,1)	591.7	590
(2,3)	620.7	615
(4,2)	753.8	750
(3,3)	788.7	779

resonant frequencies of the simply supported plate can be computed from equation (2.7). The predicted resonant frequencies are compared to the measured resonant frequencies for the test structure of interest for the first 11 structural modes. As indicated in Table 4.2, the measured and predicted resonant frequencies of the test structure are within 1.3% of each other. For the purpose of this study, the excitation frequency of the disturbance input was chosen at 550 Hz, which lies between the resonant frequencies of the (1,3) and (4,1) modes. This off-resonance driving frequency was chosen such that the structural response would be “modally rich” (i.e. composed of a variety of structural modes as opposed to one dominant mode which is the case for on-resonance excitation).

The objective function implemented in the optimization algorithm was expressed as a function of nine discrete pressure field points over one hemisphere of the plate

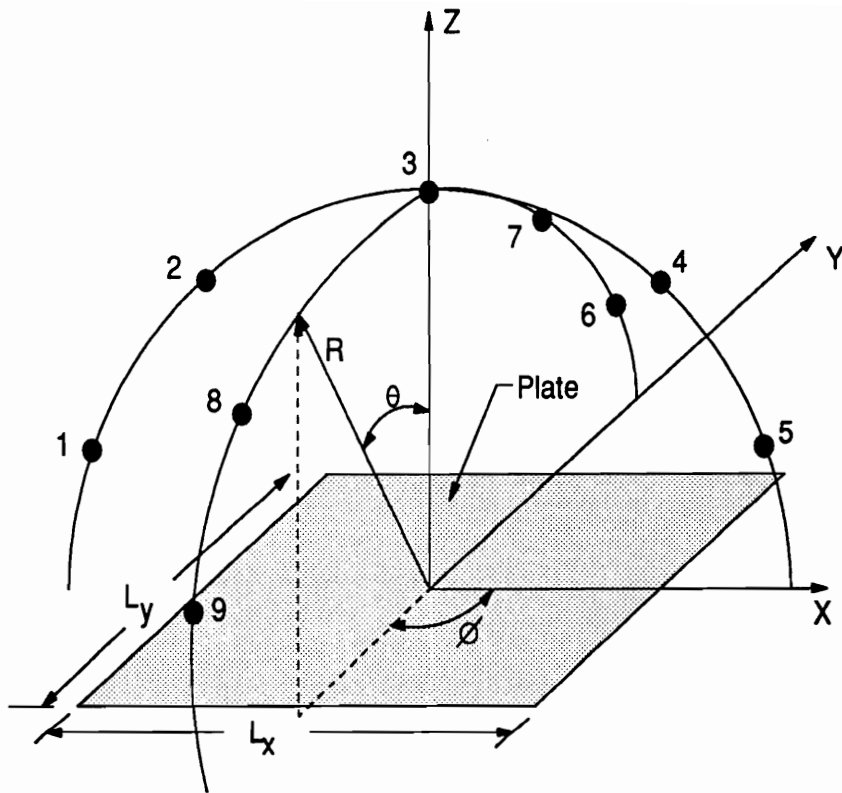


Figure 4.6: Coordinate System for Objective Function

based upon equation (4.8). The coordinates chosen to evaluate the pressure are documented in Table 4.3 with the corresponding coordinate system displayed in Figure 4.6. Notice that in this coordinate system, the origin is located at the center of the plate. This was done to convey to the reader that the discrete pressure points used in the objective function were positioned symmetrically in the hemisphere of the plate. These coordinates are readily converted into the chosen coordinate system by the appropriate coordinate transformation for computing the acoustic response of the structure as previously outlined in Figure 2.2. The pressure at each chosen acoustic field point in the objective function of equation (4.8) is evaluated with the far-field expression for the acoustic radiation from a baffled simply supported plate, which was given by Wallace (1972b) as follows:

$$\begin{aligned}
 p(r, \theta, \phi, t) = & \frac{k\rho_0 c L_x L_y}{2\pi^3 r} \exp(-jkr) \sum_{m=1}^{\infty} \sum_{n=1}^{\infty} \frac{W_{mn}^c}{mn} \left[\frac{(-1)^m \exp(-j\alpha) - 1}{(\alpha/m\pi)^2 - 1} \right] \\
 & \times \left[\frac{(-1)^n \exp(-j\beta) - 1}{(\beta/n\pi)^2 - 1} \right] \exp(j\omega t), \quad (4.22)
 \end{aligned}$$

where:

$$\alpha = kL_x \sin(\theta) \cos(\phi), \quad (4.23)$$

$$\beta = kL_y \sin(\theta) \sin(\phi). \quad (4.24)$$

Table 4.3: Coordinates for Evaluating Objective Function

Position	R (m)	θ (deg.)	ϕ (deg.)
1	1.8	75°	180°
1	1.8	45°	180°
1	1.8	0°	0°
1	1.8	45°	0°
1	1.8	75°	0°
1	1.8	75°	90°
1	1.8	45°	90°
1	1.8	45°	270°
1	1.8	75°	270°

With a means of computing the objective function, the optimization approach for the PZT control actuators was invoked.

The first design involved determining the optimal location of a single piezoelectric actuator bonded to the surface of the simply supported plate. The actuator measured 38 mm in the x-direction by 30 mm in the y-direction, and the optimal position was computed at center coordinates of (330,247.3) mm for a point force disturbance positioned at plate coordinates of (240,130) mm and an excitation frequency of 550 Hz. The relative positions of the optimal actuator and disturbance are illustrated in the schematic of Figure 4.7, and the optimal actuator is labeled 550A1. To verify that the nonlinear optimization program converged to the correct solution, a program was written whereby the optimal position was determined by a “brute force” approach. In other words, the actuator was incrementally traversed over the surface of the plate and upon computing the optimal control voltage at

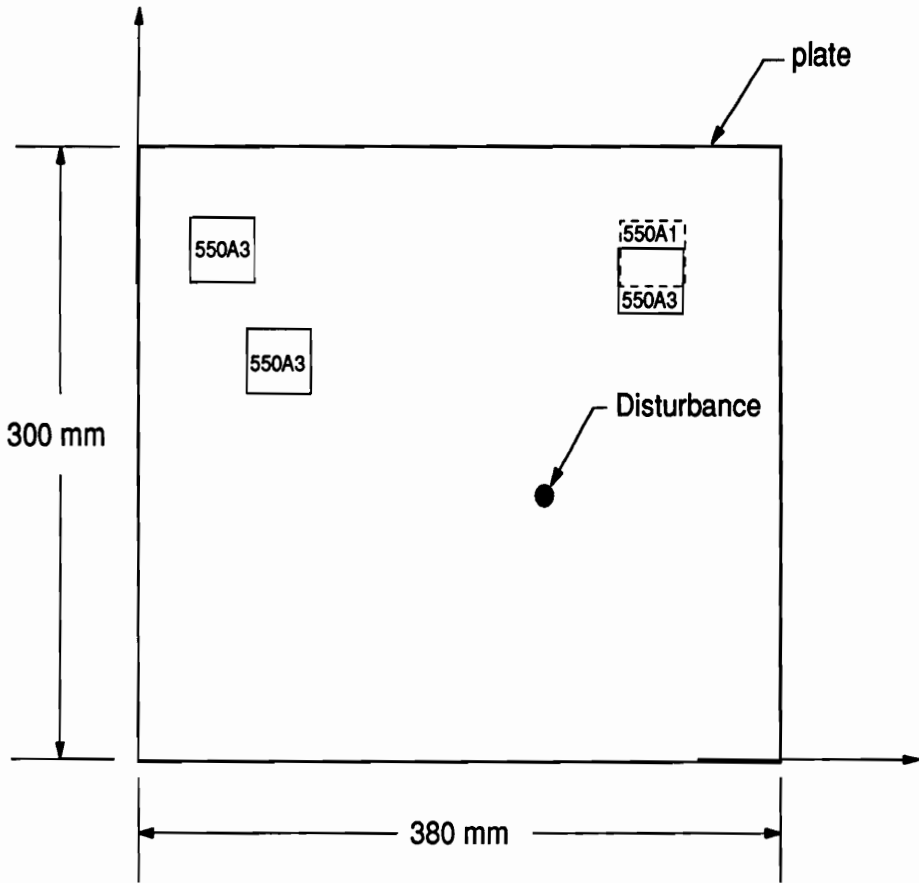


Figure 4.7: Schematic of Plate Configured with Optimal PZT Actuators

each position, the total acoustic power radiated from the structure was computed. The position corresponding to the most attenuation in total acoustic power was the same as that obtained through nonlinear optimization techniques. Since this approach was identical to that implemented by Wang *et al.*, (1991(c)), the solution was expected to converge to the optimal position.

In the second case, the positions of three actuators were simultaneously optimized such that the total sound power radiated from the structure was minimized. The actuators were of the same dimension as that used in the single actuator optimization case, and they are depicted in Figure 4.7. Each of the actuators for the three control actuator optimization case is labeled 550A3 to distinguish them from the single optimally located actuator labeled 550A1. The corresponding center coordinates of these control actuators were (302,234.5) mm, (48.5,250) mm and (82.5,196) mm. By implementing three optimally positioned control actuators as opposed to one, a 6 dB improvement in the attenuation of total sound power was observed based on the objective function.

In the case of the three actuator design problem, one of the actuators is located very near the optimal design position for the single control actuator design position. As was previously noted by Wang *et al.*, (1991(c)), this phenomenon suggests that the design process should be executed sequentially, increasing the number of control actuators implemented in the optimization routine until all have been optimized. Hence, upon finding the optimal location for a single control actuator, this position was used as a trial location for one of the actuators in the two actuator optimization case. Upon determining the optimal location of two PZT control actuators, these

positions were used as guesses for two of the actuators in the three actuator optimal design. The primary difference in the approach implemented in this study was that the optimal position from each previous design case was simply used as a *guess*. The actuator was not constrained to this position while searching for the optimal location of the next actuator. Greater stability was noted in the solution based upon this design approach, and the computational effort was significantly reduced by performing this sequential addition of control actuators in the optimal design technique.

Upon reviewing the positions of the optimal control actuators, one should recognize that all of the actuators are located near the boundaries of the plate. Since the position and dimensions of the control actuators create a “spatial” window when attached to the surface of the structure, the position dictates the relative magnitude of response for individual modes as indicated by the cosine terms in equation (2.14) which is recalled below.

$$W_{mn}^p = \frac{4C_o \epsilon_{pe}}{\rho L_x L_y (\omega_{mn}^2 - \omega^2 + j2\eta\omega_{mn}\omega)} \times \left[-\frac{\gamma_m^2 + \gamma_n^2}{\gamma_m \gamma_n} (\cos(\gamma_m x_1^p) - \cos(\gamma_m x_2^p)) (\cos(\gamma_n y_1^p) - \cos(\gamma_n y_2^p)) \right].$$

As the actuator draws closer to the boundaries of the plate, fewer nodal lines of structural modes are covered by the actuator. Hence, the control actuator can effectively couple into a greater number of structural modes. For example, a control actuator capable of coupling into all structural modes would be very small and positioned in one of the corners of the plate. This design approach is impractical since

an extremely high control voltage would be required to elicit response due to the high structural input impedance at this location. Further interpretation of the optimal actuator positions will be restricted to chapter 6 when the experimental and analytical results are compared. This preliminary discussion is provided to convey the physical mechanisms involved in studying the structural acoustic control problem.

4.2.4 Optimal Design of PVDF Sensor Location and Dimensions

Upon determining the appropriate piezoelectric control actuator positions, path 2 of the algorithm presented in Figure 4.4 was executed and the optimal position and dimensions of the rectangular PVDF structural error sensors was computed. In addition to finding the optimal design for the structural sensors, path 2 was executed for the design of the acoustic near-field error sensors. Each of these design approaches are outlined in the following sections.

4.2.4.1 PVDF Structural Sensors

The optimal positions and dimensions of the rectangular PVDF structural error sensors based upon an excitation frequency of 550 Hz are presented in Table 4.4 and are illustrated in the schematic of Figure 4.8. Similar to the notation used in Figure 4.7, the single optimally positioned PVDF sensor is labeled 550S1, and the three optimally positioned PVDF sensors are labeled 550S3 to differentiate between the two designs. As discussed earlier in this chapter, a “spatial window” is created as a result of the position and dimensions of the structural PVDF error sensor.

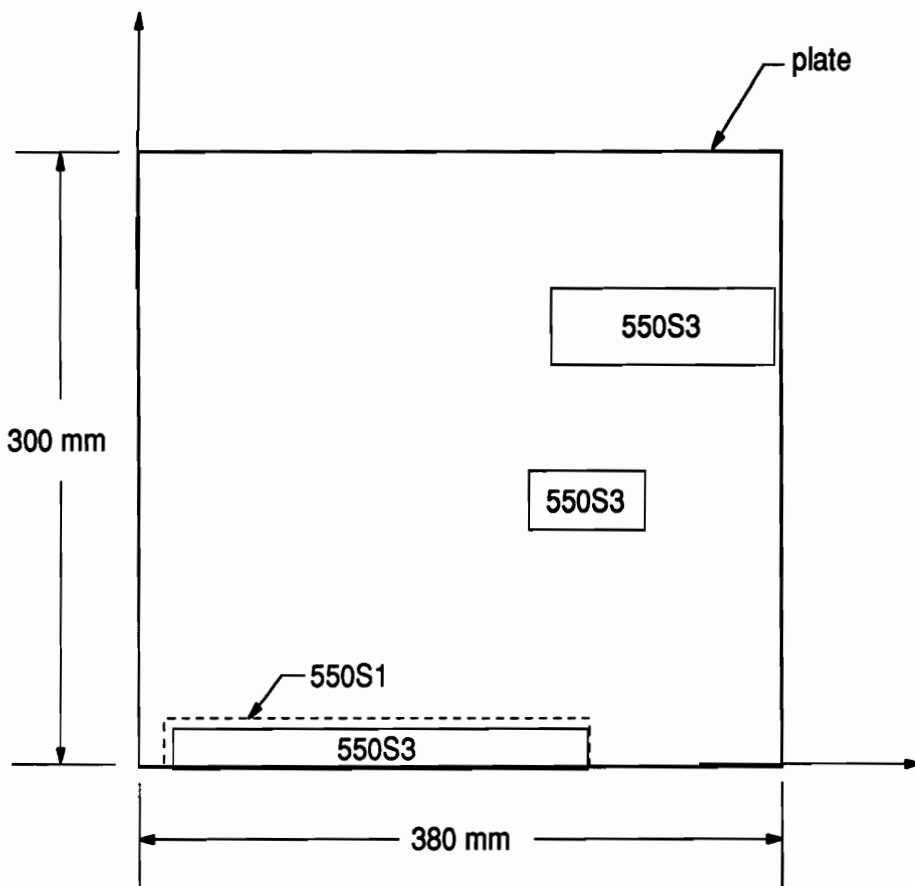


Figure 4.8: Schematic of Plate Configured with Optimal PVDF Sensors

Table 4.4: Positions of Optimally Designed PVDF Sensors

Sensor Design	center (mm)	x-dimension (mm)	y-dimension (mm)
550S1	(139,11)	252	22
550S3-1	(142,9)	244	18
550S3-2	(264,131)	68	27
550S3-3	(309,215)	31	36

Considering the single sensor optimization, upon studying the relative weighting of the first 9 structural modes, insight is gained into the physical mechanisms resulting from the design optimization.

The modal weighting of the first 9 modes was normalized with respect to the magnitude of the dominant mode observed by the single optimally configured PVDF sensor. As illustrated in Figure 4.9, the (1,3) mode is dominant in terms of modal weighting in the sensor response. For an excitation frequency of 550 Hz, the resonant frequencies of the (1,3) mode and the (4,1) mode are below and above this frequency respectively. While the (3,2) mode has a resonant frequency very close to that of the (1,3) mode, the mode is essentially unobserved by the PVDF sensor. This stems from the fact that the sensor was optimally positioned very near the nodal line corresponding to all modes in the (3,*) family (i.e. the (3,1), (3,2), (3,3) mode, etc.). At this particular excitation frequency, the radiation efficiency of the (3,2) mode is approximately 5 times less than that of the (1,3) mode as illustrated in Figure 1.1 for $k/k_s = 0.3$, hence significant spillover into the structural response at this mode will have very little effect on the total sound power radiated due to its relatively poor radiation efficiency and so it is not necessary to observe this structural mode. In addition to the observation of relative radiation efficiency, one should

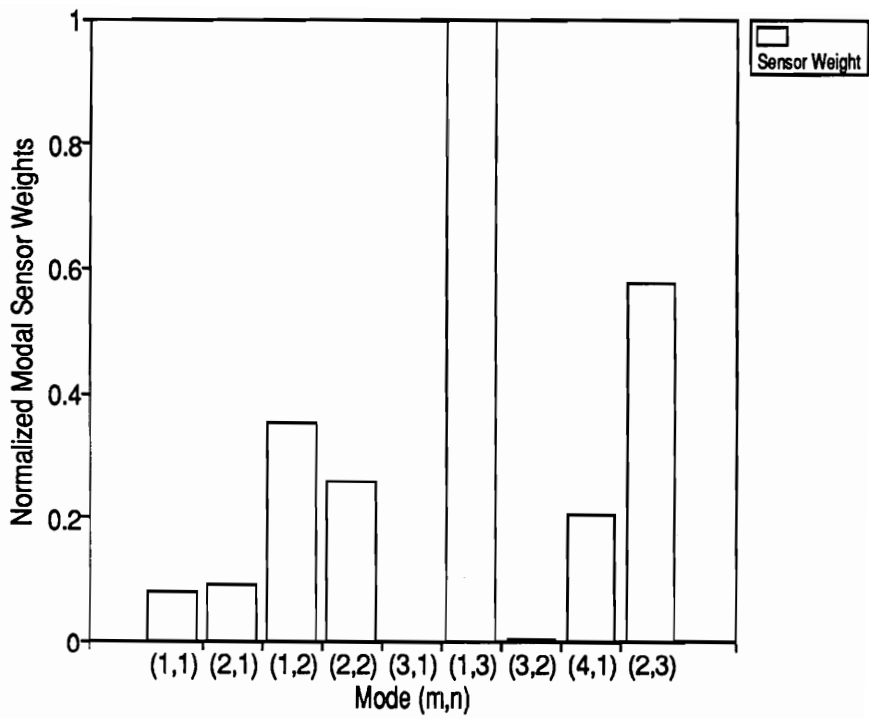


Figure 4.9: Modal Weighting of Single Optimal PVDF Sensor

recognize that the position of the PVDF sensor is on the boundary of the plate. The (1,3) mode is considered a y-edge radiator as depicted in Figure 1.3(c), suggesting that to control the sound radiated from this structure at an excitation frequency of 550 Hz, the sound radiation from this edge radiating mode must be reduced by way of both modal suppression and modal restructuring. Further interpretation of the optimal sensor design positions will be restricted to chapter 6 when the complete set of experimental and analytical results are presented.

4.2.4.2 PVDF Acoustic Near-Field Sensors

Before discussing the optimal locations of the PVDF acoustic near-field sensors, the method of computing the electrical response of these sensors induced by the acoustic radiation from the structure will be discussed. Consider the schematic diagram of the acoustic loading of the sensor resulting from the sound radiation from the plate presented in Figure 4.10. As opposed to a microphone diaphragm, the dimensions of the acoustic near-field sensor are large (i.e. several orders of magnitude greater than that of the microphone diaphragm). Hence when placed in close proximity to a structure with some velocity profile, the acoustic loading must be computed by integrating the load over the surface of the error sensor. Ideally, one would evaluate the pressure over infinitesimal regions of the sensor and compute the electrical response based upon the superposition of these harmonic acoustic disturbances. However the pressure over each discrete region must be obtained by numerical integration of Rayleigh's integral for the chosen structure. As a result of this numerical integration, the sensor must be divided into a practical finite number of subregions to evaluate the response. In this study, each sensor was subdivided into 100 elements,

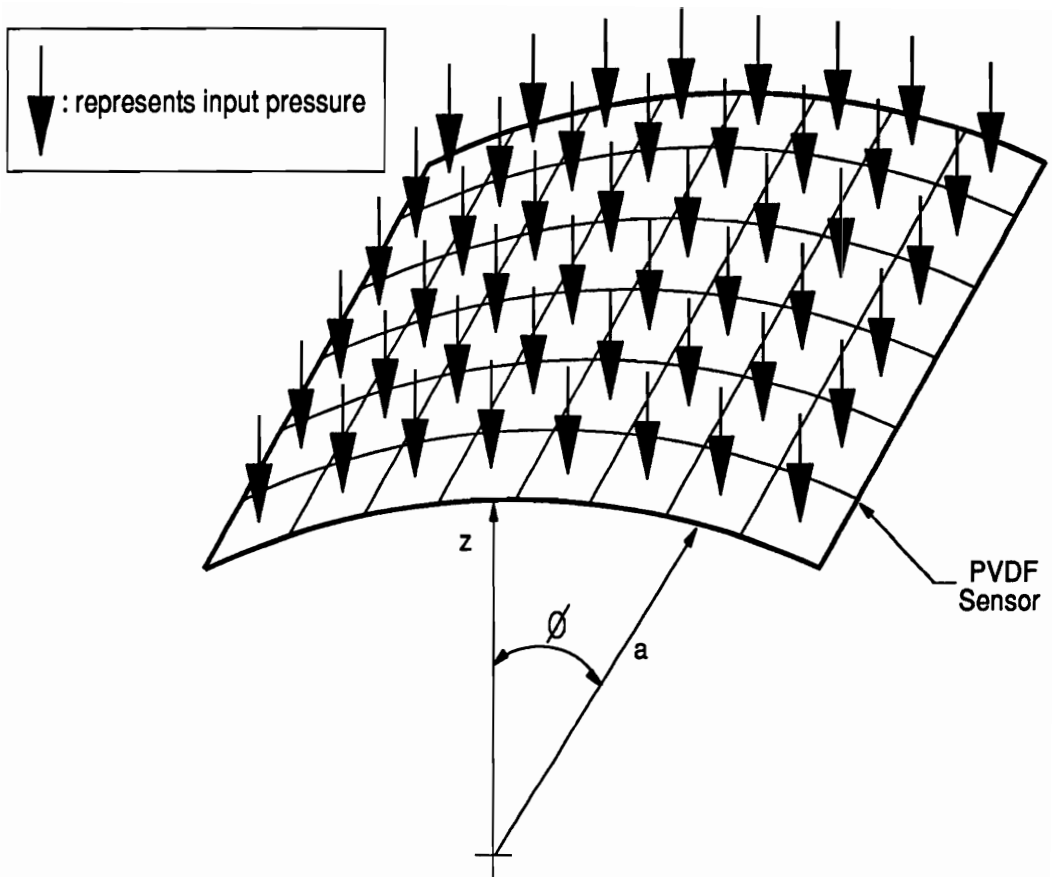


Figure 4.10: Schematic of Near-field Sensor Pressure Distribution

as further subdividing the sensor resulted in little improvement in the numerical results. The pressure was computed at the center of each element as depicted in Figure 4.10. As discussed in chapter 2, the near-field sensor was constructed in the shape of a shell segment; as depicted in Figure 4.10. The pressure at each point was assumed to be uniformly distributed over the respective element of interest, and the response of the sensor was computed as a result of the superposition of 100 acoustic disturbances.

A modal expression for computing the response of the sensor was given in equation (2.32) and is recalled below.

$$q(t) = - \sum_{m=1}^M \sum_{n=1}^N \left[\left(\frac{ae_{32}\alpha}{n\pi} \right) A_{mn} + e_{31} \left\{ \left(\frac{L}{m\pi} \right) B_{mn} + \left(\frac{\alpha L}{mn\pi^2} \right) C_{mn} \right\} \right] (1 - \cos(n\pi))(1 - \cos(m\pi)) \exp(j\omega t).$$

As discussed earlier, the modal response is coupled in three dimensions, resulting in three separate modal amplitudes for the response in each respective direction, x, y and z of the shell as illustrated in Figure 2.6. For a linear system (which is assumed in this case), the electrical response of the sensor can be computed from a superposition of the modal response of the structure due to each respective pressure input computed. In other words, for each of the 100 subregions of the sensor, a separate set of modal amplitudes A_{mn}^l , B_{mn}^l and C_{mn}^l can be computed where the superscript l is used to designate the subregion. Hence the electrical response of the sensor can be expressed as follows:

$$q(t) = - \sum_{l=1}^{100} \sum_{m=1}^M \sum_{n=1}^N \left[\left(\frac{ae_{32}\alpha}{n\pi} \right) A_{mn}^l + e_{31} \left\{ \left(\frac{L}{m\pi} \right) B_{mn}^l + \left(\frac{\alpha L}{mn\pi^2} \right) C_{mn}^l \right\} \right] \times (1 - \cos(n\pi))(1 - \cos(m\pi)) \exp(j\omega t). \quad (4.25)$$

The modal coefficients are obtained in the discrete pressure case as outlined in Appendix A.

In performing the optimal design, the position of a near-field sensor was optimized in the x-y plane of the structure. The position in the z-direction was fixed at 2.54 cm, and the dimensions of the sensor were fixed as well. For the single sensor design optimization, the projection of the sensor measured 101.6 x 50.8 mm in the x and y-directions respectively. The radius of curvature, a , depicted in Figure 2.6 used to create the shell segment was 190 mm. A nonlinear optimization algorithm converged to the solution for the optimal location of this sensor in 6 hours of computational time on the IBM VM1 computing system. The amount of CPU time required is a direct result of the 100 discrete pressure inputs which must be computed numerically from Rayleigh's integral.

The projection of the sensor on the surface of the plate is illustrated in Figure 4.11. The acoustic near-field sensor was centered about the coordinates (132,59.5) mm in the x-y plane of the plate. The objective was to sequentially increase the number of error sensors to achieve a design for three channels of control; however, upon computing the optimal design for two PVDF near-field sensors, this objective was abandoned. In determining the optimal location of two error sensors simultane-

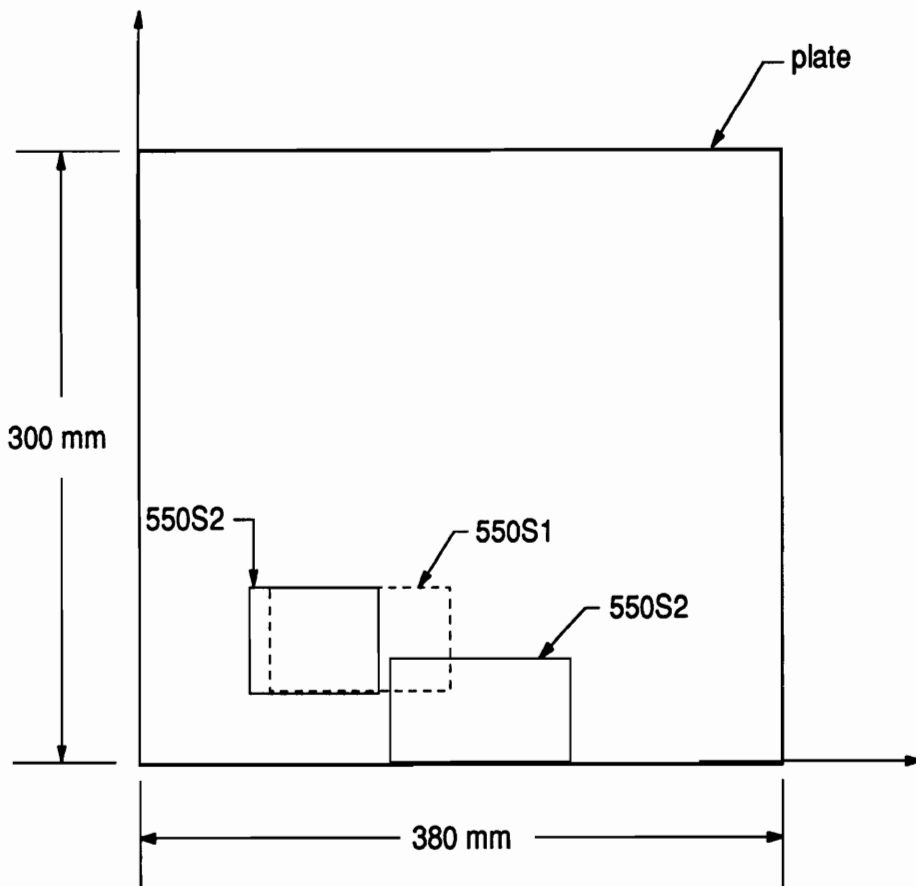


Figure 4.11: Schematic of Optimal Locations of Near-field Sensors

ously, the central processing unit (CPU) time increased from 6 hours to 24 hours before converging to a solution. The projection of the second PVDF sensor measured 76.2 x 50.8 mm in the x and y-directions respectively. The size of the second sensor was varied slightly in the design optimization to determine if this variation would afford greater design flexibility. Typically the size is included as a design parameter as was the case for the structural PVDF error sensors; however due to the CPU time required simply to compute the optimal position of the sensor, this approach was abandoned. Results from this design optimization were compared to those with sensors having identical dimensions. Little if any difference was observed in the resulting controlled acoustic response of the structure. The optimal locations for the chosen acoustic near-field sensors were determined at center coordinates of (193,24.5) mm and (102,60.5) mm for the first and second PVDF near-field sensor respectively, and the projection of each sensor on the surface of the plate is illustrated in Figure 4.11. Approximately 36 hours of CPU time was spent on the IBM VM1 computing system trying to determine the optimal location for three PVDF near-field sensors; however, in view of the success achieved with the structural sensors and the CPU time required to optimize the position of two near-field sensors, this approach was halted. Further interpretation of sensor design is restricted to the results section of chapter 6 where the predicted and measured acoustic response of the structure are compared.

Since the distance of the PVDF sensor from the surface of the plate was fixed in the optimal design approach, several designs were conducted while varying the distance from the plate surface from 2 to 10 cm. In general, little variation was observed in the optimal design location of the respective sensors. However, as the sensor is

moved further from the plate, the number of subregions required to compute the acoustic disturbance over the surface of the sensor decreases. In fact if the sensor is moved several acoustic wavelengths from the source and $kR \gg L_x$ and $kR \gg L_y$, a uniform pressure can be computed and applied over the surface of the sensor. At this point, the sensor can no longer be considered a near-field sensor, but rather an acoustic far-field sensor, yielding a response similar to that of a large microphone centered at the same field point.

4.2.5 Optimization of Discrete/Distributed PVDF Sensor

As observed in the previous discussion of optimal design approaches for PVDF structural and near-field sensors, each resulting design is frequency dependent. Hence as the harmonic disturbance changes, a new optimal sensor design is required. To address this problem and provide a foundation for future work, an alternative design approach was considered. As opposed to optimizing the dimensions and positions of the structural PVDF error sensors, the plate was configured with an array of sensors as depicted in Figure 4.12. In this case the response of each element of the PVDF array was computed based on equation (4.2) and assigned a weighting factor ranging between 1 and -1. Ideally this weighting would be incorporated with an analogue circuit or digitally with a digital signal processing board. The weighting factor for each element of the PVDF sensor array was chosen as a design variable to be optimized in the nonlinear optimization approach outlined earlier. By summing the weighted response of the PVDF sensor array, a single error response was computed. Upon converging to the optimal solution, minimizing the weighted response of the sensor array results in a corresponding reduction of the structural acoustic

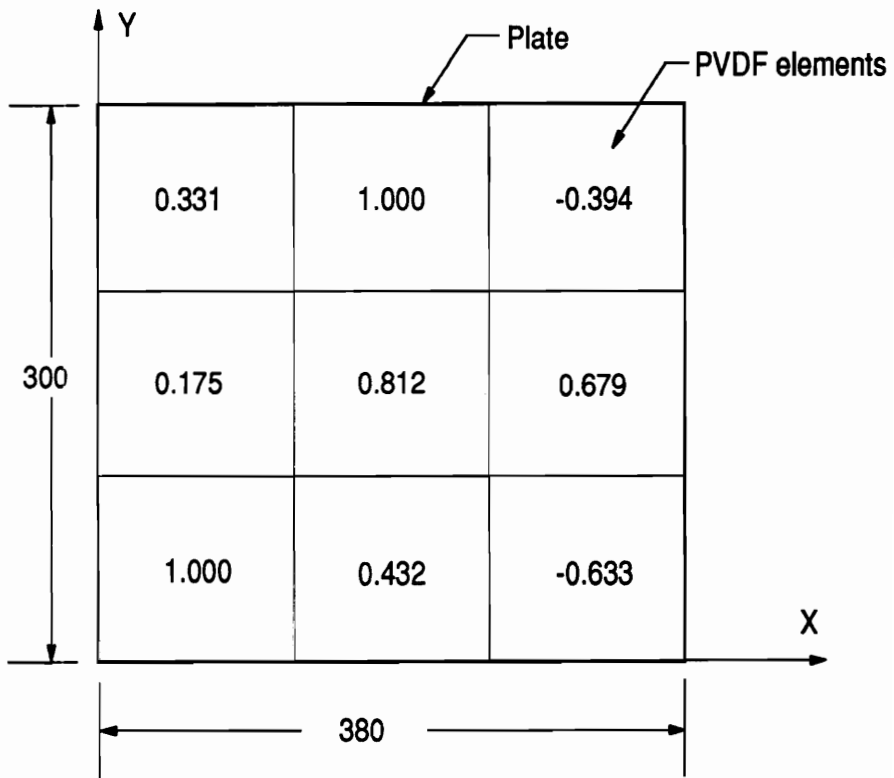


Figure 4.12: Schematic of Discrete/Distributed PVDF Sensor Array

response.

As an example, the weights for the sensor array presented in Figure 4.12 are the results of a design optimization for minimizing the structural acoustic response of the simply supported plate at an excitation frequency of 550 Hz as in the previous optimal design approaches. The normalized modal weighting of the sensor array after completing the design optimization is presented in Figure 4.13. Comparing the modal filtering characteristics of the weighted PVDF sensor array presented in Figure 4.13 with that of the single optimally positioned PVDF sensor presented in Figure 4.9, one quickly observes that the modal filtering characteristics are very different. With the exception of the (2,3) mode, the relative weighting of each structural mode is nearly uniform. Based on the modal filtering characteristics of this sensor, one would assume from the graph of Figure 4.13 that modal suppression is the desired method of control. However, further inspection reveals that the (1,2) mode and the (3,1) mode are filtered 180° out of phase with respect to the other structural modes. Hence modal restructuring also plays an important role in the filtering characteristics of this optimal sensor design. Since the summed response of each element of the PVDF sensor array is weighted with a number between +1 and -1, favorable phase relationships between modes can be incorporated into the structural acoustic sensor design.

The primary difference between this sensor design approach and that outlined earlier for optimally positioning and dimensioning the structural PVDF sensors is that the array of PVDF sensors affords more flexibility in the design. Modal restructuring for destructive interference can be included in the design since relative phase

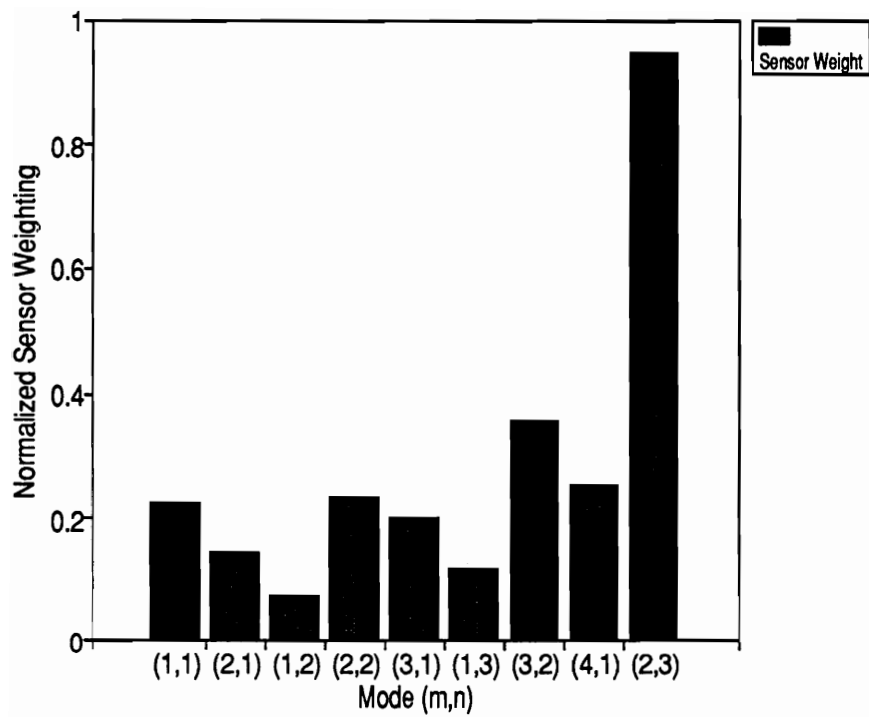


Figure 4.13: Modal Weighting of PVDF Sensor Array

tionships between structural modes are now included in the design process as well as relative weighting of individual modes. In addition, if the disturbance excitation frequency changes, the optimal weights for the array of sensors can be adjusted to compensate for this change. Hence, one need not configure the structure with another sensor for each excitation frequency. Ideally the optimal weights for the PVDF sensor array could be controlled by a variable parallel weighting scheme such as a neural network. This is beyond the scope of this work; however, in light of the observations made, it is worthy of pursuit in future studies.

4.2.6 Summary of Computational Effort

As outlined by Wang (1991(a)) in his dissertation, over 70% of the CPU time for optimizing the position of the piezoelectric actuators is devoted to evaluating the gradient of the objective function and the constraints in the nonlinear optimization algorithm. Similar results were observed in this study for optimization of either the PZT actuator position or the PVDF structural error sensor size and dimensions. As previously mentioned by Wang (1991(a)), the percentage of CPU time required in this step increases as the number of actuators or sensors to be optimized increases. In the case of the acoustic near-field sensor optimal design, similar percentages of CPU time were observed; however, the amount of actual CPU time required to find the optimal location of the near-field sensor was 2 orders of magnitude greater than that required for the structural actuators and sensors. This increased time is a direct result of the numerical integration required to compute the acoustic near-field response of the structure over each element of the sensor. While acoustic near-field sensors can be realized, based upon computational time required in optimal design

approaches, if given a choice between structural sensors and acoustic near-field sensors, the obvious choice is the structural sensor. However, some applications may dictate the sole use of acoustic near-field sensors.

4.3 Modal Shaped PVDF Strain Sensor Design Theory

The objective is to design a shaped PVDF sensor bonded to the surface of the structure, whereby minimizing the electrical response of the sensor is equivalent to minimizing the sound radiated at one or more chosen microphone locations in the acoustic field. The key to the following design approach is to recognize that choosing one or more microphone locations for minimizing the far-field sound radiation is independent of where the control actuator is located on the structure. This observation stems from the fact that the modal weighting of an acoustic sensor positioned at a fixed field point is constant for a fixed frequency of excitation (i.e. the radiation filters are fixed). Hence the corresponding structural error sensor required to yield the same controlled acoustic directivity pattern must exhibit the same characteristic.

4.3.1 Design Approach

Without concerning ourselves with the details of the control implementation at this point, let us assume that given some primary disturbance represented in modal coordinates by W_{mn}^F , we can minimize the sound radiation at some chosen acoustic field point (r, θ, ϕ) . This is accomplished with linear quadratic optimal control

theory as discussed in chapter 3, and the optimal control input to the structure due to excitation with a piezoelectric actuator is represented in modal coordinates by W_{mn}^p . Hence the controlled modal response of the structure can be expressed as follows:

$$W_{mn}^c = W_{mn}^F + W_{mn}^p, \quad (4.26)$$

where W_{mn}^c is the controlled modal response obtained by superposition of the input disturbance and the optimal control input. Now, if the shaped PVDF sensor is chosen such that the design is a function of the system eigenfunctions, then the sensor shape can be expressed as follows:

$$\Gamma(x, y) = \sum_{n=1}^N S_n \phi_n(x, y), \quad (4.27)$$

where N represents the number of modes included in the response and $\phi_n(x, y)$ represents the system eigenfunctions. Recalling the expression for the electrical response of the PVDF:

$$q(t) = \frac{(h_p + h_s)}{2} \int_A P_o(x, y) F(x, y) \left(e_{31} \frac{\partial^2 w}{\partial x^2} + e_{32} \frac{\partial^2 w}{\partial y^2} + 2e_{36} \frac{\partial^2 w}{\partial x \partial y} \right) dx dy.$$

As outlined earlier, $F(x, y)$ describes the effective surface electrode and $P_o(x, y)$ represents the polarization profile. Both of these factors become important for practical implementation of shaped sensors.

If we let $FP_o(x, y) = \Gamma(x, y)$ and $e_{36} = 0$ (i.e. no skew angle) and substitute into the previous equation, we obtain the sensor response as a function of the mode shape

$$q(t) = -\frac{(h_p + h_s)}{2} \int_A \sum_{n=1}^N S_n \phi_n(x, y) (e_{31} \frac{\partial^2 w}{\partial x^2} + e_{32} \frac{\partial^2 w}{\partial y^2}) dx dy. \quad (4.28)$$

For a simply supported beam, letting $\phi_n(x, y) = \sin(n\pi x/L_x)$ one can readily show (Clark *et al.*, 1992(b)):

$$q(t) = -\frac{(h_p + h_s)e_{31}}{4L_x} \sum_{m=1}^M (m\pi)^2 S_m W_m^c(\omega) \exp(j\omega t). \quad (4.29)$$

An important observation can be made at this point upon viewing equation (4.29). The sensor response as a function of modal coordinates is weighted as a function of m^2 since the electrical output is proportional to the second derivative of the structural response (i.e. strain). Hence small changes in the physical shape of the sensor for modes with large modal indices result in significant changes in the electrical response of the sensor. This result stems from the fact that the PVDF senses the integral of strain over the area of application, making it much more sensitive to the higher modes. This observation will prove important when studying the sensor shapes.

For the simply supported plate, an expression for the electrical output can be developed similarly. At this point it is convenient to define the assumed sensor shape function in terms of the separable eigenfunctions of the structural response:

$$\phi(x, y) = \sum_{r=1}^M \sum_{s=1}^N \sin\left(\frac{r\pi x}{L_x}\right) \sin\left(\frac{s\pi y}{L_y}\right) \quad (4.30)$$

Using this terminology, the response of a shaped PVDF sensor applied over the surface of the plate can be expressed as follows

$$q(t) = -\frac{L_x L_y (h_p + h_s)}{8} \sum_{m=1}^M \sum_{n=1}^N [e_{31}(m\pi/L_x)^2 + e_{32}(n\pi/L_y)^2] \times S_{mn} W_{mn}^c(\omega) \exp(j\omega t). \quad (4.31)$$

where both the modal sensor weighting S_{mn} and the controlled modal response W_{mn}^c are defined in terms of the separable eigenfunctions. As in equation (4.29) for the sensor response as a function of the strain in the simply supported beam, the sensor response for the simply supported plate of equation (4.31) is weighted more heavily with increasing modal indices. Again this factor is important when interpreting the sensor shape. One should also recognize that while the PVDF sensor is not homogeneous in the x and y-direction (i.e. $e_{31} \neq e_{32}$), this non-homogeneous property is included in the expression for the sensor response as illustrated in equation 4.31.

For a multi-input/single-output control case, the shaped PVDF sensor must be designed such that the electrical response of the sensor is zero when the desired controlled structural acoustic response is obtained. This is accomplished by computing the controlled structural acoustic response when implementing one or more microphone error sensors at chosen acoustic field points. In the case of the simply supported beam, this condition is satisfied when the following expression is satisfied:

$$\sum_{m=1}^M (m\pi)^2 S_m W_m^c = 0, \quad (4.32)$$

and for the simply supported plate

$$\sum_{m=1}^M \sum_{n=1}^N [e_{31}(m\pi/L_x)^2 + e_{32}(n\pi/L_y)^2] S_{mn} W_{mn}^c = 0. \quad (4.33)$$

In both cases, if the equation is normalized with respect to the first modal sensor shape (S_1 for the beam and S_{11} for the plate), then there are $M - 1$ unknowns for the sensor design equation (4.32) of the simply supported beam and $M \times N - 1$ unknowns for the sensor design equation (4.33) of the simply supported plate. To obtain the remaining $M - 2$ or $M \times N - 2$ respective equations necessary to solve for the sensor weights, we solve for the controlled modal response with the control actuator located at different spatial coordinates on the structure. Minimizing the acoustic response at one or more chosen coordinates for the microphones is independent of the chosen actuator coordinate for a controllable and observable system as will be illustrated in section 4.3.2 on practical implementation.

As an example, the system of equations required to design the shaped PVDF sensor for the simply supported beam can be expressed as follows

$$[A][S^c] = [B] \quad (4.34)$$

where:

$$[A] = \begin{bmatrix} 2^2 W_2^{c1} & 3^2 W_3^{c1} & 4^2 W_4^{c1} & \bullet & M^2 W_M^{c1} \\ 2^2 W_2^{c2} & 3^2 W_3^{c2} & 4^2 W_4^{c2} & \bullet & M^2 W_M^{c2} \\ 2^2 W_2^{c3} & 3^2 W_3^{c3} & 4^2 W_4^{c3} & \bullet & M^2 W_M^{c3} \\ \bullet & \bullet & \bullet & \bullet & \bullet \\ 2^2 W_2^{c(M-1)} & 3^2 W_3^{c(M-1)} & 4^2 W_4^{c(M-1)} & \bullet & M^2 W_M^{c(M-1)} \end{bmatrix}, \quad (4.35)$$

$$[S'] = \begin{bmatrix} S'_2 \\ S'_3 \\ S'_4 \\ \bullet \\ S'_M \end{bmatrix}, \quad (4.36)$$

and

$$[B] = \begin{bmatrix} -1^2 W_1^{c1} \\ -1^2 W_1^{c2} \\ -1^2 W_1^{c3} \\ \bullet \\ -1^2 W_1^{c(M-1)} \end{bmatrix}. \quad (4.37)$$

Since the sensor shape is normalized with respect to the first modal weight, the solution for the remaining sensor weights is designated by S' . In addition, since $M - 1$ equations are required to solve for the desired modal sensor weights, the symbol for the modal response W_m^{ci} was modified to include the indice i to represent the $M - 1$ independent coordinates chosen for the control actuator.

One should note that the solution to the system of equations presented in equation (4.34) is in general complex. Hence a complex sensor design is required to achieve the desired response characteristics. A complex sensor is one which requires modal

weighting with both a real and imaginary part. Upon first consideration one might abandon this approach as a result of this observation; however as will be outlined in the discussion of the instrumentation in chapter 5, a method of achieving this complex sensor design is discussed. Essentially, two separate sensors are designed, one to measure the real part and one to measure the imaginary part. The phase of the sensor shaped to measure the imaginary part must simply be shifted by 90° and summed with the sensor shaped to measure the real part to create the desired “complex” sensor response.

4.3.2 Practical Implementation

Two shaped PVDF sensors were designed for the simply supported beam and were physically implemented on the test structure as will be outlined in the results of chapter 6. The first sensor was designed as a structural sensor to control only the first mode of the beam. The second sensor was designed to represent an acoustic field point located in the far-field. The far-field expression for the acoustic radiation from a simply supported beam was previously derived by Wallace (1972(a)):

$$p(r, \theta, \phi, t) = \sum_{m=1}^M W_m^c \frac{-\omega^2 \rho \exp(-jkr)}{2\pi r} \int_0^{w_b} \int_0^{L_x} \sin\left(\frac{m\pi x}{L_x}\right) \times \exp\left[-j\left(\alpha \frac{x}{L_x} + \beta \frac{y}{w_b}\right)\right] dx dy \exp(j\omega t), \quad (4.38)$$

where (r, θ, ϕ) is the polar coordinate of the observation point as shown in Figure 2.1.

$$\alpha = kL_x \sin(\theta) \cos(\phi), \quad (4.39)$$

and

$$\beta = kw_b \sin(\theta) \sin(\phi). \quad (4.40)$$

If the field point is chosen at an angle of $\theta = 0$ in the acoustic far-field, the resulting modal components of the expression for the acoustic radiation at this point are observed to be independent of frequency as illustrated below:

$$p(r, 0, \phi, t) = \sum_{m=1}^M W_m^c \frac{-\omega^2 \rho \exp(-jkr)}{2\pi r} \int_0^{w_b} \int_0^{L_x} \sin\left(\frac{m\pi x}{L_x}\right) dx dy \exp(j\omega t). \quad (4.41)$$

Upon evaluating this integral, the acoustic response can be expressed as follows:

$$p(r, 0, \phi, t) = \frac{-j\omega \rho_0 c k w_b L_x}{2\pi^2 r} \exp(-jkr) \sum_{m=1}^M \frac{W_m^c}{m} (1 - (-1)^m) \exp(j\omega t). \quad (4.42)$$

Consider the following component of equation (4.42):

$$\frac{(1 - (-1)^m)}{m}.$$

This term is defined as the radiation filter for the chosen acoustic field point and as observed, this modal filter is independent of both frequency and the position of

either the disturbance or control actuator with respect to the beam coordinates. Hence a PVDF sensor must exhibit the identical filtering characteristic to yield the equivalent controlled structural acoustic response. Burdisso and Fuller (1992(b)) previously outlined a method for designing a weighted sensor for vibration control and the design approach is very similar to that outlined in this work. In the case of the single-input/single-output system, the sensor shape is given simply by this radiation filter and hence the sensor design can be obtained as follows (Clark *et al.*, 1992(b)):

$$S_m = \frac{(1 - (-1)^m)}{m^3}. \quad (4.43)$$

Hence one need not solve the system of equations presented in equation (4.34) to obtain the desired sensor shape. However, for the multi-input/single-output control case, the PVDF sensor shape will be a function of multiple radiation filters, and the equation (4.34) must be solved to determine the appropriate design. In addition, the far-field coordinate chosen for the sensor design presented is unique since it is the only acoustic field point for which the sensor design is independent of frequency. In general, the sensor shape will be a function of frequency as indicated in equation (4.39) and equation (4.40). However, for the case presented, the sensor design is applicable for broad band as well as harmonic control applications.

For comparison, the PVDF structural acoustic sensor is superposed against a mode 1 PVDF sensor in the schematic of Figure 4.14 to emphasize that a very small change in the shape of the sensor significantly alters the designed response characteristics. The modal weighting required to create the two shaped sensors is given in Table 4.5.

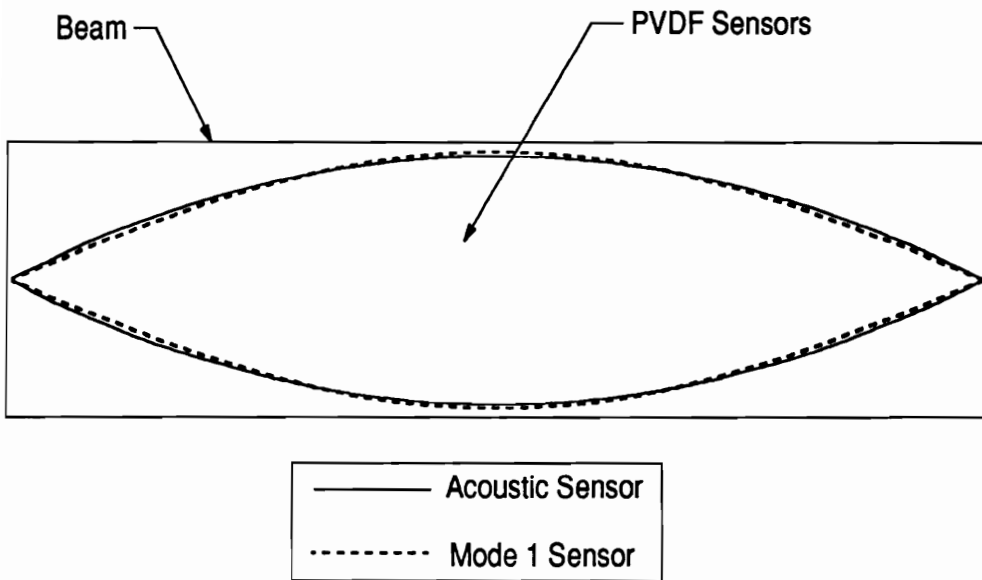


Figure 4.14: Schematic of Modally Shaped 1-D PVDF Sensor

Table 4.5: Design Normalized Modal Sensor Weighting Distribution for Simply Supported Beam.

Mode	Real Part	Imaginary Part
1	1.00	0.00
2	0.00	0.00
3	3.70E-2	0.00
4	0.00	0.00
5	8.00E-3	0.00
6	0.00	0.00
7	2.91E-3	0.00
8	0.00	0.00
9	1.37E-3	0.00
10	0.00	0.00

To achieve the mode 1 sensor, one simply must set all terms but the mode 1 term equal to zero in the table. In the case of the structural acoustic sensor, the modal filters were expressed in equation (4.43) and are normalized with respect to S_1 in Table 4.5. The contributions of modes with increasing modal indices appears to decrease rapidly; however, one must remember that each mode is further weighted by the square of the modal indices as demonstrated in equation (4.32). Practical design techniques are discussed in chapter 5; however, it should be noted that the change in polarization profile as a function of the x-dimension of the beam can be achieved by shaping the sensor as a function of the desired modal weighting. This stems from the fact that the structural response of the beam is a function of the x-dimension only.

For purpose of comparison, a shaped sensor was designed for the simply supported plate at the same corresponding far-field coordinates (i.e. $\theta = 0$). The far-field

expression for the acoustic radiation from the simply supported plate was previously derived by Wallace (1972(b)) and was presented earlier in equation (4.22). The expression is recalled here for convenience.

$$p(r, \theta, \phi) = \frac{k\rho_0 c L_x L_y}{2\pi^3 r} \exp(-jkr) \sum_{m=1}^{\infty} \sum_{n=1}^{\infty} \frac{W_{mn}^c}{mn} \left[\frac{(-1)^m \exp(-j\alpha) - 1}{(\alpha/m\pi)^2 - 1} \right] \\ \times \left[\frac{(-1)^n \exp(-j\beta) - 1}{(\beta/n\pi)^2 - 1} \right],$$

where:

$$\alpha = kL_x \sin(\theta) \cos(\phi),$$

$$\beta = kL_y \sin(\theta) \sin(\phi).$$

Letting $\theta = 0$ in equation (4.22) results in the following expression for the acoustic radiation:

$$p(r, \theta, \phi) = \frac{k\rho_0 c L_x L_y}{2\pi^3 r} \exp(-jkr) \sum_{m=1}^{\infty} \sum_{n=1}^{\infty} W_{mn}^c \left[\frac{(-1)^m - 1}{m} \right] \\ \times \left[\frac{(-1)^n - 1}{n} \right], \quad (4.44)$$

in which the modal components are independent of frequency as was the case for the simply supported beam. Again since only one acoustic field point was chosen in the sensor design, the modal filtering characteristics are totally described by the following radiation filters:

$$\left(\frac{(-1)^m - 1}{m}\right)\left(\frac{(-1)^n - 1}{n}\right).$$

Hence the PVDF shaped sensor can be expressed as a function of the desired modal radiation filters, the stress per charge constants of the PVDF material and the dimensions of the plate as follows:

$$S_{mn} = \frac{\left(\frac{1-(-1)^m}{m}\right)\left(\frac{1-(-1)^n}{n}\right)}{e_{31}\left(\frac{m\pi}{L_x}\right)^2 + e_{32}\left(\frac{n\pi}{L_y}\right)^2}. \quad (4.45)$$

The shaped PVDF sensor for the simply supported plate which yields an equivalent controlled response to a microphone positioned at the chosen acoustic field point is illustrated in Figure 4.15. The scale has been suppressed from the schematic since the modal weighting was simply normalized with respect to S_{11} . One should recognize that this sensor shape is very similar to the shape of the first structural mode of the plate, which is not surprising considering that the sensor response is a function of strain (i.e. the square of the modal indices). While the response characteristics of this sensor are desirable in the development of smart structures for active structural acoustic control, practical implementation of this sensor is complicated by the required variation in polarization profile in two dimensions. As a result, physical implementation of this sensor is an extremely difficult problem to solve.

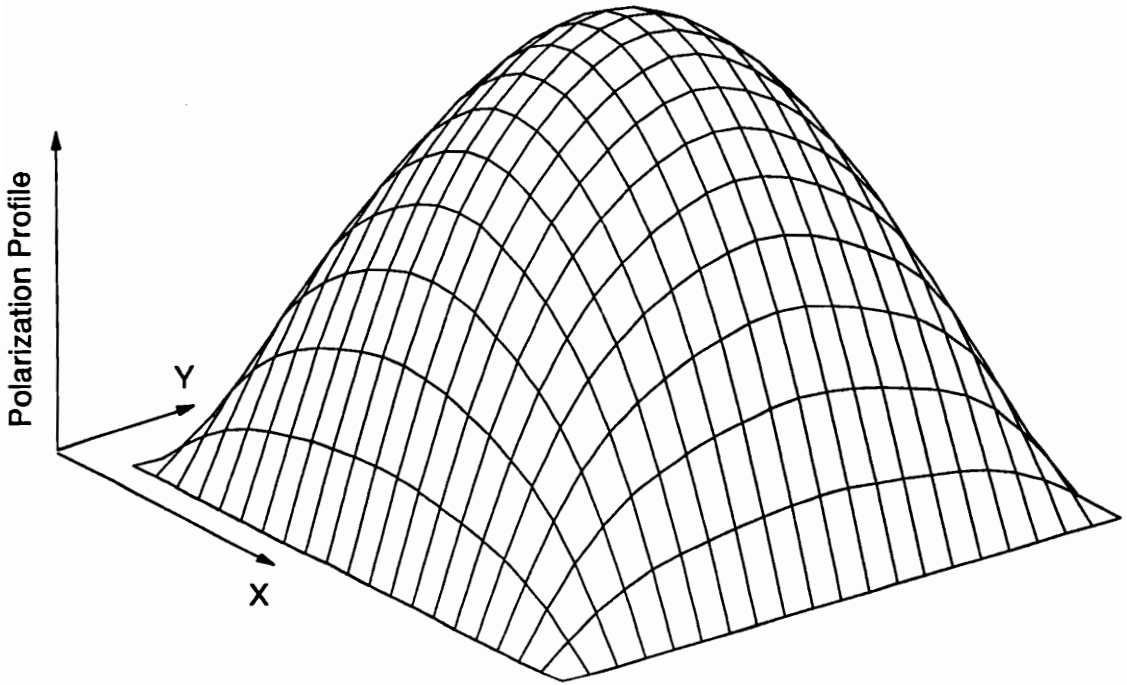


Figure 4.15: Schematic of Modally Shaped 2-D PVDF Sensor

4.4 Summary

In the preceding sections, several design approaches have been outlined as methods of achieving smart structures for active structural acoustic control. Each of the previously discussed design approaches will be evaluated analytically and experimentally in chapter 6. PVDF sensors shaped as a function of the structural mode shapes appear to provide a unique method for achieving directional control in the acoustic field for simple one-dimensional structures. However, this design approach offers little promise for more complex two dimensional structures such as the simply supported plate since the polarization profile is a function of two dimensions, and thus a three dimensional “weighted” sensor must be constructed to achieve the design objective.

As a result of this observation, optimal design techniques, whereby rectangular sensors are optimally located and dimensioned on the surface of the structure such that the “spatial” window created by the sensor yields an electrical response representative of the sound radiated from the structure, appear to be more appropriate for structures whose response is a function of two spatial dimensions. Acoustic near-field sensors were designed for similar applications; however, the required CPU time to achieve the desired design objective makes them less appealing. However, some design implementations may dictate a sensor which does not contact the structural surface and hence require the implementation of acoustic near-field sensors. Perhaps the best design compromise exists in the array of distributed PVDF sensors in which the response of each element of the array is individually processed, optimally

weighted and summed with the response of the remaining elements to achieve the desired optimal sensor design.

Chapter 5

Experimental Arrangement

The purpose of this work was not simply to suggest alternative sensors for active structural acoustic control, but to implement them on structures such as the simply supported beam and simply supported plate to evaluate and experimentally confirm their respective performance. As a result of this design objective, the experimental arrangement must be discussed in detail such that these preliminary design concepts can be extended to more complex structures. Methods of attaching both PZT actuators and PVDF error sensors to the structure will be outlined in addition to the appropriate instrumentation required to implement each. An overview of the controller as well as the signal processor required to implement the multi-channel version of the filtered-x adaptive LMS algorithm is presented. Instrumentation required to measure both the structural response and structural acoustic response is discussed in this chapter as well. Upon completing an overview of the electro-mechanical equipment, the test structures and methods of achieving the desired boundary conditions are reviewed.

5.1 Electro-Mechanical Equipment

5.1.1 PZT Actuators

The piezoceramics used in all experiments were obtained from Piezo Systems, an advanced group for Piezo Electric Products, Inc. The piezoceramics were G1195 (Navy Type-II) material constructed from a lead zirconate titanate composition with material properties previously listed in Table 2.1. Mounting of the piezoceramic patches required a number of procedures of which the first was to cut the patch. Each piezoceramic patch was cut to the desired dimensions with a razor blade and sanded along its cut edges until smooth. A small rectangular electrical lead made of brass shim stock (1/1000 in. thick) was then soldered to one face of the crystal. This lead would provide an electrical connection to the underside of the patch so that a voltage could be applied across the poling axis of the piezoceramic (Clark *et al.*, 1991(b)). Before each piezoceramic patch was bonded to the plate, a thin insulating glue layer was applied to the plate surface. This was to insure that the piezoceramic and plate would not be connected electrically once the piezoceramics were attached. A cyanoacrylate based adhesive, M-Bond 200, was used to attach the piezoceramic to the plate.

After the insulating layer was examined for completeness, additional glue was sparingly applied over the layer and the piezoceramic was placed onto the plate such that the brass lead was on the underside of the patch. Finally, a thin wire was soldered to the lead and a second wire directly to the top surface of the piezoceramic patch as illustrated in Figure 2.3. Typical adhesive layer thickness was measured in the range of 0.08 mm to 0.14 mm (Fleming 1990). Piezoceramic patches were

always bonded to the plate in pairs. For every patch adhered to the front face of the plate, a patch of the same size was bonded directly behind it on the other side of the plate. The electrical leads of each patch pair were connected such that the front patch would be activated by a voltage 180 degrees out of phase with the voltage activating the rear patch, causing the simultaneous expansion of one patch and contraction of the other, resulting in pure bending about the neutral axis of the beam or plate. Piezoceramic patches wired in this configuration are termed actuators as outlined by Dimitriadis *et al.*, (1991), and a schematic of the actuator configuration was previously presented in Figure 2.3.

Since the voltage required to drive the test structures used in this study ranged from 50 to 200 Volts amplitude, a power amplifier configured with a transformer was required to drive each actuator. The output from the controller, which ranged from 0 to 1 volt amplitude, was amplified with an NEC variable gain stereo power amplifier and the output of this amplifier was passed through a transformer which increased the voltage output by a factor of 17.1. The actuators were observed to respond in a linear manner as long as the voltage supplied was below 200 Vrms (Clark *et al.*, 1991(a)). Previous studies by Fleming (1991) and Clark *et al.*, (1991(b)) were devoted to characterizing the response of these actuators with respect to the structures used in this study. The models previously documented in equation (2.9) and equation (2.14) were observed to result in a reasonable prediction of the modal response of the structure (i.e within 10%) over the frequency range of interest for this study (0-800 Hz). Greater details of this work can be found in the previously listed references.

5.1.2 PVDF Sensors

The sensors used in this study were purchased from the Pennwalt Corporation and were constructed from sputtered NiCu PVDF film sheets measuring $28\mu\text{m}$ thick. The corresponding properties of this material were previously listed in Table 2.2. Two types of sensors were constructed from the PVDF material, a structural sensor and an acoustic near-field sensor. The design and physical implementation of each respective sensor is outlined separately; however, the equivalent electrical circuit and the required signal conditioning for the sensors are the same. Hence this material is unified in sections corresponding to each topic.

5.1.2.1 Physical Implementation of Structural Sensors

The PVDF material was attached to the structure with Tuck carpet tape, and electrical connections were made with copper tape. This is an excellent method for quickly achieving prototype sensors; however, more permanent techniques should be used for design implementation. Suffice to say that the sensor can be permanently attached to the structure with 3M Super 77 spray adhesive, and leads can be permanently attached with conducting epoxy. For a detailed outline of more permanent lead attachment and sensor attachment, the reader is referred to a report by Collins, Miller, and von Flotow (1991). When attaching leads to the sensors with copper tape, one must be sure to make all solder connections to the copper tape in advance of attaching the tape to the sensor as soldering after attaching the copper tape will result in a melted sensor.

In shaping the PVDF sensors, based upon a rectangular format or on some modal

pattern as depicted in Figure 4.14, two different options exist. The first technique involves transferring the desired shape of the sensor from a computer generated pattern on the metallization of the PVDF and simply cutting the sensor with scissors. The second method of obtaining the desired shape involves etching the surface electrode with PCB etchant. The desired modal pattern is first transferred to double sided tape, and this pattern is then attached to the PVDF, with respect to the coordinate system of the sensor. Upon attaching the tape pattern to the sensor, the etchant can be used to remove the metallization on one surface of the sensor. Previous studies by Lee *et al.*, (1991(a,b)) have demonstrated that the active portion of the material is that which remains covered by the metallization electrodes. Both techniques were used to achieve the desired shaped sensor and tests were conducted comparing theory and experiment. Before providing examples, the equivalent electrical analogies and required signal conditioning for the PVDF sensors are detailed.

5.1.2.2 Physical Implementation of Acoustic Near-Field Sensors

In designing the acoustic near-field sensors, a frame was required to support the material at the boundaries. This frame was constructed from spruce wood due to ease in cutting and shaping the material. Spruce is used by many model builders due to its structural rigidity, light weight and relative ease in shaping. As depicted in Figure 2.6, a shell segment was required to achieve the prototype sensor. A picture of the prototype sensor is presented in Figure 5.1. As required, the support boundaries were curved in one dimension and straight in the other. The curvature was created from a cylindrical pattern with a radius of 0.190 m and spruce wood was used to create the curved boundary of the frame. The PVDF material was bonded

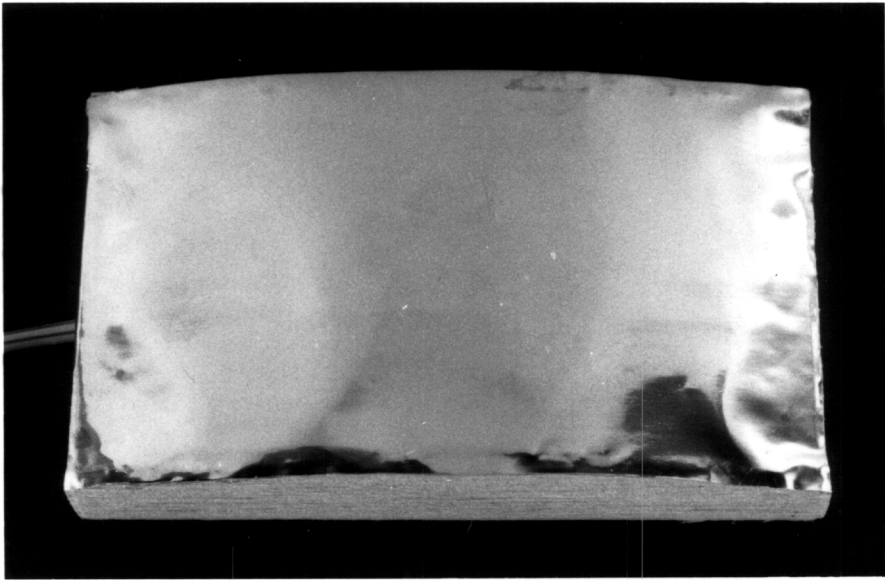


Figure 5.1: Picture of Prototype Near-Field Sensor

to the boundaries of the frame with M-bond 200 adhesive and leads were attached as outlined in the previous section. A comparison between the predicted and measured response of the pictured prototype sensor is presented later in the section devoted to practical implementation; however, appropriate signal conditioning of the electrical response must first be considered.

5.1.2.3 Equivalent Electrical Analogies

Since the goal of this work is not simply to outline the theoretical aspects of sensor design theory, but to implement sensors on structures, a review of the equivalent electrical analogies for PVDF should be considered before designing a sensor and placing it on the structure. A schematic of the equivalent circuit for the PVDF sensor is depicted in Figure 5.2. The sensor response can be viewed in terms of a charge source with a capacitor and resistor in parallel. Both the capacitance and resistance of the sensor can be computed based on material properties given in the *Kynar Piezo Film Technical Manual* (1987). The resistivity of the sensor is very high (1.5×10^{13} ohm-m), and hence is typically ignored in the equivalent sensor circuit. However, the resistance of the circuit is extremely important upon considering signal conditioning techniques.

5.1.2.4 Signal Conditioning

Depending on whether the desired response is in terms of strain or rate of strain, a voltage amplifier or a current amplifier can be used to increase the electrical response of the sensor. If rate of strain is required, the reader is referred to the previously

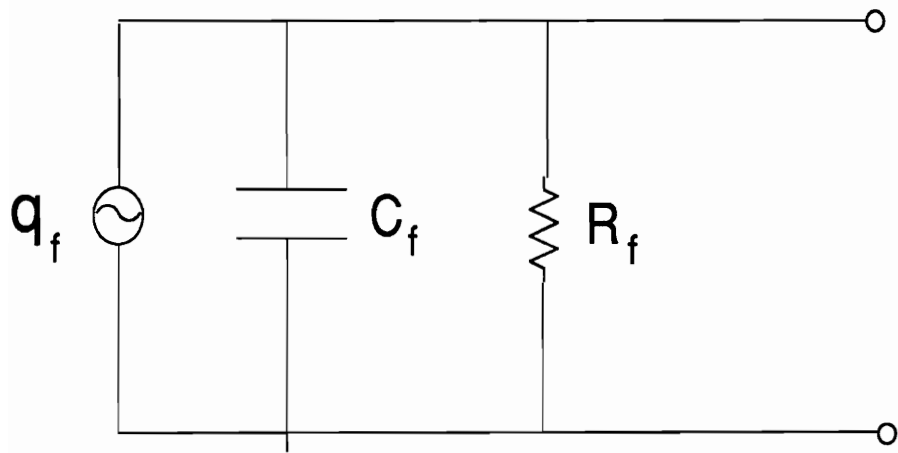


Figure 5.2: Schematic Diagram of PVDF Electrical Circuit

outlined discussion on current amplifiers by Lee *et al.*, (1991(b)). Regardless of the chosen circuit, care must be taken in choosing the appropriate amplifier due to the high output impedance of the sensor. Based on work conducted at VPI&SU, an operational amplifier with an input impedance on the order of giga ohms is suggested (i.e. much larger than that of the sensor). This amplifier is required to eliminate impedance mismatch and hence loading of the circuit. If a response proportional to strain is desired, a circuit can be designed with a voltage follower implementing the high impedance amplifier, and then a lower quality amplifier can be used to provide gain and protect the high impedance amplifier from loading due to the typically low impedance electrical cables which are connected to the amplifier output. A circuit diagram for this voltage amplifying signal conditioner is presented in Figure 5.3.

An important concept raised earlier by Lee *et al.*, (1991(a)) concerns that of shielding the sensor. The PVDF sensor acts as an antenna when not properly shielded, and Lee suggests folding the sensor upon completing the shape such that the side of the sensor which encloses the inner surface can be tied to ground to provide electrical shielding. In addition to this method of shielding, the sensor can be protected from the electric fields created by the piezoelectric actuators and other sources by grounding the test structure (as long as the test structure is electrically conducting). Both methods of shielding were studied during the course of this work and were found to yield the identical electrical response both in phase and magnitude. It should be noted that if electrical shielding is not used, both the phase and magnitude of the electrical response can be erroneous.

When designing modal sensors, to achieve the required orthogonality condition be-

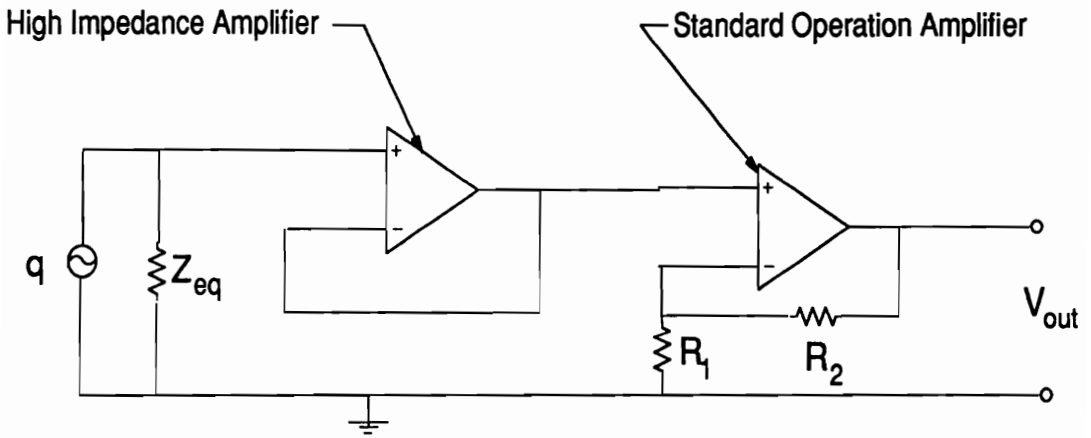


Figure 5.3: Schematic of Voltage Amplifier

tween the spatial window created by the sensor and the mode shape of the structure, 180° phase changes are required between nodes of the sensor, with the exception of the mode 1 sensor which has nodes at the boundaries of the structure only. It is best to view each element of the sensor which requires a phase change as a separate sensor element. For the sensor design chosen in this study no phase changes were required due to the characteristics of the radiation filter at the chosen acoustic field point; however, details of this general sensor design approach are outlined for future implementation.

For example, a sensor designed to measure only the response of the third mode of the simply supported beam can be viewed as three independent sensors since two nodal points exist within the boundaries of the structure. The polarity of the middle element must be reversed as indicated in Figure 5.4. This can be accomplished by ordering material with a different polarization profile across the surface, which is very expensive, or by electrically reversing the polarity of sensor elements with appropriate wiring techniques. If we consider the electrical equivalent of each element of the PVDF sensor and wire them in parallel, reversing the polarity on the middle sensor to achieve the appropriate phasing, an equivalent circuit can be drawn as in the top portion of Figure 5.5. Treating the charge sources as current sources when developing equivalent networks, the sensor response can be expressed in terms of a single charge and a single impedance as indicated in the bottom portion of Figure 5.5. The equivalent impedance of the circuit can be expressed as follows:

$$Z_{eq} = \frac{1}{\frac{3}{R_f} + \frac{1}{R_i} + j3C_f\omega} \quad (5.1)$$

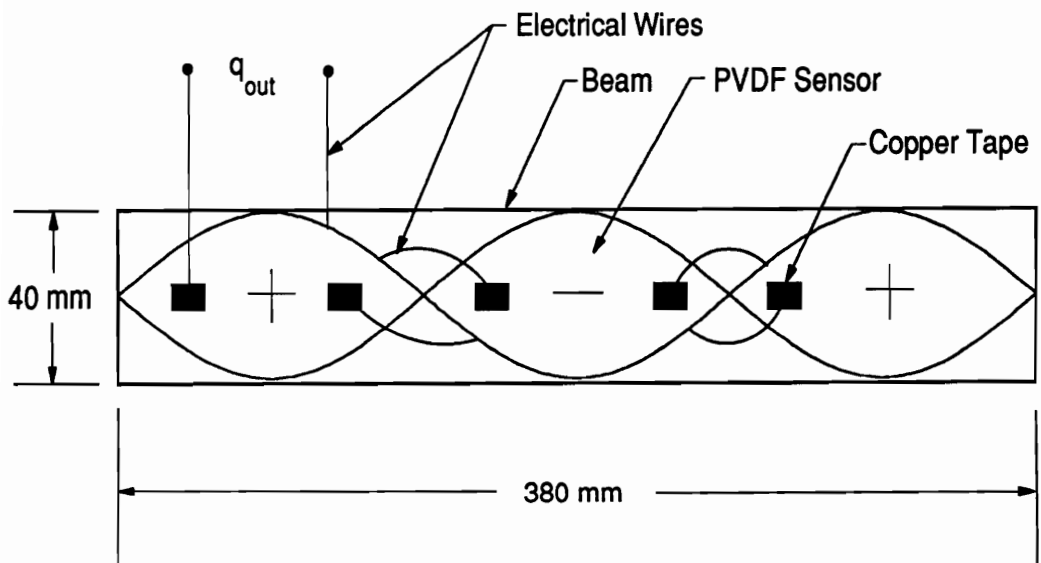


Figure 5.4: Schematic of 3-Mode Sensor

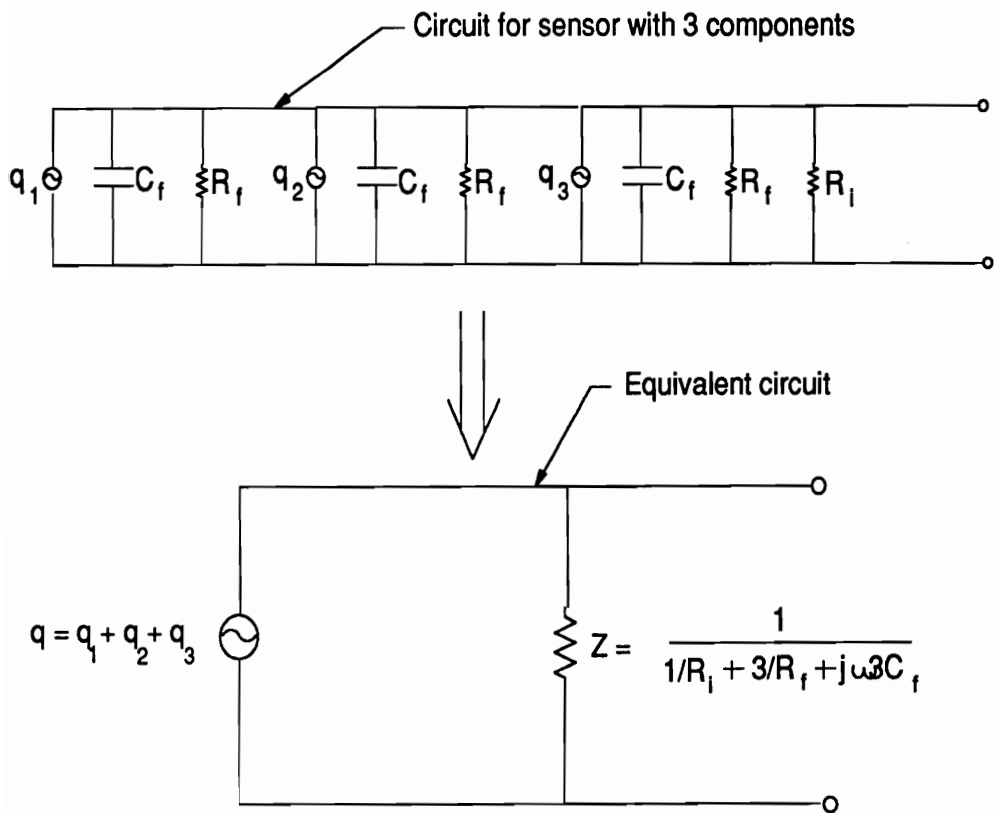


Figure 5.5: Schematic of Equivalent Circuit for 3-Mode Sensor

where:

- R_f = resistance of each sensor element
- R_i = resistance of instrumentation amplifier
- C_f = capacitance of each sensor element.

If we assume harmonic excitation of the sensor, the charge can be expressed as follows:

$$q(t) = q \exp(j\omega t). \quad (5.2)$$

The current is expressed as the derivative of the charge:

$$i(t) = j\omega q \exp(j\omega t). \quad (5.3)$$

If we assume that $R_f \ll R_i$ and $R_f C_f \omega \gg 1$, as is typically the case, then

$$Z_{eq} = \frac{1}{j3C_f\omega}, \quad (5.4)$$

and

$$V(t) = \frac{q}{3C_f} \exp(j\omega t). \quad (5.5)$$

This parallel configuration of the individual sensor elements is equivalent to the desired analytical design of the modal sensor due to the summing nature of the charge over each sensor element. With this said, a comparison between the predicted and

measured transfer functions between a distributed PVDF sensor and harmonic point force input is in order.

5.1.2.5 Practical Implementation

The sensor pattern depicted in Figure 5.4 was transferred to the PVDF material and the modal sensors were attached to the simply supported beam as outlined earlier. (Details of both the simply supported beam and simply supported plate are included in section 5.2.) Due to the one-dimensional nature of the beam response, the “variation in the polarization profile” over the area of application can be achieved by creating a two-dimensional sensor varying in width proportional to the desired weighting. A shaker configured with a stinger and force transducer was attached to the beam 170 mm from the left side. The structure was driven with a pseudo random input, and the frequency response function between the PVDF sensor and measured force was computed. The output of the PVDF sensor was conditioned with a high input impedance voltage amplifier for reasons outlined previously.

For comparison, the frequency response function for the chosen sensor design (in units of volts) and input disturbance (in units of Newtons) was computed based upon equation (2.3) and equation (4.29). The appropriate coordinates for the shaker (170 mm from the left of the beam) as well as PVDF sensor dimensions (380 mm x 40 mm) were substituted into each expression along with the physical dimensions of the test structure (380 mm x 40 mm x 4.67 mm). The modal response of equation (2.3) was then substituted into the expression for computing the electrical response of the shaped PVDF sensor of equation (4.29). Both the phase and magnitude of

the frequency response function were computed from the following expression:

$$\frac{q}{F} = -\frac{2(h_p + h_s)e_{31} \sin(\frac{m\pi x_d}{L_x})(m\pi)^2}{4\rho' L_x^2(\omega_m^2 - \omega^2 + j2\eta\omega\omega_m)}, \quad (5.6)$$

where the magnitude of equation (5.6) is converted to units of *Volts/Newton*s by dividing the expression by the capacitance of the sensor.

The magnitude is presented in Figure 5.6 and the phase is presented in Figure 5.7. By comparing the magnitude of the predicted response to that of the measured response, one ascertains that the properties of the material are within reasonable calibration. The on-resonance response value should not be considered in the calibration as the amount of damping (0.01%) used in the theoretical model directly affects this response characteristic. The phase response is as important as the magnitude since the assumption was that the output is a function of strain and hence should exhibit similar characteristics. As illustrated, the phase characteristics are nearly identical to those predicted, confirming that the response of the sensor is proportional to strain as modeled. The phase changes between -180° and $+180^\circ$ in the experimental data can be ignored since there is no difference between the sine of these two angles. In signal processing, this is commonly denoted “phase wrap”. As the imaginary part of the frequency response function approaches zero with a negative real component contribution, the chosen path to represent the phase can be 180° or -180° . The cosine of these two angles is identical.

In addition to comparing the measured and predicted response of a structural error sensor, the acoustic near-field sensor design was tested. The prototype sensor

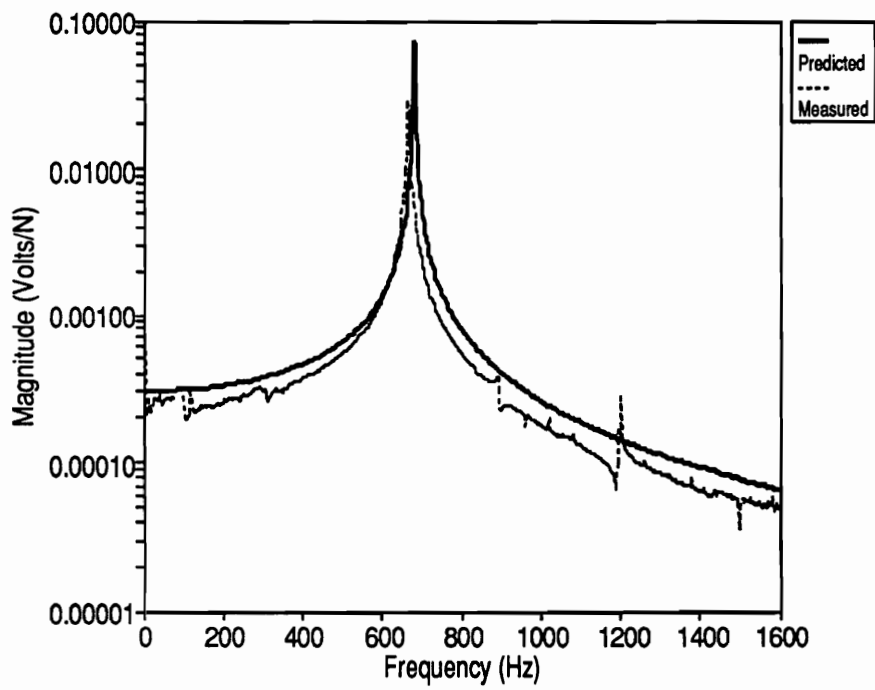


Figure 5.6: Predicted vs Measure Magnitude of FRF for 3-Mode Sensor

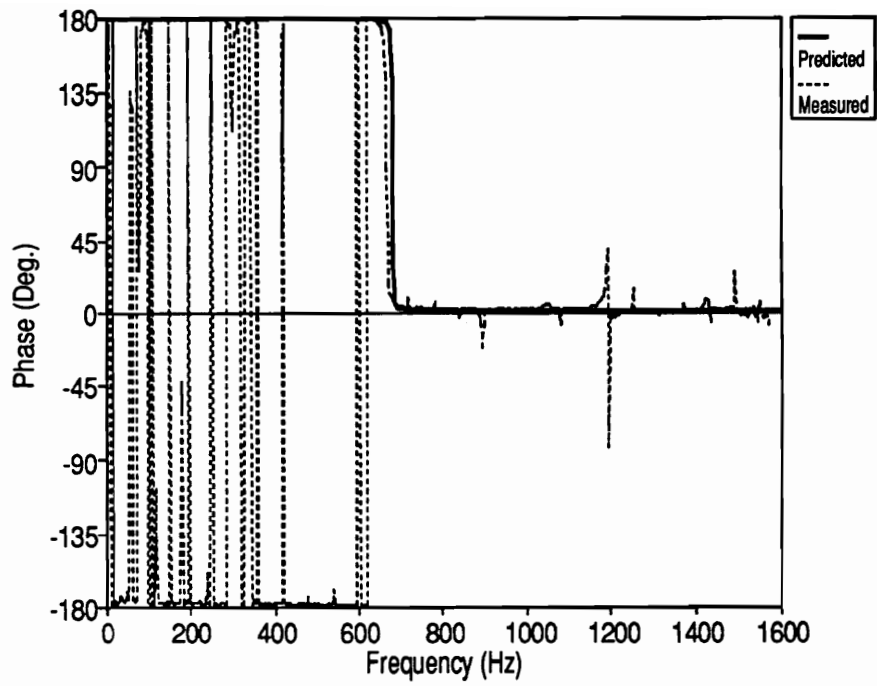


Figure 5.7: Predicted vs Measure Phase of FRF for 3-Mode Sensor

pictured in Figure 5.3 measured 28.5 mm in the y-direction by 25.4 mm in the x-direction as defined in the coordinate system of Figure 2.6. To test the sensor, a standing wave tube was used to create the input disturbance since a uniform pressure wave results when driving the source. A schematic of the apparatus used to test the PVDF acoustic near-field sensor is presented in Figure 5.8. By exciting the sensor with a harmonic uniform pressure wave, the frequency response function between the input pressure, measured with a microphone positioned at the same axial position as the PVDF acoustic near-field sensor in the standing wave tube, and the PVDF near-field sensor was obtained. The analytical response to this type of uniform pressure excitation can be computed from equation (A.33) in Appendix A.

As indicated in Figure 5.9, results compare reasonably well in the low frequency range and are observed to deviate significantly at higher excitation frequencies. This deviation results from a number of assumptions made in developing the approximate model. First, the exact solution for the system of equations is unknown. Hence an approximate solution was assumed with a set of admissible functions which were assumed to satisfy the geometric and natural boundary conditions. The geometric boundary conditions require that there be no deflection at the boundaries and the natural boundary conditions require that there be no moments at the boundaries. Secondly, in designing the prototype sensor, the PVDF was attached to the boundaries of the sensor frame with a very thin layer of M-bond 200 adhesive for lack of a better method of attachment. Boundary conditions resulting from this method of attachment are obviously not perfectly simply supported (in particular, the natural boundary condition is violated) as was assumed in the solution. Fi-

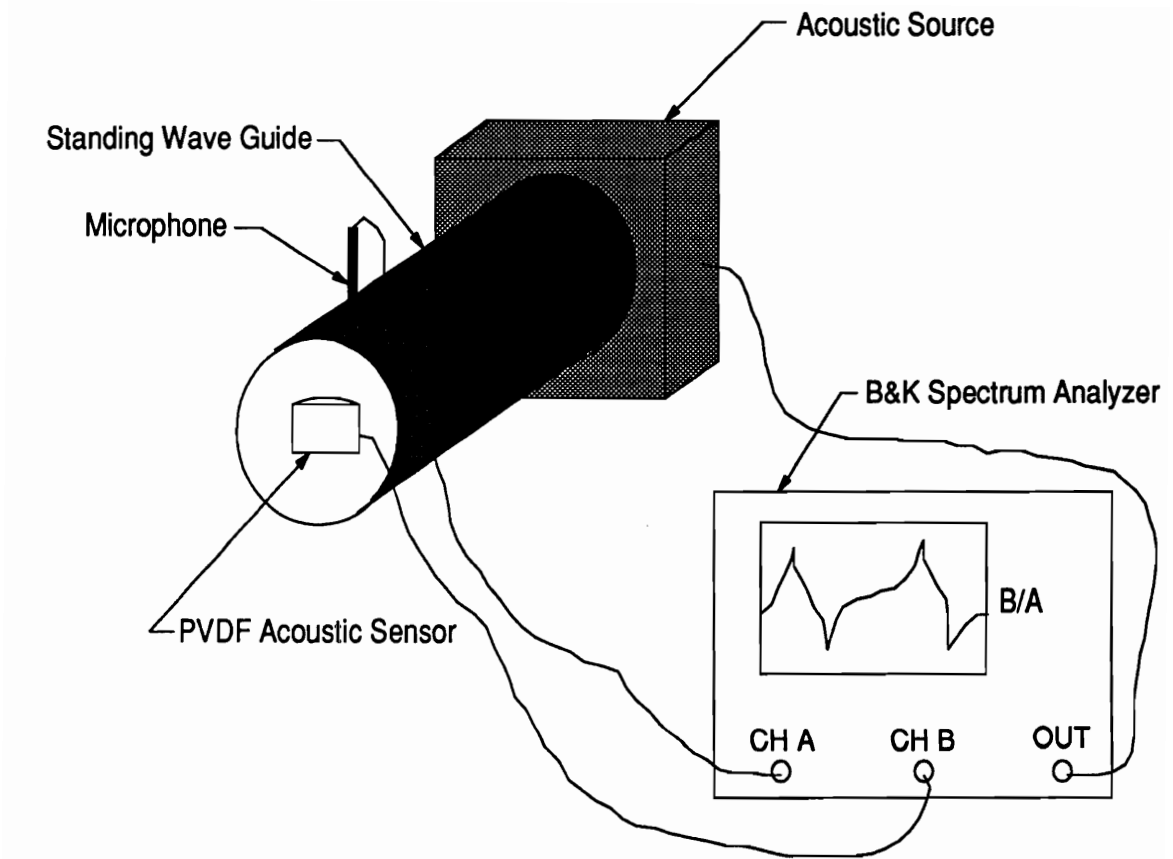


Figure 5.8: Schematic of Test Apparatus used to Evaluate PVDF Near-Field Sensor

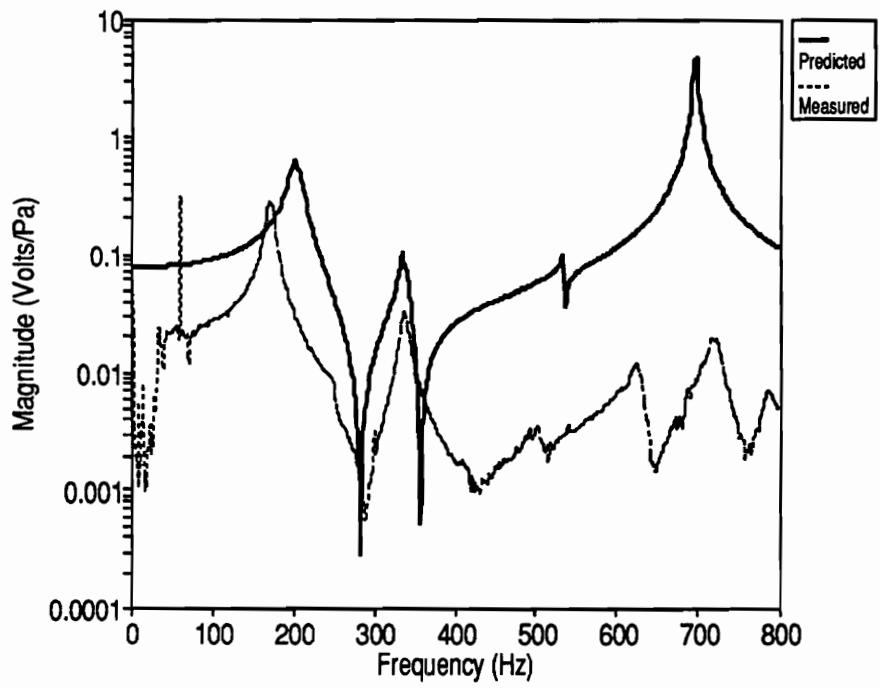


Figure 5.9: Predicted vs Measure Magnitude of FRF for Near-Field Sensor

nally, upon reviewing literature concerning fluid loaded plates (Crighton, 1980), one readily ascertains that the PVDF near-field sensor can be characterized as a fluid loaded structure even in the presence of air, hence a fully coupled model is required to accurately describe the dynamics of the system. A simply supported cylindrical plate was chosen to model the sensor dynamics, and hence the same methods used to characterize fluid loading on flat plates will be used to determine the significance of fluid loading due to air on the PVDF acoustic near-field sensor.

Fluid loading is characterized by the Mach number, which is defined as follows:

$$M = \frac{k_o}{k_b} = \sqrt{\frac{\omega}{\omega_g}}, \quad (5.7)$$

where k_o is the acoustic wavenumber, k_b is the structural wavenumber, ω is the excitation frequency and ω_g is the critical frequency. The Mach number is compared to the intrinsic fluid loading parameter (Crighton, 1980) which is defined as follows:

$$\epsilon = \frac{\rho_o}{\rho_s} \left[\frac{E}{12\rho_s c_o^2 (1 - \nu^2)} \right]^{\frac{1}{2}}, \quad (5.8)$$

where ρ_o is the density of the fluid, ρ_s is the density of the structure, E is the Young's modulus of the structure, c_o is the speed of sound in the fluid and ν is Poisson's ratio for the structure. For the given material properties of the PVDF and air, $M = 121 \times 10^{-6}$ and $\epsilon = 755 \times 10^{-6}$. Hence the mach number is of the same order of magnitude as the intrinsic fluid loading parameter, which indicates significant fluid loading (Crighton, 1980). Thus to accurately predict the response of the sensor,

a fully coupled analytical model is required. Considering the computational effort required to achieve this model and the fact that the boundary conditions are not ideal, a finite element model is suggested to improve the prediction of the dynamic response as opposed to attempting further improvements on the analytical model used in this study.

With the exception of the phase wrap at 180° and -180° , the measured and predicted phase of the PVDF near-field sensor again compare reasonably well as indicated in Figure 5.10. The general trends as well as values for the phase are in accordance, particularly in the low frequency range. The predicted response of the sensor certainly deviates from that measured as the frequency of excitation increases; however, in general, the predicted response proved accurate enough for design optimization over the frequency range of interest.

Better correlation between theory and experiment for the PVDF near-field sensor could possibly be obtained by including the fluid loading in the structural analysis as well as formulating a finite element model of the structure. However, as will be demonstrated in the results section, the model was sufficiently accurate in choosing the optimal location of the sensor for controlling the structure-borne sound from the simply supported plate. In view of the intense CPU time required to determine the optimal location of the PVDF near-field sensors coupled with the complexity of developing a fluid loaded model for the shell segment, this method of analysis is not recommended.

In general, each PVDF error sensor implemented in this study was first tested as

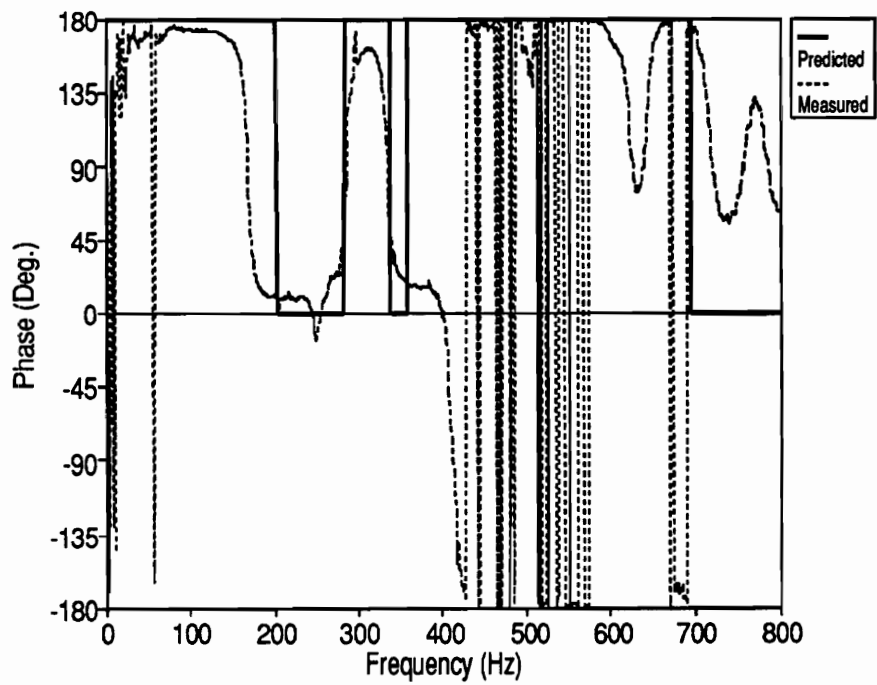


Figure 5.10: Predicted vs Measure Phase of FRF for Near-Field Sensor

previously outlined to assure that the measured and predicted frequency response functions were in agreement. By performing this experiment in advance of conducting control experiments, sensors with poor response characteristics due to inappropriate structural attachment, shaping or lead attachment were identified. This method of design review is suggested whenever implementing any form of PVDF shaped sensor or acoustic near-field sensors.

5.1.3 Controller

As briefly mentioned earlier, the multi-channel version of the filtered-x adaptive LMS algorithm was implemented on a TMS320C25 digital signal processing board in assembly language to achieve the desired feed forward control approach. The processing board, which was manufactured by Spectrum, was resident in an AT compatible host computer which was used to program the board as well as execute the controller. An interface program was written in C language which allowed the user to execute or halt the controller, set the sampling rate, perform system identification and adjust the convergence parameter of the algorithm. The controller was originally configured with three outputs and three inputs, in addition to the input required to monitor the reference signal. It was later modified to accommodate three additional inputs for the purpose of implementing the model reference control approach. All signal processing was performed on the TMS320C25 board; however, all input/output was conducted with two separate four channel I/O boards which were also manufactured by Spectrum.

Each four channel I/O board was configured with four separate input channels ca-

pable of performing simultaneous sample and hold. Each sampled input was sequentially converted from analogue to digital and passed to the digital signal processor (DSP) where the control algorithm was implemented. In addition to the four input channels, each I/O board was configured with two digital to analogue outputs. Upon determining the appropriate control response at the DSP, the desired electrical response was sent to each actuator via these digital to analogue converters. In each case, D/A or A/D, the conversion was limited to 12 bits (i.e. a dynamic range of 66 dB). A warning is provided in the manual by Spectrum (1987) that the input signals should be limited to ± 3 volts to avoid damaging the quad sample and hold chip as the dynamic range is applicable in the ± 2.5 volt range. Due to this constraint, and concern over damaging the boards, the error signal was limited to ± 1.0 volt to assure that the ± 3 volt range was not exceeded in case the controller became unstable. This reduced the dynamic range by 8 dB, but was considered a small price to pay in comparison to permanently damaging the I/O board.

All signal processing performed on the TMS320C25 was also limited to 12 bit accuracy, further restricting the dynamic range. In implementing the control algorithm, the input and output data was scaled to attempt to utilize the full dynamic range of the DSP; however, this was not entirely possible due to the number of multiplications performed during the implementation process. This trade off is best explained by example. In implementing the filtered-x LMS algorithm, one can expect 3 multiplications. The filtered-x coefficients must be multiplied by the reference input to obtain the filtered-x response. This response must be weighted by the updated coefficients (i.e. the adaptive coefficients which converge to achieve the optimal control voltage output) and further multiplied by the convergence parameter. The dynamic

range of each of these variables must be within the 12 bit dynamic range of the DSP, and the product must as well be restricted to this dynamic range. Hence the problem is obvious. If the data is scaled such that each variable utilizes the full dynamic range of the board, the product will exceed this range and hence saturate. Based on this observation, all variables must be scaled such that all resulting products are within the dynamic range of the board. This limit in the dynamic range coupled with that imposed by the ± 1.0 volt input limit resulted in a working dynamic range of approximately 40 dB. This is an important factor to consider when comparing theory and experiment, and the effect of this limited control level will be discussed in the results of chapter 6.

5.1.4 Instruments Used in Experiments

For the noise input, both test structures were driven with a Ling shaker attached to the back of the structure configured with a stinger and a Kistler force transducer. The simply supported plate, which was the base structure for the majority of the tests, was instrumented with 9 Bruel and Kjaer mini accelerometers, weighing less than 0.65 grams each, and a modal analysis of the uncontrolled and controlled response was obtained by solving a set of simultaneous equations to recover the amplitudes of independent modes on the panel (Fuller *et al.*, 1991(b)). This method is further discussed in Appendix C. The directivity pattern was obtained by traversing the acoustic field with a Bruel and Kjaer microphone in 9° increments about the horizontal mid-plane of the test structures at a radius of 1.6 m. For the frequency range of interest, this radius was not at a coordinate location where the far-field relations could be accurately used; however, this was the greatest radius possible due

to the finite dimensions of the anechoic chamber. The sound radiation directivity pattern was mapped both with and without control. In addition, a few microphones were randomly located in the chamber (i.e. out of the traverse plane) to provide a measure of the global attenuation. The output of all transducers was sampled and signal processed with a model 2032 Bruel and Kjaer spectrum analyzer.

In executing the control, several filters and amplifiers were required to condition the input and output signals. To prevent aliasing problems, a programmable low pass filter manufactured by Frequency Devices was used to condition each input from the chosen error sensors. The corner frequency of the filter was typically chosen an order of magnitude lower than the sampling frequency of the board, which was set at a factor of 10 greater than the frequency to be controlled. For example, if the disturbance input to the structure was chosen at 320 Hz, the sampling rate was set at 3.2 kHz. This sampling rate is suggested by Ackerman (1985) and was determined to be the most appropriate for consistent and stable convergence of the LMS algorithm. A schematic diagram of the instrumentation used in conjunction with the controller is presented in Figure 5.11. In addition to the filters required on each input signal, Ithaco amplifiers with variable gain adjustment were used to obtain the desired ± 1.0 volt input level. One should recognize that all sensors should be calibrated with respect to each other, and the gain should be adjusted based upon the channel with the maximum response. As a result, in the multi-channel control case, the response of some sensors will be less than ± 1.0 volt due to the different relative positions of each sensor in the acoustic field or on the structure. In addition to conditioning the input, the control output was also filtered and amplified. Since the resulting analog output is based upon a digital to analog conversion, the elec-

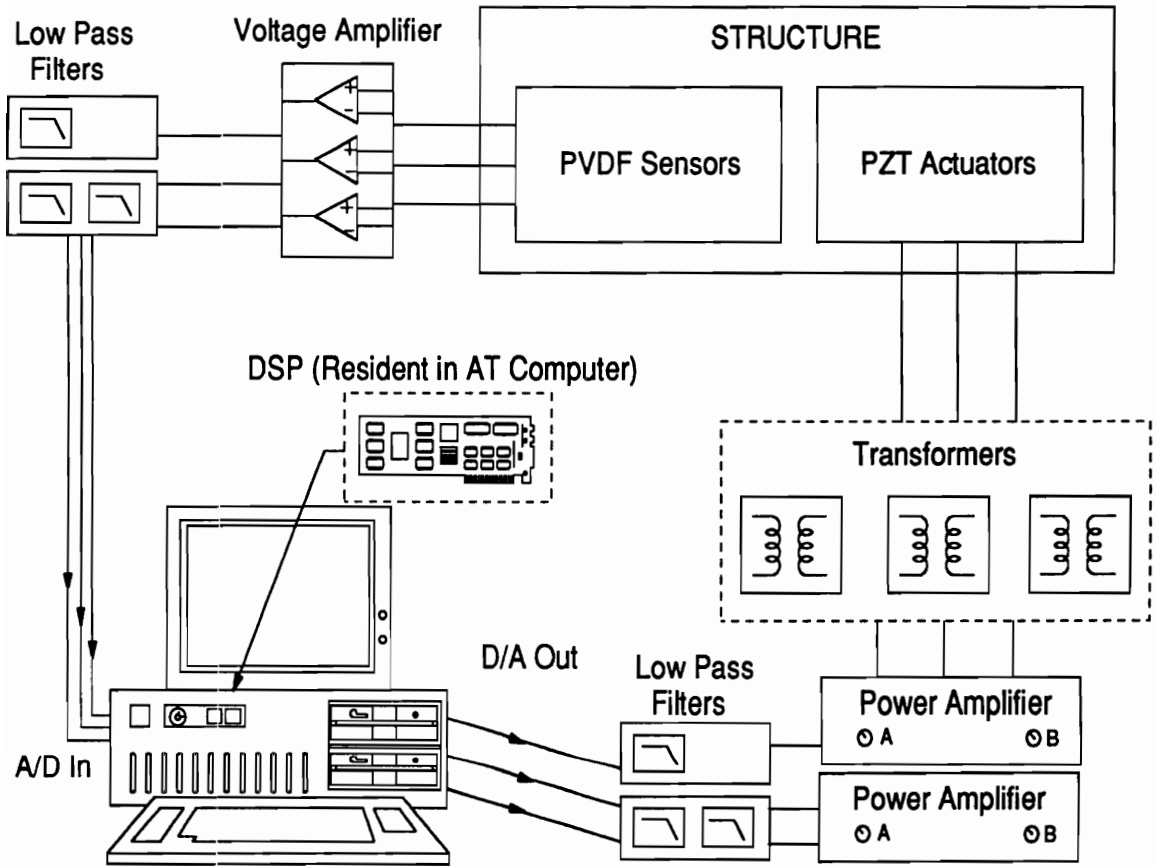


Figure 5.11: Schematic of Instruments Used in Control Approach

trical signal must be low pass filtered to eliminate the high frequency chirp created by the zero order hold. An Ithaco low pass amplifier was used to accomplish this objective and the corner frequency was adjusted to the same frequency as that used on the input. In addition, since the output, which was limited to ± 2.5 volt was used to drive the PZT actuators, the signal was passed through an NEC power amplifier and the voltage was further increased by a factor of 17.1 with a transformer. The harmonic input used to create the reference for the controller as well as drive the disturbance was created with a signal generator resident in the B&K model 2032 spectrum analyzer.

5.2 Structural Equipment

Sensor designs and control approaches were evaluated with two basic test structures, a simply supported plate and a simply supported beam. Each test structure was located in the anechoic chamber for performing the structural acoustic control experiments. The simply supported beam and simply supported plate used in this study were constructed from steel with material properties listed in Table 4.1. The beam measured 380 mm in the x-direction by 40 mm in the y-direction by 4.56 mm in the z-direction as illustrated in the coordinate system of Figure 2.1. A picture of the beam configured with a PVDF sensor is illustrated in Figure 5.12. The plate measured 380 mm x 300 mm by 1.96 mm in the corresponding directions, and a picture of the plate configured with PZT actuators and PVDF sensors is presented in Figure 5.13.

The simply supported boundary conditions were achieved by attaching thin shim

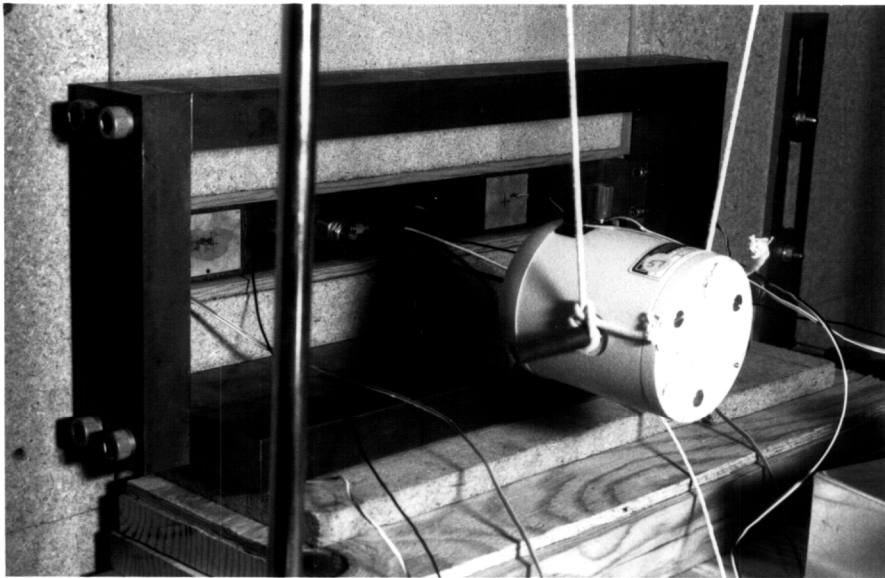


Figure 5.12: Picture of Simply Supported Beam

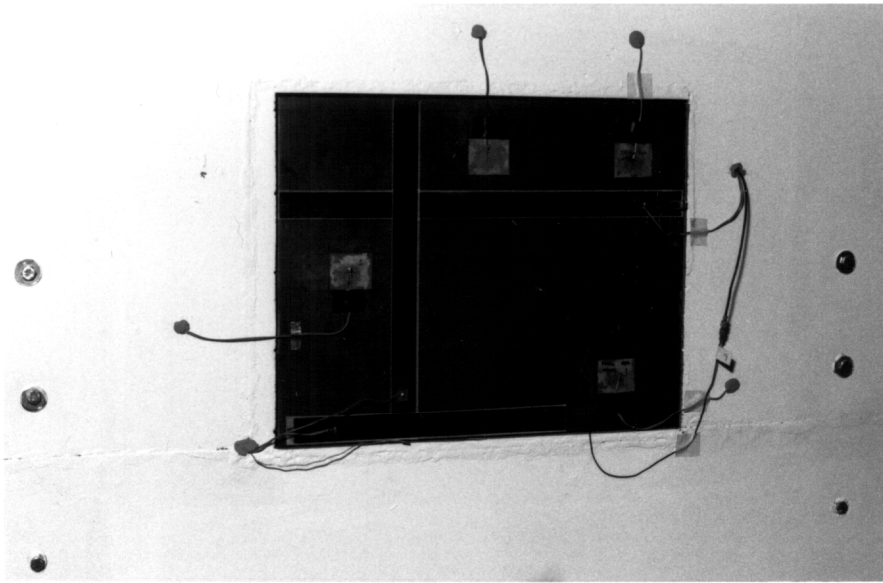


Figure 5.13: Picture of Simply Supported Plate

Table 5.1: Theoretical vs. Experimental Resonant Frequencies for Simply Supported Beam.

Mode	Theoretical f_m (Hz)	Experimental f_m (Hz)
1	76	78
2	303	304
3	681	680
4	1210	1208
5	1891	1880
6	2724	2704
7	3707	3664
8	4841	4752

spring steel to the boundaries of the plate or beam with small set screws and a sealing compound. The shims were then attached to a rigid steel frame, allowing the edge of the plate to rotate relatively freely but restricting out of plane motion at the boundaries. Previous testing has shown that this arrangement adequately models the simply supported boundary conditions (Ochs and Snowdon 1975). In addition a modal analysis of the beam (Clark *et al.*, 1991(a)) and the plate was previously performed, and the modal response of each structure was determined to be in accordance with the assumed boundary conditions. The measured and predicted resonant frequencies for the simply supported plate were presented previously in Table 4.2, and were determined to be within 1% of each other over the frequency range of interest. The resonant frequencies for the simply supported beam are presented above for the first 8 modes in Table 5.1 with a similar 1% accuracy. Establishing the simply supported boundary conditions is crucial to the modal decomposition which was detailed previously by Fuller *et al.*, (1991(b)) and is presented in Appendix C for reference.

In conducting the structural acoustic control experiments, the plate or beam, depending on which was being tested, was placed in the anechoic chamber at VPI&SU. The chamber measures 4.2 m x 2.2 m x 2.5 m and has a cut-off frequency of 250 Hz. The test structure (i.e. beam or plate) was rigidly supported on a steel frame configured with a 4.2 m x 2.2 m x 19 mm wooden baffle. The test structure was placed in the plane of the baffle to reduce the dipole effect created by the front and back of the plate as well as to facilitate later analytical comparisons. As illustrated in Figure 5.14, the plate resides in the center of the baffle. An adapter was built to extend the baffle when testing the simply supported beam. Since the beam was the same dimension in the x-direction (380 mm), the extension was required to fill the gap in the y-direction and was attached to the supporting frame above and below the simply supported beam.

5.3 Summary

Methods of attaching both PZT actuators and PVDF error sensors have been documented for physical implementation of the design approach. In addition, calibration tests were performed to assure that both the sensors and actuators were performing in accordance with the analytical predictions. This was done to provide a preliminary foundation for this work as well as to assure that each sensor or actuator implemented in the structural acoustic control experiment performed as per design specifications. Any errors in wiring or positioning of sensors was evident upon conducting these preliminary tests. The boundary conditions of the structure were established to assure that the analytical model for the simply supported beam and plate can be used in comparing theory and experiment. In addition, all appropriate

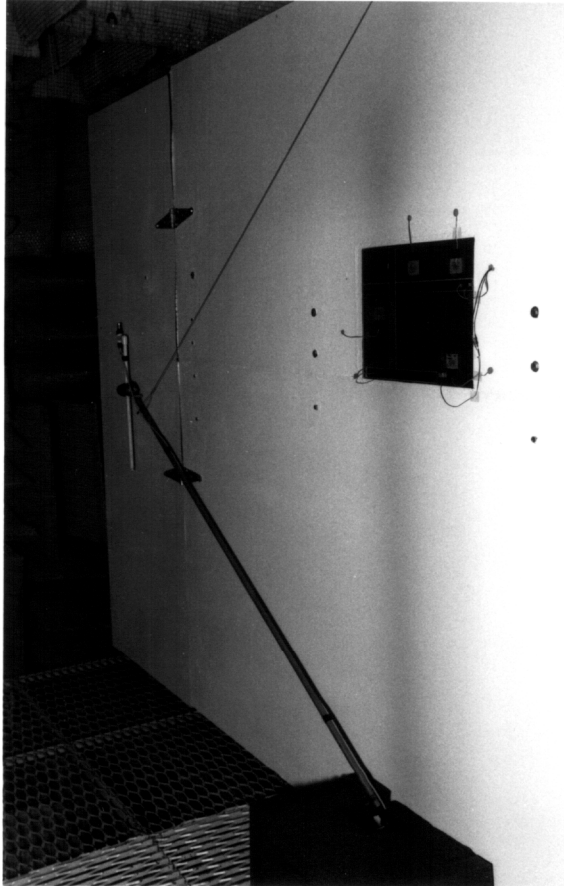


Figure 5.14: Picture of Plate/Baffle

signal conditioning required to drive the structure with PZT actuators or measure the response of the structure with PVDF sensors has been outlined. Having outlined the equipment necessary to conduct the tests as well as that required to evaluate the response of the uncontrolled and controlled response, the results of this work follow.

Chapter 6

Experimental and Analytical Results for ASAC

Each unique sensor design and implementation previously discussed in Chapter 3 and Chapter 4 was first studied with the analytical models and later implemented on the chosen test structures for single frequency harmonic excitation. Before initiating experiments to study the different types of structural and acoustic near-field sensors, several tests were conducted with microphone error sensors, and results were compared to theory. In computing the theoretical uncontrolled and controlled acoustic response of the structure, Rayleigh's integral was evaluated numerically to obtain the pressure at the chosen acoustic field point. Comparing results from these fundamental experiments with the predicted structural acoustic response provided a foundation for determining the dynamic range and limitations of the feed forward controller as well as the applicability of the analytical models for predicting the acoustic response of the structure based upon excitation with piezoelectric actuators and point force disturbances created with a shaker. As will be discussed in the following overview, the dynamic range of the controller as well as the physical implementation of the shaker as the primary disturbance play an important role in the controlled and uncontrolled structural acoustic response. Upon establishing the

appropriate analytical models and method of implementation, each of the sensors studied in this work are discussed. Since microphone error sensors placed in the acoustic field provide an estimate of the desired cost function, (the total radiated acoustic power), results from control experiments implementing these sensors are discussed first. In addition, all results from control experiments utilizing alternative sensors will be compared to experiments implementing microphone error sensors, which provide a good basis for comparison since the objective is to reduce the radiated pressure. A separate section is devoted to each error sensor studied in this work, which includes microphones, PVDF structural and acoustic error sensors, and accelerometer error sensors.

6.1 Overview

Initial control experiments implementing the feed forward filtered-x version of the adaptive LMS algorithm were performed with the simply supported plate as the test structure. The input disturbance was created with a shaker and control was achieved with piezoelectric actuators. A schematic of the test plate configured with the piezoelectric actuators is illustrated in Figure 6.1. The positions of these actuators are presented in this section as opposed to the chapter devoted to design since they were not optimally located on the plate. Their coordinates were chosen with respect to the nodal lines of the modes necessary to control over the frequency range of interest (0-600 Hz). Each actuator measured 38.1 mm in the x-direction by 31 mm in the y-direction, and the center coordinates of each actuator are (63.3,150) mm, (190,250) mm and (316.6,50) mm for C1, C2 and C3 respectively. (The reader is reminded that an actuator corresponds to two piezoelectric elements positioned

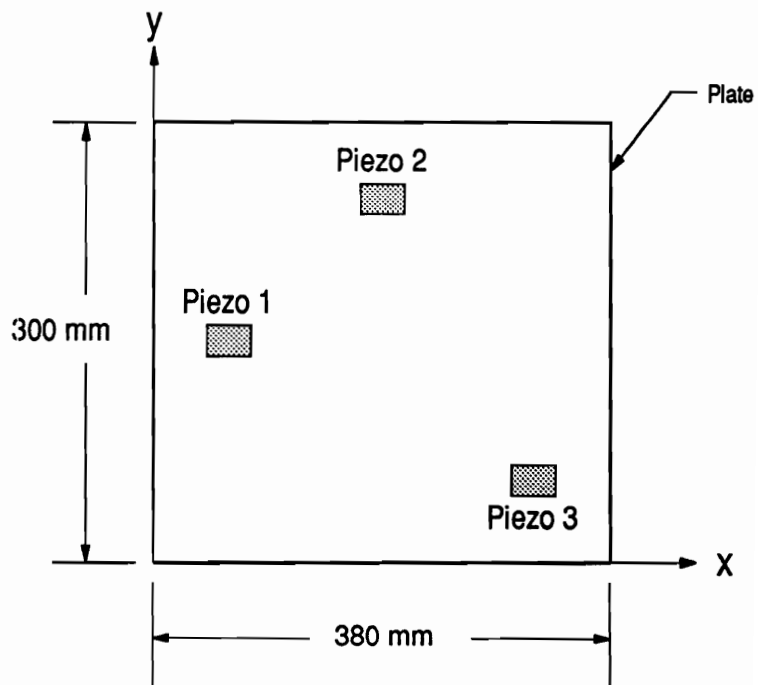


Figure 6.1: Schematic of Plate with 3 PZT Actuators

symmetrically about the plate surface and wired 180° out of phase with respect to each other to produce uniform bending about the neutral axis.) Microphone error sensors were implemented in the cost function of the controller along the horizontal midplane of the plate, and the results from these preliminary tests were compared to theory to evaluate the analytical models as well as the performance of the controller.

An immediate difference between the predicted and measured controlled acoustic response was noted upon conducting these first preliminary tests. Consider the theoretical acoustic directivity pattern presented in Figure 6.2. When computing the theoretical controlled acoustic response of the structure at 550 Hz due to an input disturbance located at spatial coordinates of (240,130) mm, the limit in attenuation at the chosen error sensors is a function of the computational accuracy, which is 16 digits in double precision. In other words, for the three-input, three-output control case presented, the acoustic response at the chosen acoustic field points can be driven to zero machine accuracy. This is not practical in physical systems since the A/D converters as well as the signal processors are each limited to a finite dynamic range. For the purpose of this study, each was limited to 12 bit accuracy (i.e. 66 dB). Due to limitations placed on the inputs to protect the A/D converters as well as scaling performed on the signal processing unit while implementing the control approach, the dynamic range of the controller was limited to 40 dB, as discussed previously. To prevent further reduction in the dynamic range, all experiments were conducted at an acoustic level well above the noise floor of the anechoic chamber, which was approximately 20 dB relative to $20 \mu\text{Pa}$. Thus for harmonic inputs, the coherence between the input disturbance and the response at any chosen error sensor was always close to unity at the driving frequency.

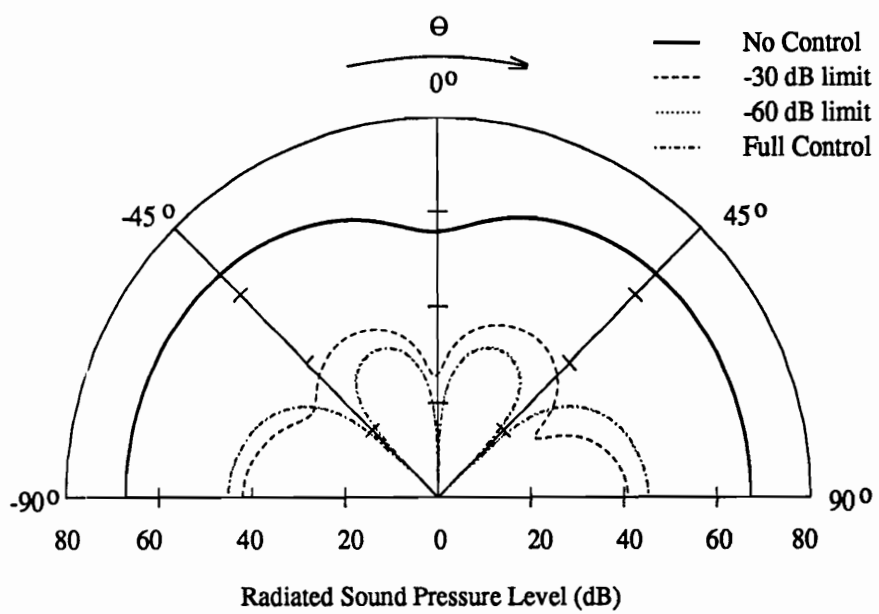


Figure 6.2: Comparison of Acoustic Directivity Pattern as a Function of Dynamic Range (550 Hz)

Since the level of attenuation at each error sensor was in practice limited to 40 dB, the same limitation was imposed on the analytical model. This limit in attenuation was essentially implemented by the same technique used to implement the model reference control approach. The desired response was computed by dividing the uncontrolled response at each error sensor by 100, resulting in a desired response 40 dB less than that of the uncontrolled response. A comparison of the variations in the directivity patterns for an excitation frequency of 550 Hz is presented in Figure 6.2 to illustrate the effect of a limited dynamic range on the overall controlled response. The legend of the figure indicates the limit in the level of attenuation constrained at the chosen error microphones which were positioned about the central axis of the plate at angles (θ, ϕ) corresponding to $(45^\circ, 0^\circ)$, $(45^\circ, 180^\circ)$ and $(0^\circ, 0^\circ)$. The -45° angle depicted in Figure 6.2 is used to indicate $(45^\circ, 180^\circ)$ in the coordinate system of Figure 4.6. As is evident from the results, increasing the dynamic range of the controller serves to increase the level of attenuation possible at the chosen error sensors; however, an increase in spillover is observed in some regions of the residual acoustic field as well. While this level of spillover is relatively small, one quickly concludes from the case presented that little is gained by having a large dynamic range. In fact, the dynamic range of the controller need simply be equivalent to the theoretical level of attenuation possible in the residual acoustic field to yield a successful control implementation. This result is pleasing since all real systems will be restricted to some finite level of attenuation due to noise floors on instrumentation as well as finite dynamic ranges in the A/D and D/A conversion processes.

In addition to the limited dynamic range of the controller, other factors must be

considered when comparing the controlled acoustic response of the structure. One such factor concerns the attachment of the shaker to the structure. While the shaker was attached with a stinger at the desired coordinates and was suspended from a flexible bungee cord, some mass loading of the test structure occurs. This mass loading is not observed when driving the system with the shaker alone since the dynamics of the shaker are used to create the desired harmonic input force. However, upon trying to control the response of the structure with piezoelectric actuators, the dynamics of the shaker are “observed” by the control actuators. The ideal means of analysis would require a coupled dynamic model; however, this would dictate some form of substructure synthesis or a finite element model coupled with a boundary element model for computing the acoustic response of the structure.

As opposed to this complex approach, the mass loading of the shaker is modelled by the assumed modes method, which is simply a form of the Rayleigh Ritz method. The comparison functions chosen are the eigenfunctions of the simply supported plate since they satisfy the natural and geometric boundary conditions. Both the structural response and acoustic response of the simply supported plate can be computed analytically by this method as outlined in Appendix D. The computational effort required increases by a factor of the number of original modes squared; however, a significant difference is noted in the predicted response of the structure based on this approach and justifies implementation. In addition to modeling the mass of the shaker, the torsional stiffness of the boundaries resulting from the shim stock used to approximate the simply supported boundary conditions was included in the model. The modified differential equation is presented in Appendix D, and as observed, the mass is modelled by means of a kinetic energy term and the torsional

springs are included with a potential energy term. Burdisso and Fuller (1991) formulated a similar model for the simply supported beam to account for the mass loading of the shaker and the torsional spring boundary conditions imposed by the thin shim spring stock. The appropriate spring stiffness is 3.0 N/rad computed by Burdisso and Fuller (1991) and verified in this work, and the mass of the shaker armature is 0.02 kg which compares well with the 0.0178 kg mass estimated by Burdisso and Fuller (1991).

A comparison of the controlled acoustic response at an excitation frequency of 400 Hz by the original modal formulation and the modified assumed modes approach is presented in Figure 6.3. In this test case, the actuators were positioned as illustrated in Figure 6.1, and the input disturbance was located at plate coordinates of (240,130) mm. Acoustic microphone sensors were chosen at the previously described field points. As indicated by the acoustic directivity pattern, a significant difference is noted in the controlled acoustic response of the plate. Upon including the mass loading of the shaker armature and the torsional spring stiffness of the support boundaries, the controlled acoustic response was observed to increase in the residual acoustic field (i.e. field points other than those chosen for error sensors). This characteristic was also observed in the experimental results which will be presented in the following section. The previous case was presented simply to emphasize the dramatic effect that relatively small unmodelled dynamics can have on the controlled acoustic response. By no means is the model assumed to be perfect at this point. Certainly wave conversion occurs at the boundaries of the structure where traveling extensional waves couple with flexural waves. In addition, while the dynamic model of the piezoelectric actuator was determined appropriate for studies

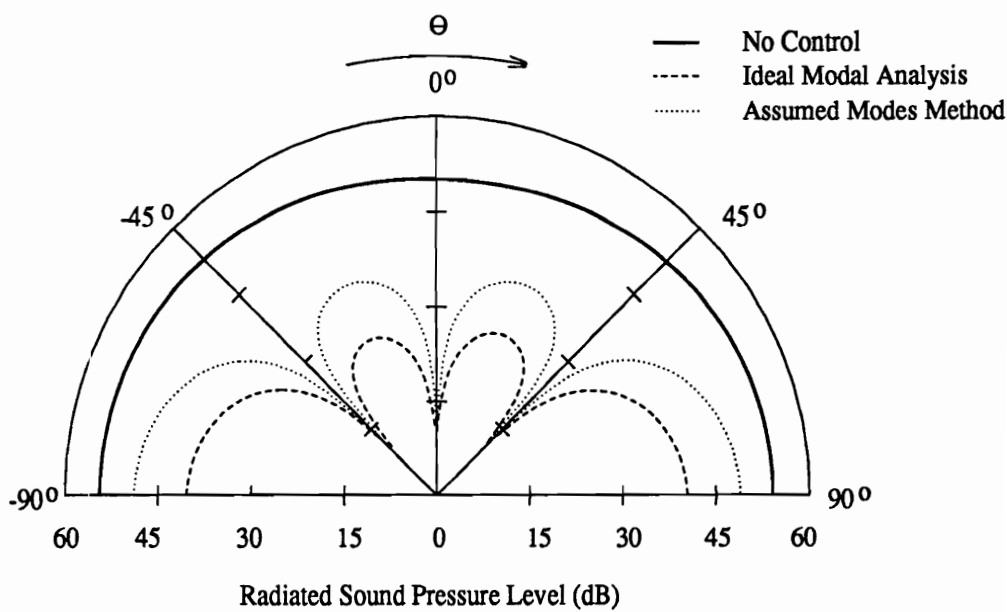


Figure 6.3: Comparison of Acoustic Directivity Pattern as a Function of Mass Loading

of this type (Fleming 1990, Clark *et al.*, 1991(a,b)), the accuracy for computing the modal response of the structure was measured at at $\pm 5\%$ for the dominant structural modes and less for the residual modes.

By implementing the assumed modes method in computing the structural response of the plate, sufficient accuracy is achieved with the analytical model for investigating different sensor designs in active structural acoustic control, which is the thrust of this work. Thus for the remainder of the theoretical test cases presented in this work, a finite dynamic range of 40 dB will be imposed, and the modal response of the structure will include the mass loading of the shaker as well as the torsional stiffness at the boundaries. In addition, all theoretical acoustic directivity patterns presented in this work are computed at a radius of 1.6 m which corresponds to the radius of the traverse used to measure the directivity pattern. This radius does not satisfy the far-field conditions outlined earlier for the frequency range of interest, and hence all computed directivity patterns are obtained from numerical integration of Rayleigh's integral to provide the best possible basis for comparison.

6.2 Microphone Error Sensors

Microphones were initially implemented as error sensors in the control approach to provide a foundation for this work. As previously discussed, these sensors were used to study the physical limitations of the control approach and to identify errors in the analytical model. Control results obtained while implementing these error sensors provide a basis for comparison since the goal is to control the radiated sound. In addition, results from control experiments conducted while implementing

microphone error sensors were studied to determine the appropriate method of interpreting the results and conveying the physical mechanisms of control. Two such test cases which encompass the physical mechanisms of structural acoustic control are presented. The first test case corresponds to on-resonance excitation near the (3,1) mode of the plate at an excitation frequency of 349 Hz. The second test case corresponds to off-resonance excitation at an excitation frequency of 400 Hz.

6.2.1 On-Resonance Response (349 Hz)

For the on-resonance case, the measured acoustic directivity pattern of the baffled simply supported plate is presented in Figure 6.4. Up to three control channels were implemented while the number of error sensors were maintained at three for the duration of the test. In this study, the number of control channels will always pertain to the number of control outputs implemented. Since the objective was to minimize the radiated sound globally, the maximum number of acoustic error sensors, three, were implemented for each control case. For this particular test, the input disturbance, which was created with the shaker, was located at spatial coordinates of (240,130) mm on the plate and the piezoelectric actuators were positioned as discussed in the previous section and as illustrated in Figure 6.1. In the legend of Figure 6.4, C# indicates the control actuator used and the numbers -45, 0, and 45 are used to indicate the angle, θ in units of degrees, about the midplane of the plate where each microphone error sensor was positioned. Rather than confuse the figure with directions for both θ and ϕ , a negative sign was used to designate the direction corresponding to $\phi = 180^\circ$.

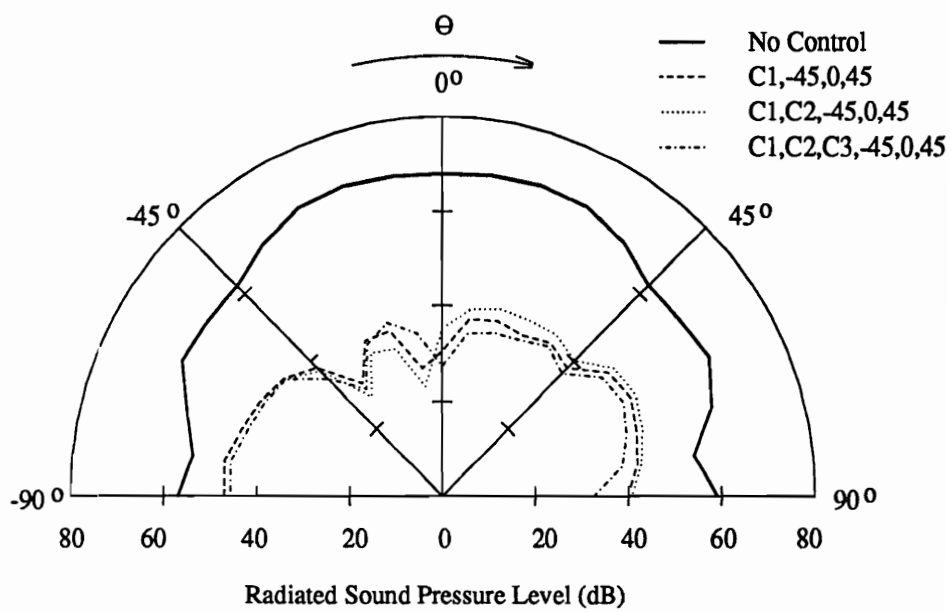


Figure 6.4: Measured Acoustic Directivity Pattern of Plate (349 Hz)

As indicated by the acoustic directivity pattern of Figure 6.4, little if any improvement in sound attenuation was obtained for the on-resonance response of the simply supported plate upon increasing the number of control inputs. Even at the positions of the error microphones, an increase in attenuation of only 1 dB was observed with increasing number of control inputs. As much as 40 dB of sound attenuation was noted in the region between -45° and $+45^\circ$, while the average level of sound attenuation was on the order of 30 dB.

For comparison, the predicted uncontrolled and controlled acoustic response of the structure is presented in Figure 6.5. As discussed earlier, the assumed modes method was used to predict both the structural and acoustic response of the plate. The input force used to predict the response was obtained by measuring the magnitude of the force input to the plate with the force transducer discussed in chapter 5. The single channel control results correspond quite well with those measured in the anechoic chamber. However, greater deviation between theory and experiment is noted with increasing number of control channels. Details noted in the directivity pattern for the two and three channel control cases were not observed in the measured response presented in Figure 6.3. In addition, the “notches” typically expected at the field points chosen for the microphones are not apparent since the level of attenuation was limited to 40 dB as discussed earlier. In theory, the structural and acoustic response of the structure can be driven to nearly zero for on-resonance applications. While general levels of sound attenuation are acceptable, the noted differences observed in the multi-channel control case are proposed due to a number of nonlinearities.

As noted previously the accuracy of the model for predicting the modal response of

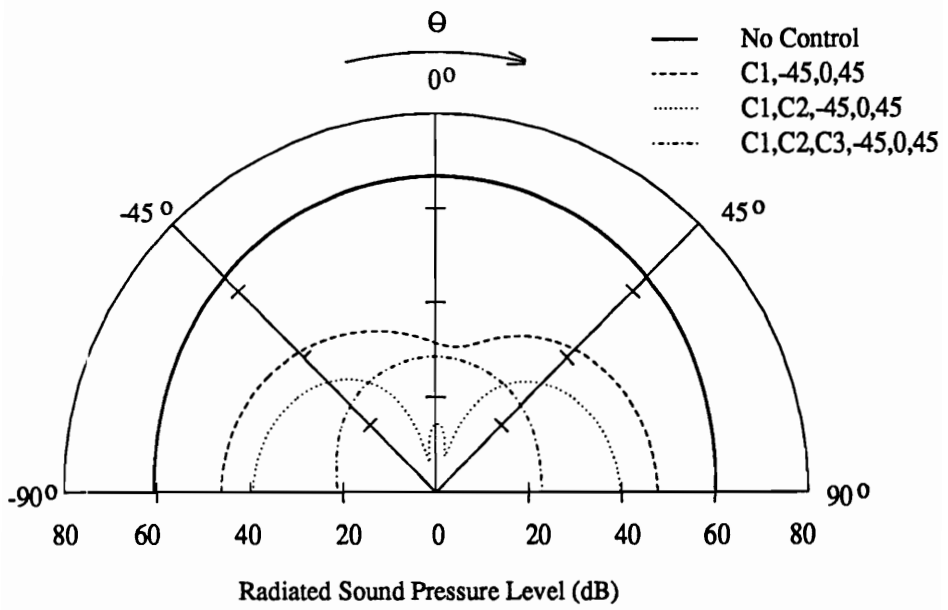


Figure 6.5: Predicted Acoustic Directivity Pattern (349 Hz)

the structure based upon excitation with piezoelectric control actuators decreases with increasing number of piezoelectric control actuators implemented (Fleming, 1990 and Clark *et al.*, 1991(a,b)). In essence, if only $\pm 5\%$ error is associated with a single control actuator, this error compounds as the number of control actuators increases. In addition, slight errors in the position of the traversing microphone can result in deviations in the directivity patterns. Any asymmetry in the plate as well as nonlinearities introduced by the boundary conditions contribute to the noted deviation. Finally the baffle is of finite dimensions which is in contrast to the assumed infinite extent required to develop the analytical model for the acoustic response of the structure. These noted discrepancies are not outlined to discredit the work presented, but merely to explain deviations observed in the details of the acoustic directivity patterns when comparing theory and experiment. In general, the overall levels predicted for the acoustic response are in agreement with that measured in the anechoic chamber.

As outlined in Appendix C, the modal response of the plate was decomposed into the eigenfunctions of the simply supported plate. While the closed-loop eigenfunctions of the structure are in general different than the open-loop eigenfunctions as previously demonstrated by Burdisso and Fuller (1991), the modal response was represented in terms of the uncontrolled modes of the structure such that the response before and after control could be compared. Considering the experimental modal distribution presented in Figure 6.6, one readily observes that the mechanism of control involves *modal suppression*. Modal suppression was previously defined by Fuller *et al.*, (1989(b)) and involves the uniform reduction of all modal amplitudes (i.e. the total plate response is attenuated). However the dominant (3,1) mode was

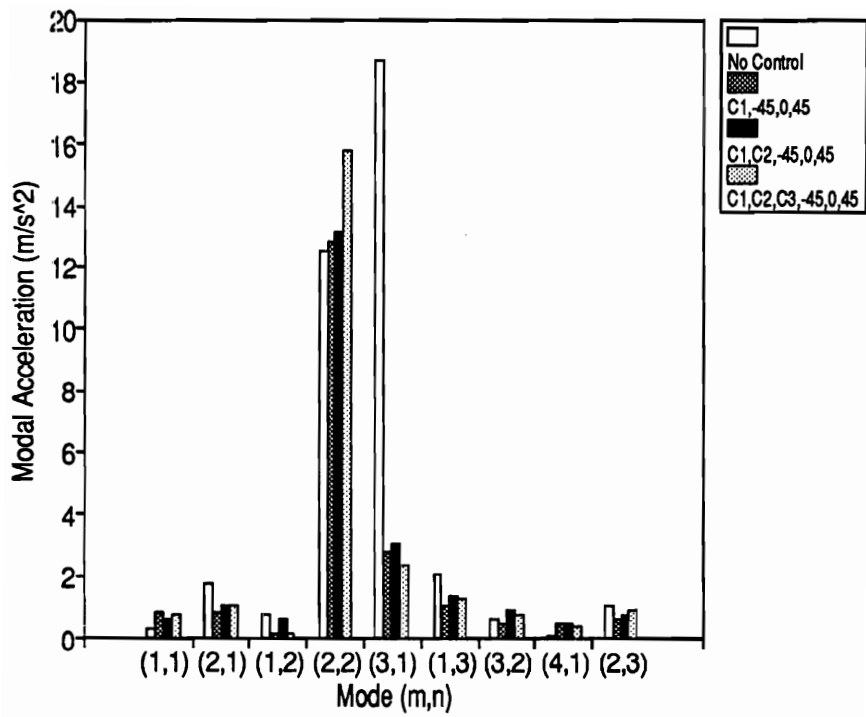


Figure 6.6: Measured Modal Response of Plate (349 Hz)

reduced by approximately 15 dB, which does not account for the 30 dB of global sound reduction. Upon further inspection, one observes that the response of the (1,1) mode increased a small amount and is approximately 10 times less than that of the (3,1) mode. Since the radiation efficiency of this mode is approximately 10 times that of the (3,1) mode as indicated in Figure 1.1 at the frequency of operation, one concludes that the remaining attenuation in the sound field resulted from *modal restructuring*. In modal restructuring, the amplitudes of modes can increase; however, phasing between modes is such that destructive interference occurs in the acoustic field. For the case presented, this corresponds to the (3,1) mode and (1,1) mode being 180° out of phase with each other when control is applied. The slight increase in the (2,2) mode is of little significance since its radiation efficiency is several orders of magnitude below that of the (3,1) mode as illustrated in Figure 1.1. Thus upon achieving control, the overall radiation efficiency of the plate is reduced.

While this method of analyzing the structural response is relatively simple for on-resonance test cases, interpretation is complicated when studying off-resonance response. To alleviate this problem, the wavenumber transform was computed from the decomposed modal response to convey the mechanisms of structural acoustic control. The wavenumber transform of the modal response presented in Figure 6.6 is illustrated in Figure 6.7. Only a finite number of modes were obtained from the modal decomposition due to limitations imposed by the number of accelerometers used in the array to measure the structural response of the plate. Hence, the wavenumber transform is based simply on those modes resolved from the experimental modal decomposition. For the frequency range of excitation in this study, the number of modes included in the modal decomposition is sufficient to obtain an

accurate description of the structural response.

As indicated, a uniform reduction in both the supersonic and subsonic regions occurred, which supports the conclusion that the primary mechanism of control was modal suppression. Note that the supersonic region lies between $k = -6.5$ and $k = 6.5$ in Figure 6.7. In reality, the wavenumber transform is computed in two dimensions; however, for visual clarity only one axis is presented in this work, corresponding to the axis of the traversing microphone used to measure the acoustic directivity pattern. One can readily determine the mechanism of control by studying the change in the supersonic region of the wavenumber transform since this region corresponds to the radiated sound to the acoustic far-field. Also note that the peaks in the subsonic region of the wavenumber transform correspond to a structural wavenumber of approximately 24, which agrees well with the predicted structural wavenumber of the (3,1) mode (i.e. $k_x = m\pi/L_x = 24.8$).

6.2.2 Off-Resonance Response (400 Hz)

The simply supported plate was driven with the shaker located at the same coordinates as that of the previous test case at an excitation frequency of 400 Hz which lies between the resonant frequencies corresponding to the (3,1) and (1,3) structural modes. The acoustic directivity patterns corresponding to the measured uncontrolled and controlled response are presented in Figure 6.8. In contrast to the previous test case, the level of acoustic attenuation increased markedly with increasing numbers of control inputs. While sound attenuation on the order of 5 dB was noted with the single control actuator test case, approximately 20 dB of global

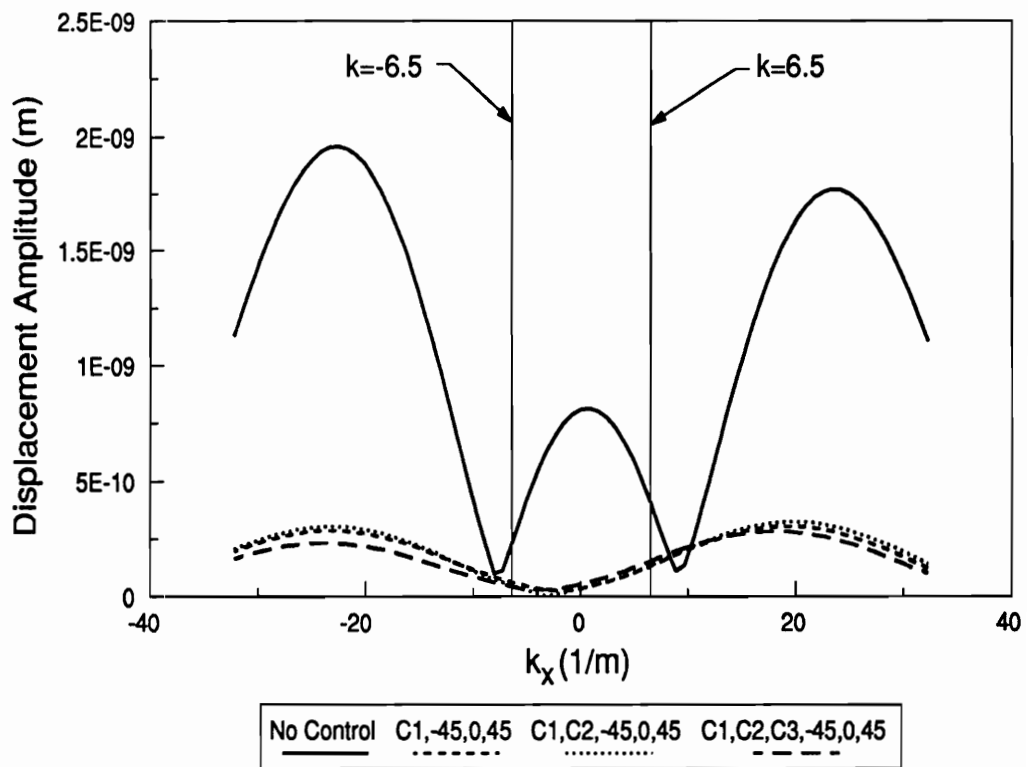


Figure 6.7: Wavenumber Transform of Measured Modal Response (349 Hz)

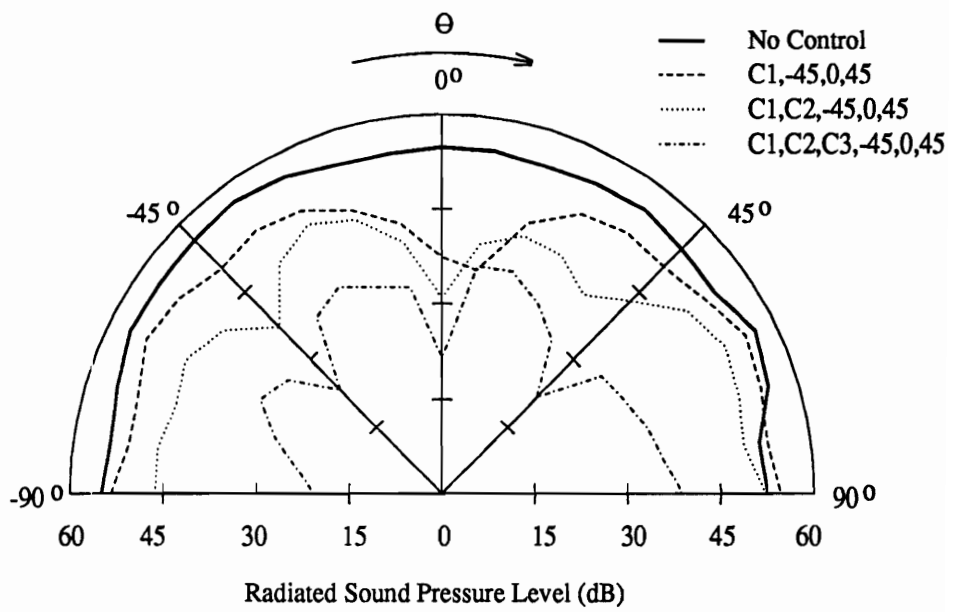


Figure 6.8: Measured Acoustic Directivity Pattern of Plate (400 Hz)

sound reduction was observed when implementing three control actuators.

The corresponding predicted acoustic directivity patterns for the multi-channel control cases are presented in Figure 6.9 for comparison. As in the on-resonance test case, the measured and predicted directivity patterns for the single input control case are very similar both in magnitude and shape. Some characteristics of the directivity pattern are lost as the number of control inputs increases; however, general levels of acoustic attenuation compare well. The deviation in the measured and predicted acoustic response noted near the boundaries of the baffle are proposed due to the finite dimension of the baffle used in the physical system. The obvious “notches” created at the spatial field points of the microphones are predicted and measured as indicated in Figure 6.8 and Figure 6.9 for the three input control case. In this case, since the number of inputs equals the number of outputs, the structural response can be arranged such that the response is driven to zero at the accuracy of the signal processing board. This result is not apparent when the number of control inputs is less than the number of error sensors since the system is under determined. Based upon this observation, in typical operating conditions it may be advantageous to have more error sensors than control actuators to reduce the level of control spillover into the residual acoustic field. Driving the response at the error sensors to zero can lead to spillover as illustrated in Figure 6.2. Thus the increased level of acoustic attenuation at the chosen error microphones can be detrimental to the levels of attenuation obtained in the residual acoustic field.

Considering the modal decomposition of the response of the structure presented in Figure 6.10, one quickly recognizes that the primary mechanism in achieving control

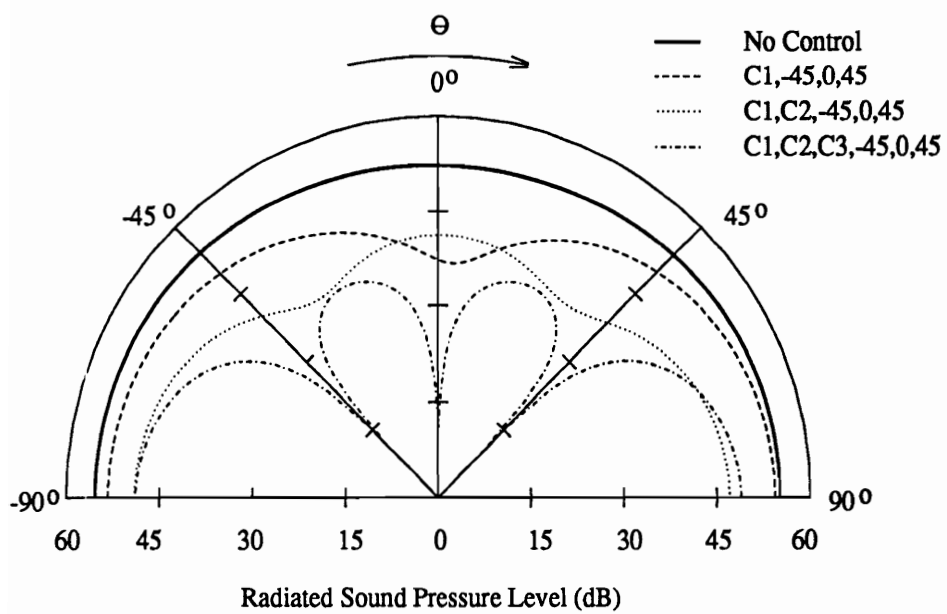


Figure 6.9: Predicted Acoustic Directivity Pattern (400 Hz)

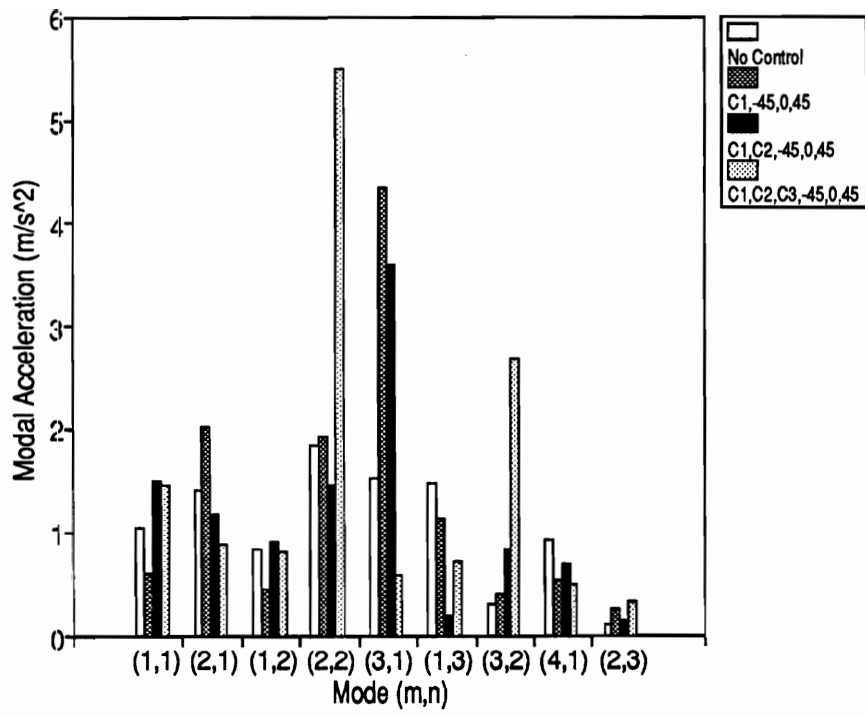


Figure 6.10: Measured Modal Response of Plate (400 Hz)

is modal restructuring. The modal response and hence the total vibration response of the plate increases as sound reduction is achieved in the acoustic field. Thus the overall radiation efficiency of the controlled structure decreases through destructive interference in the acoustic field.

The physical mechanisms of control are more readily conveyed in the wavenumber transform presented in Figure 6.11. As shown in Figure 6.11, the response in the supersonic region of the wavenumber transform decreases significantly under control conditions. The supersonic region is defined between $k = -7.4$ and $k = 7.4$ for the frequency range of interest as indicated in Figure 6.11. The response in the subsonic region is observed to increase to a level beyond that of the uncontrolled case; however, this is of little concern since the subsonic components do not radiate. As previously outlined, this is characteristic of modal restructuring and is thus the method of achieving a lower radiation efficiency of the structure. Sound reduction has been achieved while the plate response has increased! One should note that modal restructuring tends to occur in off-resonance acoustic control applications since the modal density is richer, resulting in greater opportunity for interactions between structural modes.

6.3 Polyvinylidene Fluoride Error Sensors

A variety of sensing techniques, both structural and acoustic were evaluated with specially design PVDF sensors. Rectangular structural sensors as well as shaped structural sensors were tested to determine the most appropriate method of implementation. In addition, acoustic near-field sensors were designed from the material

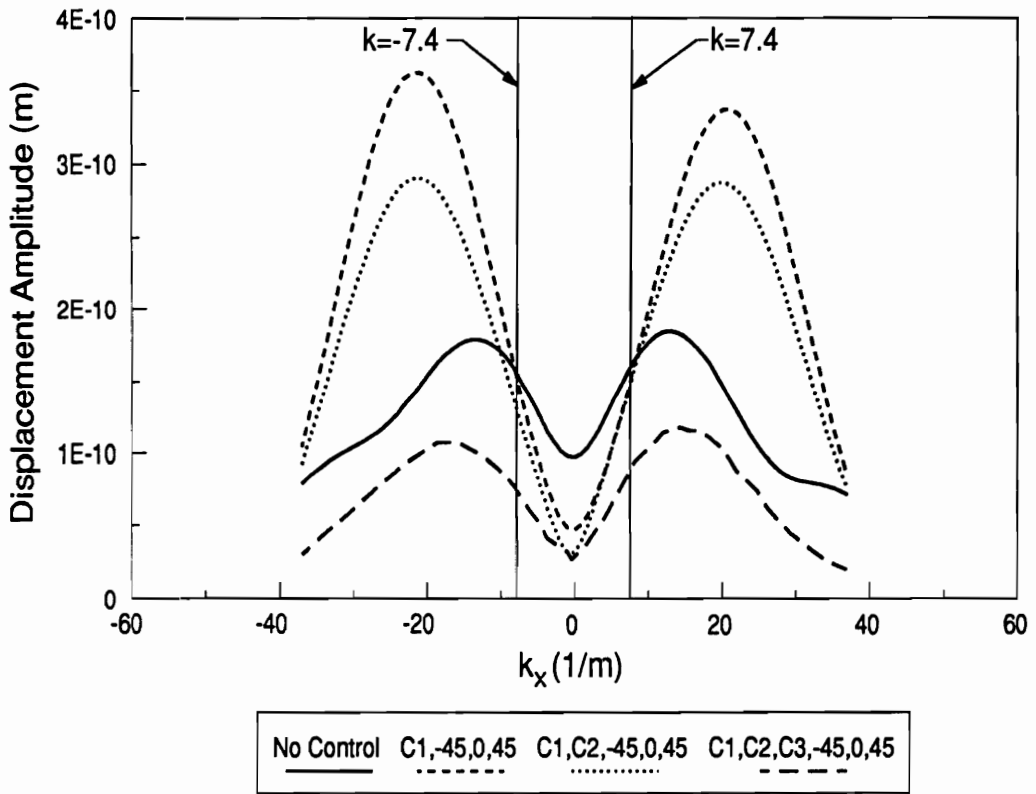


Figure 6.11: Wavenumber Transform of Measured Modal Response (400 Hz)

and implemented in the control approach. Results from each of these unique sensing techniques as applied to active structural acoustic control are discussed in the following sections.

6.3.1 Rectangular Strip PVDF Sensors

Initial studies were performed implementing two piezoelectric control actuators and two rectangular strips of PVDF as structural error sensors as discussed in section 4.1 and presented in Figure 4.1. (The number of control actuators must always be less than or equal to the number of error sensors to assure that the feed forward LMS algorithm converges to a minimum.) These sensors were the initial prototypes for achieving wavenumber filters for active structural acoustic control. Only two PVDF sensors were required to perform the desired filtering in the x and y-direction of the structure to provide an estimate of the structural acoustic response of the more efficient radiating modes. The details of the design are outlined in section 4.1. This prototype sensor design was based upon the observation that the radiation efficiency of modes with odd modal indices is greater than that of modes with even modal indices for low k/k_s . Hence these sensors were implemented such that the response of modes for which both modal indices were even would not be observed. While each of these sensors selectively filters even modes in their respective direction (i.e. (even,*) modes in the x-direction and (*,even) modes in the y-direction), a true two dimensional sensor would be required to eliminate the response of all modes with an even modal indice. However, due to the radiation efficiency of some (*,even) modes and (even,*) modes, this is not necessarily desirable.

Two test cases are presented for this preliminary study, both on and off-resonance. In each test case, two PVDF error sensors were implemented in the cost function and thus two piezoelectric control actuators were utilized to achieve control. As illustrated in Figure 4.1, the actuators are positioned on the structure with respect to nodal lines of modes with odd modal indices to increase control authority over these modes. Since the objective is to yield a controlled acoustic response similar to that obtained with microphone error sensors, results from control experiments implementing the PVDF sensors are compared to those implementing microphone error sensors at the previously discussed acoustic field points. The wavenumber transform of the experimentally obtained modal response was then compared to convey the physical mechanisms of control.

6.3.1.1 On-Resonance Response (349 Hz)

The plate was driven slightly below resonance for the (3,1) mode in the first test case at an excitation frequency of 349 Hz. This excitation frequency was chosen since it is nearly impossible to determine the exact resonant frequency of the (3,1) mode, coupled with the fact that a 180° phase change occurs on resonance and can lead to control instability if the response flips back and forth through this phase change. The predicted acoustic directivity pattern for the given sensor design implementation and frequency of excitation is presented in Figure 6.12. While exact details of the directivity pattern do not correspond to those of the measured response in Figure 6.13, general levels of predicted sound attenuation match within ± 3 dB. Approximately 20 dB of sound attenuation was predicted and measured when implementing the PVDF error sensors. The level of attenuation was predicted

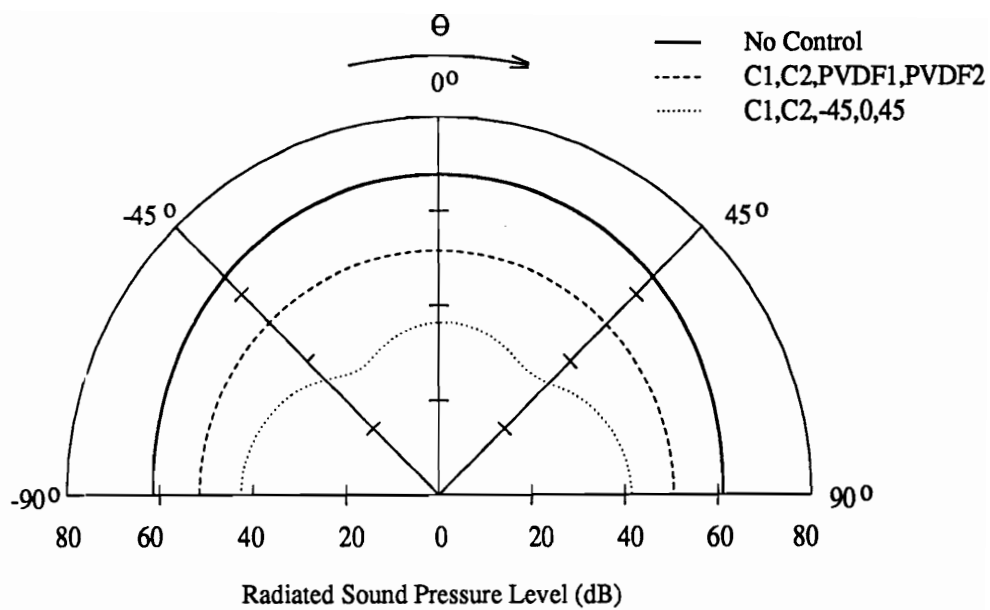


Figure 6.12: Predicted Acoustic Directivity Pattern of Plate (349 Hz)

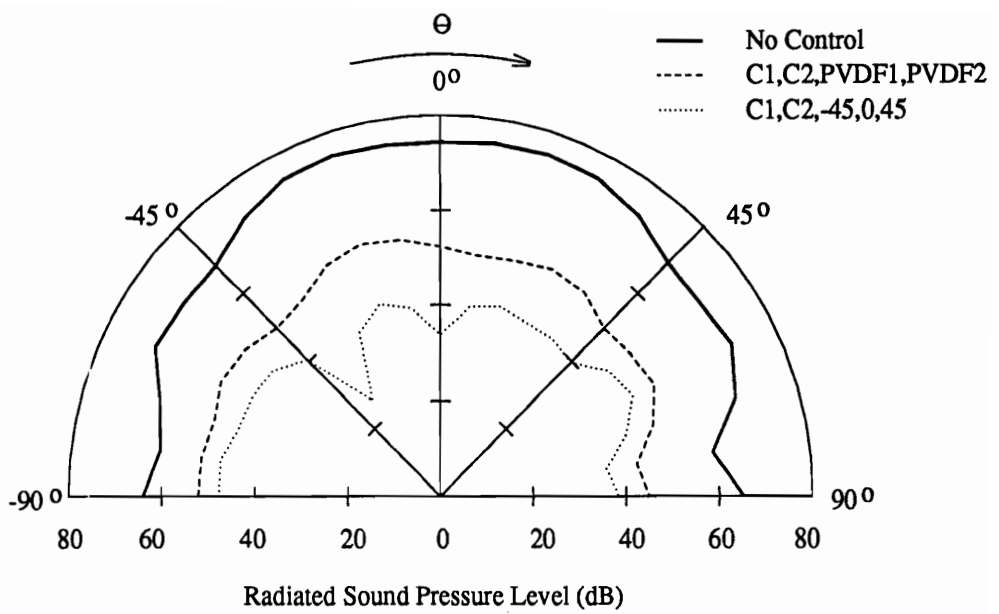


Figure 6.13: Measured Acoustic Directivity Pattern of Plate (349 Hz)

to improve by roughly 10 dB when implementing the microphone error sensors. This improved level of acoustic attenuation was also measured as evident in the measured directivity pattern of Figure 6.13. General trends from these directivity patterns compare well and suggest that the analytical model can be used to design PVDF structural sensors for active structural acoustic control applications.

As illustrated by the acoustic response presented in Figure 6.13, sound attenuation on the order of 20 dB was obtained when implementing the PVDF structural error sensors. In the legend of the figure, “C#” indicates the piezoelectric actuator used in the control implementation and “PVDF#” indicates the chosen PVDF error sensor. Each of the numbered elements is depicted in the plate schematic of Figure 4.1. Results from the modal decomposition given in Figure 6.14 indicate that control was achieved by modal suppression of the dominant (3,1) mode with an increase in the response of the (1,1), (2,2) and (4,1) structural modes. The control spillover into the (2,2) mode has little effect on the structural acoustic response due to the low radiation efficiency of this mode at $k/k_s = 0.24$; however, the small increase in response of the (1,1) mode limits the level of sound attenuation since the radiation efficiency of this mode is approximately 10 times greater than that of the (3,1) mode.

When implementing the microphone error sensors located at $+45^\circ$, 0° and -45° in conjunction with the same piezoelectric control actuators, the level of acoustic attenuation improved by approximately 10 dB as indicated in Figure 6.13. Thus the residual acoustic response of the structure was observed to decrease by approximately 30 dB upon applying control as indicated in Figure 6.13. While the general shape of the directivity patterns resulting from control with either microphone er-

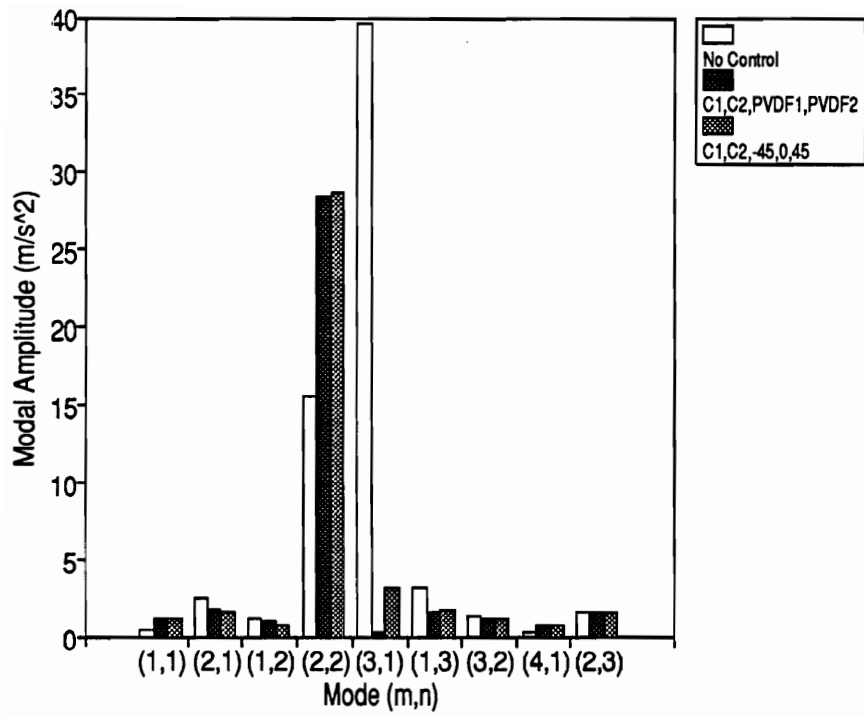


Figure 6.14: Measured Modal Response of Plate (349 Hz)

ror sensors or PVDF error sensors is similar, greater levels of acoustic attenuation resulted when implementing the microphone error sensors. Referring to the modal response presented in Figure 6.14, control was achieved in this case by two mechanisms. First of all, the dominant (3,1) mode, which is an efficient acoustic radiator, was reduced (modal suppression). However some increase in the amplitude of the (2,2) mode was observed. As discussed earlier, this spillover into the (2,2) mode has little effect on the level of sound radiation since the radiation efficiency of this mode is approximately 15 times less than that of the (3,1) mode for $k/k_s = 0.25$ as can be seen in Figure 1.1. Upon comparing the structural modal response when applying control with the PVDF error sensors to that when applying control with the microphone error sensors, one observes that the controlled modal amplitudes are nearly identical with the exception of the (3,1) mode. Less attenuation of the (3,1) mode occurred when using the microphone error sensors. Upon achieving control, the (3,1) mode was reduced; however, upon reaching a level where the sound radiation from the (1,1) mode and (3,1) mode were comparable, the phase relationship between the modes was restructured such that the (3,1) mode and (1,1) mode were out of phase with each other, explaining the increased level of attenuation observed when implementing the microphone error sensors.

Considering the wavenumber transform of the structural response presented in Figure 6.15, the modal suppression and restructuring mechanisms are evident. The acoustic wavenumber for the frequency of excitation is 6.5 as illustrated in Figure 6.15, defining the supersonic and subsonic regions. The response in the supersonic region of the wavenumber transform was significantly reduced when using either PVDF or microphone error sensors; however, a greater level of attenuation was ob-

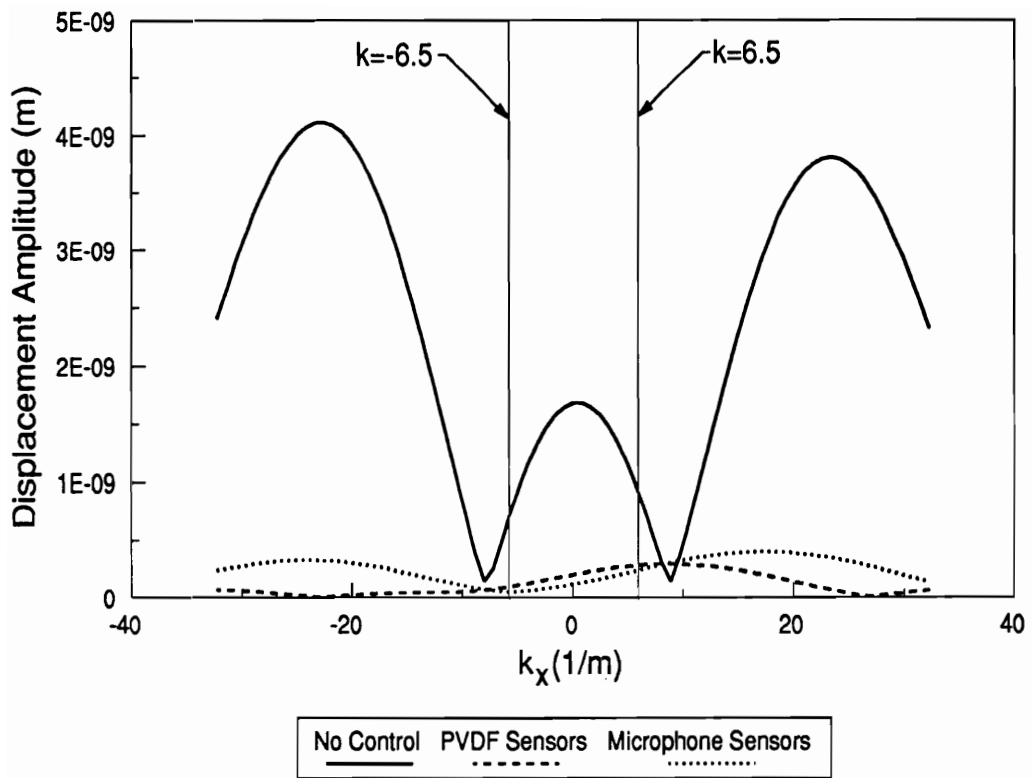


Figure 6.15: Wavenumber Transform of Measured Modal Response (349 Hz)

served when implementing the microphone error sensors. In the subsonic region, the amplitudes of the spectrum are greater when applying control with the microphone error sensors than that observed when applying control with the PVDF error sensors. Recalling the results presented in Figure 6.13, greater levels of sound attenuation were observed when implementing the microphone error sensors. This illustrates that the modal restructuring required to achieve greater levels of sound attenuation with microphone error sensors serves to increase spillover into the subsonic region of the wavenumber spectrum in comparison to that resulting from control with PVDF error sensors. This spillover can be attributed to the differences noted in the modal response of the (3,1) mode corresponding to the two control cases. Thus while less sound attenuation was achieved when implementing the PVDF error sensors, the level of control spillover was reduced, which could be an important issue if the vibration response of the structure is also a point of concern.

6.3.1.2 Off-Resonance Response (320 Hz)

The second test case was conducted off-resonance at a driving frequency of 320 Hz, which lies between resonant frequencies corresponding to the (1,2) and (2,2) modes of the structure. The same control actuators and error sensors implemented in the on-resonance case were used to achieve control in the off-resonance test case. Before conducting the experiments, the sensor design was evaluated with the analytical model and results illustrating the controlled acoustic response are presented in the directivity patterns of Figure 6.16. As indicated, approximately 10 dB of sound attenuation was predicted when implementing the PVDF structural error sensors. The general shape of the directivity pattern corresponds well with that measured

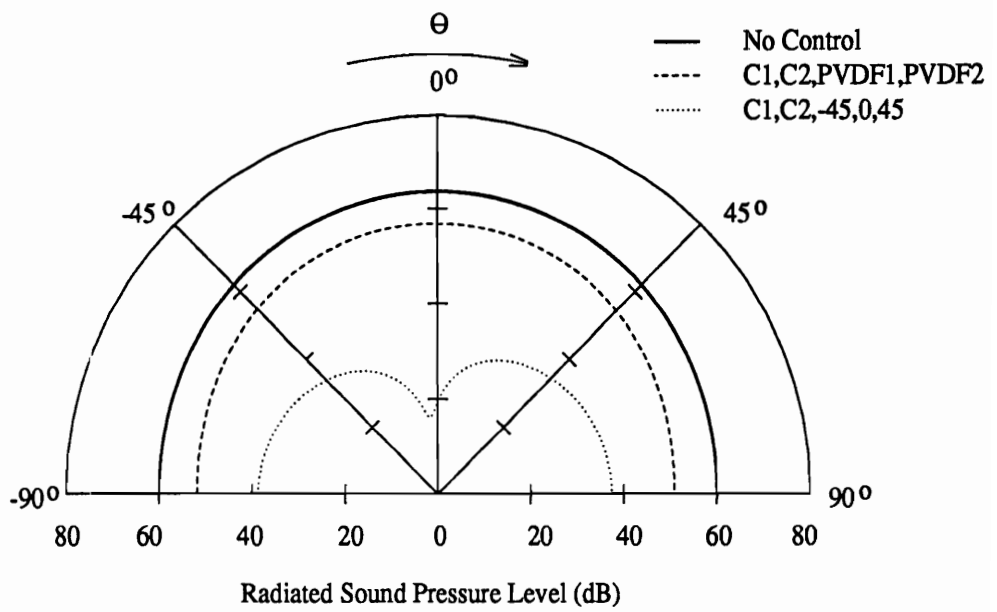


Figure 6.16: Predicted Acoustic Directivity Pattern of Plate (320 Hz)

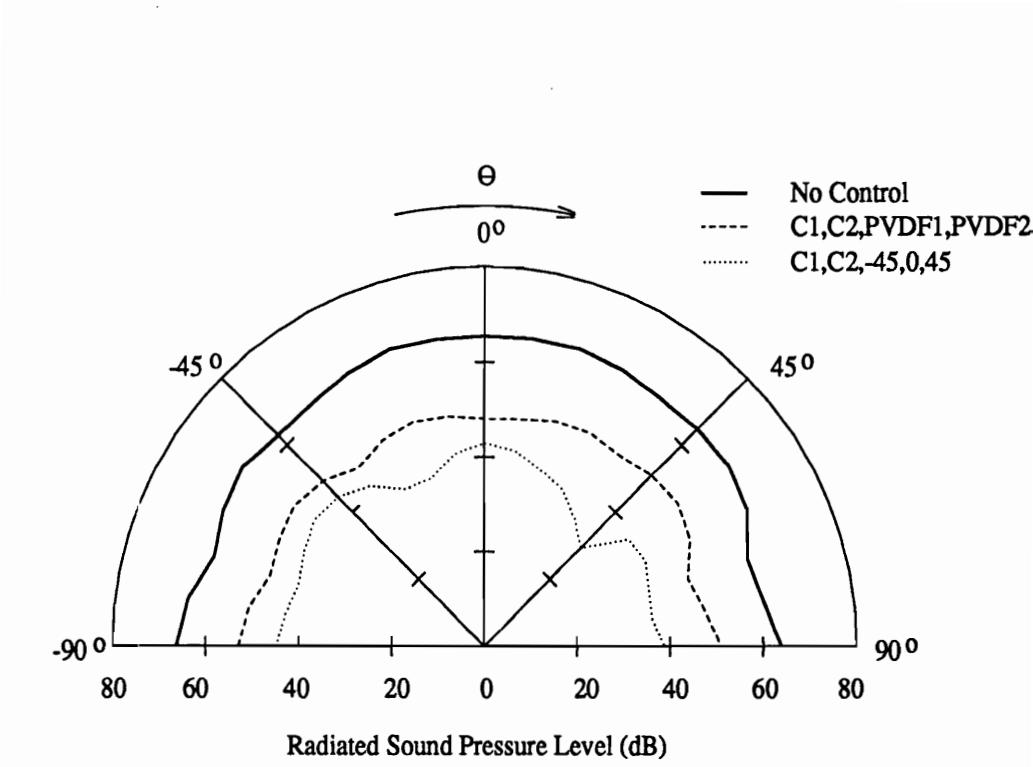


Figure 6.17: Measured Acoustic Directivity Pattern of Plate (320 Hz)

in Figure 6.17, while the level of acoustic attenuation achieved on the structure was approximately 15 dB, slightly greater than that predicted. This difference in predicted and measured response could be due to nonlinearities in the structural response, inaccuracies in predicting the actual mass loading of the plate and torsional springs at the boundaries or any of the other reasons previously stated to address this problem. In any event, correspondence between theory and experiment was accurate enough for choosing the given design.

As indicated in Figure 6.17, approximately 15 dB of global sound attenuation was obtained after minimizing the response of the PVDF distributed sensors. The modal structural response of the plate given in Figure 6.18 was observed to decrease at every mode under control conditions, with the exception of the (1,2), (1,3) and (4,1) modes. Of these three modes, the (1,2) mode is of primary concern since the modal amplitude after control is of a comparable level with that of the (3,1) mode before control. Fortunately, the radiation efficiency of the (3,1) mode is approximately 3 times greater than that of the (1,2) mode for $k/k_s = 0.22$, hence the spillover into the (1,2) mode does not prevent attenuation of the radiated sound.

For comparison, microphones positioned at $+45^\circ$, 0° and -45° were again utilized as error sensors, and two channels of control were implemented. As can be seen in Figure 6.17, levels of sound attenuation on the order of 20 dB resulted. It is apparent from Figure 6.18 that in the case implementing microphone error sensors, control was achieved through modal suppression of the (3,1) and (1,1) mode as well as modal restructuring between these modes. As demonstrated in the on-resonance test case presented in Figure 6.13, the (3,1) mode and (1,1) mode were phased for

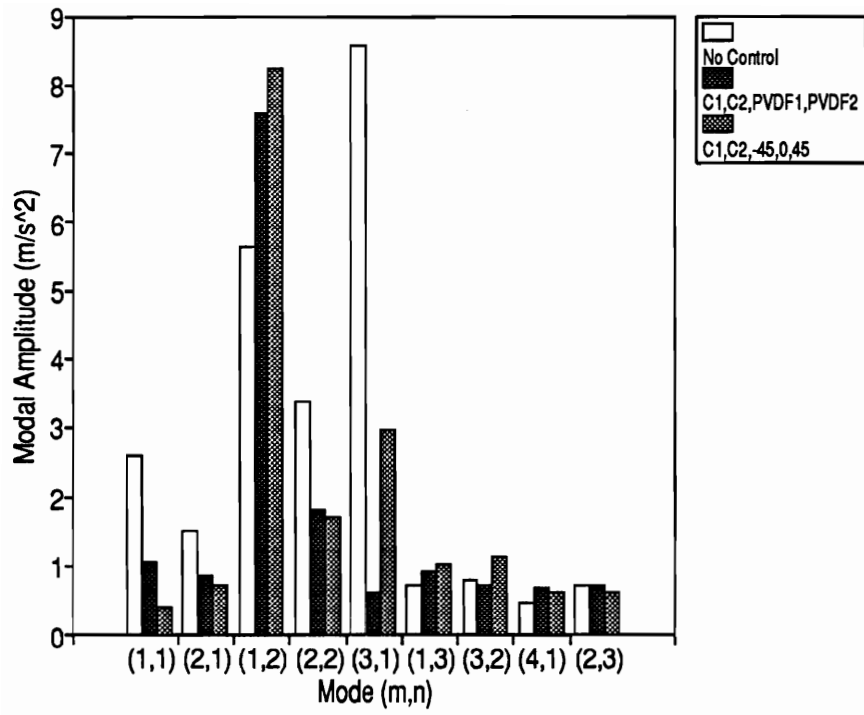


Figure 6.18: Measured Modal Response of Plate (320 Hz)

destructive interference upon achieving control. This again serves to explain why the amplitude of the (3,1) mode was attenuated less when implementing the microphone error sensors than when implementing the PVDF error sensors. Since the radiation efficiency of the (1,1) mode is approximately 10 times greater than that of the (3,1) mode, the modal response of the (3,1) mode must be greater than that of the (1,1) mode for destructive interference to occur (with the appropriate phase relationship). The residual plate response thus had a lower overall radiation efficiency upon achieving control with the microphone error sensors. This lower overall radiation efficiency is achieved primarily through modal suppression of the dominant acoustic radiating modes and lower order modal restructuring between these modes.

The wavenumber transform of the modal structural response presented in Figure 6.18 is depicted in Figure 6.19. With an excitation frequency of 320 Hz, the corresponding acoustic wavenumber is 5.9. The amplitudes of the wavenumber transform were significantly decreased as illustrated in Figure 6.19, and the method of control is again predominantly described by modal suppression whether PVDF or microphone error sensors were implemented in the control approach. This result was also observed in Figure 6.18 with the exception of an increase in the amplitude of the (1,2) mode of the structure, resulting from control spillover. As indicated in Figure 6.19, whether PVDF or microphone error sensors were implemented in the control approach, the amplitude of the wavenumber spectrum in the supersonic region as well as the subsonic region decreased. However, when implementing the microphone error sensors, the amplitude of the wavenumber spectrum was significantly less in the supersonic region than in the subsonic region compared to the controlled re-

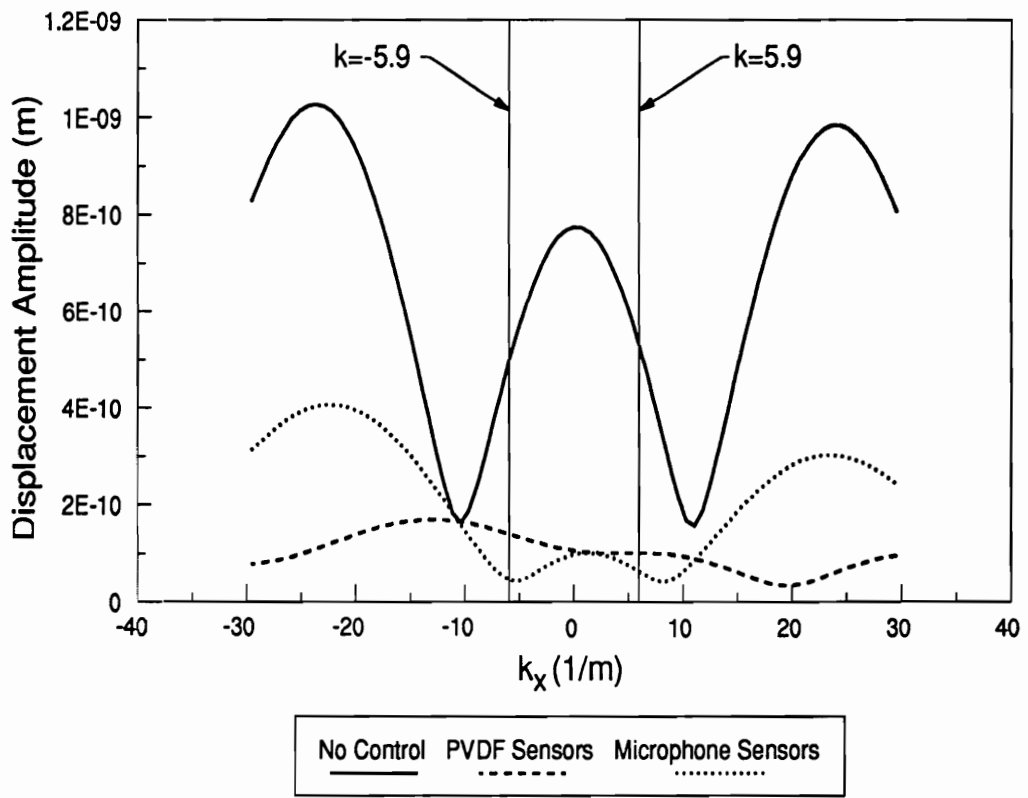


Figure 6.19: Wavenumber Transform of Measured Modal Response (320 Hz)

sponse when utilizing the PVDF error sensors.

The greater levels of attenuation in sound radiation can thus be attributed to the spillover into the subsonic region of the wavenumber spectrum. The structural wavenumber of the (3,1) mode is 27, which is approximately the location of the two maxima corresponding to the controlled response when implementing the microphone error sensors. As indicated in Figure 6.18 the controlled response when implementing microphone error sensors resulted in less attenuation of the (3,1) mode than that resulting from applying control with the PVDF error sensors. The phasing between the (3,1) mode and (1,1) mode serves to further reduce the response in the supersonic region at the expense of less attenuation in the subsonic region. Thus as observed in the on-resonance test case, the PVDF error sensors result in less control spillover in the subsonic region of the wavenumber transform, which may be an advantage of these sensors in cases where structural spillover is a problem.

6.3.1.3 Summary of Rectangular Strip PVDF Sensors

While significant levels of sound attenuation were obtained when implementing the PVDF error sensors for both on and off-resonance test cases, greater levels of sound attenuation were observed when implementing the microphone error sensors. This results from the fundamental differences in the two sensors. The PVDF error sensors weight each structural mode as a function of their shape and position on the structure (i.e. spatial window created by the sensors as illustrated in Figure 4.2 and Figure 4.3) and as a function of the modal indices since the response is proportional to the integral of strain over the surface of application as evident in equation (4.2).

Hence, the sensor becomes increasingly responsive to higher order modes; however, the response of these modes at low frequencies of excitation are filtered due to the frequency response characteristics of the structure. When the controlled modal amplitudes of the dominant lower order modes (for structural acoustic control) are of comparable levels with the higher order modes, the PVDF sensor “shifts interest” to these higher order modes. This explains why the amplitude of the (3,1) mode was always reduced to a level comparable to that of the (1,1) mode. The (3,1) mode is weighted approximately three times greater than that of the (1,1) mode since the sensor yields an electrical response proportional to the integral of strain over the surface of application.

In contrast, the microphone error sensors obviously include the structural acoustic transfer function and hence are ideal error sensors for this application. The radiation efficiency of each mode is automatically included in the cost function since the electrical response of the microphone is sensitive to the resulting sound radiated from each structural mode and not the amplitudes of the structural modes. This serves to explain why the (3,1) mode was attenuated less when implementing microphone error sensors than when implementing the PVDF error sensors. As the response of the (3,1) mode was reduced to a level where the radiation efficiency was comparable to that of the (1,1) mode, the phase relationship between the two modes was simply configured for destructive interference (i.e. out of phase). When implementing the PVDF error sensors, the (3,1) mode was observed to be out of phase with the (1,1) mode; however, the amplitude was reduced to a level where destructive interference of the acoustic response was not possible since the PVDF sensor is sensitive to the *integral* of strain over the surface of application.

6.3.2 Optimal Design of Rectangular PVDF Structural Sensors

Given the success obtained with the rectangular strip PVDF structural error sensors, the optimization routine described in section 4.2 was implemented to determine the optimal dimension and location of rectangular PVDF error sensors for given design applications. To demonstrate the feasibility of the optimal design theory, two test cases were chosen. In both cases, the structure was driven at an excitation frequency of 550 Hz. Optimal design techniques, as discussed in Chapter 4, were utilized to determine the optimal location of the piezoelectric control actuators and the optimal size and location of the PVDF structural sensors. Previous work by Wang *et al.*, (1991(b)) was devoted to optimal design procedures for single and multiple actuator control applications. Since the focus of this work concerns design and implementation of sensors in active structural acoustic control, the reader is referred to several references by Wang *et al.*, (1991(a,b)) as well as a comparison of experimental and theoretical results by Clark and Fuller (1991(e)) for more details on optimal design implementing piezoelectric control actuators. The two cases presented in this work are devoted to a single-input/single-output optimal design for the simply supported plate and a three-input/three-output optimal design.

6.3.2.1 Single-Input/Single-Output (550 Hz)

The first test case considered involved optimization of the position of a single piezoelectric control actuator and the size and position of a single PVDF structural error sensor. The optimal design approach was outlined in section 4.2 and as discussed

the objective function was formulated as an estimate of the radiated acoustic power. Hence the design optimization was conducted such that the control actuator and PVDF error sensor were optimally configured to minimize the radiated acoustic power for the harmonic input disturbance chosen. The optimal designs for both the control actuator and PVDF error sensor are presented in Figure 4.7 of section 4.2.3 and Figure 4.8 of section 4.2.4.1 respectively. The structure was driven with a shaker positioned at spatial coordinates of (240,130) mm from the lower left corner of the plate as in previous cases discussed. Control was achieved by minimizing the response of the optimal PVDF structural error sensor with a piezoelectric control actuator. As illustrated in Figure 6.20, approximately 15 dB of sound attenuation was predicted based on the analytical model for the optimal design case. Since the PVDF sensor was designed to yield a controlled acoustic response approximating that of an array of microphones placed in the acoustic field, the controlled response of the structure was predicted implementing acoustic error sensors at field points of $\theta = -45^\circ$, $\theta = -0^\circ$ and $\theta = 45^\circ$ as discussed in the previous test cases presented. As illustrated in Figure 6.20 marginal improvement in sound attenuation is predicted near the baffle (i.e. $\theta = \pm 90^\circ$); however, less attenuation is predicted normal to the plate at $\theta = 0^\circ$ when implementing the microphone error sensors.

The optimal design was implemented on the test structure and the plate was positioned in the baffle of the anechoic chamber as illustrated in Figure 5.14. Results from the controlled response of the plate implementing the optimal design coordinates for the actuator and sensor are illustrated in Figure 6.21. From the acoustic directivity pattern, one observes that the measured level of sound attenuation was close to 15 dB when implementing the optimally designed PVDF error sensor and

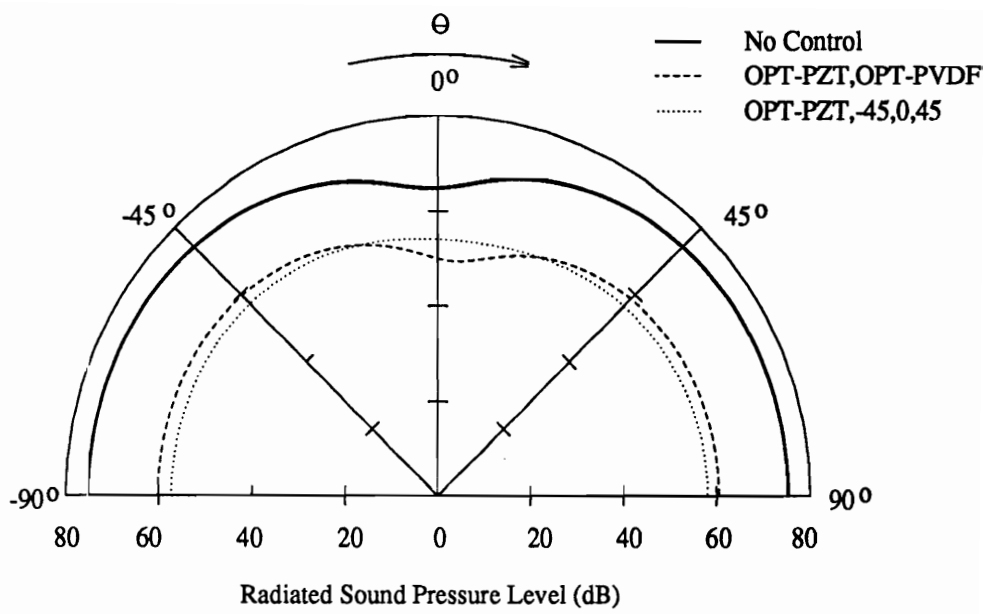


Figure 6.20: Predicted Acoustic Directivity Pattern with 1 Actuator (550 Hz)

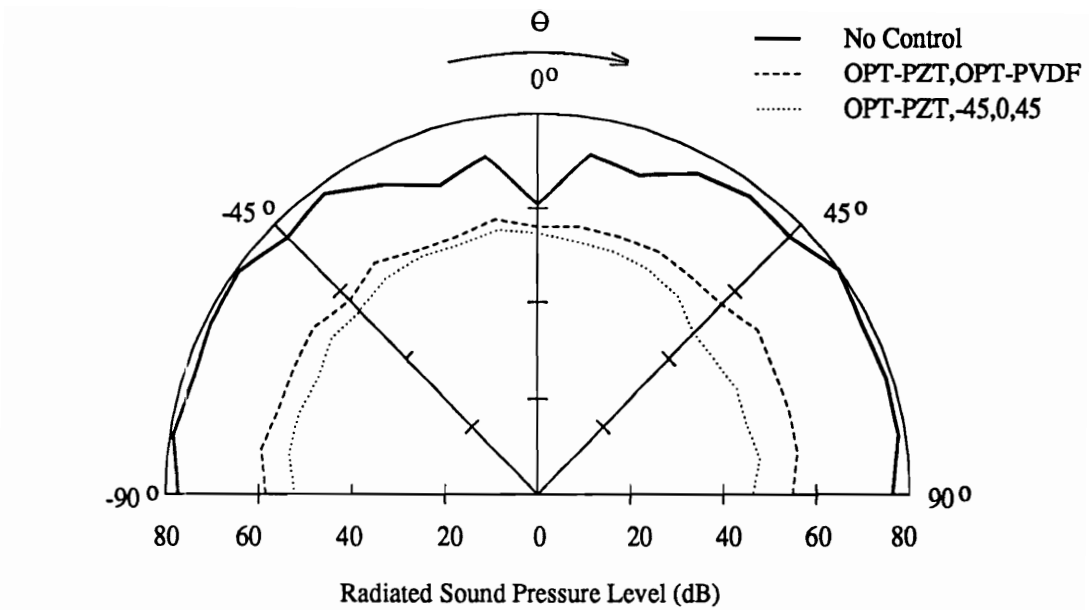


Figure 6.21: Measured Acoustic Directivity Pattern with 1 Actuator (550 Hz)

20 dB when implementing the microphone error sensors. The general shape of the directivity pattern for the uncontrolled and controlled acoustic response are in agreement as well as the predicted level of response as is apparent when comparing the results from Figure 6.20 to those of Figure 6.21. Hence the analytical models used to optimize the position of the control actuator as well as the position and dimensions of the PVDF error sensor proved successful for the single-input/single-output control case.

Further analysis of the structural response before and after control indicates that the acoustic response was attenuated primarily by modal reduction when implementing the PVDF error sensor or the microphone error sensors as is evident in Figure 6.22. The modal structural response before control was dominated by the (4,1), (1,1), (2,1), (1,2) and (2,2) modes as illustrated. The radiation efficiency of the (4,1) mode at this excitation frequency, corresponding to $k/k_s = 0.3$, is approximately one fourth that of the (1,1) mode as is the radiation efficiency of the (1,3) mode. Clearly the response of these modes must be reduced to attenuate the far-field sound radiation. Consider the modal weighting distribution for the optimal PVDF sensor which was previously presented in Figure 4.9. All of these modes are well represented in the electrical response of the sensor. Notice that the (3,2) mode is essentially unobserved by the sensor due to its location and dimension. This result is due to the poor radiation efficiency of this mode at the chosen excitation frequency. As a result, little attenuation of this structural mode was observed upon achieving control as indicated in Figure 6.22. In addition, notice that the controlled structural response when implementing the microphone error sensors is nearly identical to that when implementing the optimal PVDF error sensor. Hence the desired cost

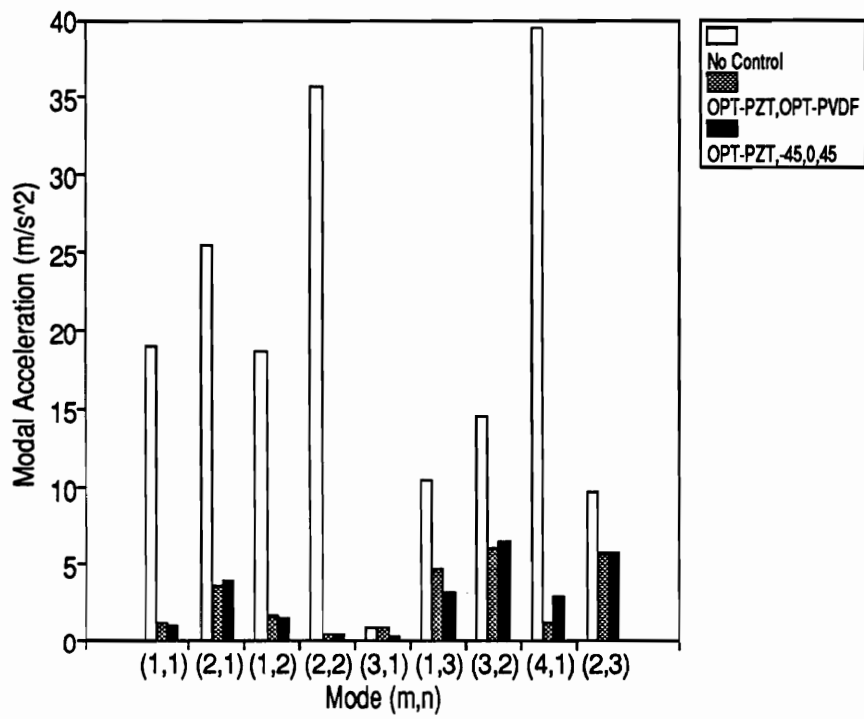


Figure 6.22: Measured Modal Response of Plate with 1 Actuator (550 Hz)

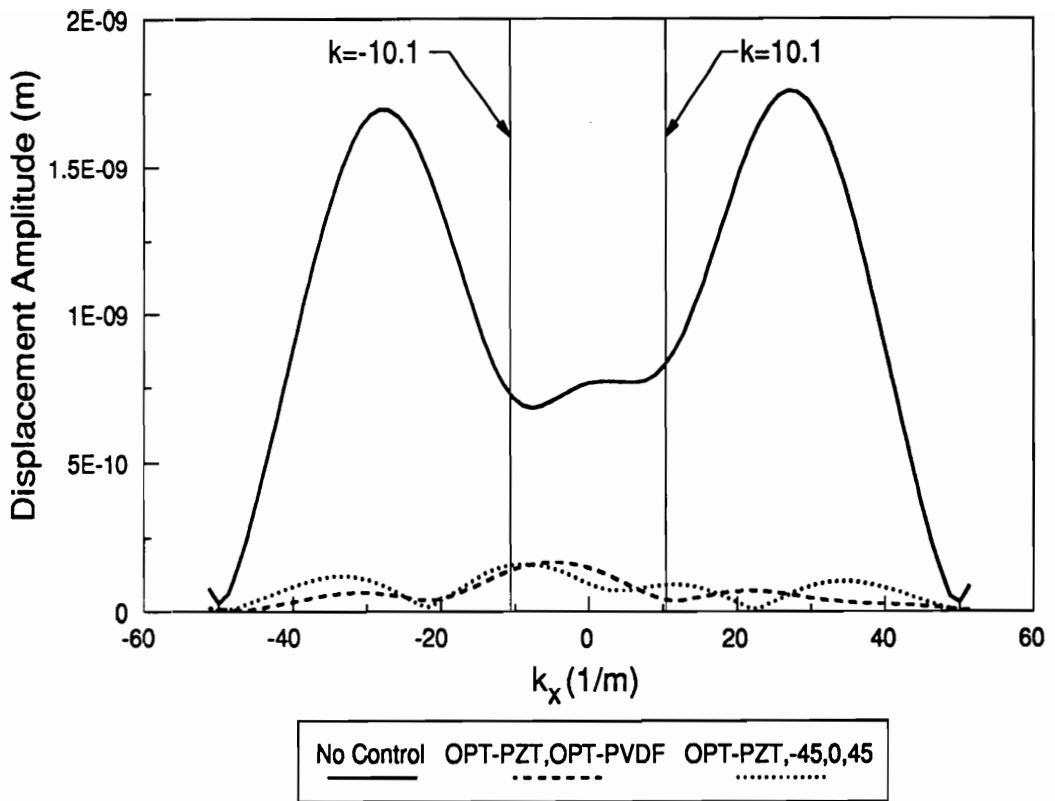


Figure 6.23: Wavenumber Transform of Measured Modal Response with 1 Actuator (550 Hz)

function (i.e. the acoustic response), is incorporated into the optimally designed PVDF sensor. A wavenumber transform of the structural response also confirms the observation that the dominant mechanism in the control implementation was modal reduction as is apparent in Figure 6.23. As in the modal response of Figure 6.22, little difference is observed between the measured response when implementing the PVDF error sensor or the microphone error sensors. The same structural acoustic response was thus obtained with one optimally designed structural sensor as opposed to three acoustic error sensors. In addition to the fact that the PVDF sensor is more compact and less expensive, it has reduced the order of the control system.

6.3.2.2 Three-Input/Three-Output (550 Hz)

The second design incorporated three optimally positioned piezoelectric control actuators and three optimally positioned and dimensioned PVDF structural error sensors as illustrated in Figure 4.7 of section 4.2.3 and Figure 4.8 of section 4.2.4.1 respectively. The predicted acoustic response of the controlled simply supported plate is presented in Figure 6.24. Only 2 dB of improvement in the level of sound attenuation is predicted when implementing the three optimal control actuators and the three optimal PVDF error sensors as is apparent upon comparing the directivity patterns presented in Figure 6.20 and Figure 6.24. In contrast, approximately 15 dB of improvement in the sound attenuation is predicted when implementing the three actuators in conjunction with the microphone error sensors. This limit, which is imposed by the implementation of the structural error sensors, is thought to be due to the fact that the phase relationship between any given structural mode cannot

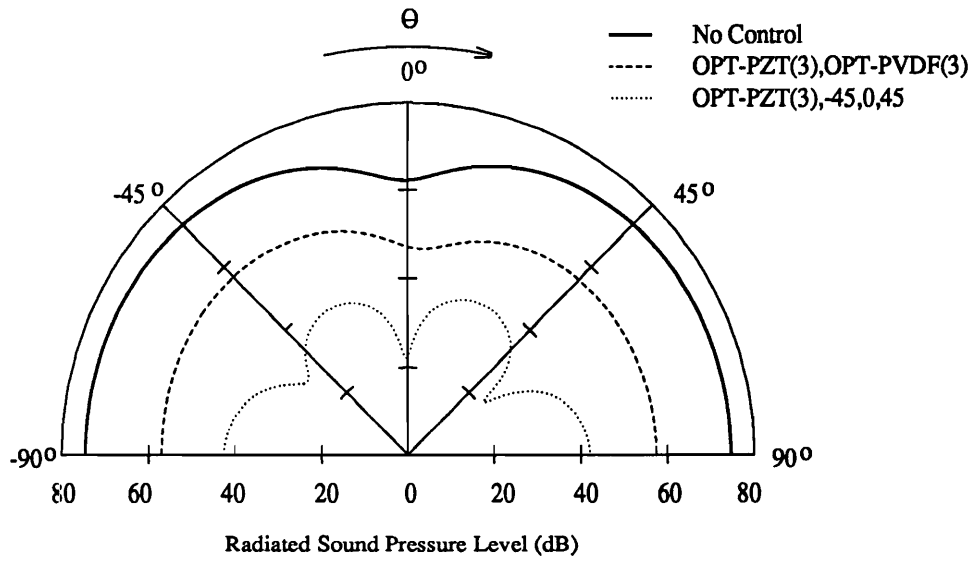


Figure 6.24: Predicted Acoustic Directivity Pattern with 3 Actuators (550 Hz)

be changed by the filtering characteristics of the rectangular sensors. Hence, modal restructuring cannot be incorporated into the optimal PVDF sensor design to the same degree obtained when implementing a point microphone error sensor.

Results from the experimental study support those obtained from the analytical models. As indicated in Figure 6.25, close to 25 dB of sound attenuation was achieved when controlling the structure with the three piezoelectric actuators and three PVDF structural error sensors. Upon implementing the microphone error sensors, the level of sound attenuation was on the order of 35 dB as illustrated in the directivity pattern. Hence an additional 10 dB of sound attenuation was gained by implementing the microphone error sensors as opposed to the structural PVDF error sensors. However, 25 dB of sound attenuation is certainly an acceptable level when incorporating the structural error sensors to achieve the desired “adaptive structure”. Since the spatial filtering characteristics of the rectangular PVDF error sensors are such that specified phase relationships between modes cannot be incorporated in the design, a finite limit exists in the level of sound attenuation which can be achieved, unless of course a sufficient number of control actuators are used to drive the total response of the structure to zero.

The modal response of the structure upon achieving control is very similar to that of the modal response for the single channel control case as is illustrated in Figure 6.26. Again, the dominant mechanism of control is modal suppression; however, further insight into the control process can be gained by studying the wavenumber transform of the structural response plotted in Figure 6.27. One observes that the magnitude of the wavenumber spectrum was reduced in both the subsonic and su-

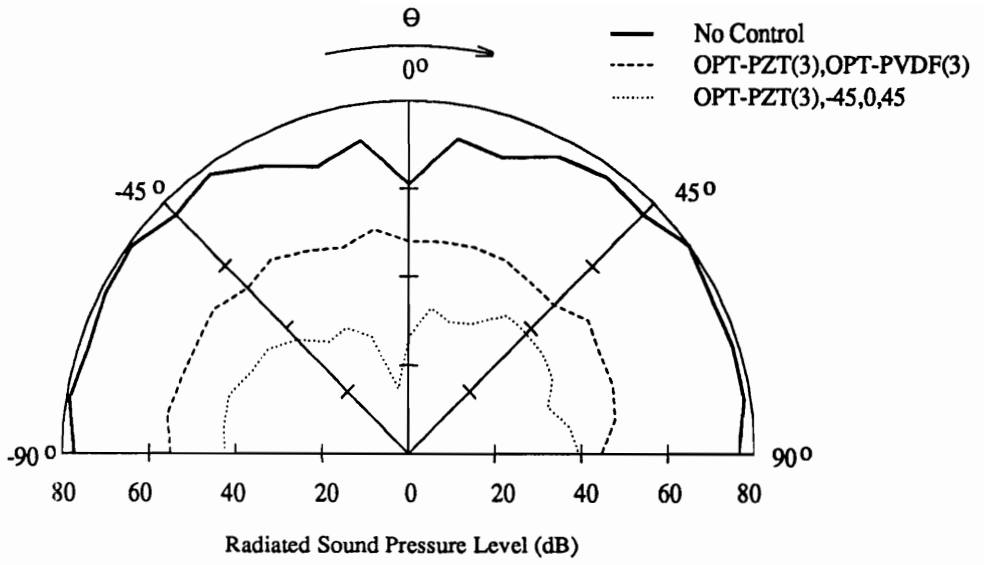


Figure 6.25: Measured Acoustic Directivity Pattern with 3 Actuators (550 Hz)

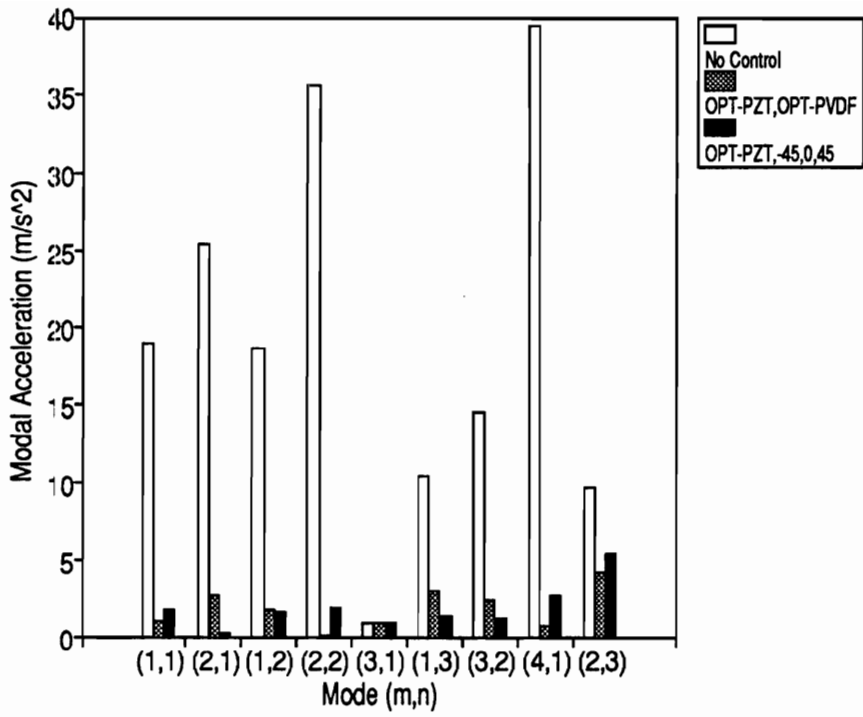


Figure 6.26: Measured Modal Response of Plate with 3 Actuators (550 Hz)

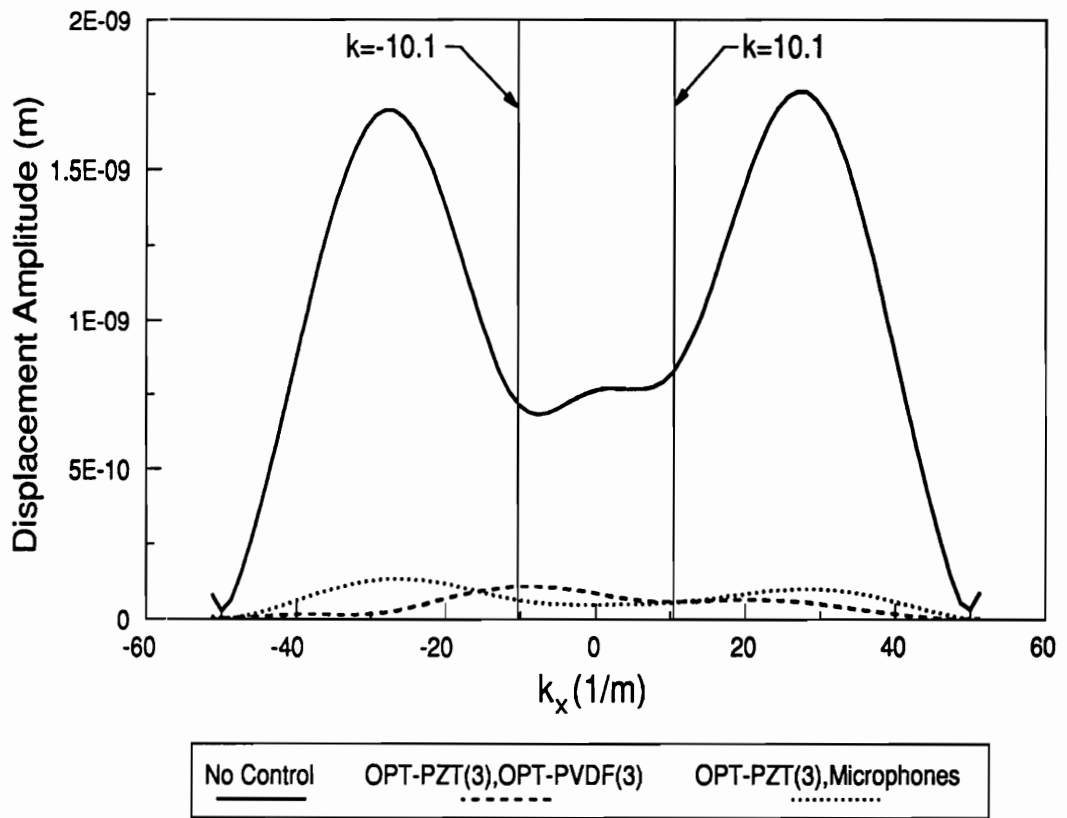


Figure 6.27: Wavenumber Transform of Measured Modal Response with 3 Actuators (550 Hz)

personic region. However, in the case where microphones were implemented as error sensors in the cost function, greater reduction is observed in the supersonic region, while less reduction is observed in the subsonic region compared to that when implementing the PVDF structural sensors. Hence, as discussed earlier, this additional attenuation of sound is due to lower order modal restructuring upon minimizing the response of the structure. The reduced modal response is further rearranged for destructive interference between modes when implementing the acoustic error sensors yielding greater levels of attenuation in the radiated sound and spillover into the subsonic region of the wavenumber spectrum.

6.3.2.3 Summary of Optimal Design

Optimal design techniques were implemented to determine the optimal location of piezoelectric control actuators and the optimal size and location of rectangular PVDF structural error sensors. As illustrated in Figure 4.7, the optimal locations for the control actuators were in the vicinity of the corners of the plate. This makes physical sense when one considers the modal response of the structure. As the number of modes contributing to the response of the structure increases, the likelihood of locating an actuator close to a nodal line for a given mode increases, rendering it ineffective for controlling that mode. As the actuator nears the corner of the structure, the number of nodal lines covered by the actuator is decreased. Hence an infinitely small actuator placed in the corner of the plate could theoretically couple with all structural modes; however, due to the infinite input impedance of the structure at this location, this approach is not practical in view of driving the actuator with some finite voltage. In addition, in some cases locating an actuator on or near

a nodal line is valid, specifically if there is no need to control the mode (i.e. the mode has a low radiation efficiency with respect to other dominant modes).

Considering the optimal locations and dimensions of the PVDF structural error sensors, one quickly observes that in the single channel control implementation, the sensor is located at the edge of the plate as illustrated in Figure 4.8. One also observes that it is positioned about the anti-node of the (4,1) mode. Hence the electrical response of the sensor is most sensitive to the (4,1) mode of all the plate modes contributing to the response. Significant response to the (1,3) mode and (1,1) mode is observed as well. Considering the discussion in Chapter 1 pertaining to edge radiators and the radiation efficiency, the location and dimension of this sensor is logical. The structural acoustic response of the plate is controlled by minimizing the response of the efficient acoustic radiators, the (1,1), (1,3) and (4,1) modes, and the edge radiating (1,3) mode is controlled by the location of the actuator along the appropriate edge. The multi-channel control case is obviously more complicated; however, one of the PVDF sensors is observed to be located and dimensioned in a similar manner to that of the single channel control case. Greater insight into the multi-channel control case can be gained by considering the acoustic intensity in the z -direction at the surface of the structure (computed as outlined in equation (2.49)). The theoretical acoustic intensity of the uncontrolled plate response is presented in Figure 6.28. As illustrated, a significant amount of the sound power is radiated from the edges of the plate. Upon achieving control, the total power is minimized; however, a significant reduction in the sound radiation at the edges is also observed as illustrated in Figure 6.29. Hence, the locations of the PVDF structural error sensors make physical sense when considering the sound power radiated from the

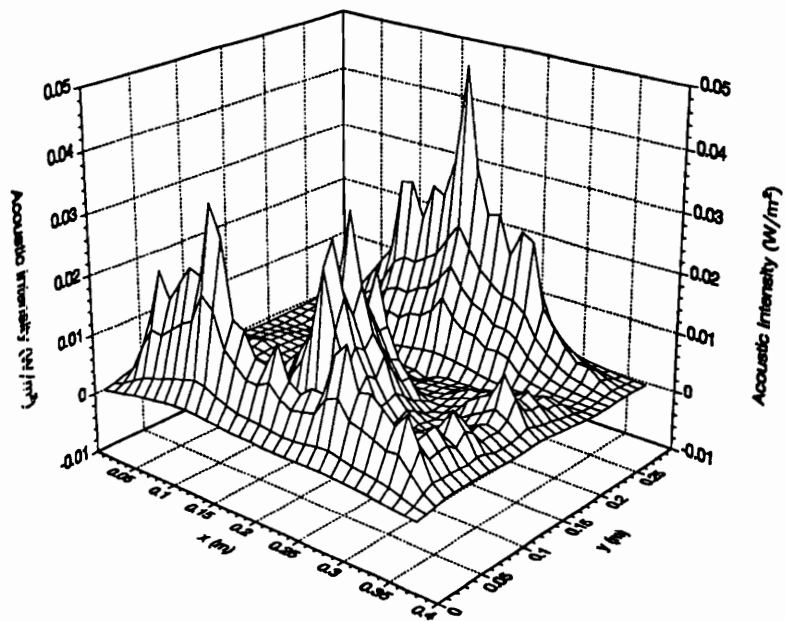


Figure 6.28: Acoustic Intensity of Uncontrolled Plate Response (550 Hz)

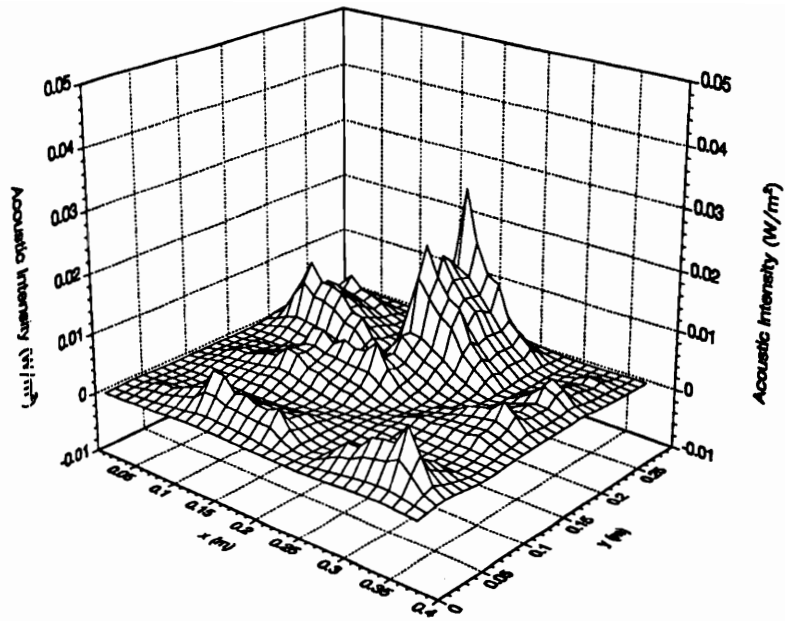


Figure 6.29: Acoustic Intensity of Controlled Plate Response with 3 Actuators (550 Hz)

structure.

6.3.3 Shaped Modal PVDF Structural Sensors

Design methods for achieving shaped sensors based upon the modal response of the structure were previously outlined in Chapter 4. In the case of the simply supported beam, the shaped modal sensor can be readily achieved since the variation in the polarization profile as a function of position on the structure can be incorporated into the shape of the sensor as illustrated in Figure 4.15 of section 4.3.2. For the simply supported plate, the response is two-dimensional and thus requires a three-dimensional shaped sensor to achieve the desired variation in polarization profile as a function of both the x and y-direction. The surface of the plate must be totally covered by the PVDF and the polarization profile must vary as a function of the z-direction of the structure. Since a three-dimensional sensor is not readily realizable at this stage, experiments were conducted only for the simply supported beam and corresponding shaped sensor design.

To demonstrate the potential of shaped modal sensors, a PVDF sensor was designed to control sound radiation in the far-field at an angle of $\theta = 0^\circ$ from the baffled simply supported beam. This angle was chosen since the modal acoustic response of the structure is independent of frequency at this angle as illustrated in equation (4.43). In addition, a sensor designed to respond only to the first structural mode of the beam was implemented to demonstrate the significant difference in the controlled acoustic response with slight variations in the sensor design as illustrated in Figure 4.15. Control experiments were conducted with the simply supported beam, which

measured 380 mm x 40 mm x 4.57 mm as previously discussed in chapter 5. The input disturbance was positioned 240 mm from the end of the beam as illustrated in Figure (5.12), and the control actuator measured 38 mm long x 30 mm wide and was positioned 95 mm from the end of the beam. The actuator was centered over the nodal line of the fourth mode since this mode does not significantly contribute to the acoustic response of the structure at the chosen frequencies of excitation. The predicted and measured acoustic directivity patterns are compared in the following sections for the shaped sensor design implementation.

6.3.3.1 Off-Resonance Response (660 Hz)

For an excitation frequency of 660 Hz, which is just below the resonant frequency of the third structural mode, a significant reduction in the radiated sound is predicted when minimizing the response of the PVDF “Microphone” sensor as indicated in Figure 6.30. However, minimizing the response of the PVDF “Mode 1” sensor results in an increased acoustic response for this excitation frequency. This results primarily from control spillover into the dominant third structural mode. For the range of excitation used in this study, the first and third structural modes are the most dominant acoustic radiators. An experiment was conducted in the anechoic chamber with a baffled simply supported beam as outlined earlier, and the experimental results for the identical test case are presented in Figure 6.31. As predicted, sound attenuation is achieved when using the PVDF “Microphone” sensor, and the sound field increases when using the PVDF “Mode 1” sensor.

General trends in the predicted and measured acoustic directivity patterns compare

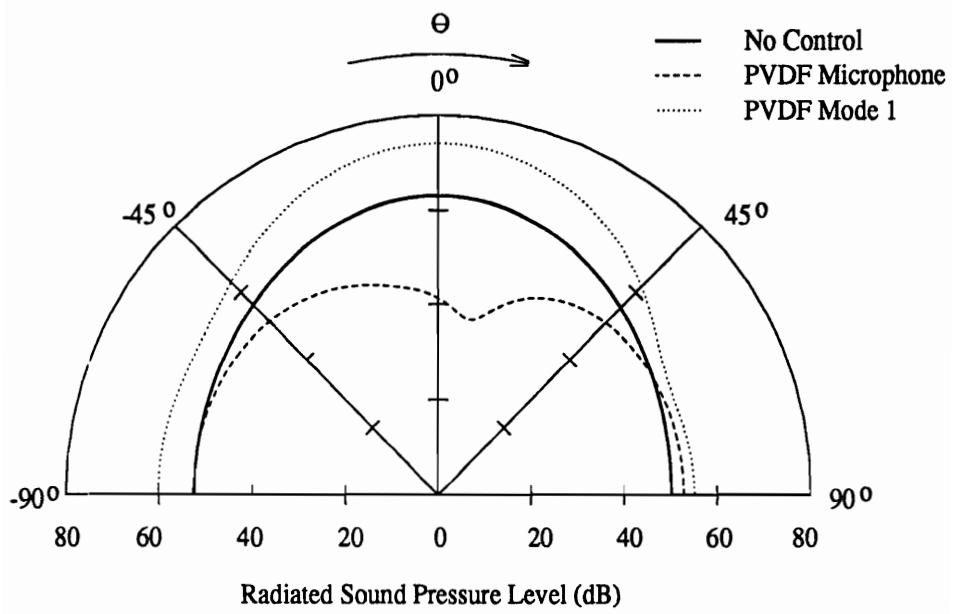


Figure 6.30: Predicted Acoustic Directivity Pattern (660 Hz)

well, and the magnitude of the response for the controlled and uncontrolled cases are within reason. As in the previous test cases with the baffled simply supported plate, the most significant difference in the directivity patterns are noted near the baffle, which as previously discussed is likely due to deviation from the assumed infinite extent of the baffle in computing the theoretical directivity pattern. One should also recognize that the “notch” in the controlled acoustic response of the beam does not appear at $\theta = 0^\circ$ in the theoretical directivity pattern or the measured directivity pattern. Recall however that the PVDF microphone sensor was designed to yield the same controlled response as that achieved with a microphone positioned in the acoustic far-field at $\theta = 0^\circ$. As previously discussed, due to the dimensions of the anechoic chamber and the chosen operating frequency range, the traversing microphone position does not satisfy the far-field conditions. The far-field directivity patterns are thus not developed at this radius, explaining why the “notch” does not appear at the expected angle.

6.3.3.2 Off-Resonance Response (700 Hz)

The excitation frequency was increased to 700 Hz, which is 20 Hz above the resonant frequency of the third structural mode, and the control experiments were repeated to provide another test case. As illustrated in Figure 6.32, little attenuation is observed in the predicted controlled acoustic response of the beam configured with the PVDF “Microphone” sensor; however, an acoustic notch in the directivity pattern is observed near $\theta = 0^\circ$. (Again, since the sensor was designed to yield the same controlled acoustic response as a microphone positioned in the acoustic far-field, the directivity patterns are not fully developed at the radius used in this study, 1.6 m

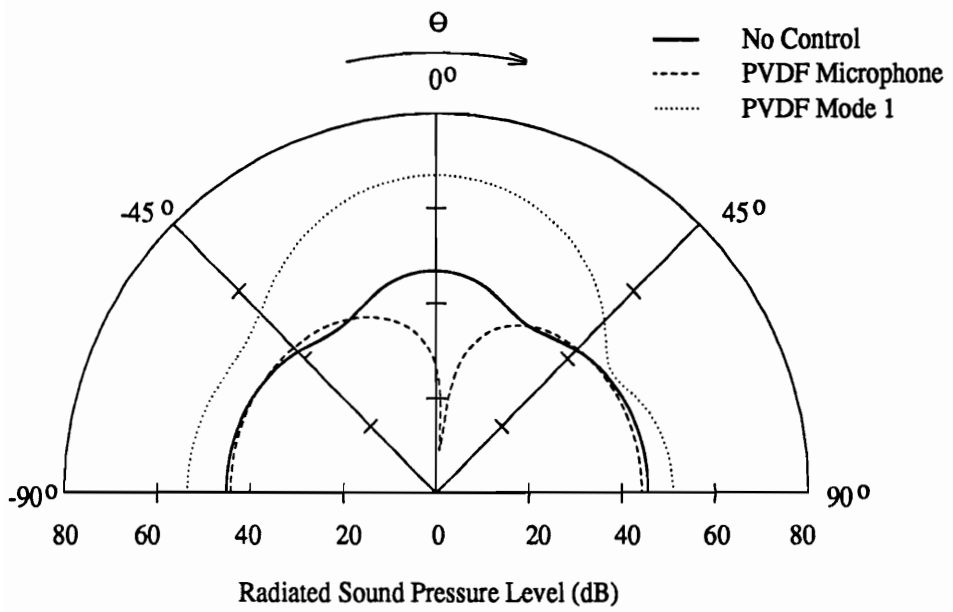


Figure 6.32: Predicted Acoustic Directivity Pattern (700 Hz)

and hence the notch does not appear at $\theta = 0^\circ$.) For the PVDF “Mode 1” sensor, the predicted acoustic response upon achieving control is greater than that before control. Minimizing the response of the PVDF “Mode 1” sensor results in spillover into the third structural mode, resulting in increased sound radiation. Experimental results for the same test case confirm the predicted acoustic response as illustrated in Figure 6.33, suggesting that the desired sensor shape was achieved. As in the previous test case, both the magnitude and trends of the acoustic directivity patterns are within reasonable agreement. The most significant deviation between theory and experiment is noted near the baffle, and reasons for this discrepancy have been given in the previous sections.

6.3.3.3 Summary of Modal Shaped PVDF Sensors

In both of the test cases previously presented, one might question why an acoustic notch in the directivity pattern was not observed at an angle corresponding to exactly $\theta = 0^\circ$. In all test cases presented, the acoustic response of the structure was computed by numerically integrating Rayleigh’s integral at the chosen acoustic field point since all measurements in the anechoic chamber were taken at a radius of 1.6 m from the structure. As discussed earlier, this radius does not satisfy the far-field conditions required to approximate the acoustic response. Since the PVDF shaped sensor was designed to approximate a microphone positioned at $\theta = 0^\circ$ in the *acoustic far-field* (i.e. a radius much greater than 1.6 m), the notch in the directivity pattern is not apparent at exactly $\theta = 0^\circ$. The dominant acoustic directivity patterns which would produce the notch at the desired coordinate are not present at the radius required to measure the acoustic response of the structure in the anechoic

chamber due to interactions between the non-radiating part of the sound field and the radiating part. By predicting the acoustic near-field response analytically, limitations imposed by the finite dimensions of the anechoic chamber were overcome, and good correlation between experimental and analytical results were observed in the region between -45° and 45° away from the baffle. As a final comment, one observes that a greater level of global attenuation occurred for an operating frequency of 660 Hz than 700 Hz. The resonant frequency of the third mode for the simply supported beam used in this study was at 680 Hz. Hence, upon passing through the resonant frequency, a phase change between the first and third mode of the beam occurred. This phase change resulted in attenuation at the desired angle with very little attenuation predicted or observed in the remaining residual acoustic field.

6.3.4 Optimally Located PVDF Acoustic Near-Field Sensors

Acoustic near-field sensors constructed from PVDF were optimally positioned in the x and y -direction with respect to the plate surface to control the radiated sound. The relative positions of the near-field sensors are illustrated in Figure 4.11 of section 4.2.4.2. Due to the computational requirements discussed earlier, optimization of both size and dimension was not feasible. Since some deviation was noted between the measured and predicted response of the sensor, as illustrated in Figure 5.9, sensors of similar size were implemented in the multi-channel control case such that the magnitude and phase response of the sensors displayed similar characteristics. The two test cases were chosen at an excitation frequency of 550 Hz since a significant number of modes contribute to the structural and acoustic response at this frequency. In addition, the optimal actuator locations illustrated in Figure

(4.7) can be used for this study as well. A single-input/single output control case is presented first, and the multi-channel control case was performed with two actuators and two acoustic near-field sensors. Three channels were not implemented since the computational time required to optimize the two sensor control case was on the order of 24 hours on the IBM VM1 computing system as discussed earlier in Chapter 3. Results from this study are presented below.

6.3.4.1 Single-Input/Single-Output (550 Hz)

The predicted acoustic response for the single-input/single-output optimal design is presented in Figure 6.34. In the legend of the figure, the use of an optimal actuator is designated by the symbol, "OPT-PZT", and the use of an optimal acoustic near-field sensor is designated by the symbol, "OPT-NFPVDF". As illustrated, upon optimizing the position of the acoustic near-field sensor, the predicted level of sound attenuation was approximately 15 dB as was the case when implementing the microphone error sensors with the same optimally configured piezoelectric control actuator. The predicted and measured results are consistent as is apparent when comparing the directivity patterns of Figure 6.34 to those of Figure 6.35. Approximately 15 dB of sound attenuation was achieved whether the optimally configured acoustic near-field sensor was implemented in the control approach or the three microphones positioned as in the previous test cases.

Comparing the experimental modal response of the structure before and after control one observes that both modal suppression and modal restructuring play a role in reducing the radiated sound pressure. While in both control cases, the modal ampli-

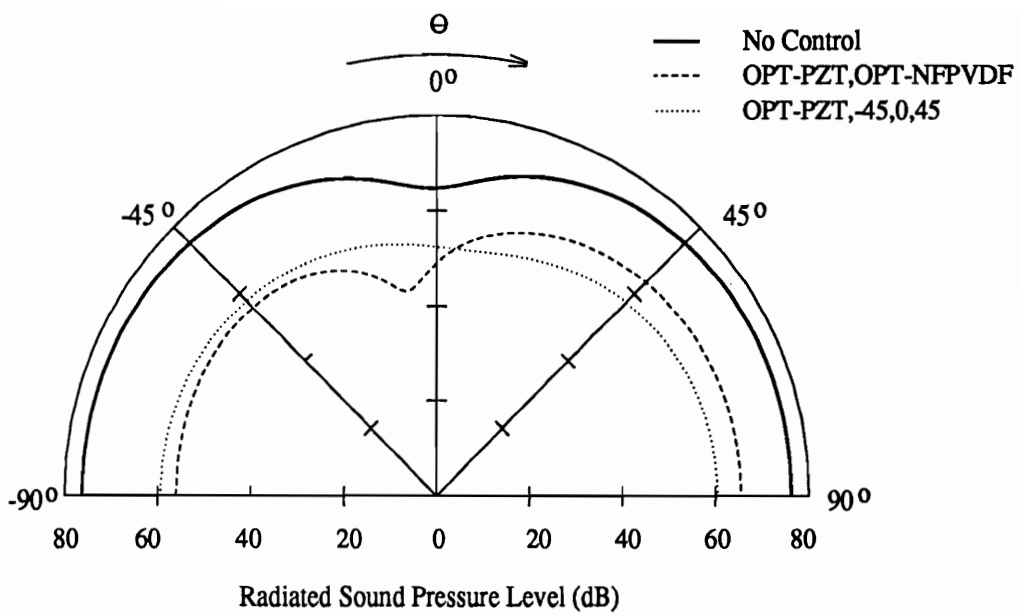


Figure 6.34: Predicted Acoustic Directivity Pattern (Single-Input/Single-Output, 550 Hz)

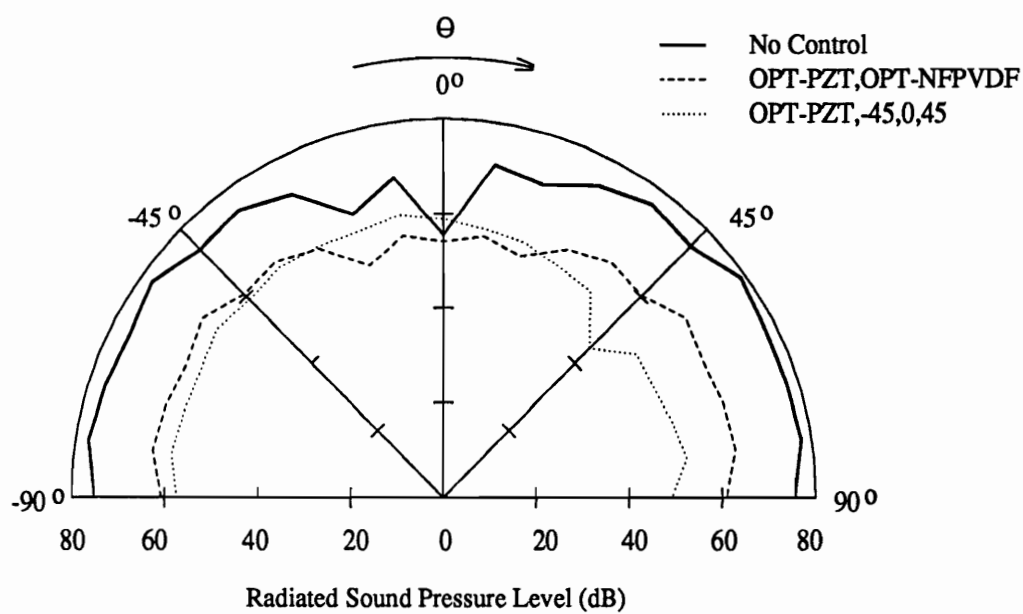


Figure 6.35: Measured Acoustic Directivity Pattern (Single-Input/Single-Output, 550 Hz)

tudes were observed to decrease for the most part, some increase in the (1,1) mode and (2,3) mode is observed when implementing the microphone error sensors as illustrated in Figure 6.36. These results are readily interpreted upon considering the wavenumber transform of the structural response presented in Figure 6.37. As illustrated, the supersonic region of the wavenumber transform is reduced significantly in both cases; however a greater reduction is noted at $k_x = 0$, which corresponds to $\theta = 0$ as discussed in chapter 4, for the PVDF error sensors. The observed increase in sound attenuation results from the lower order modal restructuring which results in control spillover in the subsonic region of the wavenumber spectrum.

6.3.4.2 Two-Input/Two-Output (550 Hz)

The second test case was conducted with two control actuators and two optimally positioned acoustic near-field sensors as discussed earlier in section 4.2.4.2 and depicted in Figure 4.11. As illustrated in the directivity pattern of Figure 6.38, the predicted level of acoustic attenuation improved by roughly 10 dB when implementing the microphone error sensors in the control approach as compared to the PVDF acoustic near-field sensors. Sound attenuation on the order of 20 dB was predicted when implementing the PVDF near-field sensors, and as illustrated in Figure 6.39, close to 20 dB of sound attenuation was measured. This is roughly a 5 dB improvement in the level of acoustic attenuation observed in the single channel control case discussed previously. Upon implementing the microphone error sensors, approximately 30 dB of sound attenuation was predicted, and as illustrated in Figure 6.39, roughly 30 dB of sound attenuation was measured. The predicted and measured controlled and uncontrolled acoustic directivity patterns are similar in shape as well,

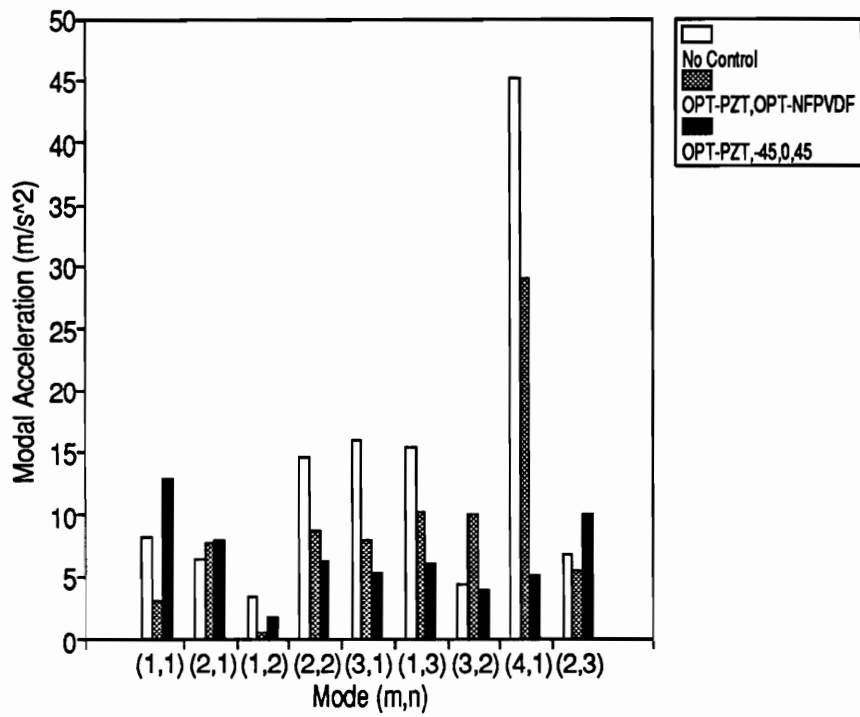


Figure 6.36: Measured Modal Response of Plate (Single-Input/Single Output, 550 Hz)

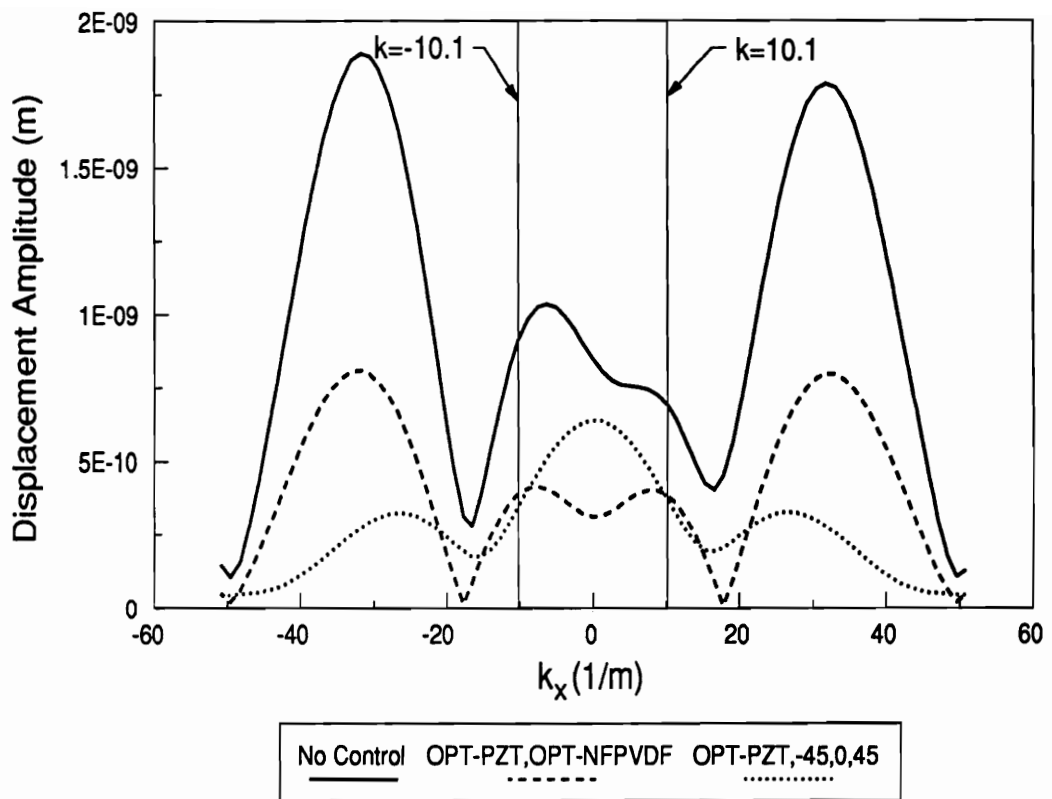


Figure 6.37: Wavenumber Transform of Measured Modal Response (Single-Input/Single-Output, 550 Hz)

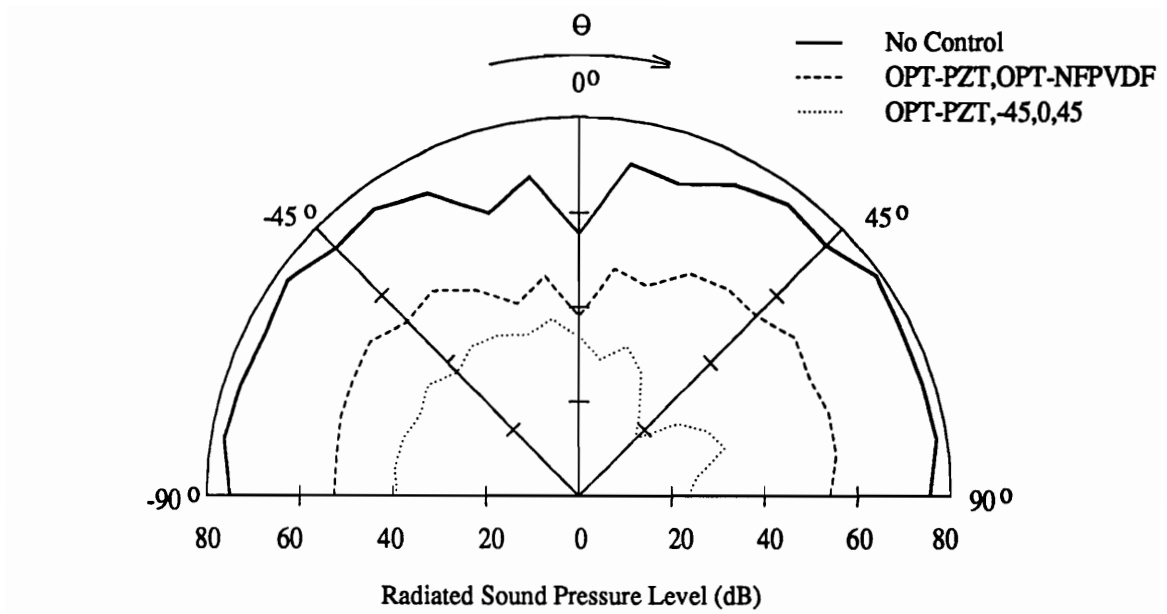


Figure 6.39: Measured Acoustic Directivity Pattern (Two-Input/Two-Output, 550 Hz)

suggesting that the analytical models were sufficient for achieving the desired design.

Upon comparing the modal response of the structure before and after control, one recognizes that the dominant mechanism of control is modal suppression. All structural modes, with the exception of the (2,3) mode which increased only 5%, were reduced as can be seen in Figure 6.40. The dominant acoustic radiating (4,1), (1,3) and (1,1) modes were reduced significantly under control conditions.

As expected, the wavenumber spectrums of the structural acoustic response corresponding to the two control cases are similar as illustrated in Figure 6.41; however, greater reduction is noted in the supersonic region of the wavenumber transform when implementing the microphone error sensors in the control approach. The supersonic region is defined between $k = -10.1$ and $k = 10.1$ as indicated in Figure 6.41. A significant reduction is observed in the subsonic region of the spectrum as well, which is characteristic of the mechanism of control termed modal suppression. Hence in the two-channel control case presented here, the acoustic near-field sensors function as predicted in achieving the desired controlled response of the structure. However, as was the case with the optimally configured structural PVDF sensors, the level of acoustic attenuation possible appears to be limited.

6.3.4.3 Summary of Acoustic Near-Field PVDF Sensors

Results from control experiments performed with the PVDF acoustic near-field sensors confirm that these sensors can be optimally positioned near the surface of the

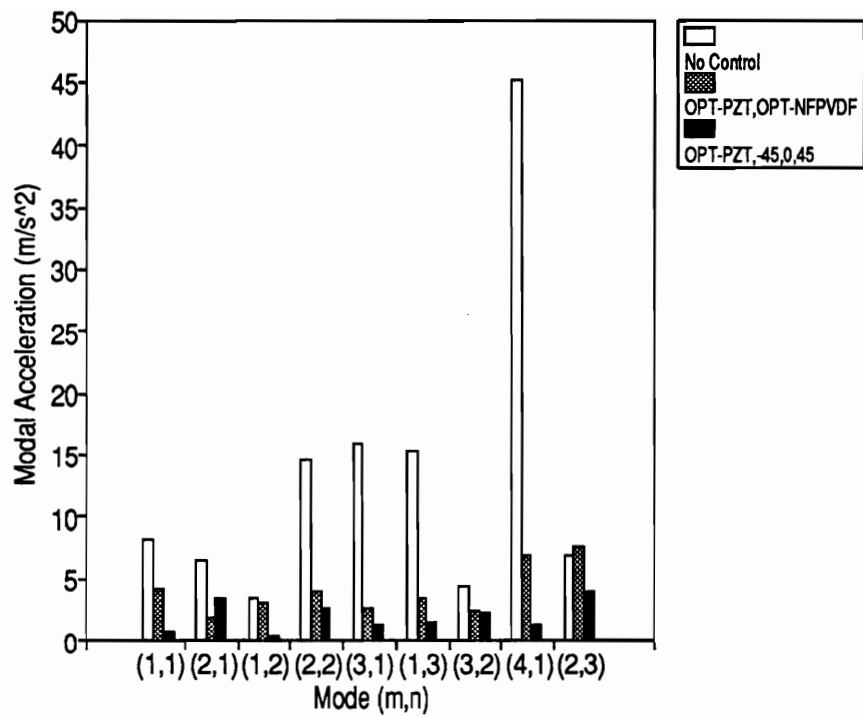


Figure 6.40: Measured Modal Response of Plate (Two-Input/Two-Output, 550 Hz)

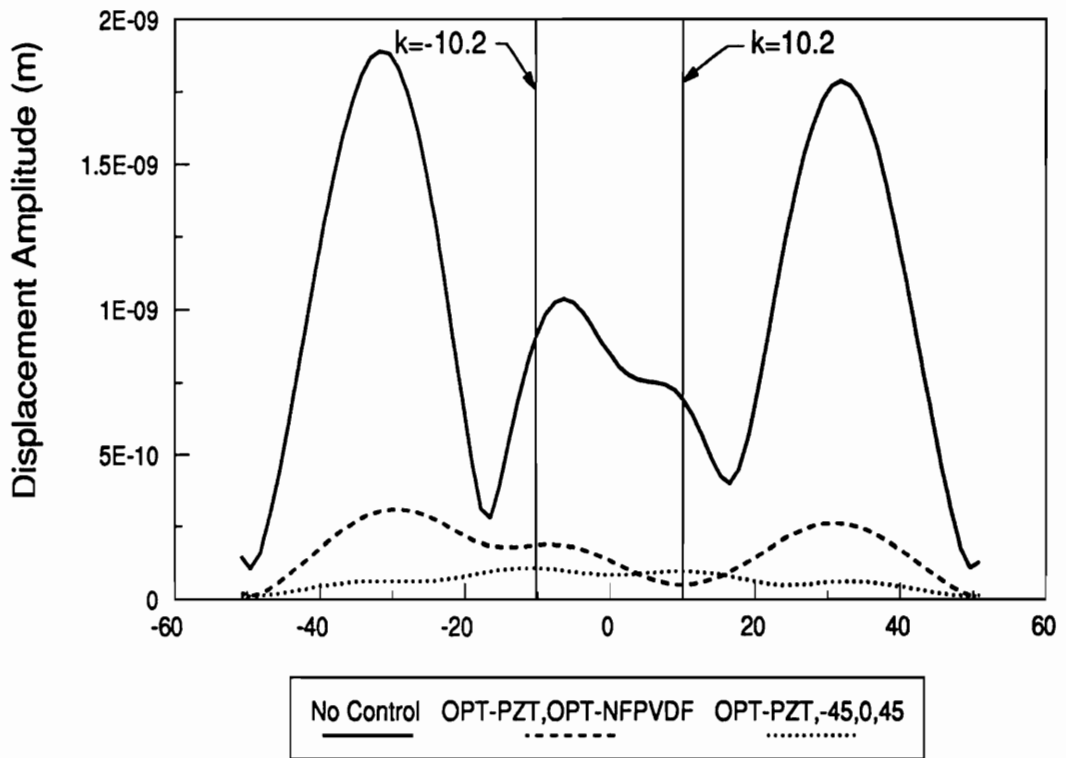


Figure 6.41: Wavenumber Transform of Measured Modal Response (Two-Input/Two-Output, 550 Hz)

structure for achieving control of far-field sound radiation. In this case, the sensors were positioned 2.54 cm from the surface of the structure to simulate realistic operating conditions, which would dictate that the sensor be very close to the vibrating surface. The design goal is to place the acoustic near-field sensor as close to the vibrating surface as possible, yet maintain the ability to predict the acoustic far-field response at the design frequency. This goal is analogous to the concept of acoustic holography. Hence the optimal distance from the surface of the structure was not specifically studied; however, sensor position was optimized at a variety of fixed distances from the plate surface as discussed in section 3.2.4.2. In general, little variation in the optimal position of the sensors was noted when located between 2 and 10 cm from the surface of the plate.

The fundamental limitation in implementing these sensors in active structural acoustic control applications results from the intense requirements on CPU time for determining the optimal design. Since the distributed acoustic response of the structure over the surface of the error sensor must be computed, a significant number of acoustic near-field computations must be made at each trial step as well as when estimating the gradient of the constraints and objective function numerically. Even for the simply supported plate chosen in this study, the Rayleigh integral must be evaluated numerically in the acoustic near-field. Hence for practical implementation this must be confronted as the primary deterrent for application. However physical implementation may dictate the use of these sensors in some applications.

6.3.5 Optimally Weighted Discrete/Distributed PVDF Structural Sensors

The final test case was studied with the analytical model only and was investigated specifically to provide a foundation for future work in designing shaped sensors for ASAC. An array of distributed rectangular PVDF error sensors (nine) were modelled on the surface of the plate as illustrated in Figure 4.12 of section 4.2.5. The response of each sensor was weighted with a number between +1 and -1 and summed to create the response of the “weighted” distributed sensor. As a result, for each different design implementation (i.e. test frequency), the same sensors can be used to create the desired equivalent error sensor by simply changing the optimal weights for each application. Optimal design techniques were implemented to determine the optimal weights for a harmonic point force disturbance located at spatial coordinates of (240,130) mm and driven at an excitation frequency of 550 Hz as in the previous optimal design tests. The PVDF sensor array and optimal weighting configuration were previously presented in Figure (4.12).

As illustrated in Figure 6.42, the predicted controlled acoustic response of the structure results in 15 dB of sound attenuation. Comparing the level of attenuation predicted in Figure 6.42 with that predicted in Figure 6.20, the controlled structural acoustic response is of the same order of magnitude as that obtained with the single optimally designed PVDF sensor. Considering the consistency in the predicted and measured response of the previous study, it is plausible to expect this level of attenuation upon conducting experiments implementing this design approach. A neural network is proposed to select the optimal weights for each frequency of excitation and is suggested as the basis for future work with distributed PVDF structural

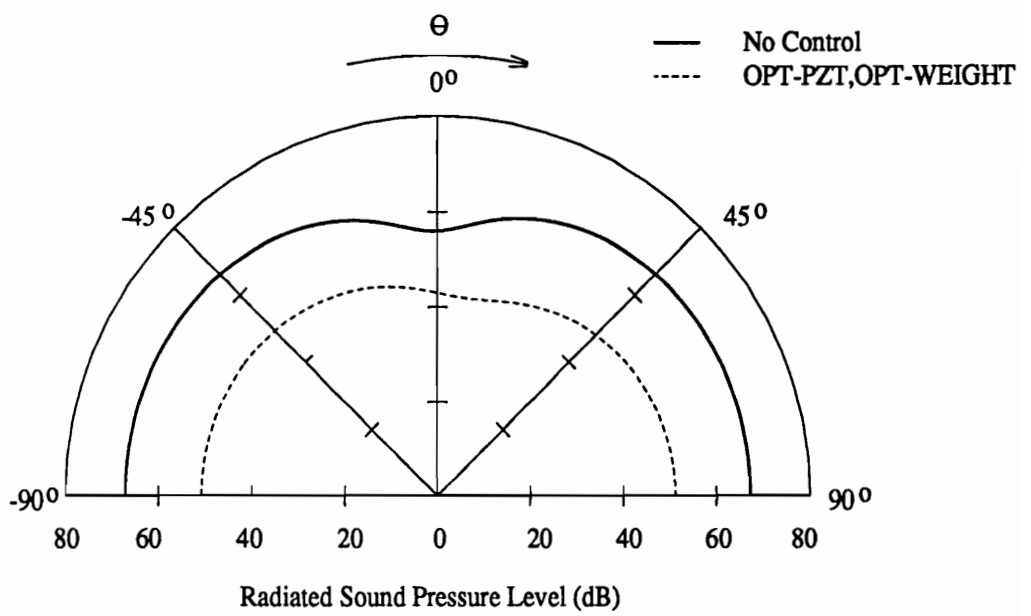


Figure 6.42: Predicted Acoustic Directivity Pattern for Distributed PVDF Sensor (550 Hz)

sensors since the same array of sensors can be used for an input disturbance with varying frequency content.

6.3.6 Summary of PVDF Sensors

A number of structural and acoustic near-field sensors of different forms constructed from PVDF have been studied for active structural acoustic control applications. Optimization of both the size and position of rectangular structural PVDF error sensors proved valid in achieving the same controlled acoustic response as obtained when implementing microphone error sensors. The optimal design was demonstrated for a harmonic input disturbance, and while the results from a sensitivity analysis are not given here, the controlled structural acoustic response (i.e. radiated field) was found to be sensitive to changes in the input frequency of the disturbance. However, as long as the optimal design frequency and thus operating range is restricted between resonant frequencies of the structure, the phase relationship between modes remains fixed and thus significant levels of acoustic attenuation can be obtained even when operating away from the *design* frequency. In general, the sensor should be optimally configured for each specific frequency to be controlled if the maximum level of acoustic attenuation is desired since the relative weighting of the structural modes changes as a function of frequency.

In addition to optimizing the structural PVDF sensors, acoustic near-field sensors were constructed from the material in the form of a cylindrical plate and optimal design techniques were implemented to determine the optimal location of each sensor. As with structural sensors, the optimal design was frequency dependent and hence

must change with each different input disturbance. In addition, the requirements on the CPU increased by two orders of magnitude with these near-field sensors since the response of the sensor must be obtained from the near-field acoustic response of the structure in the region of application. Considering the fact that the acoustic near-field sensors afford no advantage in the frequency band of operation (i.e. they are as sensitive to position and frequency as the structural sensors), structural PVDF sensors are suggested as the best alternative if this option is possible. However acoustic near-field sensors may be the only alternative in some design applications which restrict attaching the sensors to the structural surface.

Modal shaped error sensors were constructed from PVDF and tested as a design alternative to the optimally configured rectangular sensors. The PVDF was shaped according to the mode shapes such that both the relative phase and magnitude of the structural response were incorporated in the design. A test was conducted on a simply supported beam, and results indicate that the PVDF sensor can be shaped such that the modal weighting corresponds to the radiation filter characteristics associated with the far-field sound at a chosen acoustic field point. The primary limitation with this design approach concerns applications on two-dimensional structures such as simply supported plates. Since the polarization profile is a function of two dimensions in this case, a method for practically achieving the desired sensor weighting is unavailable at this time. Perhaps the best compromise of the two designs concerns the implementation of the weighted distributed/discrete array of PVDF sensors which was outlined for future work. With this method of application, if enough sensors were implemented in the array, a modal sensor could be approximated if desired. In addition, the weights could be distributed (for example) by

a neural network such that multi-frequency or broad-band disturbances could be controlled. Thus a variety of design alternatives exist with PVDF error sensors in ASAC, and the specific implementation obviously depends on the design requirements.

6.4 Accelerometer Error Sensors (Model Reference Control)

The final set of error sensors studied for ASAC were accelerometers. As was the case with the structural PVDF error sensors, the structural acoustic coupling must be incorporated into the control implementation of the accelerometer error sensors. Driving the response of an array of accelerometers arbitrarily located on the surface of a structure to zero with a multi-input/multi-output control approach will likely yield some reduction in the acoustic response if the structure is being driven on-resonance. However for the off-resonance case, any reduction in the structural acoustic response could surely be attributed to luck. Optimal design techniques could be implemented to determine the appropriate locations of the accelerometers for specific control applications as was done with the PVDF error sensors; however, an alternative approach was taken here.

Since the feed forward version of the filtered-x adaptive LMS algorithm used as the basis for control in this work is ideally suited for model reference control, the structural acoustic coupling was incorporated in a model to predict the *desired* response at an array of accelerometer error sensors. Note that the *desired* structural response corresponds to that which minimizes the sound radiation from the structure. This

approach was chosen since it provides a means of implementing structural error sensors on complex structures for which computation of the acoustic response is too complicated for optimal design techniques. Tests were performed on both the simply supported beam and the simply supported plate reported in an earlier publication by Clark and Fuller (1992(a)); however, experimental results corresponding to model reference control of the simply supported plate will be presented here since the structural acoustic response of this structure is by far the more complex complex of the two systems. Two off-resonance test cases are presented in which the harmonic input disturbance was positioned at spatial coordinates of (240,130) mm as in the previous test cases presented. The plate used in this study was configured with actuators as illustrated in the schematic of Figure 6.1.

6.4.1 Off-Resonance Response (320 Hz)

The first test case was conducted implementing a single piezoelectric control actuator, C1 as illustrated in Figure 6.1 which was centered at coordinates of (63.3,150) mm on the surface of the plate. To implement model reference control, microphone error sensors positioned at the same acoustic field points of -45° , 0° and 45° as discussed earlier were utilized as error sensors in the control cost function. Upon minimizing the structural acoustic response with the microphone error sensors, the frequency response function between the chosen accelerometers and the harmonic reference input to the controller was experimentally measured to determine the appropriate reference response. As was outlined earlier in this work and in a previous study by Clark and Fuller (1991(d)), the number of structural error sensors implemented must simply be equivalent to the number of control actuators used if

the eigenfunctions and hence the transfer function between the actuator and error sensor are unique. For the single control actuator test performed here, a single accelerometer located at spatial coordinates of (120,240) mm was chosen. The only consideration required in choosing the coordinate for the accelerometer is that some measurable change in the structural response at the spatial coordinate selected occurs upon achieving control (i.e. system is observable).

The predicted acoustic directivity patterns corresponding to the uncontrolled and controlled response of the structure are presented in Figure 6.43. Note that the controlled model reference response when implementing accelerometer error sensors is identical to the controlled acoustic response when implementing the microphone error sensors. The data set corresponding to implementation of the microphone error sensors was suppressed to eliminate any confusion caused by superimposing the two data sets. As illustrated, approximately 10 dB of sound attenuation is predicted. The measured acoustic directivity patterns corresponding to the uncontrolled and controlled response of the structure are illustrated in Figure 6.44, comparing that obtained when implementing the microphone error sensors to that obtained when implementing the single accelerometer with model reference control. In addition, the acoustic response of the structure resulting from driving the response of the accelerometer to zero as opposed to the model reference response is presented for comparison. As indicated, the directivity patterns are nearly identical whether implementing the three microphone error sensors or the single accelerometer as was predicted from theory. Approximately 10 dB of sound attenuation was both predicted and measured. Notice that driving the response of the single accelerometer to zero resulted in only 2 dB of sound attenuation, emphasizing the need for a model

incorporating the structural acoustic coupling.

6.4.2 Off-Resonance Response (400 Hz)

For the off-resonance response at an excitation frequency of 400 Hz, all three control actuators illustrated in Figure 6.1 were implemented in the control approach. Since three accelerometers are now required for the model reference control algorithm, two additional accelerometers were positioned on the structure at spatial coordinates of (180,200) mm and (280,80) mm. Again, the only consideration made in choosing the spatial coordinates of the accelerometers is that the system response is observable. The predicted acoustic directivity patterns for the uncontrolled and controlled response are presented in Figure 6.45. As illustrated, significant attenuation is predicted at the location of the three microphone error sensors. As in the single-input/single-output control case, the directivity pattern corresponding to the controlled model reference response when implementing accelerometer error sensors is identical to that obtained when implementing microphone error sensors. Upon comparing the predicted response of Figure 6.45 to the measured response presented in Figure 6.46, one recognizes that the model reference control design approach was again successful. While the resulting model reference directivity pattern was not exactly identical to that obtained when implementing the microphone error sensors, the same level of acoustic attenuation, approximately 20 dB, was observed. In addition, the controlled acoustic response of the structure is plotted for the case when the response of the three accelerometers was driven to zero as opposed to the reference response. As illustrated, the acoustic response actually increases by 3 dB, demonstrating the advantage of model reference control over simply trying to

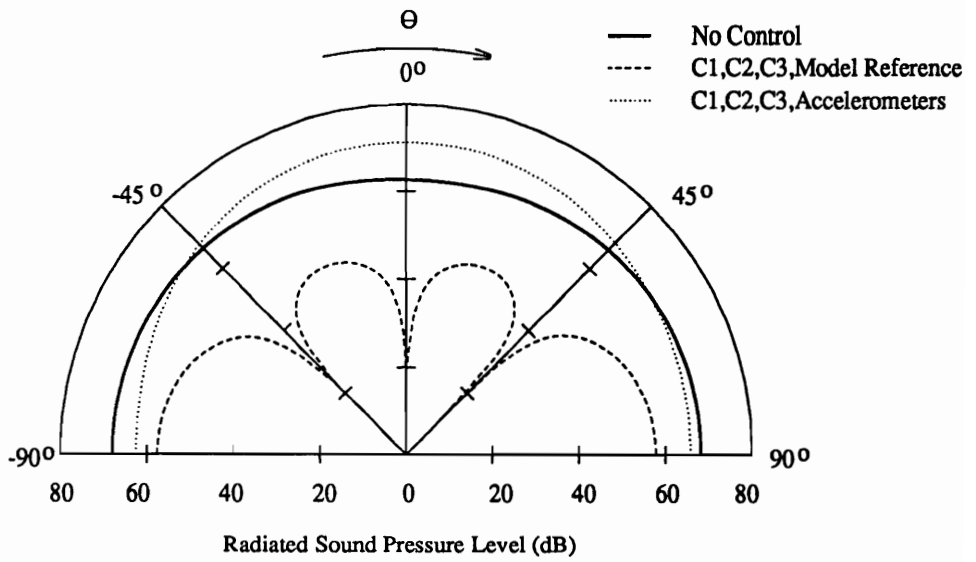


Figure 6.45: Predicted Acoustic Directivity Pattern (Model Reference, 400 Hz)

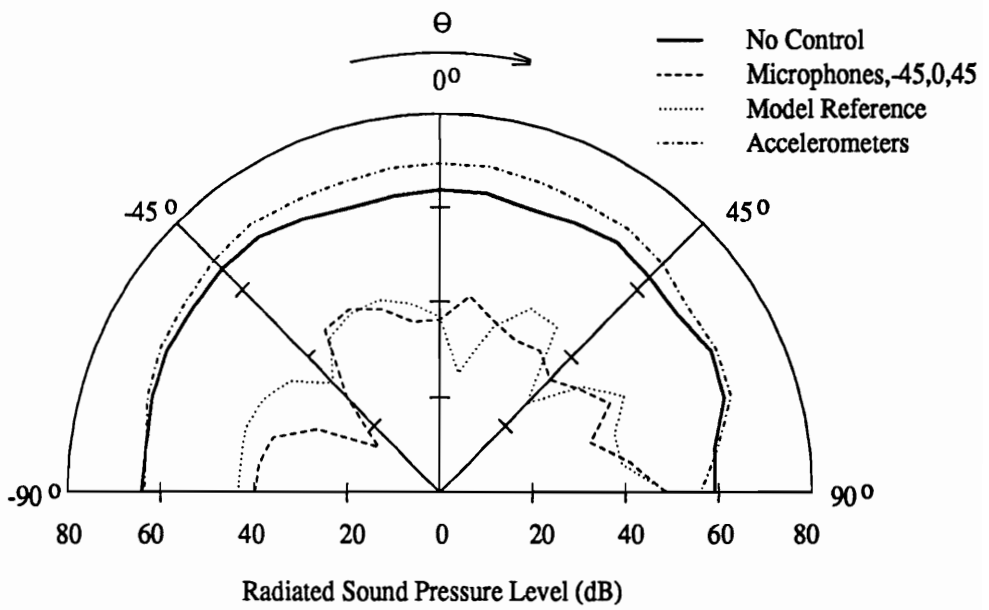


Figure 6.46: Measured Acoustic Directivity Pattern (Model Reference, 400 Hz)

control the structural response to minimize sound radiation.

6.4.3 Summary of Model Reference Approach

Model reference control can be viewed as an analogous method to optimal design for incorporating the structural acoustic coupling in the cost function of the control algorithm. This method of control affords implementation of accelerometers or other point structural sensors as error sensors for ASAC in addition to a means of eliminating microphone error sensors located in the acoustic field of complex structures. Since the reference model can be obtained experimentally or from analytical models of the system, the control approach can be readily extended to structures with a complex modal acoustic response. Thus model reference control is ideal for structures for which the input disturbance is harmonic and the structural acoustic coupling remains stationary with time (e.g. transformers or rotating machinery). Model reference control could also be extended to broad band control, although the level of system modeling will become more complex as indicated by Viperman *et al.*, (1991), who developed a feed forward adaptive LMS algorithm for controlling broad band vibration disturbances.

6.5 Discussion of Design Sensitivity

Design sensitivity is an important issue in the model reference control approach as well as the optimal design of PVDF error sensors. While both designs are sensitive to errors in modeling the system to be controlled as well as errors in shape and positioning of optimally configured error sensors, perhaps the most important parameter

in the design process is the disturbance input frequency. This study was devoted to sensor design and implementation for systems under a harmonic input disturbance. While this type of input disturbance is common in many physical systems, broad band inputs as well as multi-frequency inputs are just as common. In addition, even in the case of harmonic input disturbances, the frequency of excitation may vary with time. Hence if the sensor design or model reference control implementation is ultra sensitive to the frequency of excitation, the sensor design or model reference control implementation could be rendered useless. Previous studies by Clark and Fuller (1991(d)) have addressed the issues of design sensitivity for model reference control. These same concepts apply to the optimal design of structural PVDF error sensors and are reviewed by means of example here.

Consider the theoretical frequency response function between an accelerometer located on the simply supported plate and a point force input disturbance illustrated in Figure 6.47. The chosen coordinates for the input disturbance and accelerometer correspond to those implemented in the model reference study discussed earlier. Model reference control of the structure was demonstrated to be an effective method of attenuating structure-borne sound. One of the test cases presented was for an excitation frequency of 400 Hz. This excitation frequency is enclosed in the region termed “operating range” of Figure 6.47. In the previous study by Clark and Fuller (1991(d)), significant levels of acoustic attenuation were observed in the model reference control implementation as long as the frequency of the input disturbance remained in the designated operating range depicted, even though the design was for an excitation frequency of 400 Hz. While the levels of acoustic attenuation are not as great as that resulting from the “design” excitation frequency, Fuller and

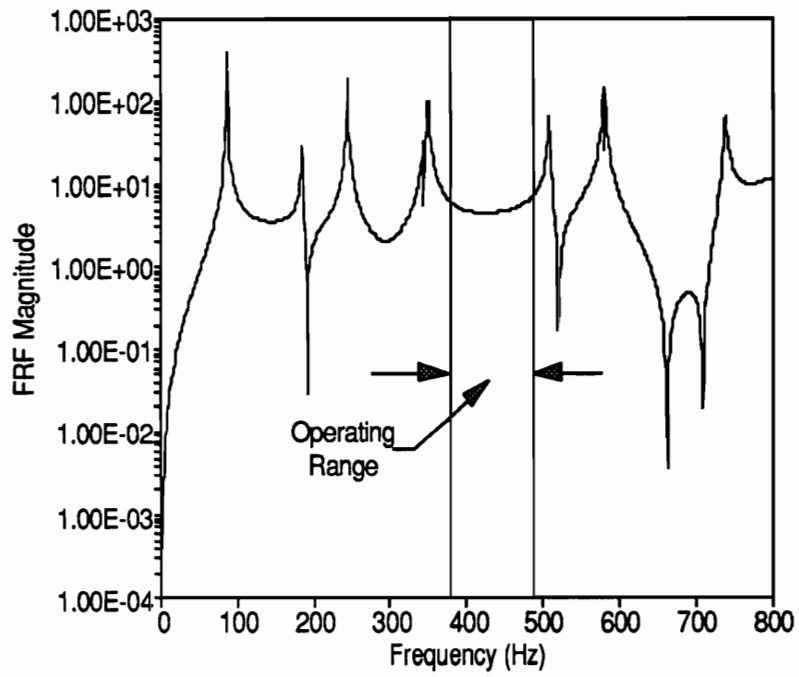


Figure 6.47: Example Frequency Response Function (Simply Supported Plate)

Clark (1991(d)) demonstrated that as much as 10 dB of global sound attenuation can be expected over the “operating range” for a test case such as that presented in Figure 6.46 where 20 dB of global sound attenuation was measured at the design frequency. The explanation for this result is based upon the modal contribution between resonant frequencies. The relative phase relationship between structural modes required to reduce the overall radiation efficiency of the structure is the same as long as the desired operating range does not cross a resonant frequency. When the operating range *does* cross a resonant point in the frequency response function, the phase relationship between the mode corresponding to that resonant frequency and the remaining modes shifts by 180° . Since the acoustic response results from a superposition of the modal acoustic response of the structure, this 180° phase change alters the necessary reference model required and thus degrades model reference control performance. The same concept holds true for the optimal design of PVDF error sensors. As long as the frequency of excitation remains in the “saddle” of the frequency response function, the relative phase relationship between structural modes remains fixed and hence significant levels of acoustic attenuation can be achieved.

Errors in modelling the desired system response for the model reference control implementation were also reviewed by Clark and Fuller (1991(d)), demonstrating that up to 5% error in both the phase and magnitude of the reference plant could be tolerated without significantly sacrificing the levels of acoustic attenuation achievable. While good correlation was noted between the predicted and measured acoustic and structural response of the systems modelled, nonlinearities in the structural response resulted in some deviation from the predicted acoustic response in the previous stud-

ies reviewed in this work. While these nonlinearities resulted in deviations between details of the acoustic directivity patterns, general levels of acoustic attenuation on the order of that predicted were achieved in all test cases reviewed in this study.

Chapter 7

Conclusions and Recommendations

The primary goal of this work was to review a variety of alternative sensors for active structural acoustic control and develop a design approach for achieving an adaptive structure with sensors and control actuators embedded in the structure or bonded to the surface. In conducting this study, a number of different error sensors were reviewed:

1. Microphones
2. PVDF Distributed Sensors
 - (a) Optimal design of rectangular structural sensors
 - (b) Optimal design of cylindrical acoustic near-field sensors
 - (c) Modal shaped structural sensors
3. Accelerometers.

Microphone error sensors were used as the basis for comparison since an approximation of the desired cost function (i.e the total acoustic far-field power) is represented

in the electrical response of these sensors.

Results from this work have demonstrated that rectangular structural PVDF error sensors can be optimally designed to incorporate the structural acoustic response of a simply supported plate in the electrical output of the sensor. Hence for narrow-band applications, wavenumber filtering can be achieved such that the supersonic region of the wavenumber transform is significantly reduced, resulting in structure-borne sound attenuation on the order of 20 dB. While this level of attenuation is approximately 10 dB less than that observed with microphone error sensors, some advantages are afforded with the structural sensors. First, the controlled structure is totally self-contained with both the control actuators and error sensors bonded to the surface. In addition, the rectangular PVDF error sensors were observed to limit control spillover into the subsonic region of the wavenumber transform, thus restricting the vibration response of the structure as well as the acoustic response.

Similar results were observed with the optimally designed PVDF acoustic near-field sensors. A non-contacting sensor constructed from PVDF was designed and placed in close proximity (approximately 2.54 cm) from the surface of the simply supported plate, and results from experiments conducted with these sensors demonstrated structure-borne sound attenuation on the order of 20 dB. The wavenumber filtering characteristics observed with these sensors was similar to that observed with the optimally designed PVDF structural sensors. The advantage afforded with these sensors is that they provide a method of achieving structural acoustic control with a non-contacting sensor placed in close proximity to the structural surface.

In addition to optimal design techniques, a method of achieving selective wavenumber filtering was demonstrated by varying the polarization profile of the PVDF material as a function of the modal weighting. In the case of the one-dimensional simply supported beam, the variation in polarization profile was physically achieved by etching away the surface electrode on the material in the y-direction to achieve the desired weighting. A structural PVDF sensor yielding an electrical response proportional to the desired radiation filter was thus achieved. For the test case presented, the radiation filter was designed for a microphone positioned normal to the center of the beam in the acoustic far-field. At this field point, the modal acoustic coupling is independent of frequency, and the sensor can thus be used in broad band as well as narrow band applications. In the case of the two-dimensional simply supported plate, a similar design procedure was outlined; however, the sensor was not tested due to the complexity of the design. To achieve the desired radiation filter for a two dimensional structure, the polarization profile must vary as a function of both the x and y-direction. Methods of achieving this three dimensional sensor are not currently practical.

As an alternative to PVDF sensors, accelerometer error sensors were implemented in conjunction with model reference control for attenuating structure-borne sound. Results from this work demonstrated that the structural acoustic coupling can be included in a reference model based on structural error sensors to achieve the same controlled acoustic response as that achieved with microphone error sensors. In fact, the reference response of the structure can be obtained experimentally if an array of microphones are initially used to achieve the desired structural acoustic response such that the reference response of the structure at the chosen array of accelerom-

eters can be measured. This technique affords greater flexibility in implementing structural sensors on complex systems with harmonic input disturbances since the entire control approach can be “designed” by experimental methods.

Hence a variety of alternative sensor design implementations have been suggested for active structural acoustic control, and depending on the chosen implementation, each has merit. For example, complex structures which cannot be modeled by analytical methods can be controlled with structural error sensors in conjunction with model reference control since the structural acoustic coupling can be measured directly. For structures with a response characterized by one dimension, the shaped modal PVDF error sensors appear most viable for achieving directional control. If the structural response is a function of two dimensions, then the optimally positioned and dimensioned rectangular PVDF error sensors appear most attractive for replacing microphones in the cost function of the control approach. Finally, if it is impossible to attach the sensor to the surface of the structure or position microphones in the acoustic far-field, PVDF acoustic near-field sensors can be implemented in the cost function of the control approach with optimal design techniques.

Future work should be devoted to studying the implementation of the weighted array of PVDF sensors in conjunction with a neural network to improve performance characteristics over a broad frequency range of input disturbances. The application of this approach as well as the previously outlined sensor designs and implementations must be extended to broad band excitation to solve the active structural acoustic control problem.

List of References

- Ackerman, J., 1985. *Sampled-Data Control Systems*, Springer-Verlag, Berlin, Germany, pp. 182-193.
- Arora, Jasbir S., 1989. *Introduction to Optimum Design*, McGraw-Hill Book Company, New York, New York, pp. 111-132.
- Auld, B.A., 1990. *Acoustic Fields and Waves in Solids*, Robert E. Krieger Publishing Company, Malabar, Florida, Volume I, pp. 265-354.
- Bailey, T. and Hubbard, J.E., 1985. "Distributed Piezoelectric-Polymer Active Vibration Control of a Cantilevered Beam," *AIAA Journal of Guidance and Control*, 6(5), pp. 605-611.
- Baumann, W.T., Ho, Fu-sheng and Robertshaw, H.H., 1991, "Active Structural Acoustic Control of Broadband Disturbances," Accepted for publication in *Journal of Acoustical Society of America*.
- Burdisso, R.A. and Fuller, C.R., 1991. "Dynamic Behavior of Structural-Acoustic Systems in Feed Forward Control of Sound Radiation," To appear in *The Journal of the Acoustical Society of America*.
- Burdisso, R.A. and Fuller, C.R., 1992(a). "Theory of Feed Forward Control System Eigenproperties," To appear in *The Journal of Sound and Vibration*.

- Burdisso, R.A. and Fuller, C.R., 1992(b). "Active Dynamic Modification of Flexible Structures," *Proceedings of the 10th International Modal Analysis Conference (IMAC)*, San Diego, California, Vol. II, pp. 1159-1166.
- Burke, S.E. and Hubbard, J., 1987. "Active Vibration Control of a Simply Supported Beam Using a Spatially Distributed Actuator," *IEEE Control System Magazine*, pp. 25-30.
- Burke, S.E. and Hubbard, J., 1991. "Distributed Transducer Vibration Control of Thin Plates," *The Journal of the Acoustical Society of America*, 90(2), pp. 937-944.
- Cady, W.G., 1964. *Piezoelectricity*, 2 volumes, Dover Publications, Inc., New York, 822 pages.
- Clark, R.L. and Fuller, C.R., 1990(a). "Experiments on Active Control of Structurally Radiated Sound Using Multiple Piezoceramic Actuators," Submitted to *The Journal of the Acoustical Society of America*.
- Clark, R.L. and Fuller, C.R., 1990(b). "Modal Sensing of Efficient Acoustic Radiators with PVDF Distributed Sensors in Active Structural Acoustic Approaches," Submitted to *The Journal of the Acoustical Society of America*.
- Clark, R.L., Fuller, C.R. and Wicks, A.L., 1991(a). "Characterization of Multiple Piezoelectric Actuators for Structural Excitation," *The Journal of the Acoustical Society of America*, 90(1), pp. 346-357.
- Clark, R.L., Fleming, M.R. and Fuller, C.R., 1991(b). "Piezoelectric Actuators for Distributed Vibration Excitation of Thin Plates: A Comparison between Theory and Experiment," Submitted to *The Journal of Vibration and Acoustics*.

- Clark, R.L. and Fuller, C.R., 1991(c). "Control of Sound Radiation with Adaptive Structures," *Journal of Intelligent Material Systems and Structures*, 2(3), pp. 431-452.
- Clark, R.L. and Fuller, C.R., 1991(d). "A Model Reference Approach for Implementing Active Structural Acoustic Control," Submitted to *The Journal of the Acoustical Society of America*.
- Clark, R.L. and Fuller, C.R., 1991(e). "Optimal Placement of Piezoelectric Actuators and Polyvinylidene Fluoride (PVDF) Error Sensors in Active Structural Acoustic Control Approaches (ASAC)," Submitted to *The Journal of the Acoustical Society of America*.
- Clark, R.L. and Fuller, C.R., 1991(f). "Active Structural Acoustic Control with Adaptive Structures Including Wavenumber Considerations," *Recent Advances in Active Control of Sound and Vibration*, Technomic Press, Eds. C.A. Rogers and C.R. Fuller, pp. 507-524.
- Clark, R.L., Gibbs, G.P. and Fuller, C.R., 1992(a). "An Experimental Study Implementing Model Reference Active Structural Acoustic Control," Submitted to *The Journal of the Acoustical Society of America*.
- Clark, R.L., Fuller, C.R. and Burdisso, R.A., 1992(b). "Design Approaches for Shaping Polyvinylidene Fluoride Sensors in Active Structural Acoustic Control," To be presented at *Conference on Recent Advances in Adaptive and Sensory Materials and Their Applications*, Blacksburg, VA, April 1992.
- Collins, S.A., Miller, D.W. and von Flotow, A.H., 1990. "Sensors for Structural Control Applications Using Piezoelectric Polymer Film," *MIT Report*, pp. 1-

- Crawley, E.F. and de Luis, J., 1987. "Use of Piezoelectric Actuators as Elements of Intelligent Structures," *AIAA Journal*, 25(10), pp. 1373-1385.
- Crighton, D.G., 1980. "Approximations to the Admittances and Free Wavenumbers of Fluid Loaded Panels," *Journal of Sound and Vibration*, 68(1), pp. 15-33.
- Curie, J. and Curie, P., April 1880. "Development par Compression de l'Electricite Polaire dans les Cristaux Hemiedres a Faces Inclinees [Development by Compression of Polar Electricity in Hemihedral Crystals with Inclined Faces]," *Bull. soc. min. Fr.*, 3(4), pp. 90-93.
- Curie, J. and Curie, P., Dec. 1881. "Contractions et Dilatations Produites par des Tensions Electriques dans les Cristaux Hemiedres a Faces Inclinees [Contractions and Dilatations Produced by Electrical Tensions in Hemihedral Crystals with Inclined Faces]," *C.r.*, 93(26), pp. 1137-1140.
- Dimitriadis, E.K. and Fuller, C.R., 1991. "Active Control of Sound Transmission Through Elastic Plates Using Piezoelectric Actuators," *AIAA Journal*, 29(11), pp. 1771-1777.
- Dimitriadis, E.K., Fuller, C.R. and Rogers, C.A., January 1991. "Piezoelectric Actuators for Distributed Vibration Excitation of Thin Plates," *Journal of Vibration and Acoustics*, pp. 100-107.
- Elliot, S.J., Strothers, I.M. and Nelson, P.A., 1987. "A Multiple Error LMS Algorithm and Its Application to the Active Control of Sound and Vibration,"

- IEEE Transaction on Acoustic Speech and Signal Processing*, ASSP-35, Vol. 1, pp. 1423-1434.
- Fahy, F., 1985. *Sound and Structural Vibration*, Academic Press, Orlando Florida, pp. 60-72.
- Fanson, J.L. and Chen, J.C., 1986. "Structural Control by the Use of Piezoelectric Active Members," *Proceedings of NASA/DOD Control-Structures Interaction Conference*, NASA CP-2447, Part II.
- Fleming, M.R., 1990. "An Experimental Investigation of the Harmonic Excitation of Simply Supported Plates with Multiple Surface-Bonded Piezoceramic Actuators," *Master of Science Thesis in Mechanical Engineering*, VPI&SU.
- Fukada, E., 1955. "Piezoelectricity of Wood," *J. Phys. Soc. Japan*, 10(2), pp. 149-154.
- Fukada, E. and Yasuda, I., 1957. "On the Piezoelectric Effect of Bone," *J. Phys. Soc. Japan*, 12(10), pp. 1158-1162.
- Fukada, E., 1968. "Mechanical Deformation and Electrical Polarization in Biological Substances," *Biorheology*, 5(3), pp. 199-208.
- Fuller, C.R., 1989(a). "Active Control of Sound Transmission/Radiation from Elastic Plates by Vibration Inputs: I Analysis," *Journal of Sound and Vibration*, pp. 1-13.
- Fuller, C.R., Hansen, C.H. and Snyder, S.D., 1989(b). "Active Control of Structurally Radiated Noise Using Piezoceramic Actuators," *Inter-Noise 89*, pp. 509-511.

- Fuller, C.R., Rogers, C.A. and Robertshaw, H.H., 1989(c). "Active Control with Smart Structures," *Fiber Optic Smart Structures and Skins II*, edited by Eric Udd, SPIE Vol. 1170, pp. 338-358.
- Fuller, C.R., Gibbs, G.P. and Silcox, R.J., 1990(a). "Simultaneous Active Control of Flexural and Extensional Waves in Beams," *Journal of Intelligent Material Systems and Structures* 1(2), pp. 235-247.
- Fuller, C.R. and Burdisso, R.A., 1991(a). "A Wave Number Domain Approach to the Active Control of Structure-Borne Sound," *Journal of Sound and Vibration*, 148(2), pp. 335-360.
- Fuller, C.R., Hansen, C.H. and Snyder, S.D., 1991(b), "Active Control of Sound Radiation from a Vibrating Rectangular Panel by Sound Sources and Vibration Inputs: An Experimental Comparison," *Journal of Sound and Vibration*, 145(2), pp. 195-215.
- Jaffe, B., Roth, R.S. and Marzullo, S., 1954. "Piezoelectric Properties of Lead Zirconate-Lead Titanate Solid-Solution Ceramics," *J. Appl. Phys.*, 25(6), pp. 809-810.
- Jaffe, B., Cook, W.R. and Jaffe, H., 1971. *Piezoelectric Ceramics*, Vol. 3 of *Non-Metallic Solids*, J.P. Roberts and P. Popper, general editors, Academic Press Inc., London, 317 pages.
- Junger, M.C. and Feit, D., 1986. *Sound, Structures, and Their Interaction*, The MIT Press, Second Edition, pp. 216-228.
- Kawai, H. 1969. "The Piezoelectricity of Poly(vinylidene Fluoride)," *Jpn. J. Appl. Phys.*, 8(7), pp. 975-976.

- KYNAR Piezo Film Technical Manual*, 1987. Pennwalt Corp., Valley Forge, PA, 65 pages.
- Lee, C.K., Chiang, W.W. and O'Sullivan, T.C., 1989. "Piezoelectric Modal Sensors and Actuators Achieving Critical Damping on a Cantilever Plate," *AIAA Paper*, No. 89-1390.
- Lee, C.K., 1990(a). "Theory of Laminated Piezoelectric Plates for the Design of Distributed Sensors/Actuators: Part I. Governing Equations and Reciprocal Relationships," *The Journal of the Acoustical Society of America*, 87, pp. 1144-1158.
- Lee, C.K. and Moon, F.C., 1990(b). "Modal Sensors/Actuators," *ASME JAM*, Vol. 57, pp 434-441.
- Lee, C.K., Chiang, W.W. and O'Sullivan, T.C., 1991(a). "Piezoelectric Modal Sensor/Actuator Pairs for Critical Damping Vibration Control," *The Journal of the Acoustical Society of America*, 90(1), pp. 374-384.
- Lee, C.K. and O'Sullivan, T.C., 1991(b). "Piezoelectric Strain Rate Gages," *The Journal of the Acoustical Society of America*, 90(2), pp. 945-953.
- Lippmann, M.G., Sept. 1881. "Principe de la Conservation de l'Electricite ou Second Principe de la Theorie des Phenomenes Electriques [Principle of Conservation of Electricity or Second Principle of the Theory of Electrical Phenomena]," *J. phq.* 10, pp. 381-394.
- Maidanik, G., 1962, "Response of Ribbed Panels to Reverberant Acoustic Fields," *The Journal of the Acoustical Society of America*, 34(6), pp. 809-826.

- Maidanik, G., 1974. "Vibrational and Radiative Classification of Modes of a Baffled Finite Panel," *The Journal of the Acoustical Society of America*, 34(4), pp. 447-455.
- Meirovitch, L., 1967. *Analytical Methods in Vibrations*, Macmillan Publishing Co., New York, New York.
- Miller, D.W., and Hubbard, J.E., 1987. "Observability of a Bernoulli-Euler Beam Using PVF_2 as a Distributed Sensors," *Dynamics and Control of Large Structures: Proceedings of the 6th VPI&SU/AIAA Symposium*, edited by L. Meirovitch, pp. 375-390.
- Miller, D.W., Collins, S.A., and Peltzman, S.P., 1990. "Development of Spatially Convolution Sensors for Structural Control Applications," *AIAA Paper*, 90-1127-CP, pp. 2283-2297.
- Ochs, J. and Snowdon, J., 1975. "Transmissibility Across Simply Supported Plates with and without Damping Layers," *The Journal of the Acoustical Society of America*, 58, pp. 832-840.
- Petterson, O.K., 1979. "A Procedure for Determining the Sound Intensity Distribution Close to a Vibration Surface," *Journal of Sound and Vibration*, 66(4), pp. 626-629.
- Piezo Systems, 1987. *Piezoelectric Motor/Actuator Kit Manual*, Piezoelectric Products Inc., Cambridge, Maryland.
- Plump, J.M., Hubbard, J.E., and Bailey, T., 1987. "Nonlinear Control of a Distributed System: Simulation and Experimental Results," *Journal of Dynamic Systems, Measurement and Control*, Vol. 109, pp. 133-139.

- Schittkowski, K., "NLPQL: A FORTRAN Subroutine Solving Constrained Non-linear Programming Problems," (edited by Clyde L. Monma), *Annals of Operations Research*, Vol. 5, pp. 485-500.
- Smith, P.W., 1962. "Coupling of Sound and Panel Vibration below the Critical Frequency," *The Journal of the Acoustical Society of America*, 36(8), pp. 1516-1520.
- Swigert, C.J. and Forward, R.L., 1981. "Electronic Damping of Orthogonal Bending Modes in a Cylindrical Mast - Part I: Theory, Part II: Experiment," *Journal of Spacecraft and Rockets*, 18(1), pp. 5-17.
- Spectrum User's Manual, 1988. *4 Channel Analog I/O Board*, Version 2.1.
- Timoshenko, S., 1940. *Theory of Plates and Shells*, First Edition, pp. 440-447.
- User's Manual: IMSL Math/Library*, 1989. Version 1.1, pp. 897-902.
- Vipperman, J.S., Burdisso, R.A. and Fuller, C.R., 1991. "Active Control of Broad-band Structural Vibration Using the LMS Adaptive Algorithm," Submitted to the *Journal of Sound and Vibration*.
- Von Hippel, A., Breckenridge, R.G., Chesley, F.G. and Tisza, L., 1946. "High Dielectric Constant Ceramics," *Ind. Eng. Chem.*, 38(11), pp. 1097-1109.
- Wada, Y. and Hayakawa, R., 1976. "Piezoelectricity and Pyroelectricity of Polymers," *Jpn J. Appl. Phys.*, 15(11), pp. 2041-2057.
- Wallace, C.E., 1972(a) "Radiation Resistance of a Baffled Beam," *The Journal of the Acoustical Society of America*, 51(3), pp. 936-945.

- Wallace, C.E., 1972(b) "Radiation Resistance of a Rectangular Panel," *The Journal of the Acoustical Society of America*, 51(3), pp. 946-952.
- Wang, B.T. and Fuller, C.R., 1990. "Near-Field Pressure, Intensity and Wavenumber Distributions for Active Structural Control of Plate Radiation: Theoretical Analysis," Accepted for publication in *Journal of Sound and Vibration*.
- Wang, B.T., 1991(a). "Active Control of Sound Transmission/Radiation from Elastic Plates Using Multiple Piezoelectric Actuators," *Doctor of Philosophy Dissertation*, Mechanical Engineering Department, VPI&SU.
- Wang, B.T., Burdisso, R.A. and Fuller, C.R., 1991(b). "Optimal Placement of Piezoelectric Actuators for Active Control of Sound Radiation from Elastic Plates," *Proceedings of Noise-Con 91*, pp. 267-275.
- Wang, B.T., Dimitriadis, E.K. and Fuller, C.R., 1991(c). "Active Control of Structurally Radiated Noise Using Multiple Piezoelectric Actuators," *AIAA Journal*, 29(11), pp. 1802-1809.
- Widrow B. and Stearns, S.D., 1985. *Adaptive Signal Processing*, Prentice Hall Inc., Englewood Cliffs, NJ.
- Wul, B.M. and Goldman, I.M., 1945. "Dielectric Constants of Titanates of the Metals of the Second Group," *C.r. (Sov.)*, 46(4), pp. 139-42.
- Wul, B.M. and Vereshchagin, L.F., 1945. "Dependence of the Dielectric Constant of Barium Titanate Upon the Pressure," *C.r. (Sov.)*, 48(9), pp. 634-636.

Appendix A

PVDF Acoustic Sensor Model

A marked increase in sensitivity of the PVDF material to an acoustic pressure wave was observed as a result of curving the surface of the material as depicted in the coordinate system of Figure (2.6). Hence sensors were constructed in the form of shell segments, and the PVDF material was attached to a rigid frame as illustrated in the picture of Figure (5.1). Based on this configuration, the dynamic response of the cylindrical plate was derived from the equations of motion for the cylindrical shell (Junger and Feit, 1986), (Timoshenko, 1940):

$$\frac{\partial^2 u_1}{\partial x^2} + \frac{1-\nu}{2a^2} \frac{\partial^2 u_1}{\partial \phi^2} + \frac{1+\nu}{2a} \frac{\partial^2 u_2}{\partial x \partial \phi} - \frac{\nu}{a} \frac{\partial u_3}{\partial x} - \bar{C} \frac{\partial u_1}{\partial t} - \bar{\rho} \frac{\partial^2 u_1}{\partial t^2} = 0, \quad (\text{A.1})$$

$$\begin{aligned} & \frac{1+\nu}{2a} \frac{\partial^2 u_1}{\partial x \partial \phi} + \frac{1-\nu}{2} \frac{\partial^2 u_2}{\partial x^2} + \frac{1}{a^2} \frac{\partial^2 u_2}{\partial \phi^2} - \frac{1}{a^2} \frac{\partial u_3}{\partial \phi} + \frac{h^2}{12a^2} \left(\frac{\partial^3 u_3}{\partial x^2 \partial \phi} + \frac{\partial^3 u_3}{a^2 \partial \phi^3} \right) \\ & + \frac{h^2}{12a^2} \left[(1-\nu) \frac{\partial^2 u_2}{\partial x^2} + \frac{\partial^2 v}{a^2 \partial \phi^2} \right] - \bar{C} \frac{\partial u_2}{\partial t} - \bar{\rho} \frac{\partial^2 u_2}{\partial t^2} = 0, \end{aligned} \quad (\text{A.2})$$

and

$$\begin{aligned} & \frac{\nu}{a} \frac{\partial u_1}{\partial x} + \frac{\partial u_2}{a^2 \partial \phi} - \frac{u_3}{a^2} - \frac{h^2}{12} \left(\frac{\partial^4 u_3}{\partial x^4} + \frac{2}{a^2} \frac{\partial^4 u_3}{\partial x^2 \partial \phi^2} + \frac{\partial^4 u_3}{a^4 \partial \phi^4} \right) \\ & - \frac{h^2}{12} \left(\frac{2-\nu}{a^2} \frac{\partial^3 u_2}{\partial x^2 \partial \phi} + \frac{\partial u_2}{a^4 \partial \phi^3} \right) - \bar{C} \frac{\partial u_3}{\partial t} - \bar{\rho} \frac{\partial^2 u_3}{\partial t^2} = -\frac{P(1-\nu^2)}{Eh}, \end{aligned} \quad (\text{A.3})$$

where all dimensions are illustrated in Figure (2.6), $\bar{\rho} = \rho(1-\nu^2)/E$ and $\bar{C} = \frac{C}{ah} \frac{1-\nu^2}{E}$ as defined by Liang and Rogers (1991).

Since an exact solution for the shell segment depicted in Figure (2.6) does not exist, a set of admissible functions which satisfy the geometric and natural boundary conditions were assumed as discussed by Timoshenko (1940). If the steady-state harmonic excitation is assumed, then the forcing function can be expressed as follows:

$$P(x, \phi, t) = \sum_{m=1}^{\infty} \sum_{n=1}^{\infty} D_{mn} \sin\left(\frac{n\pi\phi}{\alpha}\right) \sin\left(\frac{m\pi x}{L}\right) \exp(j\omega t) \quad (\text{A.4})$$

where D_{mn} is given by

$$D_{mn} = \frac{4}{L\alpha} \int_0^L \int_0^\alpha \frac{P(x, \phi, t)}{\exp(j\omega t)} \sin\left(\frac{n\pi\phi}{\alpha}\right) \sin\left(\frac{m\pi x}{L}\right) d\phi dx, \quad (\text{A.5})$$

and all dimensions are defined in the coordinate system of Figure (2.6). Harmonic displacement responses for u_1 , u_2 and u_3 are assumed as follows which satisfy the geometric and natural boundary conditions:

$$u_1(t) = \sum_{m=1}^M \sum_{n=1}^N A_{mn} \sin\left(\frac{n\pi\phi}{\alpha}\right) \cos\left(\frac{m\pi x}{L}\right) \exp(j\omega t), \quad (\text{A.6})$$

$$u_2(t) = \sum_{m=1}^M \sum_{n=1}^N B_{mn} \cos\left(\frac{n\pi\phi}{\alpha}\right) \sin\left(\frac{m\pi x}{L}\right) \exp(j\omega t), \quad (\text{A.7})$$

$$u_3(t) = \sum_{m=1}^M \sum_{n=1}^N C_{mn} \sin\left(\frac{n\pi\phi}{\alpha}\right) \sin\left(\frac{m\pi x}{L}\right) \exp(j\omega t). \quad (\text{A.8})$$

Substituting the assumed response in the equations of motion, an expression for the expansion coefficients A_{mn} , B_{mn} and C_{mn} results:

$$\{[K]_{mn} + j\omega\bar{C}[I] - \omega^2\bar{\rho}[I]\} \{X\} = \{F\}, \quad (\text{A.9})$$

where

$$\{X\} = \left\{ \begin{array}{c} A_{mn} \\ B_{mn} \\ C_{mn} \end{array} \right\}, \quad (\text{A.10})$$

and

$$\{F\} = \left\{ \begin{array}{c} 0 \\ 0 \\ D_{mn} \frac{1-\nu^2}{Eh} \end{array} \right\}. \quad (\text{A.11})$$

The stiffness matrix is defined as follows:

$$[K] = \begin{bmatrix} \left(\frac{m\pi}{L}\right)^2 + \frac{1-\nu}{2a^2}\left(\frac{n\pi}{\alpha}\right)^2 & \frac{(1+\nu)m n \pi^2}{2aL\alpha} & \frac{\nu}{a}\left(\frac{m\pi}{L}\right) \\ \frac{(1+\nu)m n \pi^2}{2aL\alpha} & \frac{1-\nu}{2}\left(\frac{m\pi}{L}\right)^2 + \frac{1}{a^2}\left(\frac{n\pi}{\alpha}\right)^2 & \frac{1}{a^2}\left(\frac{n\pi}{\alpha}\right) \\ \frac{\nu}{a}\left(\frac{m\pi}{L}\right) & \frac{1}{a^2}\left(\frac{n\pi}{\alpha}\right) & \frac{1}{a^2} + \frac{\pi^4 h^2}{12a^4}\left[\left(\frac{m a}{L}\right)^2 + \left(\frac{n}{\alpha}\right)^2\right] \end{bmatrix} \quad (\text{A.12})$$

If we let $\bar{C} = 0$ and $\{F\} = 0$, we obtain the system of equations for the eigenvalues and eigenvectors:

$$\{[K] - \omega^2 \bar{\rho}[I]\} \{X\} = \{0\}. \quad (\text{A.13})$$

Hence the system of equations can be expressed in modal coordinates as follows:

$$[M]_{mn} \{\ddot{x}(t)\}_{mn} + [K]_{mn} \{x(t)\}_{mn} = \{Q(t)\}_{mn} \quad (\text{A.14})$$

where

$$[M]_{mn} = \begin{bmatrix} \bar{\rho} & 0 & 0 \\ 0 & \bar{\rho} & 0 \\ 0 & 0 & \bar{\rho} \end{bmatrix}, \quad (\text{A.15})$$

$$\{x(t)\}_{mn} = \begin{Bmatrix} A_{mn} \\ B_{mn} \\ C_{mn} \end{Bmatrix} \exp(j\omega t), \quad (\text{A.16})$$

$$\{Q(t)\}_{mn} = \left\{ \begin{array}{c} 0 \\ 0 \\ D_{mn} \frac{1-\nu^2}{Eh} \end{array} \right\} \exp(j\omega t), \quad (\text{A.17})$$

and $[K]_{mn}$ is defined in equation (A.12).

We must first solve,

$$[M]_{mn}[u]_{mn}[\omega^2]_{mn} = [K]_{mn}[u]_{mn} \quad (\text{A.18})$$

where $[u]_{mn}$ is the modal matrix and $[\omega^2]_{mn}$ is the diagonal matrix of natural frequencies squared. If we normalize such that

$$[u]_{mn}^T [M]_{mn} [u]_{mn} = [I], \quad (\text{A.19})$$

and

$$[u]_{mn}^T [K]_{mn} [u]_{mn} = [\omega^2], \quad (\text{A.20})$$

and let

$$\{x(t)\} = [u]_{mn} \{\eta(t)\}_{mn}, \quad (\text{A.21})$$

the resulting system of equations can be expressed as follows:

$$[M]_{mn}[u]_{mn}\{\ddot{\eta}(t)\}_{mn} + [K]_{mn}[u]_{mn}\{\eta(t)\}_{mn} = \{Q(t)\}_{mn}. \quad (\text{A.22})$$

If we premultiply equation (A.22) by $[u]_{mn}^T$, we obtain:

$$[I]\{\ddot{\eta}(t)\}_{mn} + [\omega^2]_{mn}\{\eta(t)\}_{mn} = \{N(t)\}_{mn}, \quad (\text{A.23})$$

where

$$\{N(t)\}_{mn} = [u]_{mn}^T\{Q(t)\}_{mn}. \quad (\text{A.24})$$

Hence we obtain a system of equations for each assumed displacement response function as follows:

$$\{\ddot{\eta}^{(r)}(t)\}_{mn} + (\omega_{mn}^{(r)})^2\{\eta^{(r)}(t)\}_{mn} = \{N^{(r)}(t)\}_{mn}, \quad (\text{A.25})$$

where the superscript (r) is used to designate each respective direction of displacement, u_1 , u_2 and u_3 . The system response in normalized modal coordinates can thus be expressed as follows:

$$\eta_{mn}^{(r)}(t) = \frac{1}{\omega_{mn}^{(r)}} \int_0^t N_{mn}^{(r)}(t) \sin(\omega_{mn}^{(r)}(t - \tau)) d\tau. \quad (\text{A.26})$$

Since $\{\ddot{\eta}(t)\}_{mn} = -\omega^2\{\eta(t)\}_{mn}$, one can express the harmonic solution of the system of equations as follows:

$$\{\eta(t)\}_{mn} = [\Lambda]_{mn}^{-1}[u]_{mn}^T\{Q(t)\}_{mn}, \quad (\text{A.27})$$

where

$$[\Lambda]_{mn}^{-1} = \begin{bmatrix} \frac{1}{(\omega_{mn}^{(1)})^2 - \omega^2} & 0 & 0 \\ 0 & \frac{1}{(\omega_{mn}^{(2)})^2 - \omega^2} & 0 \\ 0 & 0 & \frac{1}{(\omega_{mn}^{(3)})^2 - \omega^2} \end{bmatrix}. \quad (\text{A.28})$$

Replacing $\{\eta(t)\}_{mn}$ with $[u]_{mn}^T\{x(t)\}$, the system response can be expressed as a function of the modal amplitudes:

$$\{X\} = [T]_{mn}\{F\} \quad (\text{A.29})$$

where

$$[T]_{mn} = [u]_{mn}[\Lambda]_{mn}^{-1}[u]_{mn}^T. \quad (\text{A.30})$$

All that remains is to expand the input disturbance as a function of the eigenfunctions chosen for the out of plane displacement u_3 . Two types of forcing functions were chosen. The first was based upon a harmonic uniform pressure distributed normal to the surface of the shell segment. The forcing function is representative of

the response induced when the sensor is positioned in the standing wave guide and calibrated. Hence the input is expressed as follows:

$$P(t) = \bar{P} \exp(j\omega t)(u(x) - u(x - L))(u(\phi) - u(\phi - \alpha)). \quad (\text{A.31})$$

Therefore,

$$\bar{P} = \sum_{m=1}^{\infty} \sum_{n=1}^{\infty} D_{mn} \sin\left(\frac{m\pi x}{L}\right) \sin\left(\frac{n\pi \phi}{\alpha}\right), \quad (\text{A.32})$$

Multiplying equation (A.32) by $\sin(\frac{i\pi x}{L})$ and $\sin(\frac{j\pi \phi}{\alpha})$ and integrating over the boundaries, we obtain:

$$D_{mn} = \frac{4\bar{P}}{mn\pi^2} (1 - \cos(n\pi))(1 - \cos(m\pi)). \quad (\text{A.33})$$

A similar expression can be obtained assuming that the pressure varies over the surface of application. If the sensor is broken into N_α elements in the ϕ -direction and N_L elements in the x -direction respectively, then the input pressure loading over each respective element must be used to compute the total response of the cylindrical plate.

$$P(t) = \bar{P} \exp(j\omega t)[u(x - x_i) - u(x - x_{i+1})][u(\phi - \phi_j) - u(\phi - \phi_{j+1})]. \quad (\text{A.34})$$

where the subscripts i and j range from 1 to N_L and 1 to N_α respectively. Multi-

plying equation (A.34) by $\sin(\frac{i\pi x}{L})$ and $\sin(\frac{j\pi\phi}{\alpha})$ and integrating over the boundaries, we obtain:

$$D_{mn} = \frac{4\bar{P}}{mn\pi^2} (\cos(n\pi\phi_i/\alpha) - \cos(n\pi\phi_{i+1}/\alpha)) \times (\cos(m\pi x_i/L) - \cos(m\pi x_{i+1}/L)). \quad (\text{A.35})$$

This expression can be used to compute the distributed response of the sensor for a finite number of acoustic inputs as illustrated in Figure (4.10). Hence an approximate model for the dynamic response of the cylindrical plate can be obtained as a superposition of the modal response resulting from a finite number of acoustic disturbances in equation (A.35). For both loads previously discussed, \bar{P} is used to represent the input pressure applied over the area of interest.

In either case, we seek the strain resulting from the dynamic response of the cylindrical plate such that the electrical output of the PVDF sensor can be computed. To this end, expressions for the strain in the x and ϕ -directions are given as follows:

$$\epsilon_x = \frac{\partial u_1}{\partial x} = - \sum_{m=1}^M \sum_{n=1}^N \frac{m\pi}{L} A_{mn} \sin\left(\frac{n\pi\phi}{\alpha}\right) \sin\left(\frac{m\pi x}{L}\right), \quad (\text{A.36})$$

and

$$\epsilon_\phi = \frac{\partial u_2}{a\partial\phi} - \frac{u_3}{a}$$

$$= -\frac{1}{a} \sum_{m=1}^M \sum_{n=1}^N \left(\frac{n\pi}{\alpha} B_{mn} + C_{mn} \right) \sin\left(\frac{n\pi\phi}{\alpha}\right) \sin\left(\frac{m\pi x}{L}\right), \quad (\text{A.37})$$

The electrical response of the PVDF acoustic near-field sensor can thus be expressed as a function of the strain by integrating over the surface of the sensor with respect to the stress/charge constants, e_{31} and e_{32} , as follows:

$$q(t) = \int_0^L \int_0^\alpha (e_{31}\epsilon_\phi + e_{32}\epsilon_x) a d\phi dx \exp(j\omega t). \quad (\text{A.38})$$

Substituting equation (A.36) and equation (A.37) into equation (A.38), and evaluating the integrals, an expression for the electrical response of the sensor as a function of the modal response and stress per charge constants is obtained:

$$q(t) = - \sum_{m=1}^M \sum_{n=1}^N \left[\left(\frac{ae_{32}\alpha}{n\pi} \right) A_{mn} + e_{31} \left\{ \left(\frac{L}{m\pi} \right) B_{mn} + \left(\frac{\alpha L}{mn\pi^2} \right) C_{mn} \right\} \right] \times (1 - \cos(n\pi))(1 - \cos(m\pi)) \exp(j\omega t). \quad (\text{A.39})$$

Given the above expression, the electrical response of the material can be computed for any given forcing function which can be expanded in terms of the assumed solution. Since the units on the stress/charge constants, e_{31} and e_{32} , are in terms of C/m^2 , the response of the sensor is in units of charge, C .

Appendix B

Example of Model Reference Uniqueness

In the example, the original cost function is formulated in terms of the acoustic response, and three unique coordinates are chosen to minimize the response. To simplify the example, only one control actuator is used to achieve control. Referring to equation (3.12), an expression for the optimal control voltage is obtained in terms of the transfer functions between the three error sensors and the control actuator as well as the disturbance.

$$(T_{11}T_{11}^* + T_{21}T_{21}^* + T_{31}T_{31}^*)^p \hat{V}_1^p + (T_{1D}T_{11}^* + T_{2D}T_{21}^* + T_{3D}T_{31}^*)^p F = 0. \quad (\text{B.1})$$

In the above equation, the superscript p is use to denote that the transfer functions were formulated in terms of acoustic pressure at chosen field points. The optimal control voltage can be obtained as follow:

$$\hat{V}_1^p = - \left(\frac{T_{1D}T_{11}^* + T_{2D}T_{21}^* + T_{3D}T_{31}^*}{T_{11}T_{11}^* + T_{21}T_{21}^* + T_{31}T_{31}^*} \right)^p F. \quad (\text{B.2})$$

With this optimal control voltage for the piezoceramic actuator, the modal amplitudes for the structural response can be obtained from equations (2.6) and (2.14) as follows:

$$W_m = W_m^F + W_m^{PP}. \quad (\text{B.3})$$

Upon obtaining the above modal amplitudes, the necessary information required to compute the reference response results. Since only one control actuator is used to obtain the desired acoustic response, only one structural sensor is required in the model reference approach to obtain the same controlled response. The cost function presented in equation (3.15) is now formulated in terms of the structural response where the desired response at any arbitrary coordinate on the beam is expressed as follow:

$$r\hat{e}f(x_1) = \sum_{m=1}^M (W_m^F + W_m^{PP}) \sin(\gamma_m x_1). \quad (\text{B.4})$$

Substituting equation (B.4) into equation (3.16) yields:

$$(T_{11}T_{11}^*)^a \hat{V}_1^a + (T_{1D}T_{11}^*)^a F - \left(\sum_{m=1}^M (W_m^F + W_m^{PP}) \sin(\gamma_m x_1) \right) T_{11}^* = 0, \quad (\text{B.5})$$

where the superscript a is used to differentiate the transfer functions and control voltage for the structural response from the transfer functions and control voltage previously defined in terms of the pressure. The transfer function between the structural response at coordinate x_1 and the input force, F , can be expressed as

below:

$$T_{1D}^a = \frac{1}{F} \sum_{m=1}^M W_m^F \sin(\gamma_m x_1) \quad (\text{B.6})$$

Substituting equation (B.6) into equation (B.5), we obtain:

$$T_{11}^a \hat{V}_1^a + T_{1D}^a F - \left(T_{1D}^a F + \sum_{m=1}^M W_m^{PP} \sin(\gamma_m x_1) \right) = 0. \quad (\text{B.7})$$

The expression for the modal amplitudes was given in equation (2.14) as a function of the voltage applied to the piezoelectric actuator. For simplicity, all constants in equation (2.14) will be represented by K_m^1 , and the modal amplitudes resulting from the optimal voltage obtained for minimization of the pressure can be expressed as follows:

$$W_m^{PP} = K_m^1 \hat{V}_1^p = -K_m^1 \left(\frac{T_{1D}T_{11}^* + T_{2D}T_{21}^* + T_{3D}T_{31}^*}{T_{11}T_{11}^* + T_{21}T_{21}^* + T_{31}T_{31}^*} \right)^p F. \quad (\text{B.8})$$

Substituting equation (B.8) into equation (B.7), and cancelling like terms, we see that the optimal voltage obtained from the model reference control approach is a function of the transfer functions for the far-field pressure.

$$T_{11}^a \hat{V}_1^a = - \sum_{m=1}^M K_m^1 \left(\frac{T_{1D}T_{11}^* + T_{2D}T_{21}^* + T_{3D}T_{31}^*}{T_{11}T_{11}^* + T_{21}T_{21}^* + T_{31}T_{31}^*} \right)^p F \sin(\gamma_m x_1). \quad (\text{B.9})$$

The transfer function between the structural response at coordinate x_1 and the input

voltage can be simply expressed as:

$$T_{11}^a = \sum_{m=1}^M \frac{W_m^{Pa}}{\hat{V}_1^a} \sin(\gamma_m x_1) \quad (\text{B.10})$$

Substituting equation (B.10) into equation (B.9) and cancelling like terms, the modal amplitudes resulting from model reference control can be expressed simply as a function of the acoustic transfer functions.

$$\sum_{m=1}^M W_m^{Pa} \sin(\gamma_m x_1) = - \sum_{m=1}^M K_m^1 \left(\frac{T_{1D}T_{11}^* + T_{2D}T_{21}^* + T_{3D}T_{31}^*}{T_{11}T_{11}^* + T_{21}T_{21}^* + T_{31}T_{31}^*} \right)^p \times F \sin(\gamma_m x_1); \quad (\text{B.11})$$

therefore,

$$W_m^{Pa} = -K_m^1 \left(\frac{T_{1D}T_{11}^* + T_{2D}T_{21}^* + T_{3D}T_{31}^*}{T_{11}T_{11}^* + T_{21}T_{21}^* + T_{31}T_{31}^*} \right)^p F. \quad (\text{B.12})$$

Since the modal amplitudes resulting from model reference control implementing a single structural sensor are identical to those obtained by minimizing the far-field pressure at three error sensor locations, the resulting control voltage applied to the piezoceramic actuator must be the same as that obtained when implementing the acoustic cost function. The previous example can readily be generalized for an arbitrary but equal number of actuators and error sensors.

Appendix C

Modal Decomposition

The modal decomposition follows a method previously outlined by Hansen *et al.*, (1989). For a simply supported plate, the displacement response, w , can be represented as follows

$$w(x, y, t) = \sum_{m=1}^{\infty} \sum_{n=1}^{\infty} A_{mn} \sin\left(\frac{m\pi x}{L_x}\right) \sin\left(\frac{n\pi y}{L_y}\right) \exp(j\omega t) \quad (\text{C.1})$$

where m and n represent the mode number, L_x and L_y are the plate dimensions, ω is the frequency of vibration, and A_{mn} are the modal amplitudes.

Nine accelerometers were randomly placed on the plate, and an additional reference accelerometer was placed on the plate away from nodal lines of modes desired in the decomposition. Since only two channels of A/D were available on the spectrum analyzer, a reference accelerometer was required to obtain phasing of the measurements. The frequency response function between each randomly placed accelerometer and the reference accelerometer was measured as well as the autospectrum of the reference accelerometer. The autospectrum provides a means of scaling the data in

terms of engineering units. By computing the frequency response function, phase information is also obtained. If the plate is assumed to respond as predicted in the theoretical analysis, a matrix of spatial coefficients can be generated from the theoretical eigenvectors by substituting the spatial coordinates of the randomly positioned accelerometers into the equation. For nine independent measurements, nine distinct modal amplitudes can be computed, resulting in a nine by nine matrix of the eigenvectors. After measuring the acceleration at each of these coordinates, a system of linear algebraic equations results.

$$[W] = [S][A] \tag{C.2}$$

where the matrix of measurements is

$$[W] = \begin{bmatrix} W_1 \\ \bullet \\ \bullet \\ \bullet \\ W_k \end{bmatrix} \tag{C.3}$$

while modal amplitudes are

$$[A] = \begin{bmatrix} A_{11} \\ \bullet \\ \bullet \\ \bullet \\ A_{ij} \end{bmatrix} \tag{C.4}$$

and the matrix of spatial functions is

$$[S] = \begin{bmatrix} S_{11}^1 & S_{12}^1 & S_{21}^1 & \bullet & S_{ij}^1 \\ S_{11}^2 & S_{12}^2 & S_{21}^2 & \bullet & S_{ij}^2 \\ S_{11}^3 & S_{12}^3 & S_{21}^3 & \bullet & S_{ij}^3 \\ \bullet & \bullet & \bullet & \bullet & \bullet \\ S_{11}^p & S_{12}^p & S_{21}^p & \bullet & S_{ij}^p \end{bmatrix} \quad (C.5)$$

where

$$S_{ij}^p = \sin\left(\frac{i\pi x_p}{L_x}\right) \sin\left(\frac{j\pi y_p}{L_y}\right) \quad (C.6)$$

In the above equation, i and j represent the mode number. Each of the spatial coordinates of the randomly placed accelerometers are designated with (x_p, y_p) where p is the number of measurements taken. The modal accelerations were extracted by solving this system of linear equations. If measurements are taken such that the system is overdetermined, a least mean squares approach can be taken to solve for the desired modal amplitudes.

Since there are a finite number of measurements, spatial aliasing can result. When nine measurements are made, only nine modal amplitudes can be resolved for a structure whose response is typically represented with an infinite number of modes. As a result, response of higher modes can “fold back” into the lower modes (i.e. the nine computed). When applying this technique, the response of the higher modes must be assumed negligible. This can be checked by observing the roll off in the

amplitudes of the higher order modes when included in the solution. To this end, the excitation frequency of the structure should be well below the resonant frequency of the highest mode which can be resolved.

Note that this method decomposes a system response into amplitudes or coefficients corresponding to the basis functions of equation (10). For the open loop case, these basis functions correspond to the modes of the system. For the closed loop case, the system will have new mode shapes and resonant frequencies (Burdisso and Fuller, 1991). However, it is convenient to decompose the closed loop response into the open loop modal components so that a direct comparison of the component changes can be made.

Appendix D

Assumed Modes Method

The concentrated mass due to the shaker and the end torsional springs resulting from the shim stock at the boundaries of the simply supported plate are included in the dynamic model by the assumed modes method (Meirovitch, 1967, Burdisso and Fuller, 1992). A schematic diagram of the mass loading and torsional spring boundary conditions is presented in Figure D.1. The normalized mode shapes of the simply supported plate

$$\phi_{rs}(x, y) = \frac{2}{\sqrt{\rho'' L_x L_y}} \sin\left(\frac{r\pi x}{L_x}\right) \sin\left(\frac{s\pi y}{L_y}\right) \quad (\text{D.1})$$

are selected as admissible functions. The response of the plate can thus be expanded as

$$w(x, y, t) = \sum_{r=1}^M \sum_{s=1}^N \phi_{rs}(x, y) a_{rs} \exp(j\omega t) \quad (\text{D.2})$$

where a_{rs} are the modal expansion coefficients. Equation (D.2) can then be used to compute the strain and kinetic energy of the system respectively as follows:

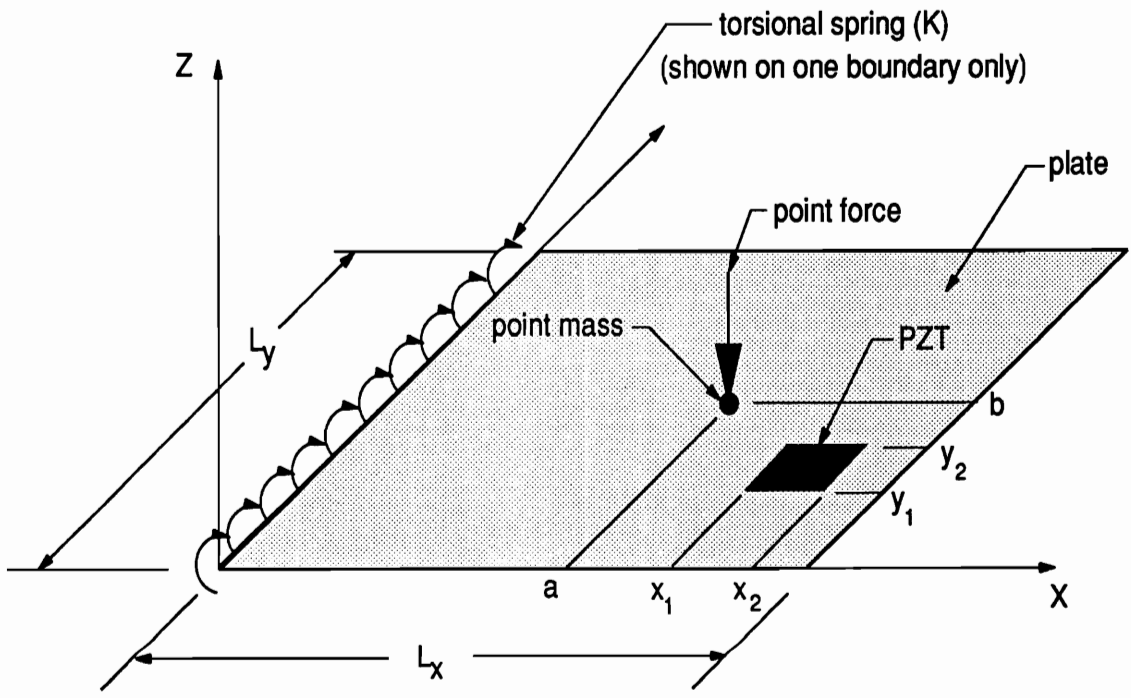


Figure D.1: Schematic of Plate Configured with Mass and Spring Boundaries

$$V(t) = \frac{1}{2} \int_0^{L_x} \int_0^{L_y} D_e [\nabla^2 w(x, y, t)]^2 dy dx + \frac{1}{2} K \left[\frac{\partial w(0, y, t)}{\partial x} \right]^2 + \frac{1}{2} K \left[\frac{\partial w(L_x, y, t)}{\partial x} \right]^2 + \frac{1}{2} K \left[\frac{\partial w(x, 0, t)}{\partial y} \right]^2 + \frac{1}{2} K \left[\frac{\partial w(x, L_y, t)}{\partial y} \right]^2 \quad (D.3)$$

and

$$T(t) = \frac{1}{2} \int_0^{L_x} \int_0^{L_y} \rho''(x, y) \left[\frac{\partial w(x, y, t)}{\partial t} \right]^2 dx dy + \frac{1}{2} M \left[\frac{\partial w(a, b, t)}{\partial t} \right]^2 \quad (D.4)$$

where $V(t)$ is the strain energy, $T(t)$ is the kinetic energy, K is the torsional spring constant, M is the concentrated mass and the spatial coordinates (a, b) define the position of the shaker (i.e. M) on the structure. Substituting equation (D.2) into equations (D.3) and (D.4) and applying Lagrange's equations (Meirovitch, 1967), the eigenvalue problem can be written as follows:

$$[K]\bar{a} = \omega^2[M]\bar{a}, \quad (D.5)$$

where $[K]$ is the stiffness matrix, $[M]$ is the mass matrix and $\bar{a} = \{a_{11}, \dots, a_{MN}\}^T$. The dimension of the matrix is thus $MN \times MN$ and the elements are given as follows:

$$k_{rskl} = \delta_{rk}\delta_{sl}\omega_{rs}^2 + K \left[\frac{\partial \phi_{rs}}{\partial x} \Big|_{x=0} \frac{\partial \phi_{kl}}{\partial x} \Big|_{x=0} + \frac{\partial \phi_{rs}}{\partial x} \Big|_{x=L_x} \frac{\partial \phi_{kl}}{\partial x} \Big|_{x=L_x} + \frac{\partial \phi_{rs}}{\partial y} \Big|_{y=0} \frac{\partial \phi_{kl}}{\partial y} \Big|_{y=0} + \frac{\partial \phi_{rs}}{\partial y} \Big|_{y=L_y} \frac{\partial \phi_{kl}}{\partial y} \Big|_{y=L_y} \right], \quad (D.6)$$

and

$$m_{rskl} = \delta_{rk}\delta_{sl} + M\phi_{rs}(a, b)\phi_{kl}(a, b) \quad (D.7)$$

where

$$\omega_{rs}^2 = \frac{D_e}{\rho''} \pi^4 \left[\left(\frac{r}{L_x} \right)^2 + \left(\frac{s}{L_y} \right)^2 \right]^2 \quad (D.8)$$

are the eigenvalues of the simply supported plate.

Upon solving the eigenvalue problem for the modified system of equation (D.5), $M \times N$ eigenvalues and corresponding eigenvectors are obtained. The eigenfunctions for the modified system are thus expressed as follows:

$$\Psi_{mn}(x, y) = \sum_{i=1}^M \sum_{j=1}^N \phi_{ij}(x, y) a_{ijmn}. \quad (D.9)$$

The modal expression for the point force induced response of equation (2.6) and the piezoelectric actuator induced response of equation (2.14) can then be expressed respectively as follows:

$$W_{mn}^F = \frac{4F}{\rho'' L_x L_y} \frac{\sum_{i=1}^M \sum_{j=1}^N a_{mni} \sin\left(\frac{i\pi a}{L_x}\right) \sin\left(\frac{j\pi b}{L_y}\right)}{(\omega_{mn}^2 - \omega^2)}, \quad (D.10)$$

and

$$W_{mn}^P = \frac{-4C_o \epsilon_{pe} \sum_{i=1}^M \sum_{j=1}^N a_{mni} \frac{\gamma_i^2 + \gamma_j^2}{\gamma_i \gamma_j} g_i(x_1, x_2) f_j(y_1, y_2)}{\rho'' L_x L_y (\omega_{mn}^2 - \omega^2)} \quad (\text{D.11})$$

where

$$g_i(x_1, x_2) = \cos(\gamma_i x_1) - \cos(\gamma_i x_2), \quad (\text{D.12})$$

$$f_j(y_1, y_2) = \cos(\gamma_j y_1) - \cos(\gamma_j y_2), \quad (\text{D.13})$$

$$\gamma_i = i\pi/L_x \quad (\text{D.14})$$

and

$$\gamma_j = j\pi/L_y. \quad (\text{D.15})$$

Hence these models can be used to predict both the structural and acoustic response of the plate to account for the mass loading and non-ideal boundary conditions. In the results of chapter 6, all predicted acoustic directivity patterns were computed based upon the assumed modes method to obtain better correlation between theory and experiment.

Vita

Robert L. Clark, Jr. was born in Clifton Forge, Virginia on January 10, 1964 and was raised in Alleghany County, Virginia, where he graduated from Alleghany County High School in 1982. Upon graduating he enrolled in the school of engineering at Virginia Polytechnic Institute and State University that same year, where he received a Bachelor of Science degree in mechanical engineering in 1987. He immediately enrolled in graduate school and obtained a Master of Science in mechanical engineering from VPI&SU in 1988. He was then hired by Michelin America Research and Development Corporation in Greenville, South Carolina, where he spent more than a year working in the Noise and Vibration group. After much consideration and discussion with Dr. Chris Fuller, he and his wife decided to return to Blacksburg in 1989 to work on a Ph.D. in the area of active structural acoustic control. In February 1992, he completed his Ph.D. in mechanical engineering and accepted a position as a research associate at VPI&SU under the ONR contract. He, his wife, Dana L. Clark and his son, Trey Clark will reside in Christiansburg, Virginia until permanent employment in industry or at a university is secured.

A handwritten signature in black ink that reads "Robert L. Clark Jr." The signature is written in a cursive style with a large initial 'R' and 'C'.